Feasibility Studies towards Accessing Generalised Distribution Amplitudes in Exclusive γ-Meson and $\gamma\gamma$ Production with $\overline{\mathrm{P}}$ANDA at FAIR

Dissertation zur Erlangung des Doktorgrades (Dr. rer. nat.)

im Fachgebiet Experimentalphysik
Prof. Dr. Kai-Thomas Brinkmann
II. Physikalisches Institut
Justus-Liebig-Universität Gießen

vorgelegt von

Faiza Khalid

Gießen, 2025

Zusammenfassung

Das Verständnis der fundamentalen Eigenschaften und Wechselwirkungen des Protons bleibt ein zentrales Thema der modernen Hadronenphysik. Seine innere Struktur sowie die Dynamik hadronischer Prozesse lassen sich durch exklusive Reaktionen untersuchen, die auf der Annihilation von Antiprotonen mit Protonen basieren.

Diese Arbeit präsentiert eine Untersuchung von drei exklusiven Kanälen: $\bar{p}p \to \pi^0\gamma$, $\bar{p}p \to \pi^0\pi^0$ und $\bar{p}p \to \gamma\gamma$, mit besonderem Fokus auf ihr Potenzial zur Erforschung der Nukleonstruktur und der Reaktionsdynamik. Die Studien wurden bei vier diskreten Strahlimpulsen von 2,5, 5, 10 und 15 GeV/c durchgeführt. Diese Untersuchungen erfolgen im Rahmen des $\overline{\text{P}}$ANDA-Experiments an der zukünftigen FAIR-Anlage in Darmstadt, welche einen hochintensiven Antiprotonenstrahl im Impulsbereich von 1,5 bis 15 GeV/c einsetzen wird. Datensätze sowohl für das Signal als auch für alle relevanten Untergrundkanäle wurden mithilfe der PandaRoot-Software generiert und simuliert. Die Studie umfasst die Optimierung des Signal-zu-Untergrund-Verhältnisses, Schätzungen der Ereignisraten sowie die Bestimmung der erwarteten Wirkungsquerschnitte mitsamt statistischer Unsicherheiten.

Die Ergebnisse zeigen, dass alle relevanten Untergrundkanäle ausreichend unterdrückt werden können. Damit wird die Durchführbarkeit der Messung dieser Reaktionen bei $\overline{\text{P}}$ANDA mit der nötigen Genauigkeit bestätigt, um wesentlich zum Verständnis der Hadronenstruktur im zeitartigen Bereich beizutragen.

Abstract

Understanding the fundamental properties and interactions of the proton remains a central focus in contemporary hadron physics. Its internal structure and the dynamics of hadronic interactions can be explored through exclusive reactions involving antiproton-proton annihilation.

This work presents a study of three exclusive channels: $\bar{p}p \to \pi^0\gamma$, $\bar{p}p \to \pi^0\pi^0$, and $\bar{p}p \to \gamma\gamma$, with a focus on their potential to probe nucleon structure and reaction dynamics. The studies are performed at four discrete beam momenta of 2.5, 5, 10, and 15 GeV/c. These investigations are carried out in the framework of the $\overline{\mathrm{P}}$ANDA experiment at the upcoming FAIR facility in Darmstadt, which will utilize a high-intensity antiproton beam in the momentum range of 1.5–15 GeV/c. Data samples for both the signal and all relevant background channels were generated and simulated using the PandaRoot framework. This study includes the optimization of the signal-to-background ratio, estimation of count rates, and determination of expected cross sections along with their statistical uncertainties.

The results demonstrate that all relevant background channels can be sufficiently suppressed, confirming the feasibility of measuring these reactions at $\overline{\mathrm{P}}$ANDA with sufficient accuracy to significantly advance the understanding of hadron structure in the time-like regime.

Contents

1 | Introduction

Protons are among the fundamental building blocks of the visible universe. As constituents of atomic nuclei, they play a central role in the structure of matter. Despite their apparent simplicity, a complete understanding of the proton's internal dynamics remains one of the key challenges in modern hadron physics. The strong force, described by Quantum Chromodynamics (QCD), governs the behavior of the quarks and gluons inside the proton, but many aspects of their interactions—particularly in the non-perturbative regime—are still being uncovered. A key to unraveling this structure lies in the study of exclusive processes that access complex partonic correlations beyond what is revealed in inclusive scattering. In this context, Generalized Parton Distributions (GPDs) and their crossed-channel counterparts, Generalized Distribution Amplitudes (GDAs), provide a powerful formalism to probe the three-dimensional structure of hadrons.

To investigate such phenomena experimentally, the $\overline{\text{P}}$ANDA detector at the upcoming FAIR facility is designed to explore a wide range of hadronic interactions, including those sensitive to GDA dynamics. This work presents a detailed simulation study of several exclusive final states that serve as potential channels to access GDA-related observables. The work is grounded in the $\overline{\text{P}}$ANDA physics program and makes use of dedicated simulation and reconstruction tools to model detector performance and signal extraction.

The first chapter of this work begins with a general motivation for studying the internal structure of hadrons, particularly the proton, and introduces the formalism of Generalized Distribution Amplitudes (GDAs) as a powerful tool for exploring hadron dynamics. The second chapter presents the $\overline{\text{P}}$ANDA physics program, highlighting its potential to address key questions in hadronic structure and spectroscopy. The relevance of $\overline{\text{P}}$ANDA to GDA-related studies is discussed, along with its broader scientific goals.

The third chapter introduces the theoretical foundations of Generalized Parton Distributions (GPDs) and Generalized Distribution Amplitudes (GDAs). The formalism is briefly reviewed, and its application to crossed-channel processes such as two-photon production and meson pair production is outlined. Chapter four provides a technical overview of the $\overline{\text{P}}$ANDA detector and the FAIR facility. The key subsystems of $\overline{\text{P}}$ANDA are described,

with a particular focus on the electromagnetic calorimeter and its role in photon detection. The fifth chapter details the simulation and reconstruction framework used throughout this work. The PandaRoot software, event generation chain, and photon reconstruction algorithms are introduced, along with relevant analysis tools.

Chapters six through eight present simulation studies of three exclusive channels: $\bar{p}p \to \pi^0\gamma$, $\bar{p}p \to \pi^0\pi^0$, and $\bar{p}p \to \gamma\gamma$. Each chapter includes the event selection strategy, methods of background suppression, and count rate estimation. Differential cross-section results are presented where applicable. The $\pi^0\gamma$ and $\gamma\gamma$ channels are of particular interest as they provide access to time-like Generalized Distribution Amplitudes (GDAs) and enable the exploration of nucleon structure and QCD dynamics in a novel regime accessible at $\overline{\text{P}}$ANDA. In contrast, the $\pi^0\pi^0$ channel does not probe GDAs directly but was studied as a key background process that needs to be accurately modeled and subtracted in the analysis of the signal channels.

2 | The $\overline{\text{P}}$ANDA Physics Program

The $\overline{\text{P}}$ANDA (antiProton ANnihilation at DArmstadt) experiment is planned to be one of the key projects at the future research complex FAIR (Facility for Antiproton and Ion Research) at Darmstadt (Germany). Situated at at the High Energy Storage Ring (HESR), it is anticipated that the $\overline{\text{P}}$ANDA detector will conduct investigations into the interactions between the antiproton beam and stationary target protons and nuclei. The antiprotons involved will provide momenta ranging from 1.5 GeV/c to 15 GeV/c, corresponding to center-of-mass energies between $\sqrt{s} = 2.25\,\text{GeV}$ and $\sqrt{s} = 5.47\,\text{GeV}$. Data gathering with high statistics will be feasible due to the large acceptance of the $\overline{\text{P}}$ANDA detector and its exceptional capacity to detect charged and neutral particles. .

The scientific agenda of $\overline{\text{P}}$ANDA geared towards addressing fundamental questions in QCD, particularly in the non-perturbative regime. It will provide an excellent platform to investigate QCD bound states like charmonium, D-mesons and baryon states as well as search for gluonic excitations would greatly advance our knowledge of QCD dynamics. The second focal point of research of $\overline{\text{P}}$ANDA physics program involves exploring nuclear structure. This area will primarily explore the time-like form factors of the proton, transition distribution amplitudes, and parton distributions. Furthermore, $\overline{\text{P}}$ANDA will explore the characteristics of hadrons in various states of matter and conduct investigations into hypernuclei. Figure 2.1 illustrates the research topics that can be explored with $\overline{\text{P}}$ANDA's energy level. In this figure, the blue dashed lines indicates the accessible mass range. This energy span aligns with the non-perturbative regime of QCD and facilitates the generation of heavy hadrons containing strange and charm quarks.

The following section provides an overview of the scientific program, highlighting its various physics cases. Additional details can be found in the [2].

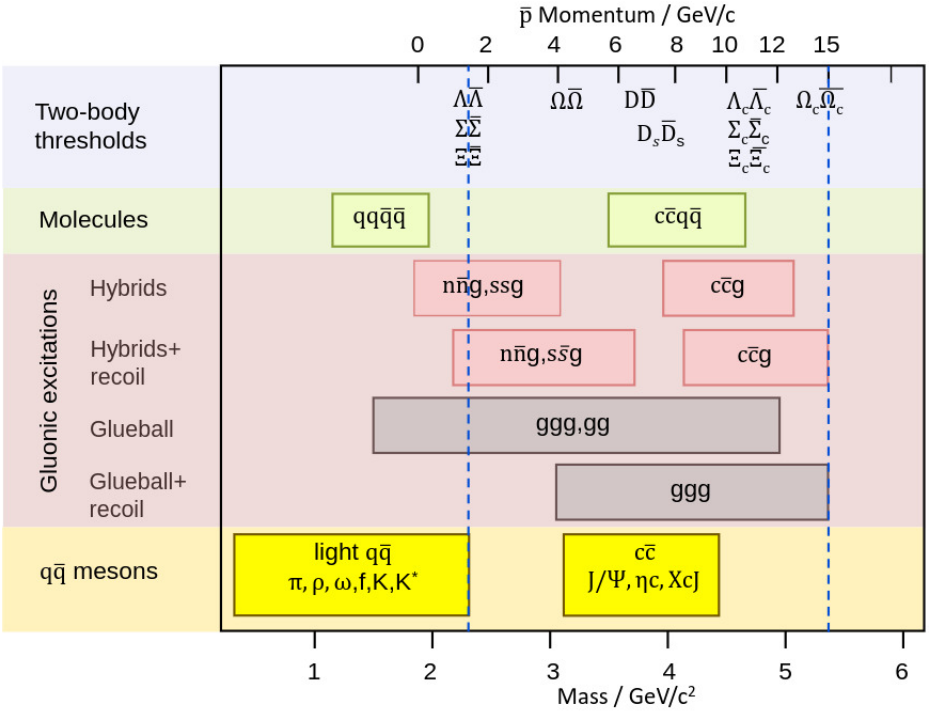

Figure 2.1: Hadrons in the mass and momentum range accessible with $\overline{\text{P}}$ANDA at FAIR.

2.1 Hadron Spectroscopy

A range of observable stable or long-lived hadrons make up the QCD hadronic spectrum. QCD can be better understood by looking into these bound states. These particle spectra are calculated and predicted using Lattice QCD, effective field theories, and non-relativistic potential models. $\overline{\text{P}}$ANDA is scheduled to host precision experiments in the fields of charmonium, open charm, and baryon spectroscopy, which are essential for verifying these methods and figuring out their free parameters. Furthermore, $\overline{\text{P}}$ANDA will look for exotic states such as glueballs, multiquark states, and hybrid quark-gluon bound states.

2.1.1 Charmonium and charmed mesons

Since its discovery in 1974, charmonium, a bound state of c and $\bar{c}$ has been an powerful tool to investigate the strong interaction. A description of the dynamical properties of the $c\bar{c}$ system in terms of non-relativistic potential models is feasible due to the high mass of the charm quark ($m_c = 1.5\,\text{GeV}/c^2$). In these models, the functional form of the potential is selected to replicate the asymptotic properties of QCD. A comparison of these models with the experimental data can help to ascertain the free parameters in these models.

Charmonium has primarily been measured in e^+e^- and $\overline{p}p$ collisions. Direct charmonium creation in e^+e^- annihilations is limited to states with the photon $J^{PC} = 1^{--}$ quantum numbers. Whereas, in $\overline{p}p$ collision processes, all charmonium states can form directly due to the coherent annihilation of the quarks with their antiquark companion. Proton-antiproton annihilation allows for high mass and width resolution for all the charmonium states, limited only by the beam momentum spread and not by the detector resolution. This high accuracy enables the measurement of the widths of exceedingly small states. Though the strong hadronic background that results from $\overline{p}p$ annihilation reactions is a drawback.

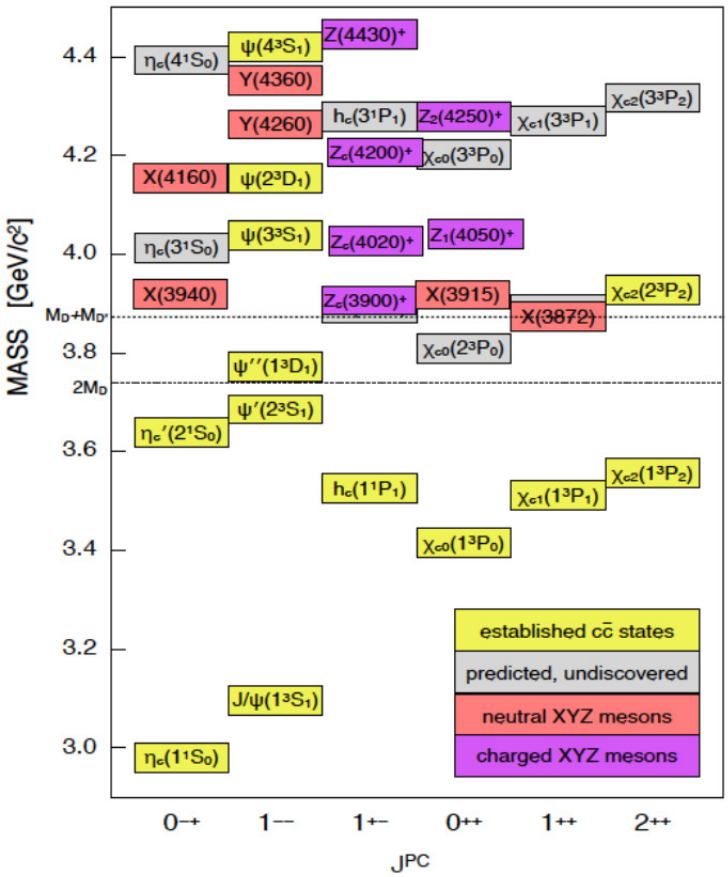

Figure 2.2: The charmonium mass spectrum including all discovered and predicted states shown as a function of spin-parity J^{PC}. The dashed line represents the mass threshold for open-charm production ($D\bar{D}$). Established charmonium states are shown in yellow, predicted but undiscovered states in grey, and the so-called exotic states (XYZ mesons) are highlighted in purple (charged) and red (neutral) [2].

Figure 2.2 shows the charmonium spectrum of the predicted and verified charmonium states as well as the newly discovered resonances with unknown characteristics. The charmonium states that have already been predicted and confirmed are depicted by the yellow boxes; the states that have been predicted but not yet discovered are shown in the grey boxes; and the recently discovered (unpredicted) charmonium-like states (XYZ) are shown in red/purple boxes. The charmonium states below the $D\overline{D}$ threshold of 3.7 GeV^2 are called the open-charm threshold. All eight states of charmonium in this region have been observed which are in good agreement with the experimental data. However, interesting new physics has been discovered above the $D\overline{D}$ threshold, i.e. predicted excitations which are still not observed and states are observed which are not predicted. These states are called the X,Y,Z states and have unusual properties which do not fit in the current theoretical picture. Z states are charged states and therefore cannot be $c\bar{c}$ states, whereas Y states are neutral states with $J^{PC} = 1^{--}$. The discovered states are linked to charmonium due to charmonium states, such as J/ψ or the ψ', being the main mode of decay [3]. While some of the states are also recognized as conventional states, the so-called exotic states are thought to be potential markers of physics beyond the conventional quark model [4]. Figure 2.3 shows the conventional hadrons (mesons and baryons) as well as the non-conventional hadrons. The exotic states are candidates for a variety of types of non-standard hadrons, including molecular states, diquark–diantiquarks, hybrids, glueballs and hadrocharmonia with the following theoretical descriptions [5, 6]:

- **Glueballs:** Hadronic states comprised only of gluons, with no quarks.
- **Hybrid states:** States with an excited gluonic degree of freedom.
- **Tetraquarks:** Four tightly bound quark states that differ from molecular states in their properties. They are organized into color-triplet scalar and vector clusters with a diquark-diantiquark structure, where spin-spin interactions predominate.
- **Molecular states:** Two mesons are described that are loosely bound by two mechanisms: pion exchange at large distances and quark/color exchange for interaction at short distances. It is anticipated that the pion exchange will be the main mechanism.
- **Hadro-quarkonium:** This classification holds significance exclusively for heavy-light $\overline{Q}Q\,\overline{q}q$ states. The light $\overline{q}q$ state envelops the heavy $\overline{Q}Q$ akin to how an electron surrounds a proton, with quark content $[\overline{Q}Q][\overline{q}q]$.

Glueballs Although they lack an electric charge, gluons—the massless mediator of the strong interaction—do possess the color charge that gives rise to the strong interaction.

QCD permits bound states with no quarks at all, known as glueballs. Due to the fact that gluons themselves are massless, their bound states will not be, making them particularly well-suited to study the mass creation of strongly interacting particles. Glueballs are hard to find because their predicted masses overlap with mesons [7]. Because of their identical quantum numbers, they also interfere with mesons, making identification even more difficult. The energy region covered by $\overline{\text{P}}$ANDA is predicted to have fifteen distinct glueball states [2]. According to the calculations with LQCD, the mass of the glueballs is predicted in the range of 1.4 GeV/c^2 - 5 GeV/c^2. Nonetheless, a sizable portion of glueballs are expected to have masses between 3 GeV/c^2 - 5 GeV/c^2 [8], a mass region that greatly facilitates identification due to the significantly lower number of meson states, which are also expected to be much narrower than those in the light-quark sector. For the first time, a systematic search of the predicted glueball states will be feasible with the $\overline{\text{P}}$ANDA detector [2].

Hybrid states Hybrid states with an excited gluon and a quark-antiquark pair are also conceivable since gluons can couple to quarks. These hybrids are able to assume exotic quantum numbers like $J^{PC} = 0^{--}, 0^{+-}, 1^{-+}$ and 2^{+-} that are not possible for conventional mesons due to the extra degrees of freedom carried by the gluon. It is possible to easily distinguish hybrid states from conventional $q\overline{q}$ mesons thanks to these unusual quantum numbers. Some of the exotic particles with $J^{PC} = 1^{-+}$ exhibit properties inline with predictions from the flux tube model. This model interprets the binding of quark-antiquark pairs through a gluon string [9]. Theoretical predictions for hybrids of charmonium mainly come from the bag model, the flux tube model, the constituent gluon model, and lattice QCD. Many of the glueball and hybrid candidates that lattice QCD calculations predicted are anticipated to exhibit masses ranging from approximately 3 GeV/c^2 to 5 GeV/c^2 that is within the mass region of the $\overline{\text{P}}$ANDA experiment.

Multiquarks Predictions for exotic, multiquark states were made well before the emergence of QCD and even before recent experimental discoveries. Gell-Mann introduced the concept of quarks with mesons as $\overline{q}q$ and baryons as qqq, as well as highlighted the potential existence of $\overline{q}\overline{q}qqq$ mesons and $\overline{q}qqqq$ baryons [10]. QCD imposes no particular constraint on the quark composition of hadrons. However, whether conventional or exotic, both types of states must be color neutral. It is feasible for hadrons made up of four, five, or six quarks and antiquarks to exist. Such hadrons are referred to multiquarks. Tetraquarks are hadrons with a $\overline{q}\overline{q}qq$ content. In the model proposed by Maiani et al [11], the tetraquark is depicted as a diquark-diantiquark structure, where the quarks form color-triplet scalar and vector clusters. The predominant interactions are governed

by a straightforward spin-spin interaction. The idea of a bound state consisting of two mesons was initially proposed by Jaffe in the 1970s for the light mesons a(980) and f(980). Jaffe proposed a distinct tetraquark model considering both scenarios—that is, as being composed of four quarks and as diquark-antidiquark systems. This notion was later applied to the X(3872) observed by Belle [12]. More recently, another potential tetraquark candidate, the $Z_c(3900)$, has been independently observed by Belle and BESIII [13]. A distinguishing prediction for multiquark states containing a $\bar{c}c$ pair, as opposed to conventional charmonia, is the potential presence of multiplets that include members with non-zero charge ($cu\bar{c}\bar{d}$), strangeness ($cd\bar{c}\bar{s}$), or both ($cu\bar{c}\bar{s}$) [4].

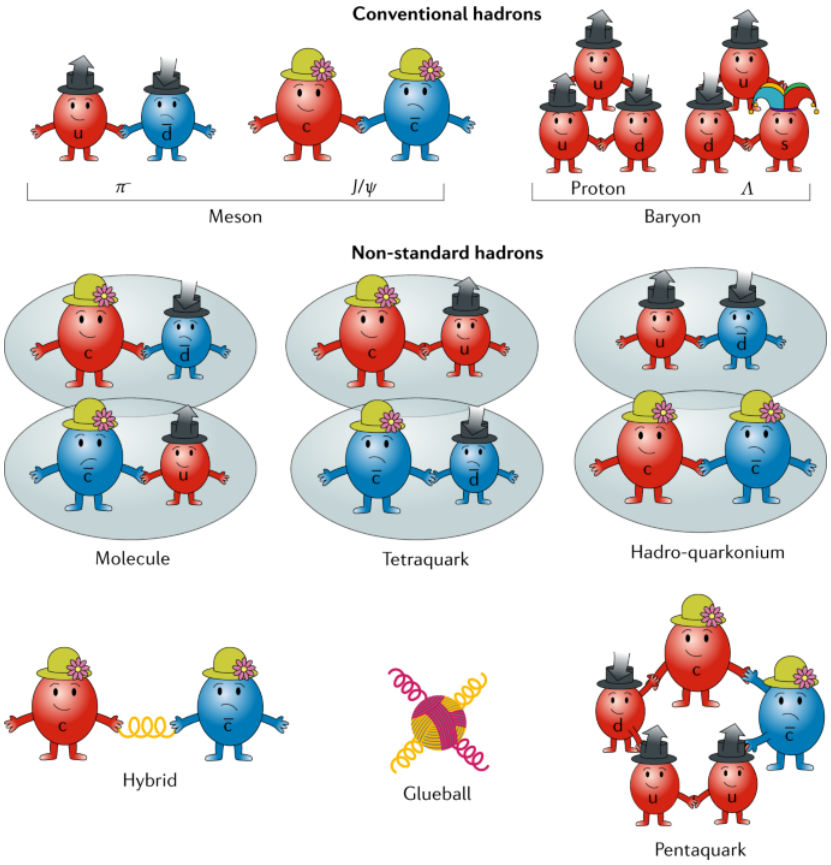

Figure 2.3: Conventional and non-conventional hadrons [5].

2.2 Hypernuclear Physics

A hypernucleus is formed when an up or down quark in the nucleus of a proton or neutron is replaced with a strange quark. This leads to the introduction of an additional quantum number, the strangeness, to the nucleus. Unlike neutrons and protons, hyperons are not constrained by the Pauli exclusion principle, allowing them to populate a wide range of

nuclear states. This unique property offers two intriguing possibilities. Firstly, a strange baryon integrated into a nuclear system can serve as a sensitive tool for scrutinizing the structure of the nucleus and any potential modifications induced by the presence of the hyperon. Secondly, substantial changes in the properties of hyperons when situated within a nucleus can consequently provide an exceptional opportunity to explore fundamental characteristics of hyperon-hyperon interaction. Additionally, comparing the hypernuclei with conventional nuclei can yield new perspectives on the underlying factors responsible for nuclear spin-orbit forces. An important goal is to determine the level spectra and decay properties of hypernuclei, which are essential for validating the energies and wave functions.

The precise spectroscopy of multi-strange hypernuclei at $\overline{\text{P}}$ANDA offers an exceptional opportunity to investigate the interaction between hyperons. At the $\overline{\text{P}}$ANDA experiment, a two-step production mechanism, as depicted in Fig 2.4, is implemented, utilizing a bound Ξ hypernuclear state as a transitional phase to create double Λ hypernuclei. It is anticipated that the reactions $\overline{p}p \rightarrow \Xi^{-}\Xi^{+}$ and $\overline{p}+ n \rightarrow \Xi^{-}\Xi^{0}$ will be employed to generate low energy Ξ baryon which is subsequently subject to rescattering within the primary target nucleus. The outgoing Ξ hypernucleus is stopped in an external secondary target and transformed into double Λ hypernucleus. These hypernuclei can then be studied by γ-ray spectroscopy i.e. the excited hypernuclei transition to ground state by emitting γ rays. The Germanium-based detectors planned for use in $\overline{\text{P}}$ANDA will measure these γ rays.

2.3 Nucleon Structure

A substantial portion of $\overline{\text{P}}$ANDA's physics program is dedicated to investigating the non-perturbative domain of Quantum Chromodynamics (QCD). Nonetheless, the anticipated experimental configuration at $\overline{\text{P}}$ANDA will also provide a chance to investigate hard perturbative reactions, giving insight on the intermediate region that signifies the transition towards the effects of perturbative Quantum Chromodynamics (pQCD).

Generalized Parton Distribution The theoretical framework of Generalized Parton Distribution (GPDs) has been developed recently to study the internal 3-dimensional nucleon structure. The GPDs provide detailed information about the longitudinal momentum and transverse position distribution of the partons, allowing for a 3-dimensional characterization of the nucleon [14]. Amplitude-level QCD factorization theorems facilitate access to GPDs in various hard exclusive reactions in the form of Compton Scattering processes, including Deep Virtual Compton Scattering (DVCS) $e^{-}p \rightarrow e^{-}p\gamma$ (Figure

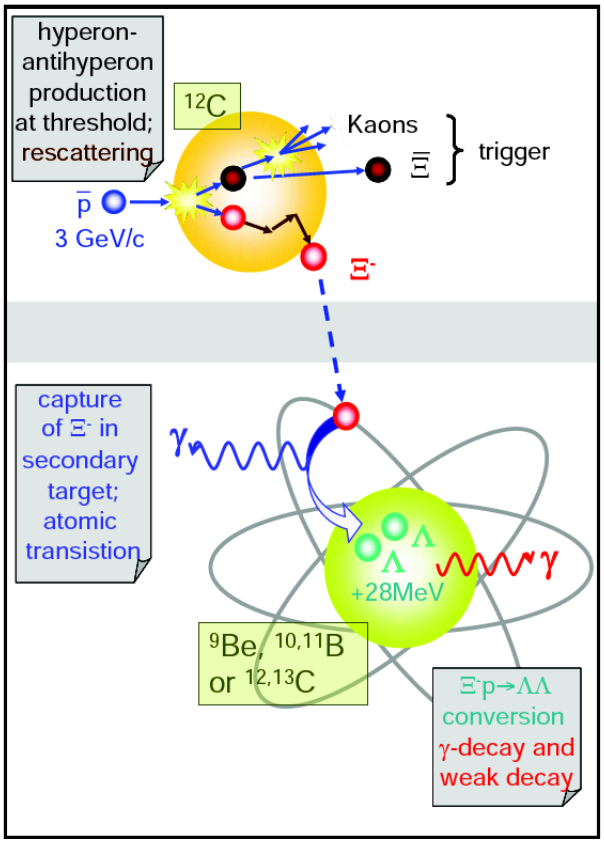

Figure 2.4: Steps of production mechanism for double Λ hypernuclei at $\overline{\mathrm{P}}$ANDA. A Ξ is created in the reaction, rescattered in the primary target, and then stopped in the exterior secondary target. The Ξ is converted into two Λ hypernuclei after being caught in the nucleus [2].

2.5a), where the emitted photon originates from the nucleon, and Wide Angle Compton Scattering (WACS) $\gamma p \to \gamma p$.

These processes are described by the QCD *handbag diagram*. The amplitude of this reaction process can be separated into two distinct components: a hard perturbative QCD process and a soft part which is parametrized by GPDs.

At $\overline{\text{P}}$ANDA, it is expected to investigate the reaction $\bar{p}p \to \gamma\gamma$ which is the crossed process of WACS (Figure 2.5b). The crossed diagram of WACS represents the proton-antiproton pair annihilation into two photons at a large polar angle in the center-of-mass system. The soft part of the time-like WACS process is parametrized by the Generalised Distribution Amplitudes (GDAs), which are the counterparts of the GPDs. More about GPDs and GDAs is discussed in Chapter 3.

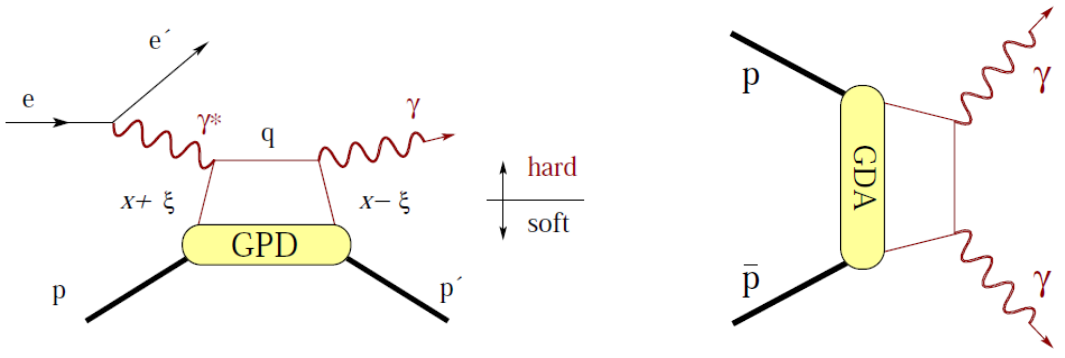

(a) **(b)**

Figure 2.5: (a): The process of Deeply Virtual Compton Scattering (DVCS) can be explained through the handbag diagram, which involves the factorization of the amplitude into a hard upper part described by perturbative QCD and QED and a soft lower part described by Generalized Parton Distributions (GPDs). (b): The diagram for the inverted Wide Angle Compton Scattering (WACS) processes $\bar{p}p \to \gamma\gamma$ described by GDAs [2].

Electromagnetic Form Factors of the Proton $\overline{\text{P}}$ANDA offers the opportunity to explore the structure of the nucleon using electromagnetic processes. The distribution of electromagnetic charge within a hadron is characterized by electromagnetic form factors(EMFF), comprising an electric form factor (G_E) and a magnetic form factor (G_M). These form factors are determined through scattering processes involving charged leptons and hadrons. The electromagnetic form factors are functions of the momentum transfer square, q^2.

The structure of the nucleon can be parameterized with electromagnetic form factors, which are defined across the complete q^2 complex plane and are termed as space-like when the momentum transfer is negative ($q^2 < 0$) and time-like when the momentum transfer is positive ($q^2 > 0$). Space-like electromagnetic form factors can be determined from the cross section of the elastic scattering process, such as ($e^- + p \rightarrow e^- + p$). Whereas process of significance for measuring the electromagnetic form factors of protons within the time-like region entail the presence of two leptons in the final state ($\overline{p}p \rightarrow l^+l^-, l = e, \mu, \tau$). Despite the fact that the $\overline{p}p$ annihilation reaction permits the generation of tau leptons with opposing charges in the final state, this particular channel will not be employed at $\overline{\text{P}}$ANDA. The decision is attributed to its exceedingly low cross-sectional yield and the elevated production threshold, primarily stemming from the substantial rest mass of the tau lepton. The diagram which contributes to the tree-level amplitude of this process assuming one-photon exchange is shown in Figure 2.6. It will be possible to measure the time-like electromagnetic form factors of proton with $\overline{\text{P}}$ANDA over a wide kinematical range of q^2.

The $\overline{p}p \rightarrow e^+e^-$ process will be thoroughly examined to precisely determine the form factor of the proton within the time-like region, covering the q^2 regions that $\overline{\text{P}}$ANDA can access [15]. Furthermore, $\overline{\text{P}}$ANDA stands as the pioneering experiment that would measure the proton form factor using the $\overline{p}p \rightarrow \mu^+\mu^-$ process [16]. The measurement of the muon channel not only serves as a validation of the extracted FF values obtained through the $\overline{p}p \rightarrow e^+e^-$ process but also presents an excellent opportunity to test lepton universality. Notably, $\overline{\text{P}}$ANDA will have the capacity to compare the FF values derived from both the muon and electron channels within the time-like regime of q^2 using the same set of data, further enhancing the reliability of the results. Additionally, it will be feasible to assess the proton's form factors below the proton production threshold of $4m_p$, where m_p is the mass of the proton, using the $\overline{p}p \rightarrow e^+e^-\pi^0$ Dalitz decay process [16, 17].

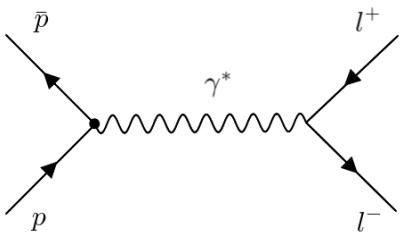

Figure 2.6: Tree-level contributing diagram to the reaction amplitude of the process $\overline{p}p \rightarrow l^+l^-$.

Drell-Yan Processes and Transition Distribution Amplitudes (TDA's) Drell-Yan (DY) processes, such as $\bar{p}p \to \mu^+\mu^- X$, are commonly employed as a conventional method for exploring the partonic composition of hadrons. These processes provide valuable insights into transverse spin effects and the distribution of the transverse momentum within the nucleon. The Drell-Yan (DY) process is an electromagnetic process occurring when a quark and its corresponding anti-quark, originating from a pair of interacting hadrons, annihilate into a virtual photon and result in the production of a high-energy lepton pair. $\overline{\text{P}}$ANDA offers the opportunity to measure the exclusive Drell-Yan annihilation reaction $\bar{p}p \to e^+e^- X$. The Feynman diagram for this process is illustrated in Figure 2.7. The reaction amplitude for this process can be factorized by a hard subprocess and a soft part containing Transition Distribution Amplitudes (TDA's) [18, 19]. TDA's are non-perturbative objects and parameterize the transition between two different particles.

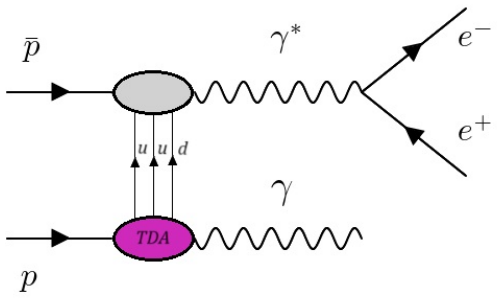

Figure 2.7: The reaction amplitude for the process $\bar{p}p \to e^+e^-\gamma$ can be factorized by a hard subprocess and a soft part containing Transition Distribution Amplitudes (TDA's).

3 | Generalized Parton Distribution and Generalized Distribution Amplitudes

3.1 Generalized Parton Distribution

Understanding how the nucleon and other hadrons are constructed from quarks and gluons, the fundamental degrees of freedom in QCD, is one of the primary unanswered questions in the theory of strong interactions. The study of deep inelastic scattering processes, where individual quarks and gluons are resolved, is the key tool to explore hadron structure. The distribution of longitudinal momentum and polarization carried by quarks, antiquarks, and gluons within a fast-moving hadron is encoded by the parton densities that may be extracted from such processes. They have contributed significantly to the development of our physical understanding of hadron structure.

Generalized Parton Distributions (GPDs) are functions that describe the internal structure of hadrons, such as protons and neutrons, in terms of their quark and gluon content. They provide a unified description of both the longitudinal momentum distribution and the transverse spatial distribution of partons (quarks and gluons) inside the hadron. GPDs are an extension of the concept of Parton Distribution Functions (PDFs), which only provide information about the longitudinal momentum of partons. It is now well understood that GPDs are accessible through a variety of hard-exclusive procedures, including the formation of a meson-photon pair, Time-like Compton Scattering (TCS), Deeply Virtual Compton Scattering (DVCS), Deeply Virtual Meson formation (DVMP), and Double DVCS. The following section provides a concise overview of the theoretical framework of GPDs and highlights the foremost experimental discoveries in the study of GPDs.

3.1.1 Theoretical Framework of GPDs

The concept and framework of GPDs was established by Müller et al [20], Radyushkin [21, 22] and Ji [23, 24] in the late 90s. It was introduced as a "parton-hadron" → "parton-hadron" amplitude.

For the definition of GPDs, the following notations are used [25]:

$$P = \frac{p + p'}{2}, \quad \Delta = p' - p, \quad t = \Delta^2,$$

where p and p' are the four-vector of the incoming and outgoing hadron respectively. The standard definitions for the lepton scattering component are as follows:

$$Q^2 = -q^2, \quad W^2 = (p + q)^2, \quad x_B = \frac{Q^2}{2p \cdot q},$$

where $q = k - k'$ is the four-vector of the incident virtual photon, obtained from the incoming k and scattered k' lepton.

Another key variable is the skewness ξ, which can be approximated as $\xi \approx \frac{x_B}{2-x_B}$ under the Bjorken limit, where the photon virtuality Q^2 and the squared hadronic center-of-mass energy W^2 are large, and x_B remains fixed.

3.1.2 Domain and Partonic Interpretation

In hadron physics, the fact that GPDs rely on two distinct light-cone momentum fractions, x and ξ, leads to intriguing and distinctive outcomes. Several regimes of GPD can be defined by looking at the (x, ξ) plane (see Figure 3.1). As illustrated in Ref. [25], the GPD support is restricted to the square $(x, \xi) \in [-1, 1]^2$ throughout the entire plane. We differentiate two sorts of regions within this square: the inner one where $|\xi| \geq |x|$, known as the ERBL (Efremov-Radyushkin-Brodsky-Lepage) area, and the outer one for which $|x| \geq |\xi|$, also known as the DGLAP (an abbreviation for Dokshitzer, Gribov, Lipatov, Altarelli, Parisi). The partons involved in these two locations are interpreted differently. The ERBL kinematic regime can be extended to $|\xi| \geq 1$, giving rise to time-like GPDs, also referred to as Generalized Distribution Amplitudes (GDAs) which can be studied, for instance, in proton–antiproton annihilation experiments.

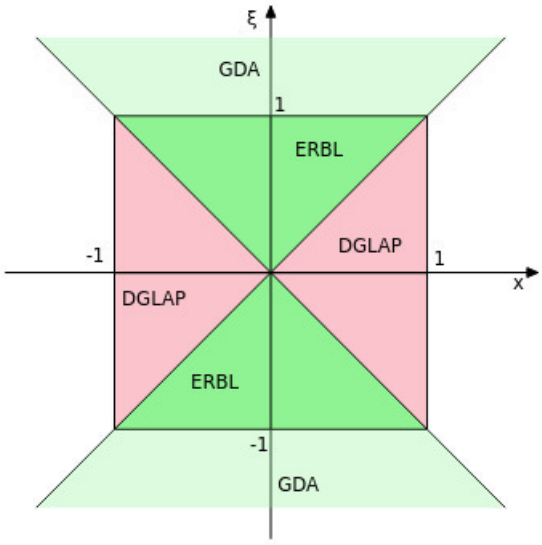

Figure 3.1: The GPD support in the (x, ξ) plane is shown, with the DGLAP (or outer) region highlighted in pink, where $|x| \geq |\xi|$, and the ERBL (or inner) region in green, where $|x| \leq |\xi|$. The lighter green areas indicate the extensions of the ERBL region for $|\xi| \geq 1$, which correspond to the kinematic domain of GDA, extending up to the crossing symmetry. Image adapted from [26].

3.1.3 Partonic Interpretation

Both the variables x and ξ have support in the interval [-1, 1] and the partonic process can be interpreted in various ways.

- For region $-1 \leq x \leq -\xi$, both momentum fractions $\xi - x$ and $-x - \xi$ are both negative. This is known as the DGLAP region and the GPDs correspond to the emission and reabsorption of an antiquark.
- The region $-\xi \leq x \leq \xi$ (ERBL) represents momentum fractions $x+\xi$ and $\xi-x$. The momentum fractions are now positive and negative which correspond to the quark and antiquark interpretation respectively. The GPD can be viewed as a process to extracts quark-antiquark pairs from a hadron without breaking it.
- The region $\xi \leq x \leq 1$ (DGLAP) corresponds to the emission and reabsorption of quark with momentum fraction $x + \xi$ and $x - \xi$ respectively.

3.2 Experimental Access to GPDs

Until now, we have mainly highlighted the theoretical properties of GPDs. In this section, we will focus on the most common processes to measure GPDs in electron scattering

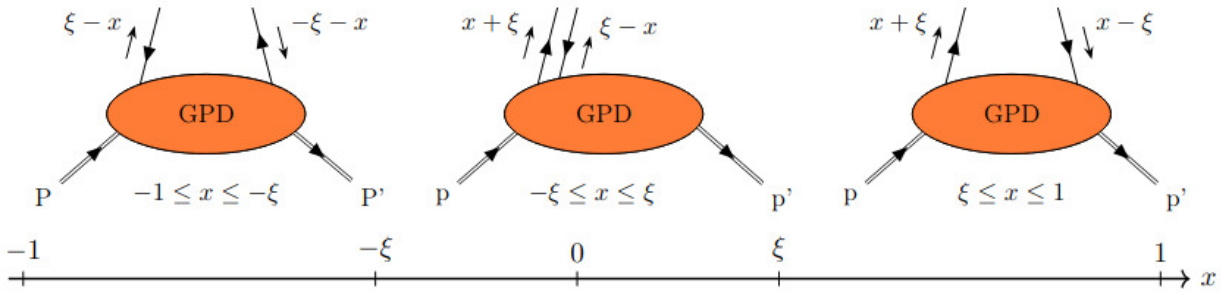

Figure 3.2: The interpretation of GPDs varies depending on the region they are explored. Image adapted from [25].

experiments.

3.2.1 Deeply Virtual Compton Scattering

The Deeply virtual Compton scattering(DVCS) process $lp \to l'p'\gamma$ is the key reaction to determine GPDs. It is also the simplest process that be described in terms of GPDs. At the Bjorken limit, characterized by a large virtuality ($Q^2 \to \infty$), high energy of the virtual photon ($\nu \to \infty$), and a fixed Bjorken variable ($x_B = Q^2/2M\nu$, where M is the nucleon mass), the process can be factorized into two distinct components: a hard subprocess, $\gamma^* q \to \gamma q$, which can be calculated perturbatively at the quark level, and a soft, non-perturbative component parameterized in terms of Generalized Parton Distributions (GPDs) [27–29], as illustrated in Figure 3.3.

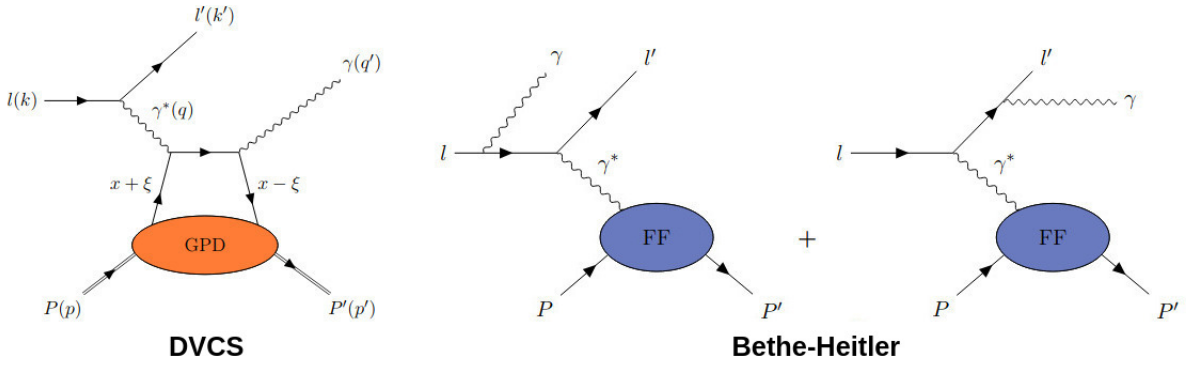

Figure 3.3: "Handbag" diagram for deeply virtual Compton scattering (DVCS) and Bethe–Heitler (BH) processes. Image adapted from [30].

DVCS is not the only process such that $ep \to ep\gamma$. It interferes with the Bethe-Heitler (BH) process, depicted in Figure 3.3, in which a real photon is emitted either by the

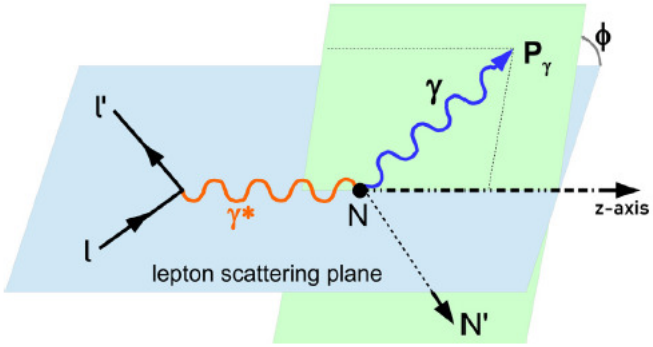

Figure 3.4: Illustration of Kinematics and reaction planes in the centre of mass frame for the DVCS process. The electron scattering plane is shown in blue and the photon-nucleon plane in green [32].

incoming or the outgoing electron. The BH process involves the nucleon form factor rather than the GPDs. As a result, the cross-section for the $ep \to ep\gamma$ process arises from the sum of the DVCS and BH amplitudes, which interfere with one another[26, 31]. The differential cross-section for an unpolarized target and a polarized electron beam is termed as below [32]:

$$d^4\sigma(e^- p \to e^- \gamma p) = d^4\sigma_{\mathrm{BH}} + d^4\sigma_{\mathrm{DVCS_{unpol.}}} + \lambda\, d^4\sigma_{\mathrm{DVCS_{pol.}}} \mp (\mathcal{I}^{\mathrm{Re}} + \lambda\, \mathcal{I}^{\mathrm{Im}}), \tag{3.1}$$

where λ is the beam or target polarisation, $d^4\sigma_{\mathrm{DVCS}}$ and $d^4\sigma_{\mathrm{BH}}$ are the cross sections of the DVCS and BH respectively, and $\mathcal{I}^{\mathrm{Re}}$ is the real and $\mathcal{I}^{\mathrm{Im}}$ an imaginary component of the interference amplitude between the two processes. We can observe that the interference terms contribute oppositely ($\mp$) for the scattering of electrons and positrons ($e^{\pm}$).

The Bethe–Heitler process is expected to dominate the contribution from the pure DVCS process for the kinematic region that is accessible from various facilities such as Jefferson Laboratory. Nonetheless, the Bethe–Heitler process may be incorporated into theoretical models with minimal uncertainties since it can be computed theoretically with high precision using QED models and the experimentally well-known proton form factors [31, 33]. Using a longitudinally polarized electron beam, the dominating BH process can be exploited: the helicity-dependent interference term proportional to the imaginary component of the DVCS amplitude can be measured. In such cases, the purely real BH contribution is effectively removed from the cross-section difference. Figure 3.4 shows the relevant angle ϕ between the lepton scattering plane and the final state production plane in the center of mass frame.

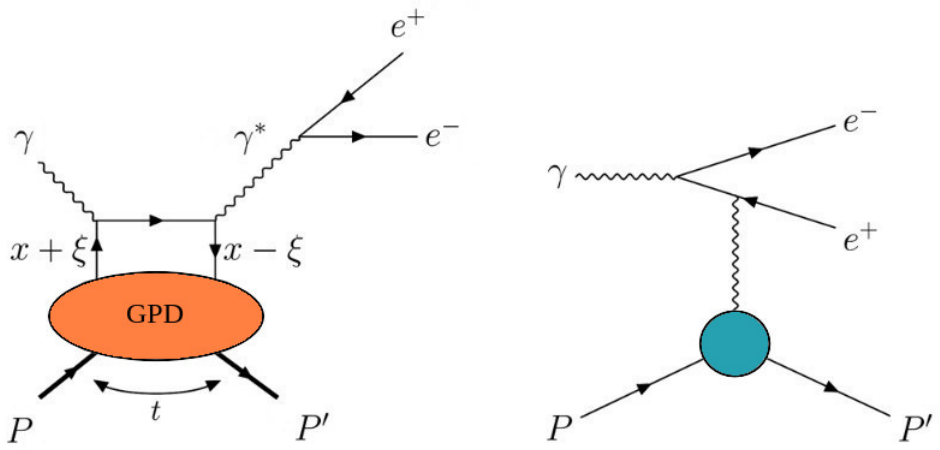

Figure 3.5: The Feynman diagram for the time like Compton scattering process (left) and the corresponding Bethe–Heitler process (right).

3.2.2 Timelike Compton Scattering

Timelike Compton scattering (TCS) is the time-reversal symmetric process of DVCS. The process of interest is $\gamma p \to \gamma^* p'$, where the incoming photon is real ($Q^2 = 0$) and the outgoing photon is virtual. The virtual photon subsequently decays into a lepton pair, which can be detected. Thus, the complete reaction is $\gamma p \to p' l^+ l^-$. Hereafter, we refer to the exclusive photoproduction of lepton pairs $\gamma p \to p' l^+ l^-$ process simply as the TCS reaction. Unlike DVCS, where the hard scale is determined by the large spacelike virtuality of the incoming photon, ensuring factorization, the hard scale in TCS is defined by the timelike virtuality Q'^2 of the outgoing photon. Factorization holds for sufficiently large Q'^2 with $t = 2$. In this process, the real incoming photon interacts with a single quark, which then emits a virtual photon.

As in the case of DVCS, a Bethe-Heitler (BH) process interferes and produces the same final state as the TCS process. The leading-order, leading-twist diagram for TCS and the corresponding BH process is shown in Figure 3.5. Thus, the pure BH ($d\sigma_{\mathrm{BH}}$) and TCS ($d\sigma_{\mathrm{TCS}}$) cross-sections, as well as the interference cross-section between the TCS and the BH process ($d\sigma_{\mathrm{INT}}$), can be used to define the cross-section of the exclusive lepton pair formation in a manner similar to that of the DVCS process [34, 35]:

$$d^4\sigma(\gamma N \to N' e^+ e^-) = d^4\sigma_{\mathrm{BH}} + d^4\sigma_{\mathrm{TCS}} + d^4\sigma_{\mathrm{INT}} \tag{3.2}$$

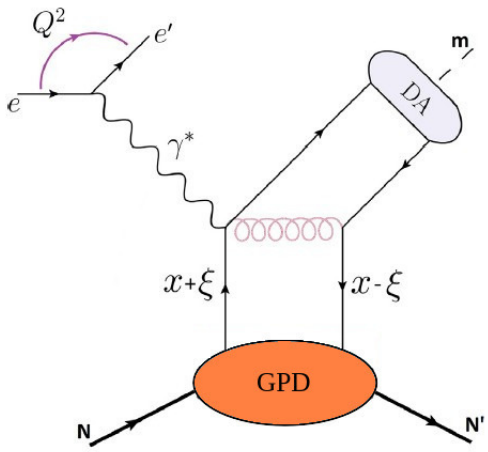

Figure 3.6: Deeply virtual meson production.

.

3.2.3 Deeply Virtual Meson Production

Deeply Virtual Meson Production (DVMP) is an exclusive electroproduction process in which a virtual photon emitted by an incoming lepton interacts with a nucleon, resulting in the production of a meson and a recoiling nucleon. A schematic diagram of the DVMP process is shown in Figure 3.6. The diagram illustrates the factorization into the hard perturbative part (photon-quark interaction) and the soft non-perturbative parts (GPDs and meson DA). The process can be expressed as:

$$lN \to l'N'm,$$

where m represents the produced meson. DVMP plays a complementary role to Deeply Virtual Compton Scattering (DVCS) in accessing Generalized Parton Distributions (GPDs) as it involves transitions between quarks with different flavors, providing additional sensitivity to specific GPD combinations.

In contrast to DVCS, where the final state involves a real photon, DVMP includes a meson that carries the quark flavor information, allowing for a partial flavor decomposition of GPDs. This unique feature enables DVMP to address two limitations observed in DVCS [26, 32]:

- Limited flavor separation capability.
- Inability to access transversity GPDs, as helicity flip contributions are suppressed in DVCS.

Through DVMP, processes involving transversely polarized virtual photons and quark helicity flips contribute significantly, making DVMP a key process for probing transversity GPDs.

The DVMP amplitude factorizes into a perturbatively calculable hard-scattering part and two soft parts: the GPDs describing the nucleon structure and the meson distribution amplitude (DA). This factorization holds at large virtual photon virtuality Q^2, high invariant energy W, and fixed Bjorken-x. Specifically, it applies when the longitudinally polarized virtual photons dominate the process [36].

DVMP allows the extraction of GPDs through specific channels involving vector mesons (e.g., ρ, ϕ, ω) and pseudoscalar mesons (e.g., π, η):

- **Vector Mesons**: Dominantly sensitive to the GPD H in the helicity-conserving amplitude. Transversity GPDs contribute marginally but can be probed through asymmetries or spin density matrix elements (SDMEs).
- **Pseudoscalar Mesons**: Provide access to the helicity-flip GPDs $\widetilde{H}$ and $\widetilde{E}$, which are less accessible in other processes.

The sensitivity to transversity GPDs in pseudoscalar meson production is particularly important, as it allows for the investigation of quark helicity-flip processes at higher twist.

Early measurements of DVMP were performed using lepton beams, such as muons and electrons, on proton and nuclear targets. These experiments confirmed the dominance of longitudinal cross-sections over transverse contributions for sufficiently large Q^2, supporting the factorization framework.

The COMPASS, HERMES, and JLab experiments have provided crucial data on DVMP, particularly for light vector mesons like ρ^0 and ϕ. Future measurements at facilities like the Electron-Ion Collider (EIC) will allow for unprecedented precision in probing gluon GPDs via heavy meson production (e.g., J/ψ, Υ).

Deeply Virtual Meson Production (DVMP) serves as a powerful tool to access and study GPDs, offering complementary information to DVCS. By allowing flavor decomposition and providing sensitivity to transversity GPDs, DVMP enhances our understanding of the three-dimensional structure of nucleons and the distribution of partons within them. Ongoing and future experiments promise to further refine the extraction of GPDs and probe the rich physics encoded in these distributions.

3.3 Generalized Distribution Amplitudes

Generalized Distribution Amplitudes (GDAs) are a theoretical framework derived from Generalized Parton Distributions (GPDs) but applied in the $t \to s$ crossed channel. They extend our understanding of hadron structure by parameterizing the transition of quark-antiquark ($q\bar{q}$) or gluon-gluon (gg) pairs into hadronic states. This connection stems from the crossing symmetry in quantum field theory, which allows the interchange of incoming and outgoing particles, resulting in a complementary perspective to GPDs. As GDAs are the crossed channel counterpart of GPDs, the diagram in Figure 3.2 would show a GDA with incoming partons and outgoing hadrons if it were upside down (i.e. rotated by $\frac{\pi}{2}$) [37].

While GPDs describe the partonic structure and dynamics of a nucleon in scattering processes, GDAs encapsulate the dynamics of hadronization, describing how quark-antiquark or gluon pairs form bound states like mesons. These amplitudes are essential for understanding exclusive processes such as timelike Compton scattering and meson pair production, providing insights into non-perturbative QCD dynamics.

3.3.1 Definition and Properties of GDAs

As outlined in [25, 38], we adopt the following conventions for the GPD momenta:

$$\begin{aligned} P_1' &= P_2, & k_1' &= k_2, \\ P_2' &= -P_1, & k_2' &= -k_1. \end{aligned}$$

In the context of GDAs, the momenta of the hadron and quark (denoted with a prime) are labeled as 1, while the antihadron and antiquark are labeled as 2. P represents hadrons, and k denotes partons, following the same notation convention used for GPDs.

The GDAs are characterized by three invariant scalar quantities, defined as:

$$\begin{aligned} z &= \frac{k_1'^+}{P_1'^+ + P_2'^+}, \\ \zeta &= \frac{P_1'^+}{P_1'^+ + P_2'^+}, \\ s &= (P_1' + P_2')^2. \end{aligned}$$

We observe that the Mandelstam variable $s \geq 0$ corresponds to the momentum transfer $t \leq 0$ in the framework of GPDs, but within the timelike domain. As a result, GDAs,

which are timelike quantities, represent the analytic continuations of GPDs, which are spacelike quantities.

Here:

- z: The light-cone momentum fraction of the quark or gluon.
- ζ: The skewness parameter, related to the momentum asymmetry between the produced hadrons.
- s: The invariant mass squared of the two-hadron system.

GDAs are defined through the matrix elements of non-local operators on the light cone, but unlike GPDs, they describe transitions between the vacuum and a two-hadron state. For instance, the quark and gluon GDAs for the production of a two-pion system $\gamma^*\gamma \to \pi\pi$, are expressed as:

$$\Phi_q(z,\zeta,s) = \int dx^- \frac{e^{i(2z-1)P^+x^-}}{2\pi} \langle \pi^+(p)\pi^-(p')|\bar{q}(-\frac{x^-}{2})\gamma^+ q(\frac{x^-}{2})|0\rangle,$$

$$\Phi_g(z,\zeta,s) = \frac{1}{(P^+)} \int dx^- \frac{e^{i(2z-1)P^+x^-}}{2\pi} \langle \pi^+(p)\pi^-(p')|G^{+\mu}(-\frac{x^-}{2})G^{+\mu}(\frac{x^-}{2})|0\rangle.$$

Symmetry Properties

GDAs inherit symmetry properties from the underlying QCD processes:

- Charge conjugation and isospin symmetry constrain their functional form.
- GDAs obey crossing relations with GPDs, linking the skewness parameter ζ in GDAs to the analogous variable in GPDs.

3.3.2 Physical Interpretation

GDAs offer a complementary perspective to GPDs by focusing on the dynamics of hadronization:

1. **Hadronization Dynamics**: GDAs describe the formation of hadronic systems from partons, offering a detailed view of hadronization mechanisms in exclusive processes.
2. **Crossing Symmetry**: Crossing symmetry links GDAs and GPDs mathematically, transforming variables such as momentum fractions and skewness between the two

frameworks.

3. **Three-Dimensional Imaging**: While GPDs provide spatial imaging of nucleons, GDAs focus on the spatial and momentum distribution of partons within a forming hadronic system.

3.3.3 Experimental Access to GDAs

Several experimental processes can probe GDAs a shown in Figure 3.7

1. **Two-Photon Annihilation**: Processes like $e^+e^- \to \gamma^*\gamma \to h\bar{h}$, where h denotes hadrons, are ideal for studying GDAs. For example, the Belle and BABAR experiments have measured the cross sections for $\gamma^*\gamma \to \pi^+\pi^-$, providing direct access to pion GDAs.

2. **Proton-Antiproton Annihilation**: Reactions like $\bar{p}p \to \gamma\gamma$ and $\bar{p}p \to \gamma m$, where m denotes a meson, provide an alternative channel for probing the dynamics described by GDAs.

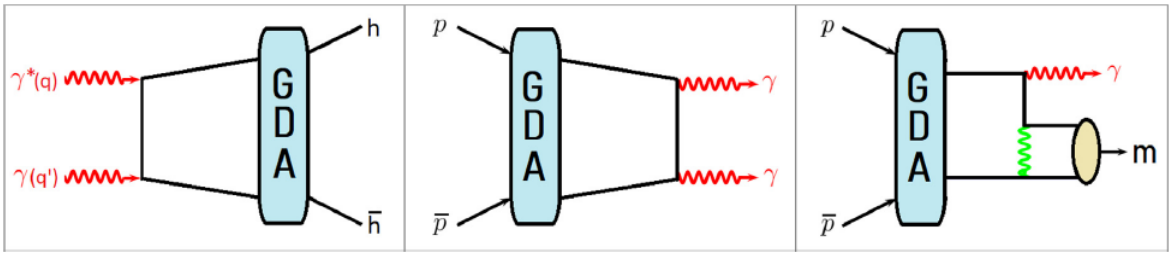

Figure 3.7: Generalized Distribution Amplitudes in two-photon interactions during e^+e^- collisions (left panel) and in proton-antiproton annihilation events (center and right panels). Image adapted from [32].

3.3.4 Experimental Insights and GDA-Based Cross Section Estimates

Generalized Distribution Amplitudes (GDAs) play a pivotal role in describing the hadronic structure in exclusive production processes involving hadron-antihadron pairs. These amplitudes allow us to calculate differential and total cross sections for reactions in which two photons or a photon and a hadron interact to produce specific final states. GDA-based cross-section estimates provide valuable insights into the internal quark and gluon dynamics of hadrons, and they can be compared with experimental data to test QCD factorization frameworks and refine theoretical parametrizations of GDAs.

Two-photon annihilation processes, such as $\gamma^*\gamma \to \pi\pi$, offer a primary approach for accessing GDAs. Preliminary cross-section estimates for these processes measured at B-factories, BELLE, BABAR and CLEO, and LEP are presented in Ref. [14]. Cross section involving hadron pairs, such as $\gamma^*\gamma \to p\bar{p}$, $\gamma^*\gamma \to \Lambda\bar{\Lambda}$, and $\gamma^*\gamma \to \Sigma^0\bar{\Sigma}^0$, have been explored theoretically in Refs. [39, 40], indicating the versatility of GDAs in describing a wide range of hadronic processes. Much of the available data, however, is measured at rather low energies i.e. $\sqrt{s} < 4\,\text{GeV}$, limiting their interpretation in terms of GDAs due to the requirement of large s, t, and u. Cross sections for various final states have been studied by different experiments:

- $p\bar{p}$ final state: CLEO, VENUS, OPAL, and BELLE [41–44]
- Λ and Σ^0 final states: BELLE, L3, and CLEO [45–47]
- $\rho^0\rho^0$ and $\rho^+\rho^-$ final states: L3 collaboration at LEP [48]
- $\pi^0\pi^0$ final states: BELLE [49]

Proton-antiproton annihilation serves as another experimental avenue for probing GDAs. These processes have been theoretically discussed in detail in Refs. [39, 50], where differential cross sections for channels such as $\bar{p}p \to \gamma\pi^0$ were calculated using GDA-based models. Theoretical predictions for this channel were compared with experimental data from the E760 experiment [1]. Despite limitations in statistical precision and kinematic coverage, the theoretical models demonstrated good agreement with the available data, as shown in Figure 3.8, supporting the validity of GDA-based interpretations in these systems.

Future experiments, particularly $\overline{\text{P}}$ANDA at FAIR, are expected to significantly improve both statistics precision and kinematic coverage, enabling comprehensive studies of various final states. Calculations for GDA-based handbag approach are extended to a general scenario $\bar{p}p \to \gamma M$ where M represents various mesons such as π^0, η, ρ, ω, η', ϕ, J/ψ, and potential excited charmonium states [50]. In this thesis, a detailed feasibility study is carried out for the measurement of different channels with $\overline{\text{P}}$ANDA. Among them is also the process $\bar{p}p \to \gamma\gamma$ whose first cross section is available from the E760 experiment.

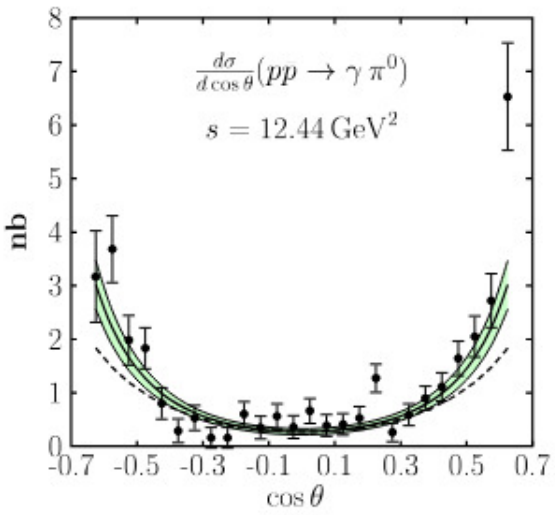

Figure 3.8: The differential cross section versus $\cos\theta$ of the process $\bar{p}p \to \gamma\pi^0$ at $s = 12.44\,\mathrm{GeV}^2$ for the data from E760 experiment. The prediction from a GDA-based model by Kroll and Schäfer is displayed by the solid line with the green uncertainty band. Image adapted from [50].

4 | The $\overline{\text{P}}$ANDA Experiment at FAIR

This chapter provides an overview of the $\overline{\text{P}}$ANDA experiment at FAIR. It begins by introducing the accelerator facility FAIR in Section 4.1 and the HESR in Section 4.2. Section 4.3 outlines the details of the $\overline{\text{P}}$ANDA detector and its component.

4.1 The Facility for Antiproton and Ion Research

The future Facility for Antiproton and Ion Research (FAIR) is presently being constructed next to the already existing GSI Helmholtz Center for Heavy Ion Research (GSI) in Darmstadt. Figure 4.1 illustrates the existing accelerators at GSI with blue lines, while the red lines represent the planned future accelerators. FAIR is engineered to investigate the composition of matter, serving as a "Universe in the Laboratory" [51]. It will accelerate antiprotons and ions to delve into fundamental inquiries in physics. The research scope at FAIR spans nuclear, hadron, particle physics, extending to plasma physics, as well as applications in material science and biophysics.

In addition to $\overline{\text{P}}$ANDA, FAIR will also host collaborations in Atomic, Plasma Physics, and Applications (APPA), Compressed Baryonic Matter (CBM), and Nuclear Structure, Astrophysics, and Reactions (NUSTAR). $\overline{\text{P}}$ANDA and APPA at FAIR are specifically designated for antiproton physics. High-energy antiprotons, reaching up to 15 GeV, will be employed in $\overline{\text{P}}$ANDA at HESR. The FAIR complex, currently in the construction phase, will include the superconducting double-synchrotron SIS100/SIS300, the Collector Ring (CR), the RESR, the NESR, an antiproton target, and the HESR. A comprehensive overview of FAIR is available in [52].

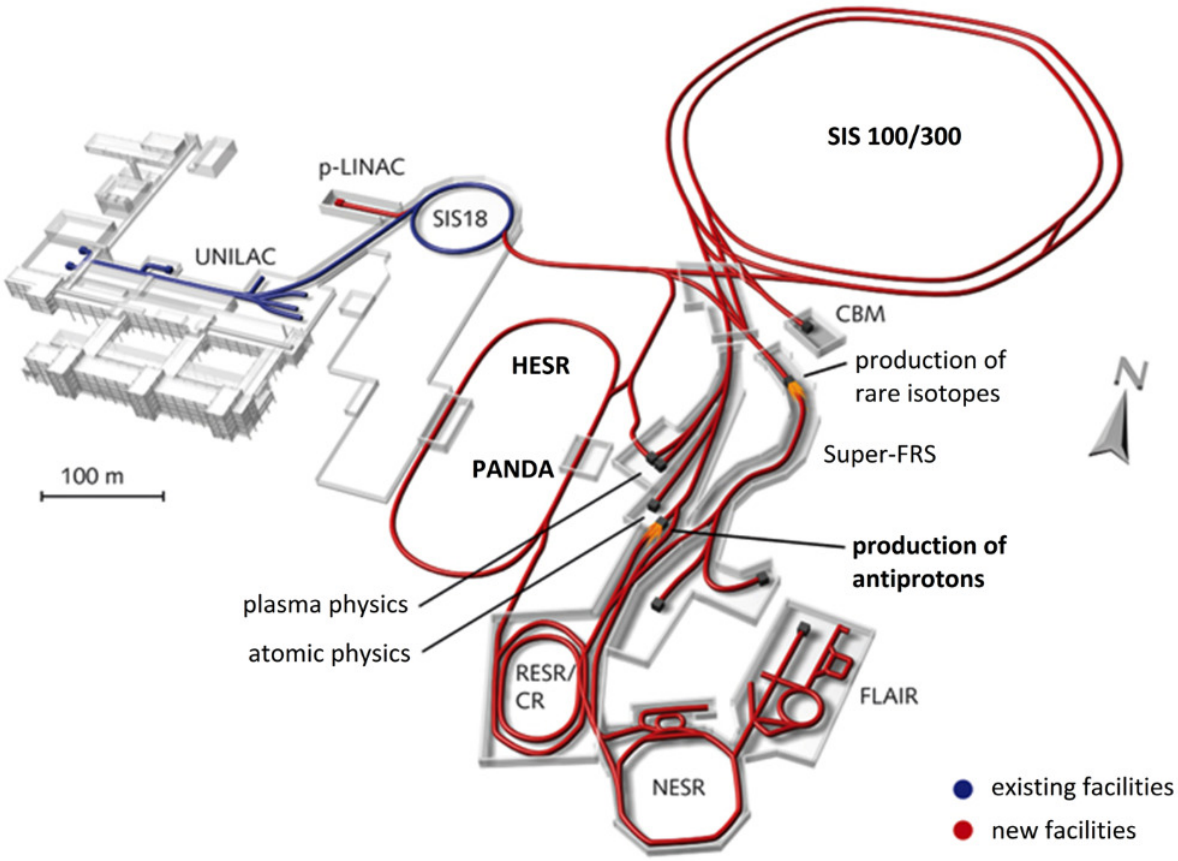

Figure 4.1: The Facility of Antiproton and Ion Research (FAIR) in Darmstadt. Existing subsystems are indicated in blue, while all planned or currently under construction accelerators, storage rings, and experiments are highlighted in red.

4.1.1 Antiproton Target and Separator

The production of antiprotons for the $\overline{\text{P}}$ANDA experiment will involve several stages. Protons will be initially pre-accelerated to a momentum of 70 MeV/c by the currently operational Universal Linear Accelerator (UNILAC) and the future proton linear accelerator (pLINAC). These pre-accelerated protons will then be directed to the Schwerionen-Synchrotron 18 (SIS-18) and subsequently to SIS-100 in a second step, where they will undergo further acceleration, reaching a momentum of 29 GeV/c. Following this, they will be directed to the antiproton production target. The high-intensity proton beam will collide with a copper target, resulting in the generation of various secondary particles, including proton-antiproton pairs [53]. A combination of a magnetic horn and a dipole magnet will be employed to separate the produced antiprotons, having a beam momentum of 3.8 GeV/c, from the main proton beam and all other secondary particles.

4.1.2 Collector-Storage Rings

The antiprotons which will separated in the Antiproton Separator will then subsequently be transferred to the Collector Ring (CR), where they undergo collection, stochastic cooling, and debunching. During the initial years of operation, this precooled beam will be directly injected into the High Energy Storage Ring (HESR), where the antiprotons will be accumulated. In the future, the Recuperating Energy Storage Ring (RESR) will accumulate the precooled antiprotons from the Collector Ring (CR) [54]. The contents of the RESR will then be transferred as a single bunch to the HESR. This process enables a higher quantity of antiprotons and, consequently, a higher peak luminosity for the $\overline{\text{P}}$ANDA experiment. Further description on CR and RESR can be found in [52].

4.2 The High Energy Storage Ring

The High Energy Storage Ring (HESR), shown in Figure 4.2, plays a crucial role in FAIR's physics program, specifically tailored for high-energy antiprotons. Configured as a race-track ring, the HESR will achieve a maximum beam rigidity of 50 Tm. Its structure will comprise of two 180° arcs and two straight sections, each spanning 155 meters, resulting in a total circumference of 575 meters. The HESR has the capability to decelerate the antiproton beam to a momentum of 1.5 GeV/c and accelerate it to a maximum of 15 GeV/c from the initial injection momentum of 3.8 GeV/c. The HESR is designed to function in two modes: the high luminosity mode and the high precision mode. Table 4.1 provides a summary of some design parameters of the HESR.

High Resolution Mode Electron cooling and stochastic phase space cooling together facilitate in achieving high momentum resolution of the beam. This leads to an improvement in the beam momentum spread to $\Delta p/p = 2 \cdot 10^{-5}$. Experiments using high precision energy scans depend on such momentum resolution. The design peak luminosity of $2 \cdot 10^{31}$ [$\text{cm}^{-2}\text{s}^{-1}$] will be attained with the RESR.

High Luminosity Mode For this mode, beam cooling is minimized to prioritize beam luminosity. The HESR functions at its peak luminosity of $2 \cdot 10^{31}$ [$\text{cm}^{-2}\text{s}^{-1}$], albeit with a trade-off resulting in a reduced momentum spread of $\Delta p/p = 2 \cdot 10^{-4}$.

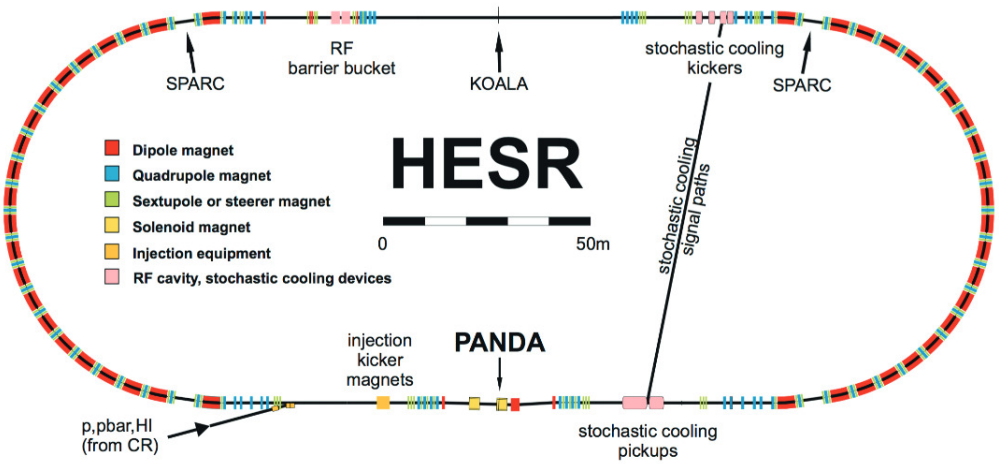

Figure 4.2: Overview of the High Energy Storage Ring (HESR) at FAIR. Image taken from [55].

Parameter	High Resolution	High Luminosity
Momentum p [GeV/c]	1.5 to 15	1.5 to 15
$\Delta p/p$ (rms)	$\approx 2 \cdot 10^{-5}$	$\approx 1 \cdot 10^{-4}$
N antiprotons	10^{10}	10^{11}
Peak Luminosity $[\text{cm}^{-2}\text{s}^{-1}]$	$2 \cdot 10^{31}$	$2 \cdot 10^{32}$

Table 4.1: Operational parameters of the HESR in the high resolution and high luminosity modes.

4.3 The $\overline{\text{P}}$ANDA Detector

The foreseen physics program of the $\overline{\text{P}}$ANDA experiment described in Chapter 2 necessitates various specifications for different components of the detector. Figure 4.3 shows the state-of-the-art $\overline{\text{P}}$ANDA detector for a fixed target experiment. The detector configuration consists of two primary components: the target spectrometer and the forward spectrometer, collectively providing coverage across almost the entire solid angle of 4π. The target spectrometer is based on a superconducting solenoid magnet and surrounds the interaction point (IP) in a shell-like structure. It will be employed to detect particles generated at larger angles. Whereas the forward spectrometer, which is based on a dipole magnet, will be used for small angle tracks. The $\overline{\text{P}}$ANDA detector was designed to

achieve high rate capability, good particle identification, high resolution for tracking, enable efficient tracking of charged particles, detect neutral particles through the calorimeter and provide a flexible readout. In the following subsections, a concise description of the components of all detector subsystems is provided [56].

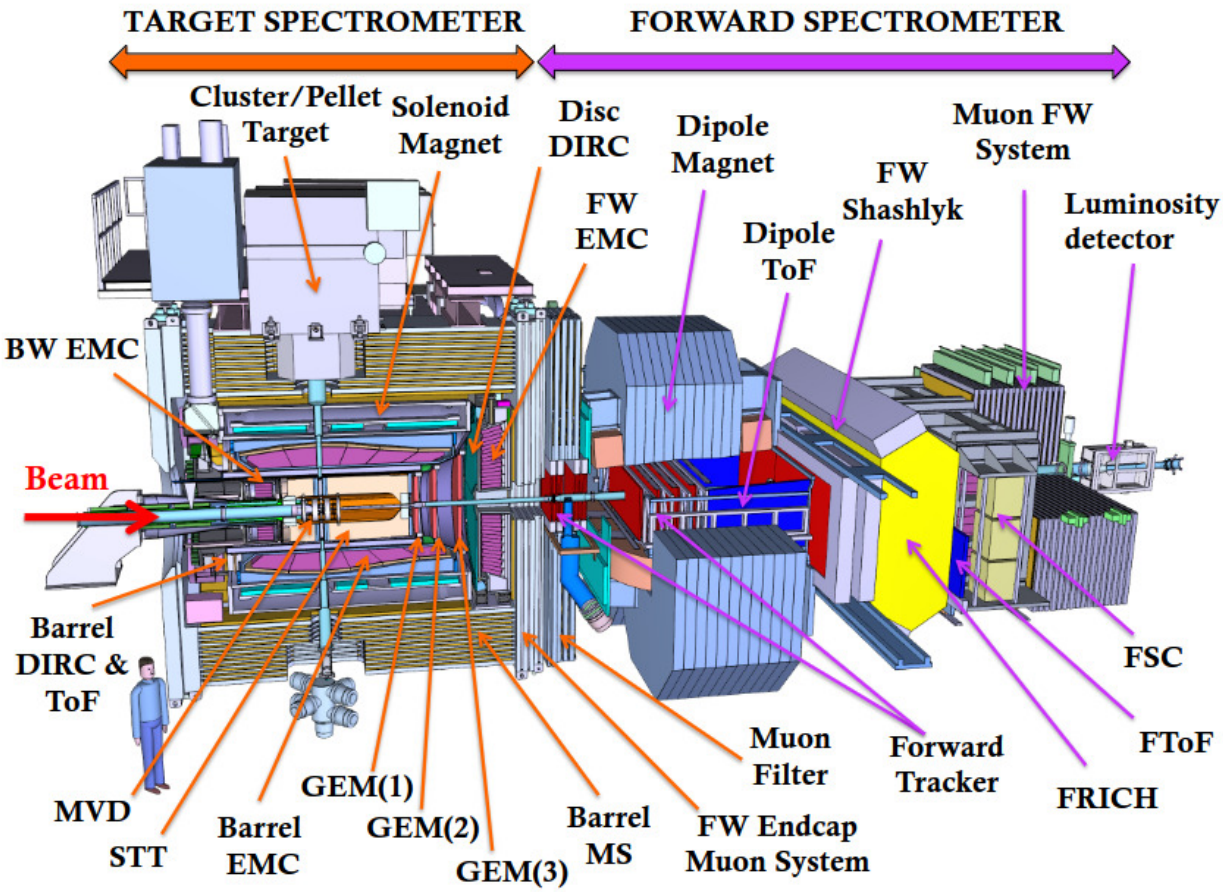

Figure 4.3: Schematic overview of the full experimental setup of $\overline{\text{P}}$ANDA. Image from [55].

4.3.1 Target Spectrometer

The interaction point is enclosed by the target spectrometer, which measures charged tracks in a 2T solenoidal field. It is comprised of detector layers arranged in an onion-shell configuration. Injection pipes for the target material must traverse the spectrometer perpendicular to the beam pipe. The target spectrometer is divided into 3 major parts: the barrel section, for polar angles 22° and an end-cap section for the forward range, reaching down to 5° vertically and 10° horizontally. One of the key design considerations is compactness to prevent the need for an excessively large and expensive magnet and crystal calorimeter.

4.3.1.1 Target System

To achieve the average maximum design luminosity of $2 \times 10^{32}\text{cm}^{-2}\text{s}^{-1}$, it is necessary to have a target thickness of approximately 4×10^{15} hydrogen atoms per cm^2. This calculation is based on the presence of 10^{11} stored antiprotons with a event rate of $2 \times 10^{7}\text{s}^{-1}$ in the HESR ring. Currently, two complementary techniques are being investigated: the cluster-jet target and the pellet target. Both methods have the capability to provide adequate hydrogen densities at the interaction point, fulfilling a significant portion of the experiment requirements.

Cluster-Jet Target A cluster-jet target is produced by introducing pre-cooled hydrogen gas into a vacuum through a Laval-type nozzle. As the gas traverses the nozzle, it undergoes further cooling via adiabatic processes, resulting in the formation of a supersonic beam. This process induces the condensation of hydrogen, leading to the creation of clusters, each composed of approximately 10^3 to 10^6 hydrogen molecules. The size of these clusters is heavily influenced by factors such as temperature, density, and nozzle geometry. The transverse spread relative to the beam direction is approximately 2-3 mm, while the longitudinal spread is around 15 mm. The clusters are separated by an average distance of less than 10 μm. A cluster-jet target satisfies $\overline{\text{P}}$ANDA's criteria for a very thin, homogenous target with a sufficiently high density by reaching areal densities of up to $2 \times 10^{15}\text{atoms/cm}^{-2}$.

Pellet Target The second option for meeting $\overline{\text{P}}$ANDA's requirements involves the use of a pellet target. An advantageous feature of the tracked pellet target is its capability to accurately determine the primary interaction vertex, offering a robust constraint for tracking particles originating from that point. The increased density of the pellet target allows for achieving higher luminosity. However, a drawback arises from significant fluctuations in the interaction rate due to the discrete nature of the pellet target, leading to large variations in thickness.

In this method, a cryogenic fluid is injected through a nozzle into a gas composed of the same element as the fluid, near its triple point. As the fluid flows through the nozzle, a piezoelement stimulates the nozzle, breaking the continuous fluid stream into droplets referred to as pellets. These pellets then enter a vacuum injection capillary, where the fluid undergoes further cooling, resulting in a stream of frozen pellets entering the vacuum of the beam pipe. Each individual pellet has a diameter of approximately 20 μm, and the pellet beam has a diameter of less than 3 mm.

A pellet target that has been previously designed and implemented at Uppsala, demonstrating successful operation at the former CELSIUS accelerator and COSY in Jülich,

produces pellets measuring 25 to 30 µm in thickness, containing approximately 10^{15} atoms per pellet. The beam intensity reaches 5000 to 20000 pellets per second within a 3 mm diameter beam [56]. The $\overline{\text{P}}$ANDA pellet target will adopt this existing design as a foundation, incorporating several enhancements to optimize its performance in an anti-proton beam environment.

4.3.1.2 Magnets

The magnet systems are employed in high energy particle studies to bend charged particles in order to determine their momenta. The Lorentz force, which is proportional to the particle's mass and velocity, is what causes this bending; particles with low momentum curve far more than those with large momentum, which curve very little. Hence, two different kinds of magnets—a dipole magnet for the forward spectrometer and a superconducting solenoid magnet for the target spectrometer—are proposed for the $\overline{\text{P}}$ANDA detector. An outline of the characteristics and specifications of the two types of magnets is provided in this section, with additional details available in [56].

Solenoid Magnet The intended spectrometer will feature a superconducting solenoid coil, generating a magnetic field with a maximum strength of 2 Tesla. This coil will have an inner radius of 1.05 m and a length of 2.8 m. Within the cryostat for the solenoid coils, two warm bores of 100 mm diameter will be positioned above and below the interaction point. This configuration allows for the insertion of the target pipe to accommodate various internal targets. To cool the coil, liquid helium will be employed. The coil is meticulously designed to achieve a field homogeneity better than 2% throughout the volume occupied by MVD and STT. Niobium-titanium (NbTi) fibers embedded in a copper matrix were selected as the material for the $\overline{\text{P}}$ANDA solenoid.

The tracking system within the solenoid is capable of reconstructing the momentum of charged particle tracks at angles as low as 5°/10°. An iron return yoke will facilitate the backflow of the magnetic flux from the solenoid magnet field. Additionally, this yoke will function as an absorber material for the muon detection system of $\overline{\text{P}}$ANDA within the target spectrometer. To prevent the presence of dead material in the front, the magnet coils will be positioned outside the Electromagnetic Calorimeter [56].

Dipole magnet Because $\overline{\text{P}}$ANDA is a fixed target experiment, the significance of the forward system cannot be overstated. Given momentum conservation, a majority of particles will be emitted at forward angles, necessitating their passage through the forward system. Within this system, a dipole magnet generating a maximum bending power of 2 Tm will provide the required magnetic field. The dipole magnet encompasses

angles ranging from 10° horizontally to 5° vertically. At the peak antiproton momentum of 15 GeV/c, the dipole magnet will deflect the antiproton beam by 2.2°. To counteract this effect, additional correction dipole magnets will be strategically positioned before and after the $\overline{\text{P}}$ANDA experiment along the HESR beam line.

4.3.1.3 Micro Vertex Detector

Micro Vertex Detector constitutes the innermost sub-detector system within the target spectrometer, specifically tailored for identifying secondary decay vertices of short-lived particles like D-mesons and hyperon decays. Additionally, the MVD aims to enhance transverse momentum resolution and particle identification by leveraging information on the energy loss per unit path length (dE/dx) of low energy particles within this sub-detector. The MVD, as illustrated in Figure 4.4, is composed of two primary parts: a barrel and a disc part.

The MVD concept relies on radiation-resistant silicon pixel detectors featuring rapid individual pixel readout circuits, along with silicon strip detectors. The MVD will encompass a radial range of up to 13.5 cm and extend 19.0 cm forward from the interaction point. The innermost and outermost layers of the barrel are slated to be positioned at distances of 2.5 cm and 13.5 cm from the interaction point, respectively. The MVD is designed to cover polar angles ranging from 3° to 150°.

The barrel MVD is designed with four layers: the two innermost layers featuring pixel detectors with a cell size of 100×100 μm^2 but varying in length and width, and the two outermost layers equipped with Double Sided Silicon Strip Detectors (DSSD). The forward section comprises six discs with pixel sensors, where the two most downstream discs along the beam pipe also include DSSD in their outermost parts. The DSSD will be rectangular for the barrel section and trapezoidal for the forward discs.

The MVD employs semiconductors (for both pixels and strips) in particle detection. When a charged particle traverses the material, the ionization process generates electron-hole pairs. Applying an electric field causes the electrons to drift toward the read-out electronics, providing 3D information about the hit position. The MVD's vertex resolution has been examined in a prior study focusing on D meson decays. Employing various vertexing tools within the $\overline{\text{P}}$ANDA software, the investigation revealed comparable resolutions in both x and y, approximately at the level of 50 μm, while the z resolution was found to be around 100 μm. A comprehensive technical description is available in [57].

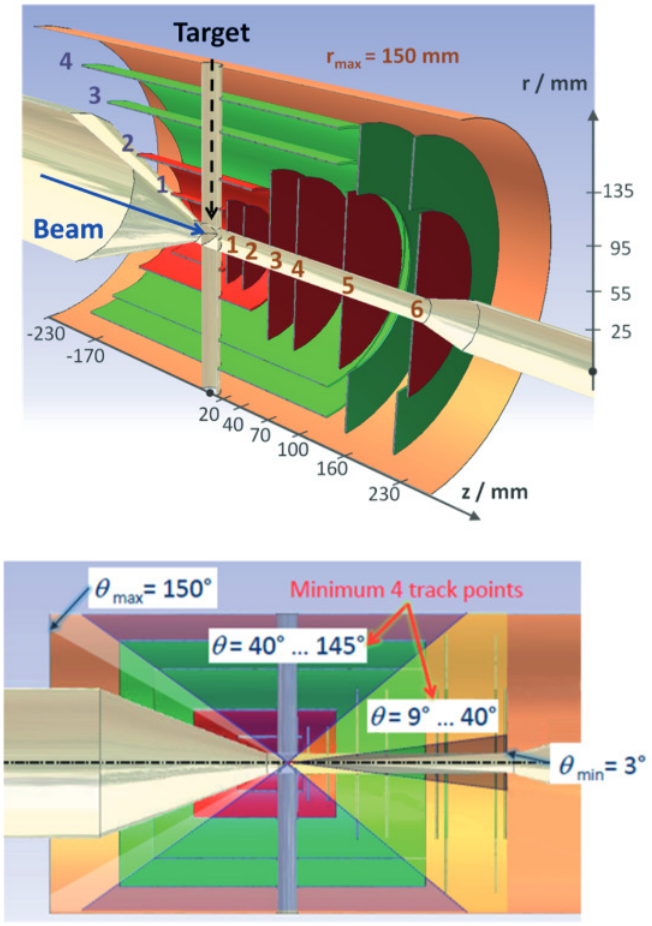

Figure 4.4: The Micro-vertex detector $\overline{\text{P}}$ANDA detector. The red barrels and discs feature hybrid pixel detectors, while the green barrels and discs incorporate double-sided strip detectors[57].

4.3.1.4 Straw Tube Tracker

The Straw Tube Tracker (STT), shown in Figure 4.5, serves as the primary tracking detector for charged particles within the $\overline{\text{P}}$ANDA target spectrometer. The STT has a straw length of 140 cm along the beam pipe and spans a radial distance of 15.0 cm to 41.8 cm. The geometrical polar angle coverage is $10° < \theta < 140°$. The STT is constructed with aluminum-coated Mylar tubes having a 10 mm diameter, incorporating a gold-plated tungsten-rhenium anode wire at the center. The gas within the tubes is Argon-based (90%) with carbon dioxide (10%) serving as a quench gas. The planned configuration involves approximately 4200 individual straw tubes arranged in planar layers which are mounted in a hexagonal pattern around the beam pipe, as depicted in Figure 4.6. The system will have up to 27 layers, with 15-19 layers of tubes arranged parallel to the beam (indicated in green) for xy-reconstruction. Additionally, eight layers (shown in red and

blue) of skewed tubes will be arranged with a tilt angle of $\pm 3^{\circ}$ for longitudinal momentum reconstruction. The position resolution in the rϕ-plane is 150 µm, and the longitudinal position resolution is 2-3 mm, where r represents the radial distance from the beam, and ϕ denotes the azimuthal angle.

As a particle passes through a tube, it ionizes the gas along its path, generating free electrons and ions. Under the influence of an applied electric field, these free electrons move towards the anode wire, knocking out additional electrons, resulting in an *avalanche*. The avalanche leads to a signal amplification by a factor of about 10^4 to 10^5. The time taken for electrons to reach the anode is referred to as *drift-time*. An electron generated near the outer wall tube has the maximum drift time which is about 250 ns. The accumulation of electrons at the anode wire produces a signal. As the particle travels through the detector, it leaves a sequence of such hits, forming a particle track. The circular path around the anode wire that intersects the point of closest approach to the wire by particles is termed an isochrone.

A signal from the anode wire signifies that a particle has traversed the tube anywhere along the isochrone. Determining the exact point on the isochrone where the true particle path intersects requires the combination of multiple hits. Figure 4.7 illustrates a particle trajectory across three straw tubes in the xy-plane where green point represents the correct hit position for the track in the middle straw tube.

In addition to track reconstruction, the STT will serve for Particle Identification (PID) by assessing the energy loss (dE/dx) of protons, kaons, and pions, particularly within the particle momentum range below 1 GeV/c. In forward direction, the STT is followed by a set a Gas Electron Multiplier Stations. Further detailed description of the STT can be found in [58].

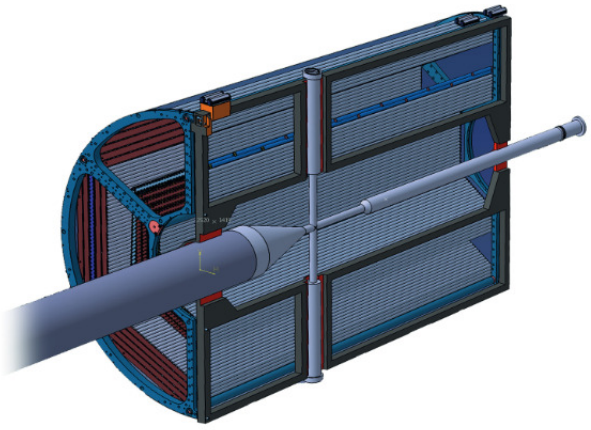

Figure 4.5: The $\overline{\text{P}}$ANDA Straw Tube Tracker in longitudinal view. Enclosed is the beam pipe and a narrow aperture on the top where the target may be inserted. Figure adapted from [57].

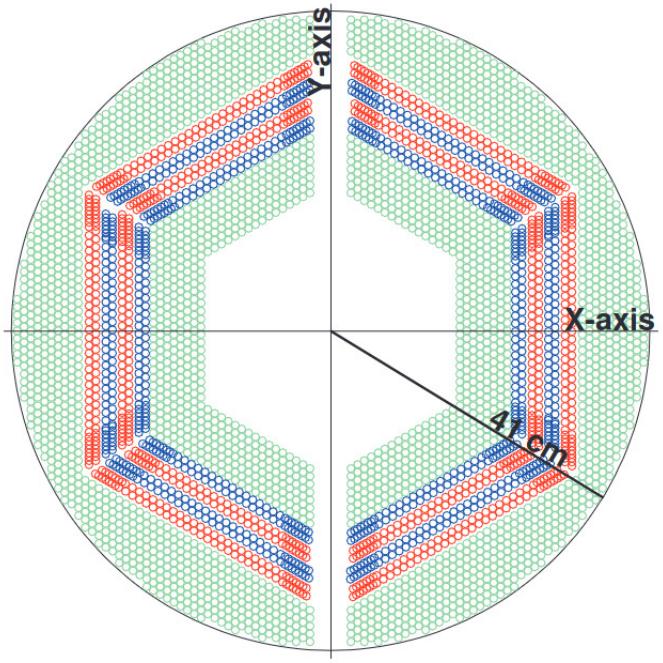

Figure 4.6: Cross-sectional view of the straw tube layout in Straw Tube Tracker. The green circles represent the parallel straws whereas the red and blue circles represent the skewed straws [58].

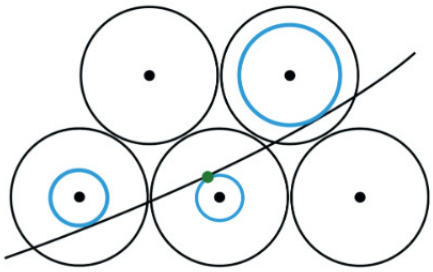

Figure 4.7: A sketch of a particle's trajectory across three straw tubes in the xy-plane. The blue circles represent the isochrones. The green point represents the correct location where the track is tangential to the isochrone and the distance to the wire is at its lowest.

4.3.1.5 Gas Electron Multiplier Stations

The region in between the target and forward spectrometers will be covered by the Gas Electron Multiplier (GEM) tracker, which will be positioned in the forward direction along the beam pipe. The polar angles covered by the GEM detector range from 3° to 22°. Three circular planes make up the GEM detector, which is seen in Figure 4.8, and is situated 117 cm, 153 cm, and 189 cm downstream from the interaction point. These GEM stations will have a diameter of 90 cm, 112 cm and 148 cm, respectively. In the future, a fourth disc station is anticipated. The location of this station is 81 cm downstream of the contact point. As a portion of this area lacks coverage from both the STT and the FTS, the data provided by the GEM planes plays a crucial role in determining the acceptance and momentum resolution in this specific region.

The GEM discs employ a method of electron multiplication within gaseous micro-pattern foils. These GEM foils are composed of insulating polyamide foils with a mere 50 µm thickness and feature a conductive coating on both sides. The surfaces of the foils are coated with a copper layer ranging from 2 to 5 µm in thickness. The foils are punctuated with hexagonally arranged holes, each having a diameter of 70 µm. Each disc station comprises a centrally located double-sided read-out disc pad. Three GEM foils are positioned on either side for signal amplification. The read-out pad captures 2D positional information in two projections, ensuring a precise position measurement with a resolution surpassing 100 µm.

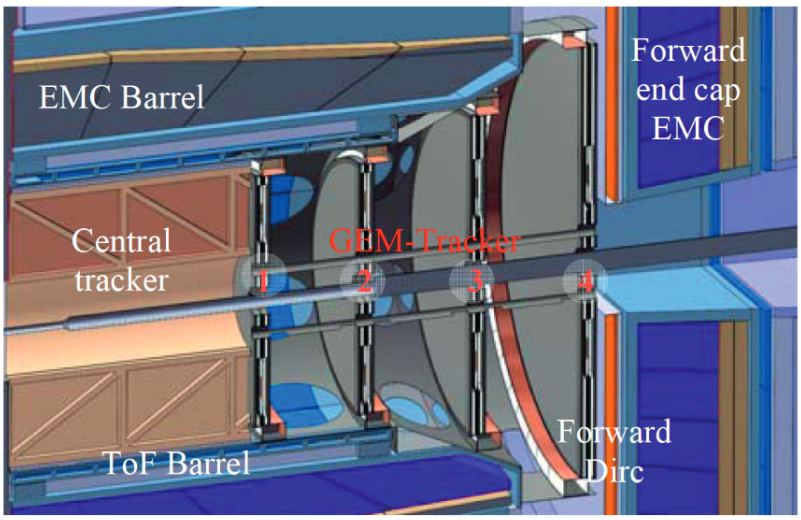

Figure 4.8: The structure of the GEM detector. Stations 2, 3 and 4 are the ones initially planned. Image adapted from [59].

4.3.1.6 Barrel Time of Flight (BToF) Detector

$\overline{\text{P}}$ANDA incorporates two Time-of-Flight (ToF) detectors, one situated in the barrel part and the other in the forward section. The detectors are composed of scintillating material. The atoms in the detector will become excited when a charged particle passes through it, and the energy will be released as visible light. The light is directed into a photocathode, which transforms the light signal into an electric signal that a photomultiplier amplifies. The light is directed to a photocathode, converting it into an electric signal that undergoes amplification by a photomultiplier. This signal facilitates the determination of a reference time, indicating when the charged particle interacts with the ToF detector, and provides position information due to the high granularity of the detector system. Given that $\overline{\text{P}}$ANDA lacks a detector offering the start time of the event, both ToF detectors serve as relative Time-of-Flight counters. Consequently, particle identification with the ToF detector in$\overline{\text{P}}$ANDA relies on an iterative algorithm. This algorithm evaluates hypotheses regarding the species of each measured particle based on the recorded times, assuming a common start time for all particles in the event.

The Barrel Time of Flight detector (BToF) in the target spectrometer covers a polar angle of 22.5° to 140° and encircles the STT with a radial radius of about 50 cm from the beam axis. Figure 4.9 illustrates the schematic representation of the BToF along with an enlarged depiction of two scintillator tiles. Additionally, as the Barrel ToF will be positioned inside the solenoid magnet, it must be constructed from non-magnetic materials, considering space limitations and event rates. To fulfill these criteria, the

detector comprises 1920 scintillator tiles, each 20 mm thick, with a surface area of 87 × 29.4 mm^2. These scintillator tiles are organized in a 2 × 60 matrix array, referred to as a supermodule. Overall, the detector consists of 16 fully independent supermodules. Each individual tile is read by four Silicon Photomultipliers (SiPM) of size 30 × 5 mm^2, one on each side. The plastic scintillators are designed for optimal fast response and excellent time resolution, achieving a remarkable time resolution of approximately $\sigma_t \sim 55$ps. This time resolution surpasses the initial design goal of 100 ps. A detailed description of the BToF can be found in [60].

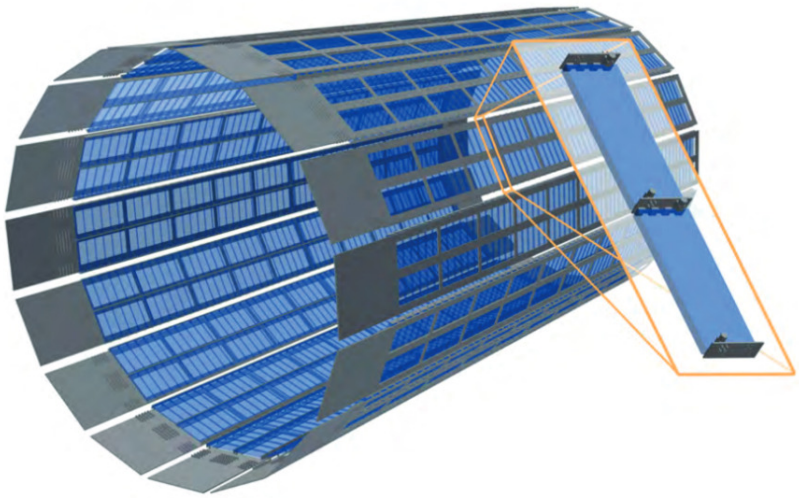

Figure 4.9: The Barrel Time-of-Flight in the target spectrometer.

4.3.1.7 Electromagnetic Calorimeter

The EMC is designed to function as a compact calorimeter comprising three sections: the backward endcap, the barrel, and the forward endcap, as depicted in Figure 4.10. Its primary functions include measuring energies, separating electrons from other charged final state particles, and detecting photons within the energy range spanning from a few MeV to several GeV. Lead-tungstate ($PbWO_4$, PWO-II) crystals, an inorganic scintillator renowned for its high density, energy resolution, and quick response, will be used to construct the EMC. Using these crystals at a temperature of -25 °C instead of room temperature, can increase the light yield by a factor of four. To obtain an energy resolution of more than 2 % at 1 GeV, the $\overline{\text{P}}$ANDA EMC's crystals are 20 cm in length. The tapered crystals will be placed with an inner radius of 57 cm and a front dimension of 2.1 × 2.1 cm^2. In total, the EMC will comprise 15,552 crystals. The barrel section will consist of 11,360 crystals organized into 16 slices, each containing 710 crystals. The forward and backward end-caps will encompass 3,600 and 592 crystals, respectively.

The EMC employs scintillating crystals to measure the energy deposits from particles. These crystals are crafted from a material that undergoes scintillation, wherein absorbed energy is re-emitted in the form of light. High energy photons primarily interact with crystals through Compton scattering or e^+e^- pair formation. As electrons (and positrons) traverse the crystals, they lose energy through bremsstrahlung emission. The emitted photons further interact with the crystal, producing more electron positron pairs, via pair-production. This cascade of processes results in a particle shower with energies lower than the initial incident particle. During this shower, the material absorbs energy, leading to the emission of scintillation light. Unlike reabsorption, this light is emitted outward from the crystal and can be detected by photosensors. Typically, a photomultiplier tube (PMT) is employed to convert the scintillation light into an amplified signal. Due to the placement of the EMC inside the solenoid magnet, PMTs cannot be used and therefore the crystals are affixed with avalanche photodiodes (APD) instead. A comprehensive description of the EMC is found in [61].

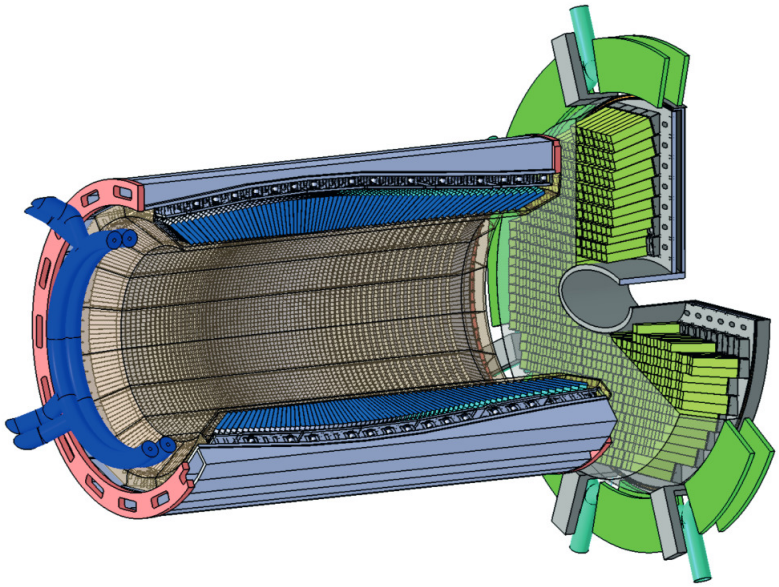

Figure 4.10: The barrel and forward endcap of the Electromagnetic Calorimeter of the $\overline{\text{P}}$ANDA Target Spectrometer. Image adapted from [61].

4.3.1.8 Cherenkov Detectors

A dedicated Particle Identification (PID) detector in the $\overline{\text{P}}$ANDA TS is the Detection of Internally Reflected Cherenkov light detectors (DIRC). The primary objective of the DIRC is to distinguish between pions, kaons, and protons within a momentum range of 0.5 to 3.5 GeV/c and polar angles of 5° to 140°. The $\overline{\text{P}}$ANDA DIRC detector, depicted in Figure 4.11, consists of two components: a barrel section and an end-cap disc section. The barrel and the disc DIRC will cover angles $22° - 140°$ and $5° - 22°$ respectively.

The DIRC principle operates as follows: when a particle moves through a medium at a velocity surpassing the speed of light in that medium, it emits electromagnetic shock waves in the form of Cherenkov light. The emission angle and the number of emitted photons are contingent upon a particle's velocity. This information, when combined with the particle's momentum, obtained from tracking detectors, can be employed to compute the particle's mass and, consequently, the identity of the particle with a certain probability.

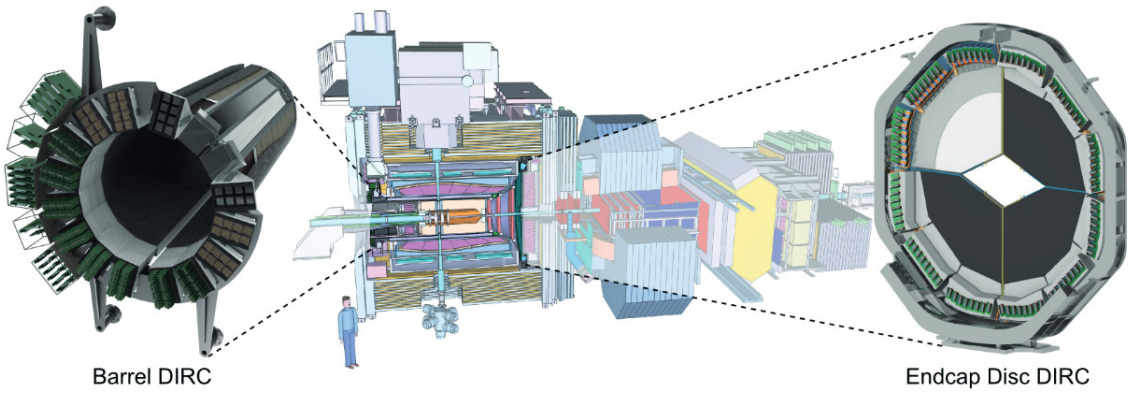

Figure 4.11: The Barrel DIRC and the End-cap Disc DIRC in the $\overline{\text{P}}$ANDA Target Spectrometer. Image adapted from [62].

4.3.1.9 Muon Detection System

The $\overline{\text{P}}$ANDA detector will include a muon detection system for muon identification, illustrated in Figure 4.12, within both the TS and FS. Further details on the FS Muon System can be found in section 4.3.2.5. The Muon System in the TS will comprise three components: a barrel part integrated with the magnet iron yoke, a forward end-cap situated downstream from the interaction point, and a detachable muon filter positioned between the TS and the dipole magnet in the FS. This muon filter serves a dual purpose by enhancing the absorber depth and functioning as an additional magnetic screen between the solenoid and dipole fields. Each segment comprises alternating layers of detection and passive iron. The detection layers consist of rectangular Mini Drift Tubes (MDT), which are made up of gold-plated tungsten anode wires encased within aluminum drift tubes. The barrel part and the forward endcap will consist of 2133 and 618 MDTs respectively whereas the muon filter consists of 424 MDTs.

4.3.2 Forward Spectrometer Detectors

The Forward Spectrometer will encompass the region extending up to $\pm 10°$ in the horizontal plane and $\pm 5°$ in the vertical plane with respect to the beam direction. The Forward Spectrometer (FS) is equipped with tracking, Particle Identification (PID), calorimetry, and muon detection capabilities identical to those in the TS. Therefore, the detection principles of sub-detectors in the FS closely resemble those of the detectors in the TS, albeit with some variations. The Forward Tracking System, in conjunction with a dipole magnet, will be responsible for track reconstruction in the FS.

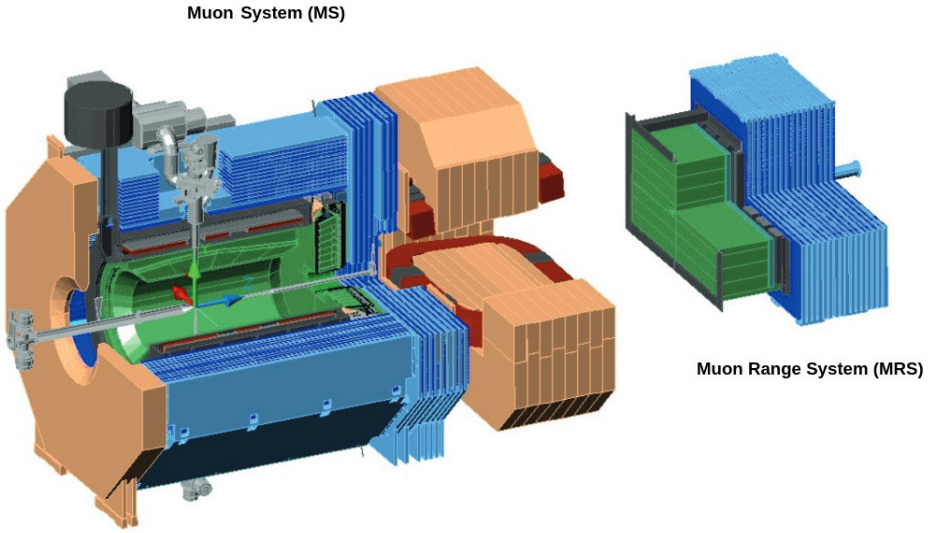

Figure 4.12: The Muon System of $\overline{\text{P}}$ANDA. Highlighted in blue are the Muon System and Muon Range System in target and forward spectrometers, respectively. The calorimeters are highlighted in green. Image adapted from [63].

4.3.2.1 Forward Tracking Stations

The Forward Tracker stations within the forward spectrometer are designed for reconstructing the tracks of charged particles within the magnetic dipole field, particularly at small forward angles. The setup, as shown in Figure 4.14, is foreseen to comprise of three pairs of tracking stations, with one pair positioned in the front, the second pair within the dipole magnet, and the third pair located behind the dipole magnet. The Forward Trackers have an angular acceptance of less than $\pm 10°$ in the horizontal plane and $\pm 5°$ in the vertical plane.

The arrangement of each tracking station will be structured similar to the STT of the target spectrometer. These modules will be positioned adjacent to each other in a plane perpendicular to the beam direction to create a double layer. To create a double layer, modules wll be arranged next to one another in a plane perpendicular to the direction of the beam. Every tracking station will be composed of four double layers: the outermost double layers (first and fourth along the beam direction) will consist of vertical straws, while the two intermediate (the second and third) double layers will have straws inclined by $+5°$ and $-5°$, respectively. The central gap in the chambers will accommodate the passage of the beam pipe.

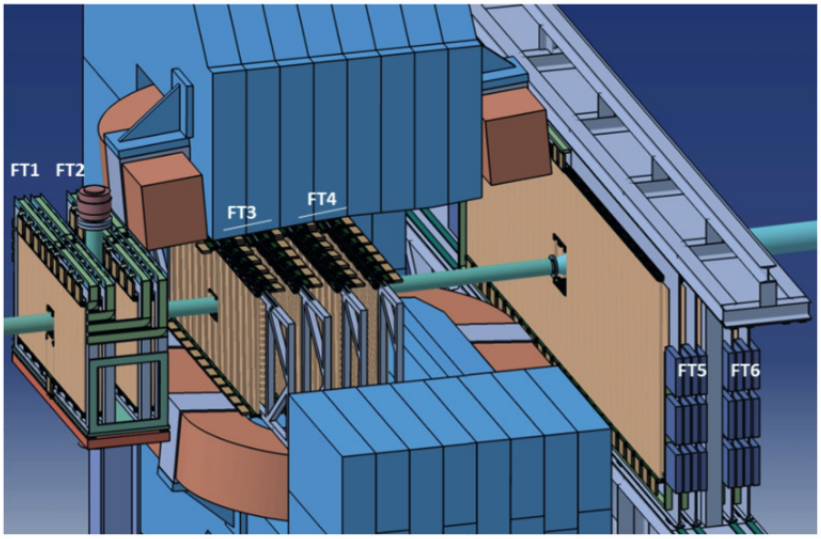

Figure 4.13: The Forward Tracking Stations in the forward spectrometer of $\overline{\text{P}}$ANDA detector. Image adapted from [64].

4.3.2.2 Forward Spectrometer Electromagnetic Calorimeter

The Forward Spectrometer Calorimeter (FSC), illustrated in 4.14, will conduct calorimetry in the forward direction. Positioned approximately 7.8 meters downstream from the interaction, behind the last FToF wall, it will span a width of 3.6 meters and a height of 2.2 meters. The calorimeter will detect particles within an energy range of 10 MeV to 15 GeV, and cover polar angles of 10° horizontally and 5° vertically. A Shashlyk-type calorimeter, characterized by its high resolution and efficiency, will be utilized to detect high momentum photons and electrons moving in the forward direction.

Individual detection cells of the FSC will be constructed with 380 alternating layers of plastic scintillator sheet and lead plates with thickness of 1.5 mm and 0.3 mm respectively. These cells are grouped into modules, each comprising four detection cells that share a common read-out. The FSC consists of 378 such modules in total. The method of detection involves using photomultipliers to read out lead-scintillator sandwiches that have wave-length-shifting fibers connected through the block. Detailed description of the $\overline{\text{P}}$ANDA Muon System can be found in [65].

The method of detection involves using photomultipliers to read out lead-scintillator sandwiches that have wave-length-shifting fibers connected through the block. Detailed description of the $\overline{\text{P}}$ANDA Muon System can be found in [65].

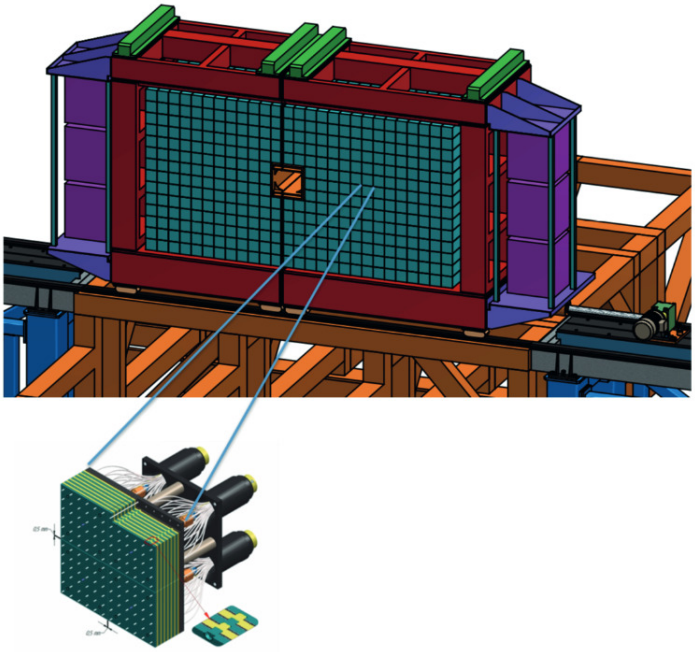

Figure 4.14: The Forward Spectrometer Calorimeter of $\overline{\text{P}}$ANDA. Image adapted from [65].

4.3.2.3 Ring Imaging Cherenkov Detector

Ring Imaging Cherenkov (RICH) detector will help in identifying particles moving in the forward region with high momenta. It will also provide separation of pions, kaons and protons in a wide momentum range of 2–15 GeV/c. Positioned 6.5 m downstream from the interaction point, the RICH employs a method similar to the DIRC located in the target spectrometer to identify particles, measuring Cherenkov radiation. The radiator materials chosen for the RICH are silica aerogel and Freon (C_4F_{10}) gas, characterized by a refractive index of n = 1.0304 and 1.00137 respectively.

4.3.2.4 Forward Time-of-Flight

The Forward Time-of-Flight (FToF) serves the same purpose, operates on the same principles, and follows a similar design as the Barrel Time-of-Flight (BToF) in the target spectrometer. However, it will be constructed as a planar detector and positioned 7.5 m downstream the interaction point. Similar to the BToF, the FToF, as seen in Figure 4.15, is a wall composed of plastic scintillators and will be constructed from BC 408. It will be comprised of 66 plates, each measuring 140 cm in length and 2.5 cm in thickness, and have a total width of 5.6 m. The exterior plates will be 10 cm in width, while the 20 innermost plates will measure 5 cm. The narrower plates are designed to manage the

anticipated increased particle influx near the beamline. Like the BToF, the FToF will achieve a time resolution of 100 ps.

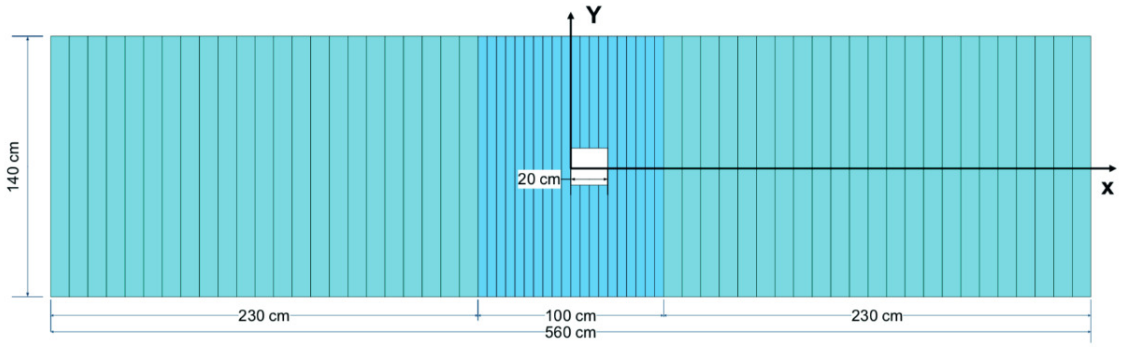

Figure 4.15: Design of the Forward Time-of-Flight wall. Image adapted from [66].

4.3.2.5 Forward Muon System

Positioned approximately 9 m downstream from the target, the forward muon range system will be situated furthest from the target. Similar to the barrel muon system, it will be composed of alternating layers of aluminum drift tubes and iron absorbers. The system enables the differentiation between pions and muons, the identification of pion decays, and the energy determination of neutrons and antineutrons with a reasonable degree of resolution. Detailed description of the $\overline{\text{P}}$ANDA Muon System can be found in [63].

4.3.2.6 The Luminosity Detector

The farthest downstream element of the $\overline{\text{P}}$ANDA detector is the Luminosity Detector (LMD), located approximately 11 m from the interaction point and will facilitate the measurement of elastically scattered particles at small angular region ranging from 3 mrad to 8 mrad. The Luminosity Detector will compose of four 15 cm-radius circular planes that hold 400 High Voltage Monolythic Active Pixel Sensors (HV-MAPS) to monitor the angular distribution of the elastically dispersed antiproton.

Accurately measuring the time-integrated luminosity L within a time interval dt is a crucial parameter for determining the cross section σ of a decay channel. The cross section and the number of occurrences N observed at a time interval dt are directly correlated, according to $N = L \cdot \sigma$ [67].

5 | Software and Reconstruction Tools

5.1 The PandaRoot Software

The software environment for the $\overline{\text{P}}$ANDA experiment comprises of FairRoot and PandaRoot, both built on the ROOT framework. Developed in C++, ROOT is an object-oriented program that provides data management, statistical analysis, visualization, and histogramming features. FairRoot is an extension of ROOT package, developed by FAIR, which serves all FAIR experiments, including NuSTAR, CBM, and $\overline{\text{P}}$ANDA. It encompasses external software dependencies and logistical support necessary for these experiments, such as providing detector geometries, event generation, particle transport, and event display. PandaRoot is an extension of the FairRoot, designed specifically for the $\overline{\text{P}}$ANDA experiment. PandaRoot provides a detailed description of the structure and subdetectors of $\overline{\text{P}}$ANDA, enabling it to generate realistic simulations of the detector performance.

5.2 The PandaRoot Analysis Chain

Within the PandaRoot framework, the simulation and analysis chain has various stages: simulation, digitization, reconstruction, particle identification and analysis. These steps are shown in Figure 5.1.

5.2.1 Event Generation

The event generation is the first stage of the simulation chain. It comprises two primary steps: particle generation and particle transport. In the first step, the physics channel of interest is generated. In PandaRoot, there are several options available, i.e. EvtGen, DPM, UrQMD, Pyhtia, FTF and Fluka, for generating decays and kinematic distributions. Another option available in PandaRoot is the box generator, also referred to as

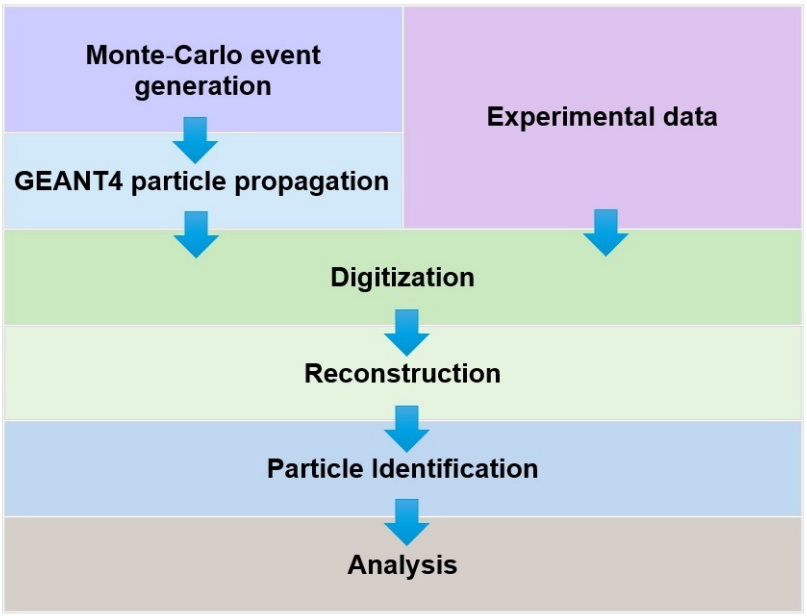

Figure 5.1: Standard analysis chain in PandaRoot.

a particle gun. This tool enables users to simulate particles within a user-defined momentum and angular range. For this study, the EvtGen generator was used. EvtGen is designed to generate physical events based on particular decay models, including flat phase space, data parametrizations, and other phenomenological models. In the particle generation step, ideal tracks known as *Monte Carlo particles* are created, representing tracks in a perfect vacuum. The output from the event generators is the four-momentum vectors and vertex positions of the final state particles.

After event generation, the final state Monte Carlo particles are propagated through the detector material using the GEANT package. GEANT (GEometry ANd Tracking) is a versatile toolkit designed for simulating passage of particles through matter. It takes into account a wide range of physics processes, including electromagnetic and hadronic interactions, as well as the effects of bending in a magnetic field and radiation-induced energy losses as particles traverse material. As a result of the propagation process, Monte Carlo (MC) tracks and points are generated, which provide information about the particle's position, momentum, energy deposition, and time across different sub-detectors. At this stage, the MC points recorded have infinite resolution as noise and other detector effects are not present.

5.2.2 Digitization

In the digitization stage, the MC points produced during simulation for each subdetector are converted into realistic observables that mimic the actual output of the subdetectors. This implies that the energy loss is transformed into electronic signals. The MC points are converted to *digis* or *hits* which contain spatial information with time-stamps. Each subdetector has a different resolution, which is determined by certain detector characteristics like granularity.

5.2.3 Reconstruction

The reconstruction process involves two main stages. The initial step, known as *track finding* (or pattern recognition), involves grouping digitized hits into clusters. The outcome of this stage is referred to as a track candidate, which comprises a collection of hits. This information is stored in the *PndTrackCand* object in PandaRoot.

In the second stage, referred to as *track fitting*, the clustered hits are used to fit a track. Various mathematical models are employed to estimate track parameters like momentum. One such offline algorithm used for refining momentum estimation is the classical Kalman filter, which is the fundamnetal component of the GenFit package. GenFit is a fitting tool created by $\overline{\text{P}}$ANDA [68]. As the fit is iterative, innital track parameter estimates are required. The fitted track characteristics, such as the momentum, charge, and position at the first and last hits of the track, are contained in the PandaRoot data object *PndTrack*. The fitting process takes into consideration the material effects and geometry of the detector as well as the radiation-induced energy losses. During track reconstruction, there are algorithms suitable for both online and offline purposes. The offline algorithms are particularly useful for improving the momentum reconstruction achieved by the online algorithms.

5.2.4 Particle Identification

After the reconstruction stage, the particle that originated each track must be assigned an identity. In the first step of particle identification, neutral particles are distinguished from the charged particle through the correlation between the EMC clusters from the charged tracks found by the tracking detectors. in the next step, the charged particles are further assessed.

To identify the particle type, information from all subdetectors must be combined, as each subdetector specializes in distinguishing certain particle species within specific momentum

ranges. As a result, particle identification is split into two stages: a local part and a global part. The local PID is performed independently using distinct algorithms within each PID subdetector of $\overline{\mathrm{P}}$ANDA. In each sub-detector, the probability of each potential final state particle species (e, μ, π, K, p) is assessed. By combining the individual local PID probabilities, a global PID probability can be computed.

In order to obtain the local PID, the following methods are employed by the detectors:

- The barrel ToF measures time-of-flight of particles below 1 GeV/c. The velocity can be calculated by combining the Time-of-Flight data with the path length obtained by the tracking detectors. The mass can be determined using the formula $p = \gamma\beta m$, which may be written as $m^2 = p^2 \cdot \left(\frac{1}{\beta^2} - 1\right)$.
- The the DIRC and RICH detectors measures Cherenkov radiation to identify particles above 1 GeV/c.
- The MVD and STT measures the energy loss. Despite being tracking detectors, their PID capabilities remain limited and rely on measuring the energy loss, dE/dx, of tracks passing through them.

5.2.5 Analysis

During the analysis stage, the user conducts event selection, where particle candidates, along with their PID probabilities, are available in an event-based structure. The Rho package [69] facilitates various tasks, including combinatorial calculations, mass selection criteria, kinematic fits, and storage of the final selection data into ROOT files.

5.2.6 Overview of Key Rho Classes for Data Analysis

In the context of data analysis within the PandaRoot framework, Rho classes play a crucial role in managing and analyzing the data related to particle events. Below is a brief description of some of the most important Rho classes:

1. **RhoCandidate:** This class represents a particle candidate, encapsulating information about a track or cluster. It can store essential properties like mass, charge, momentum, and energy. It also supports decay tree structures, allowing for the reconstruction of particle decays.
2. **RhoTrack:** A subclass of `RhoCandidate`, it specifically handles track-based information. It provides methods to access track parameters such as momentum, vertex, and particle identification hypotheses.

3. **RhoVertex:** This class handles vertex information related to particle decays. It supports the fitting of vertex positions and enables vertex-based cuts during event selection.

4. **RhoMassConstraint:** Used to constrain the mass of a composite particle to a specific value during reconstruction. This class is essential for applying kinematic constraints, improving the precision of particle identification and reconstruction.

5. **Rho4CFit:** The class uses four-momentum kinematic fitting and applies a 4-constraint (4C) kinematic fit, ensuring energy and momentum conservation in particle decays. This method is useful for improving the precision of particle reconstruction by refining momentum and energy measurements, based on the assumption that the total four-momentum (energy and three-momentum components) must be conserved.

6. **RhoKinFitter:** This class performs kinematic fitting, allowing users to fit particle candidates to particular decay hypotheses. By adjusting parameters like momentum and energy, it helps improve the consistency of the reconstructed event with the physics model.

5.3 Photon Reconstruction

Photon reconstruction in the $\overline{\text{P}}$ANDA experiment is essential for accurately detecting and analyzing electromagnetic showers produced by photons interacting with the electromagnetic calorimeter (EMC). $\overline{\text{P}}$ANDA aims to identify and measure photons, which play a critical role in many of its key physics analyses, especially in charmonium and exotic spectroscopy studies. The reconstruction process involves detecting energy deposits in the EMC crystals and then using sophisticated algorithms to group these energy deposits into clusters, correct for energy leakage, and determine the photon's original properties.

5.3.1 Cluster Finding and Bump Splitting

The first step in photon reconstruction is cluster finding. When a photon enters the EMC, it initiates an electromagnetic shower that deposits energy across multiple crystals. The group of adjacent crystals affected by this shower is referred to as a cluster. The cluster finding algorithm begins by identifying the crystal with the highest energy deposit (the seed crystal) and then adding neighboring crystals whose energy exceeds a predefined threshold. This process continues iteratively, forming a contiguous cluster of energy deposits that represents the shower from a single photon [61].

Bump splitting is a technique employed to deal with cases where multiple particles, such as photons or electrons, produce overlapping showers. This can happen when the angular separation between particles is small, causing their energy deposits to merge into a single cluster. The bump splitting algorithm identifies local maxima, or "bumps," within the cluster, each of which corresponds to a separate particle. These bumps are treated as individual sub-clusters, and their energy is calculated by distributing the total cluster energy based on the distance between the bump's center and the neighboring crystals.

The energy assigned to each bump is computed using an iterative method, where the energy of the surrounding crystals is weighted according to their proximity to the bump's center. This ensures that the energy deposits from different particles are accurately separated, improving the overall accuracy of the photon reconstruction process. The cluster finding and bump splitting algorithms employed in the EMC reconstruction software are based on code developed and effectively applied by the BaBar experiment.

5.3.2 Energy Thresholds and Photon Detection

In any high-energy physics experiment, it is important to establish energy thresholds that balance detection sensitivity with noise suppression. For photon reconstruction in $\overline{\text{P}}$ANDA, the following thresholds are applied [61]:

- $E_{xtl} = 3$ MeV: The minimum energy a crystal must register to be included in a cluster.
- $E_{cl} = 10$ MeV: The minimum total energy of the cluster for it to be considered a valid photon signal.
- $E_{max} = 20$ MeV: The minimum energy threshold to identify local maxima (bumps) within a cluster.

These thresholds are designed to detect low-energy photons while minimizing the inclusion of noise and background energy deposits. Low-energy photons are particularly important in charmonium studies and other processes where they serve as decay products. Missing low-energy photons or inaccurately reconstructing them can severely limit the experiment's ability to distinguish signal from background.

5.3.3 Photon Four-Vector Reconstruction

Once the cluster is identified, and the bump-splitting algorithm has separated individual particles, the next step is to reconstruct the photon's four-momentum vector. The four-

momentum vector consists of the energy and spatial components of the photon and is crucial for determining the kinematic properties of the event in which the photon was produced.

The energy of the photon is determined by summing the energy deposits across the crystals in the cluster. The spatial information, i.e. the position where the photon interacted with the EMC, is calculated using the energy-weighted center of the cluster, which provides an estimate of the photon's position at the time of interaction. By combining the energy and position data, the reconstruction algorithm calculates the photon's full four-vector, which is then used for further physics analysis.

5.3.4 Shower Leakage and Energy Corrections

A key challenge in photon reconstruction is dealing with shower leakage, where part of the photon's energy escapes detection because the electromagnetic shower extends beyond the boundaries of the EMC or the energy deposits occur in gaps between crystals. To correct for this, the $\overline{\text{P}}$ANDA reconstruction software applies leakage correction functions.

These correction functions are typically logarithmic and depend on both the detected energy and the photon's polar angle. Simulations have shown that applying these corrections significantly improves the accuracy of the photon's reconstructed energy, especially for high-energy photons where leakage effects are more pronounced. The correction ensures that the final reconstructed energy more closely matches the true energy of the photon, which is critical for precise event analysis.

5.3.5 Energy and Spatial Resolution

The energy resolution of the EMC is a measure of how accurately the calorimeter can reconstruct the energy of a photon. The resolution improves with the length of the EMC crystals, as longer crystals allow the shower to deposit more of its energy before it escapes. Simulations conducted for $\overline{\text{P}}$ANDA show that for low-energy photons (below 300 MeV), the energy resolution remains largely unaffected by crystal length. However, for higher-energy photons, the resolution improves significantly with longer crystals. For example, a 20 cm crystal achieves an energy resolution of approximately 1.5% for 1 GeV photons, while for photons above 3 GeV, the resolution is better than 1% [61].

The spatial resolution of the EMC, or its ability to determine the position of a photon, is also critical. The spatial resolution is measured by the uncertainty in the reconstructed position of the photon's interaction with the EMC crystals. $\overline{\text{P}}$ANDA's simulations indicate

that the spatial resolution is less than 0.3 cm for photons with energy above 1 GeV, which corresponds to approximately 10% of the crystal size. This level of precision is sufficient for many of $\overline{\text{P}}$ANDA's key physics goals, including the identification of exotic hadrons and the study of hadronic interactions.

5.3.6 Photon Identification and Background Rejection

One of the final steps in photon reconstruction is distinguishing true photons from other particles, such as electrons or charged hadrons, which may produce similar electromagnetic showers in the EMC. $\overline{\text{P}}$ANDA's reconstruction software includes photon identification algorithms that use a combination of shower shape analysis, timing information, and track matching to identify photons with high accuracy.

In addition to identifying true photons, these algorithms also play a key role in rejecting background events. By analyzing the shape and size of the cluster, the software can distinguish between electromagnetic showers caused by photons and those caused by charged particles or noise. This background rejection is particularly important in high-luminosity environments, where the rate of background events can be significant [61].

6 | The $\overline{p}p \to \pi^0\gamma$ Reaction

In this chapter, a feasibility study of the $\overline{\mathrm{p}}\mathrm{p} \to \pi^0\gamma$ reaction is presented for different beam momenta of 2.5, 5, 10, and 15 GeV/c. Section 6.1 describes the generation of signal and background samples. Event reconstruction and selection procedures, including data pre-selection and final selection, are discussed in Section 6.2. The complete analysis workflow—covering detector resolution, event weighting, angular distributions, invariant mass selection, signal efficiency, acceptance correction, and bin migration—is presented in Section 6.3. Section 6.4 presents the event rate and cross-section estimates, along with background subtraction, reconstruction efficiency, and statistical uncertainty. Optimization studies to enhance signal efficiency using correlations between photon energy and opening angle are provided in Section 6.5. Additional methods for background suppression and signal optimization are discussed in Section 6.7. Finally, Section 6.8 summarizes the cross-section estimates and associated statistical uncertainties after background suppression, while Section 6.9 presents a discussion of the results and their interpretation.

6.1 Data Generation

The initial phase of the analysis involves simulating the signal channel and the relevant background channels, which are subsequently propagated through the complete PandaRoot simulation and analysis chain. This section provides a description of the simulated data samples.

All simulations for the present work were performed with the PandaRoot Software package with the recommended versions for analysis:

- FairSoft: apr22
- FairRoot: v18.6.8
- PANDARoot: sept22 (dev-version)
- Geant4 for particle propagation

The signal and background data samples in this study were generated using the EvtGen

generator. Furthermore, as the experimental data and theoretical predictions are absent, a Phase Space(PHSP) model is chosen. The PHSP model ensures that the final-state particles are underlying the same detector acceptance by generating an isotropic angular distribution. Table 6.1 provides an overview of the number of simulated signal events and the various dedicated background channels.

6.1.1 Signal

The signal reaction is $\overline{\mathrm{p}}\mathrm{p} \to \pi^0\gamma$, where π^0 subsequently decays into a $\gamma\gamma$ pair. A total of 1 million (10^6) events were simulated for each of the four incident beam momenta: $p_{\mathrm{beam}} = 2.5, 5, 10$, and $15\,\mathrm{GeV/c}$. These correspond to center-of-mass squared energies of $s = 2.6, 3.36, 4.5$, and $5.5\,\mathrm{GeV}^2$, respectively. The $\pi^0\gamma$ pair is simulated using EvtGen with the decay file shown in Figure 6.1.

```
Decay pbarpSystem
1.0 pi0 gamma PHSP;
Enddecay

Decay pi0
1.0 gamma gamma PHSP;
Enddecay

End
```

Figure 6.1: Decay file used in the simulation of $\overline{\mathrm{p}}\mathrm{p} \to \pi^0\gamma$.

6.1.2 Background

A crucial background process for this study is the production of $\overline{\mathrm{p}}\mathrm{p} \to \pi^0\pi^0$. To simulate this process, a total of 10^6 events were generated for each of the four incident antiproton beam momenta, $p_{\mathrm{beam}} = 2.5, 5, 10$, and $15\,\mathrm{GeV/c}$. These values correspond to the center of mass energies squared of $s = 2.6, 3.36, 4.5$, and $5.5\,\mathrm{GeV}^2$, respectively. The event generation was performed with a flat phase-space distribution to ensure uniform sampling of the kinematic variables. Furthermore, the events were constrained within the angular range $|\cos\theta| \leq 1.0$, ensuring coverage of the full physical region. This simulation provides an essential reference for understanding the background contributions in the analysis. The $\pi^0\pi^0$ pair is simulated with the decay file shown in Figure 6.2.

```
Decay pbarpSystem
1.0 pi0 pi0 PHSP;
Enddecay

Decay pi0
1.0 gamma gamma PHSP;
Enddecay

End
```

Figure 6.2: Decay file used in the simulation of $\overline{\mathrm{p}}\mathrm{p} \to \pi^0\pi^0$.

Decay channel	$\overline{\mathrm{p}}\mathrm{p} \to \pi^0\gamma$
Number of signal events	1000000
Number of background events	1000000
Background channel	$\pi^0 \to \gamma\gamma$

Table 6.1: Number of simulated signal and background events.

6.2 Event Reconstruction and Event Selection

The simulation employed the default geometry, which models all detectors and simulates their responses according to the current capabilities of the software. During event reconstruction, all reconstructed neutral particles are considered under the pion mass hypothesis. No particle identification (PID) cuts are applied during this reconstruction stage.

6.2.1 Data Pre-Selection

All the data sample undergoes the pre-selection process with the goal of selecting candidate for exclusive $\overline{p}p \to \pi^0\gamma$ events. Certain cuts were fixed across all the s values, whereas others were adjusted to more appropriately align with the detector response at various energies. For the analysis at $p_{beam} = 5$ GeV/c, each event has to satisfy the following pre-selection criteria:

Final State Reconstruction and Combinatorics:

- Calorimeter clusters each with threshold > 30 MeV are accepted and stored for further analysis.
- All possible $\gamma\gamma$ combinations are combined to form π^0 candidates.
- Total number of photons in an event must satisfy $N_\gamma = 3$

Reconstructing the $\overline{p}p$ System:

- All π^0 are combined with one of the remaining γ to form initial $\overline{p}p$ system
- 4C kinematic fit is applied and events with confidence level less than 10 % are rejected.

Subsequent sections provide a detailed explanation of the pre-selection criteria.

6.2.1.1 Final State Reconstruction and Combinatorics

The reconstruction procedure starts with selecting all photons having energy > 30 MeV. Photons that do not satisfy this condition are removed. This energy cut on the calorimeter clusters helps to reduce the combinatorics. Subsequently, all $\gamma\gamma$ pairs are then combined to construct the π^0 candidates.

Photons can be produced due to *bremsstrahlung* or are secondary photons produced in the decay process and maybe detected by the detector which also creates increased combinatorics during the reconstruction process. To reduce this combinatorial background, a selection criteria is placed on the number of photons detected in each event. Hence, if an event contained exactly three photons, it was selected to create the π^0 candidates.

6.2.1.2 Reconstructing the $\overline{\mathrm{p}}\mathrm{p}$ system

After obtaining the π^0 candidates, the initial system is reconstructed. The π^0 is combined with one other γ, which is not used in the π^0 candidate itself, to form the $\overline{p}p$ system. A kinematic fit is performed, wherein energy and momentum are constrained to adhere to the characteristics of the initial system.

6.2.2 Final Data Selection

After subjecting exclusive candidate events to the initial pre-selection, additional criteria are applied to enhance background suppression. Two key selection conditions are listed below:

- All combinations of $\pi^0\gamma$ must fulfil the condition $m_{fit}(\pi^0\gamma) \pm 3\sigma$
- Total number of π^0 detected in an event must satisfy $N_{\pi^0} = 1$

These selection criteria served as the starting point for the final data selection. As the analysis progressed, the cuts were further optimized to improve signal efficiency and background suppression. The final optimized selection conditions used in the analysis are presented in the following chapters and may differ slightly from those listed here.

6.3 Analysis

In this section, the analysis of the simulated data is presented. The goal is to achieve optimal suppression of the background while maximizing the signal efficiency and optimizing the signal-to-background ratio. Due to practical computational limitations, conducting a full-scale simulation of a large enough background dataset within a reasonable time frame is unfeasible. Therefore, a quantity of 1×10^6 events is chosen for each of the background data samples. This quantity suffices for determining the background suppression factor and facilitating background subtraction. The selection strategy—previously outlined in the Section 6.2—was applied consistently across all beam momenta. The analysis at p_{beam} = 2.5, 5, 10 and 15 GeV/c is described in detail in the following subsections.

6.3.1 Resolution of the Detector

The resolution of the detector in $\cos\theta$ is determined by first choosing the bin width to be greater than the expected detector resolution; specifically, a bin width of 0.2 was used. This choice ensures that the smearing due to detector effects does not cause significant bin-to-bin migration, thereby preserving the accuracy of the measurement and simplifying the interpretation of the results. As shown in Figure 6.3, for each bin, the difference between the reconstructed and generated $\cos\theta$ values is calculated and filled into a histogram, representing the detector's angular resolution. Then a Gaussian fit function is applied on each of the peaks in the bins. The standard deviation (σ) of the fit gives an estimate of the resolution for that bin.

Figure 6.4 shows the detector resolution as a function of $\cos\theta$ for beam momenta of 2.5,

5 and 10 GeV/c, represented by blue, black, and red points, respectively. It is observed that the resolution varies significantly with both $\cos\theta$ and the beam momentum. For all momenta, the detector exhibits the poorest resolution (highest σ) in the central region around $\cos\theta \approx -0.3$ to 0.3, corresponding to particles incident at large angles relative to the beam axis. The resolution improves substantially at more forward or backward angles ($\cos\theta$ near ± 1). Furthermore, the resolution improves with increasing beam momentum, as higher-momentum beams exhibit consistently lower σ values, indicating better tracking performance due to reduced multiple scattering and improved trajectory reconstruction. Overall, the detector achieves optimal resolution at high momenta and shallow angles of incidence.

6.3.2 Event Weighting

The PHSP events exhibit a flat $\cos(\theta)$ distribution in the center-of-mass frame. To achieve a more realistic representation, the generated distributions are rescaled using weights derived from fits of various final states in the E760 data, as reported in Ref. [1]. The final absolute scaling of the cross-sections is illustrated in Figure 6.16. It is important to note that only the kinematic dependence is accounted for in this weighting procedure, while the absolute cross section is not considered. These weights, denoted as $w(c)$, are applied to both the generated and reconstructed distributions to better match experimental observations.

Figures 6.5, 6.6, and 6.7 illustrate the differential cross sections of the final states $\pi^0\pi^0$, $\pi^0\gamma$, and $\gamma\gamma$, respectively, as functions of $\cos(\theta)$ across different center-of-mass energy regimes. Specifically, for the low and intermediate energy ranges corresponding to $\sqrt{s} =$ 2911 MeV and $\sqrt{s} = 3360$ MeV, the differential cross sections are obtained from Ref. [1]. At higher energies, the $\pi^0\pi^0$ and $\pi^0\gamma$ final states are analyzed at $\sqrt{s} = 3686$ MeV, while for the $\gamma\gamma$ final state, the highest available energy is $\sqrt{s} = 4274$ MeV.

The angular distributions at these selected energies are plotted and fitted with appropriate polynomial functions. These fitted polynomial functions serve as weights for rescaling both the reconstructed and generated distributions, ensuring consistency with the experimental data.

6.3.3 Polar Angle Distributions of Final-State Signal Particles

The angular distributions of the final-state particles, namely the π^0 and the additional photon, are shown in Figure 6.8. The plots illustrate the polar angle (θ) distributions for both generated (red) and reconstructed (blue) particles at beam momenta of 2.5, 5,

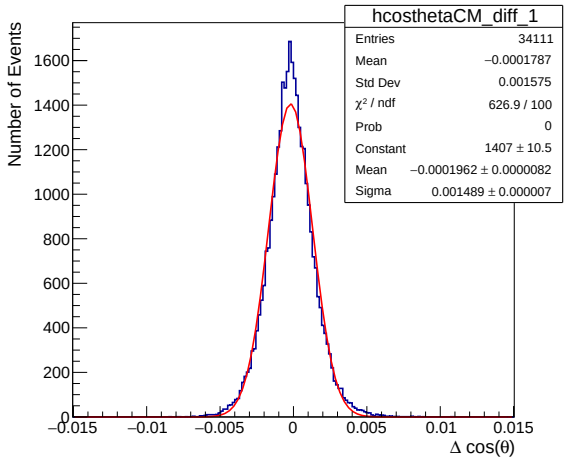

(a) $\cos\theta \in [-1.0, -0.8]$

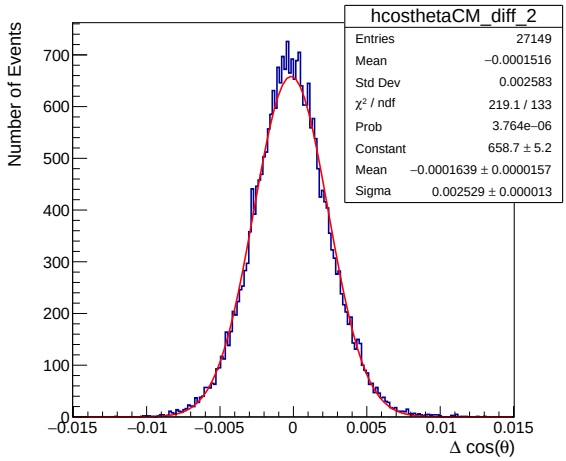

(b) $\cos\theta \in [-0.8, -0.6]$

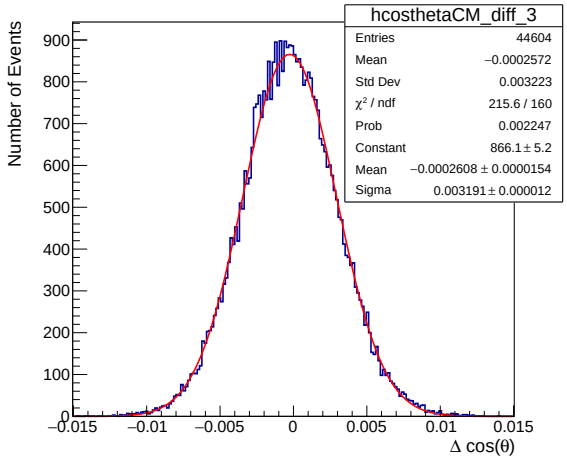

(c) $\cos\theta \in [-0.6, -0.4]$

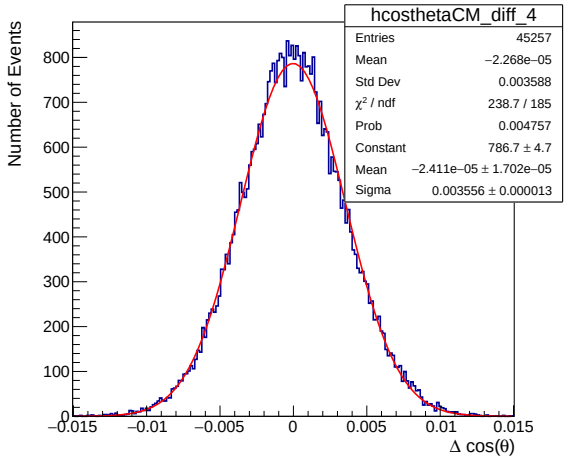

(d) $\cos\theta \in [-0.4, -0.2]$

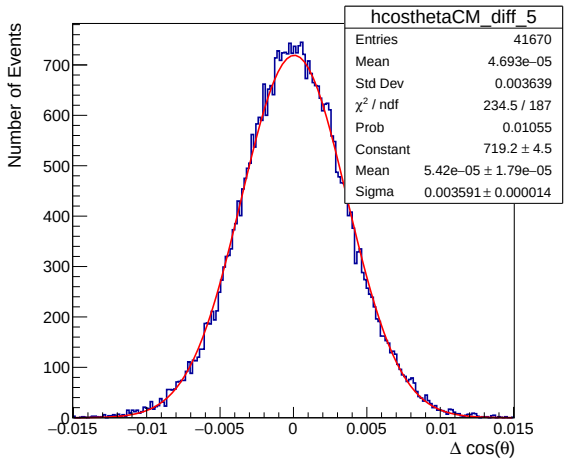

(e) $\cos\theta \in [-0.2, 0.0]$

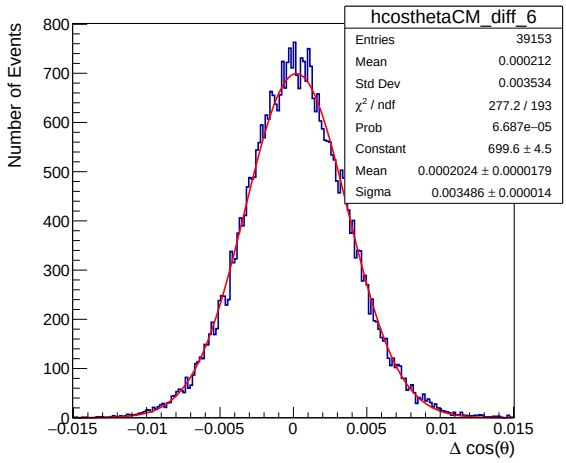

(f) $\cos\theta \in [0.0, 0.2]$

Figure 6.3: Difference between reconstructed and generated values of $\cos\theta$ shown for the first 6 out of 10 angular bins at beam momentum $p_{\text{beam}} = 2.5\,\text{GeV}/c$. Each subfigure corresponds to a specific $\cos\theta$ range and is fitted with a Gaussian to extract the angular resolution.

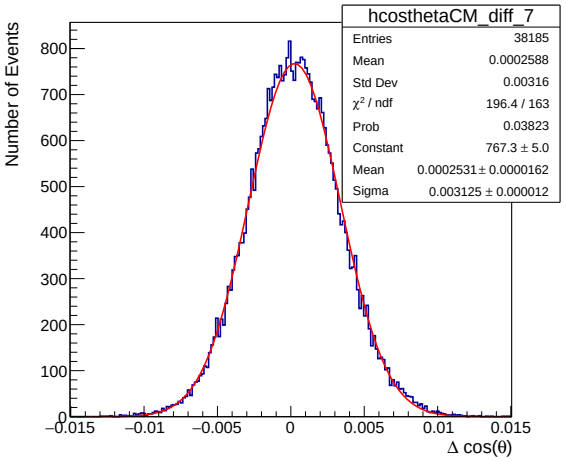

(g) $\cos\theta \in [0.2, 0.4]$

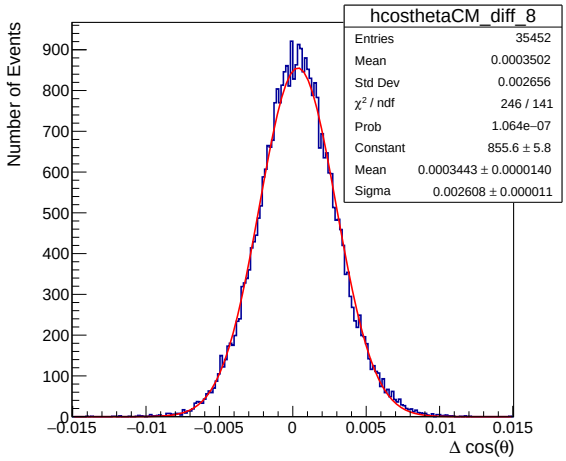

(h) $\cos\theta \in [0.4, 0.6]$

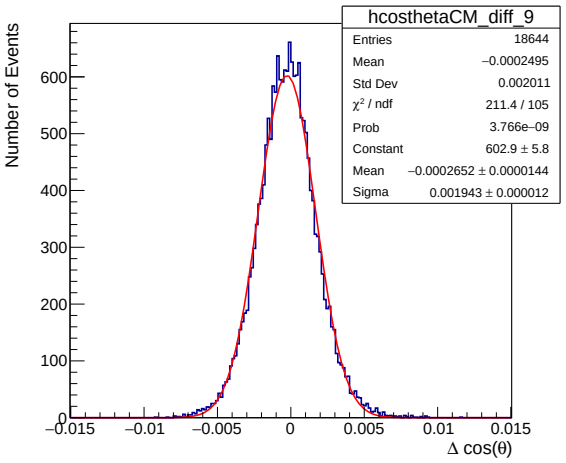

(i) $\cos\theta \in [0.6, 0.8]$

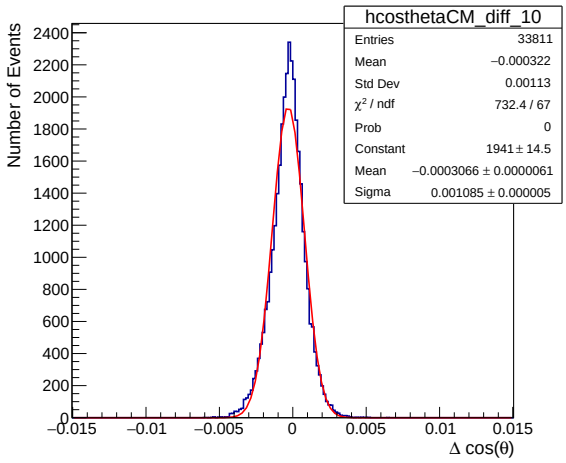

(j) $\cos\theta \in [0.8, 1.0]$

Figure 6.3: (continued) Angular resolution for bins 7 to 10 in $\cos\theta$.

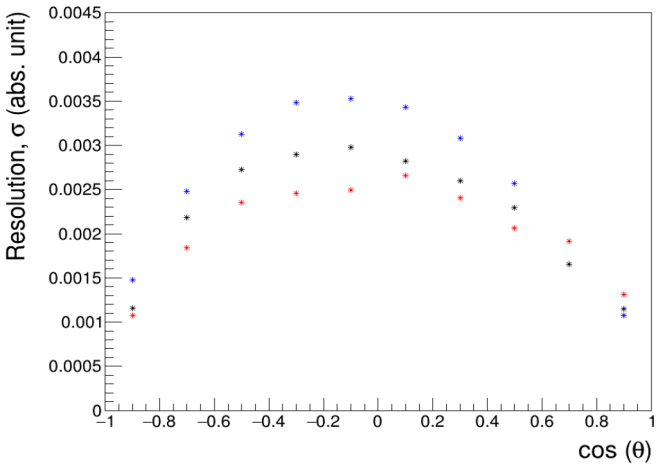

Figure 6.4: The resolution of detector as a function of $\cos\theta$ for different beam momenta. The blue, black and red colors correspond to beam momenta of 2.5, 5 and 10 GeV/c respectively.

10, and 15 GeV/c. The left column displays the π^0 distribution, while the right column shows the corresponding photon distributions. As the beam momentum increases, the angular distributions become more forward-peaked due to Lorentz boost effects in the center-of-mass frame. It is observed that there is good acceptance across the full θ range for all involved particles, which can be attributed to the extensive coverage of the $\overline{\text{P}}$ANDA electromagnetic calorimeter. Notably, the reconstructed distributions display a drop in efficiency at very small and very large angles. These edge effects reflect the finite geometrical coverage and varying resolution of the EMC, particularly in the transition regions between the barrel and endcap detectors. The close agreement between the generated and reconstructed distributions in most regions also indicates efficient reconstruction performance, particularly at higher angles.

6.3.4 Invariant Mass Selection

Although an initial pre-selection has been applied, a significant number of background events remain. To further suppress this background, a selection criterion based on the invariant mass of the reconstructed π^0 meson is introduced. The resulting invariant mass distributions after pre-selection are shown in Figure 6.9 for various beam momenta.

Each distribution is fitted with a Gaussian function to determine the mass resolution, as illustrated by the red curves in the figure. For example, at a beam momentum of 5 GeV/c, the fit yields a mean value of $\mu_{\text{fit}}(\pi^0) = 135.2$ MeV/c^2 and a standard deviation

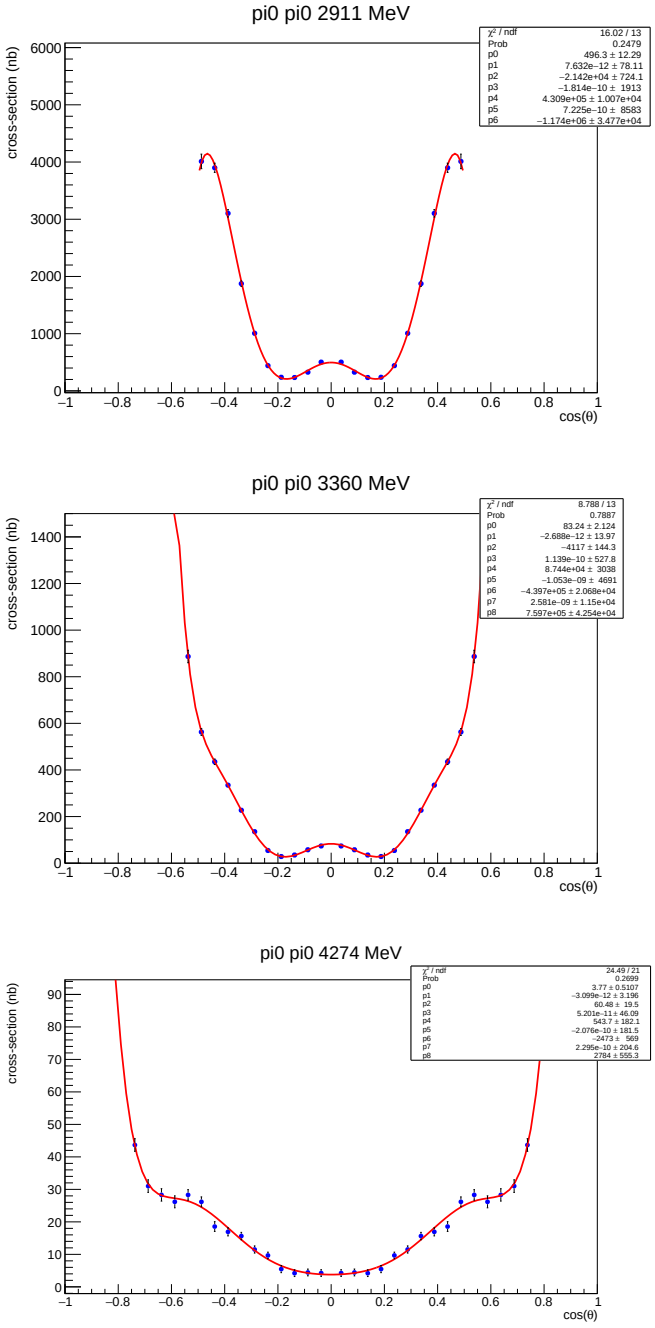

Figure 6.5: Angular distributions for $\pi^0\pi^0$ final states as a function of $\cos\theta$ at different values of the beam momentum across different energy regimes. The fits to these plots are used as weights for rescaling the reconstructed and generated distributions.

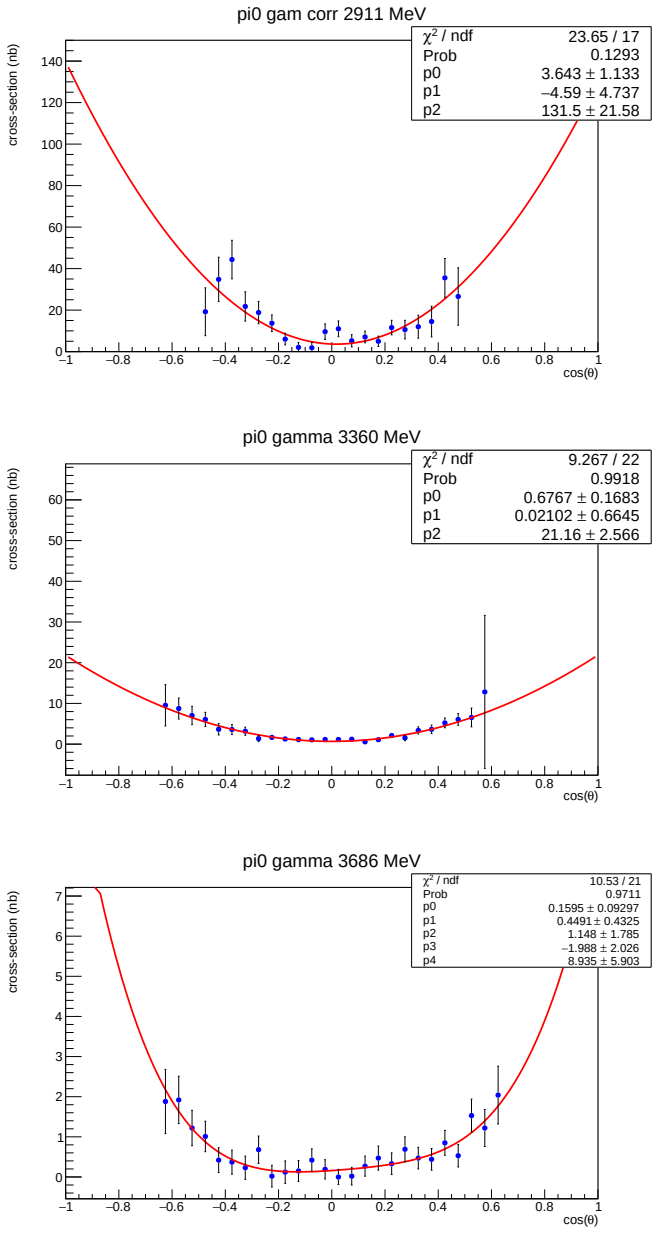

Figure 6.6: Angular distributions for $\pi^0\gamma$ final states as a function of $\cos\theta$ at different values of the beam momentum across different energy regimes. The fits to these plots are used as weights for rescaling the reconstructed and generated distributions.

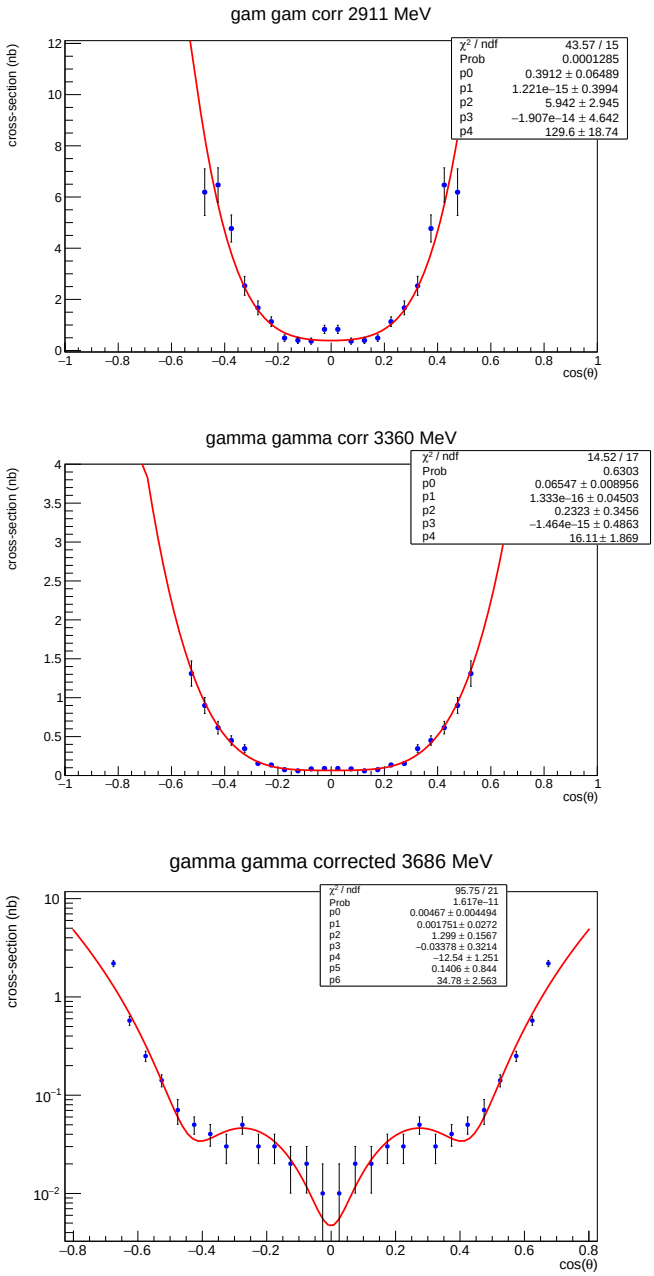

Figure 6.7: Angular distributions for $\gamma\gamma$ final states as a function of $\cos\theta$ at different values of the beam momentum across different energy regimes. The fits to these plots are used as weights for rescaling the reconstructed and generated distributions.

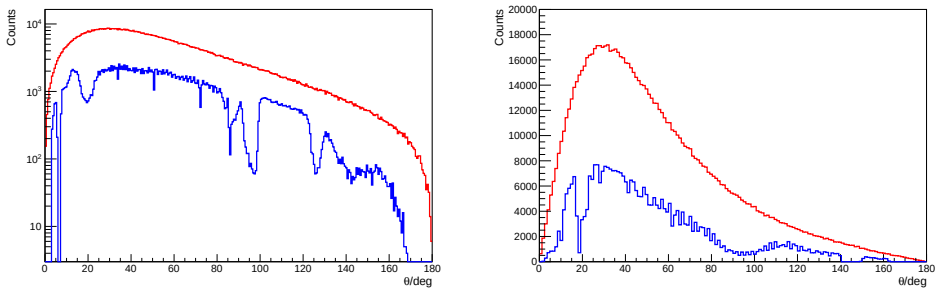

(a) $p_{\text{beam}} = 2.5$ GeV/c

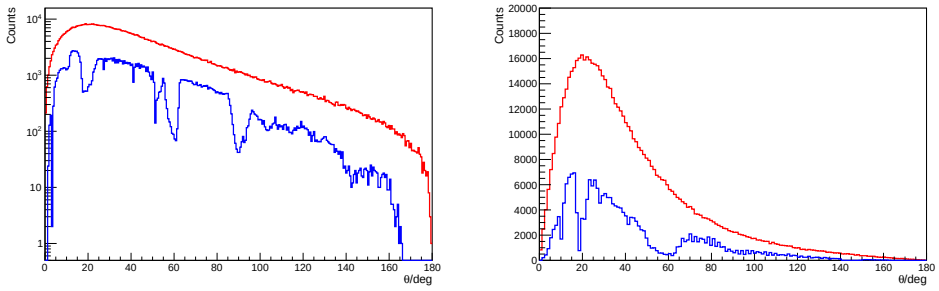

(b) $p_{\text{beam}} = 5$ GeV/c

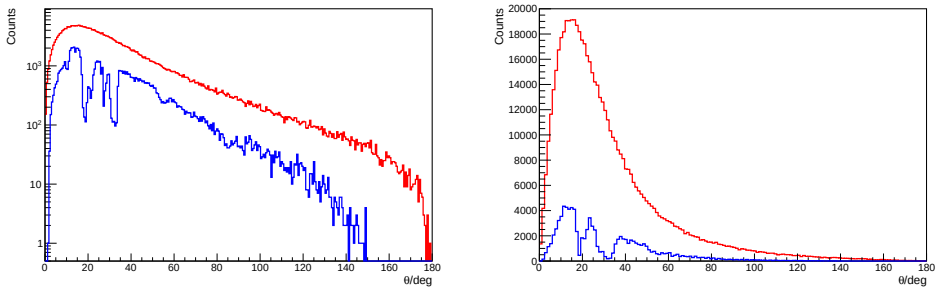

(c) $p_{\text{beam}} = 10$ GeV/c

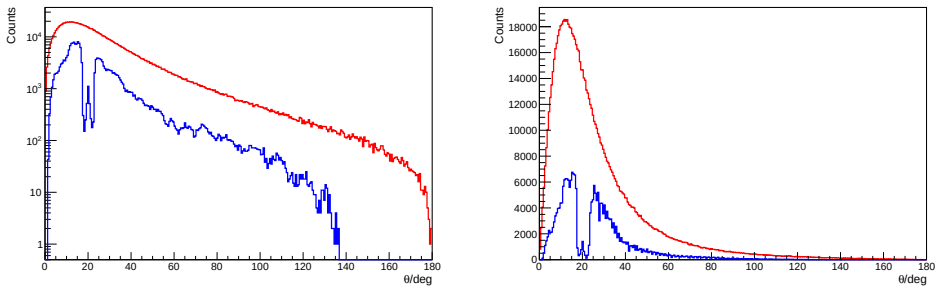

(d) $p_{\text{beam}} = 15$ GeV/c

Figure 6.8: Polar angle distributions (θ) of the reconstructed π^0 (left) and the photon (right) for the reaction $\bar{p}p \to \pi^0\gamma$ at different beam momenta: (a) 2.5 GeV/c, (b) 5 GeV/c, (c) 10 GeV/c, and (d) 15 GeV/c. Red and blue histograms represent the generated and reconstructed distributions, respectively. The plots reflect the angular phase-space coverage and resolution of the $\overline{\text{P}}$ANDA electromagnetic calorimeter.

of $\sigma_{\text{fit}}(\pi^0) = 4.56$ MeV/c^2. These values are in good agreement with the Particle Data Group (PDG) reference mass of $m_{\text{PDG}}(\pi^0) = 134.977$ MeV/c^2.

Given this agreement, a selection window is defined as $\pm 2\sigma$ around the PDG mass value to retain genuine π^0 candidates:

$$\left| m_{\text{fit}}(\pi^0) - m_{\text{PDG}}(\pi^0) \right| < 2\sigma$$

This mass window effectively enhances signal purity by rejecting background events with invariant masses outside the expected π^0 range.

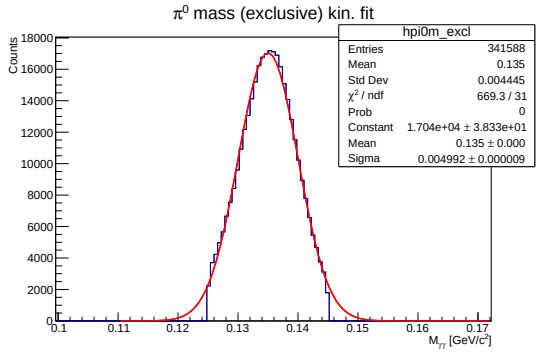

(a) $p_{\text{beam}} = 2.5$ GeV/c

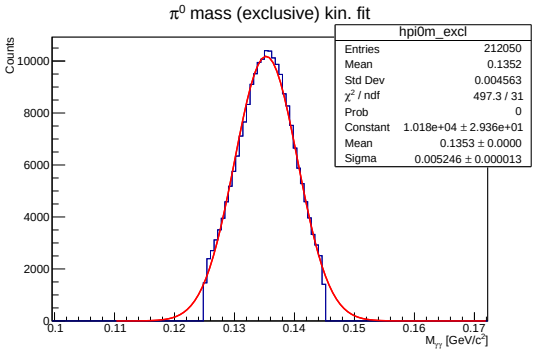

(b) $p_{\text{beam}} = 5$ GeV/c

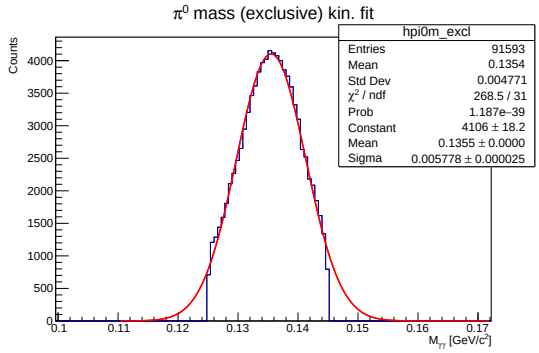

(c) $p_{\text{beam}} = 10$ GeV/c

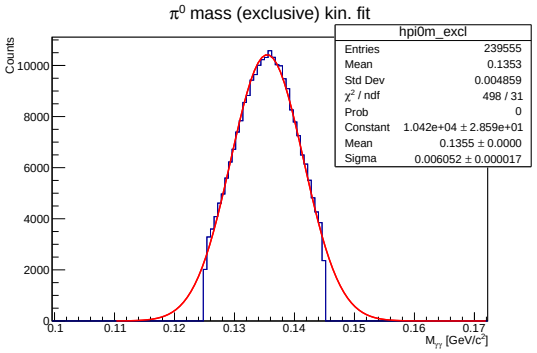

(d) $p_{\text{beam}} = 15$ GeV/c

Figure 6.9: Invariant mass distributions of the π^0 meson for different beam momenta: (a) 2.5 GeV/c, (b) 5 GeV/c, (c) 10 GeV/c, and (d) 15 GeV/c. The distributions are fitted with a Gaussian function to extract the mass resolution, indicated by the red curve.

6.3.5 Signal Efficiency

After obtaining a suitable event sample, it is necessary to apply acceptance corrections to account for both the detector's acceptance and the analysis process.

In Figure 6.10, the first column shows the generated distribution as a function of $\cos\theta$ which is a flat distribution. The reconstructed distribution of π^0 as a function of $\cos\theta$ is shown in the second column. The reconstructed is shown in PHSP distribution and it shows discontinuities attributed to the transitional zones between distinct segments of the EMC. The generated (MC) and reconstructed distributions are scaled according to the weights obtained from fits to the E760 data to give more realistic plots. These are shown in the third and fourth column respectively. Each row in Figure 6.10 corresponds to a different antiproton beam momentum: $p_{\text{beam}} = 2.5$ GeV/c (top row), 5 GeV/c (second row), 10 GeV/c (third row), and 15 GeV/c (bottom row).

In order to perform the acceptance corrections, we first extract signal efficiency of the channel $\overline{p}p \to \pi^0\gamma$. The signal efficiency is derived from events generated based on PHSP for individual $\cos\theta$ bins. The efficiency, shown as a function of the angular distribution, $\cos\theta$, is computed as the ratio of number of reconstructed events divided by Monte Carlo generated events, denoted by N_{rec} and N_{MC} respectively.

$$Acceptance = \frac{N_{rec}}{N_{MC}}$$

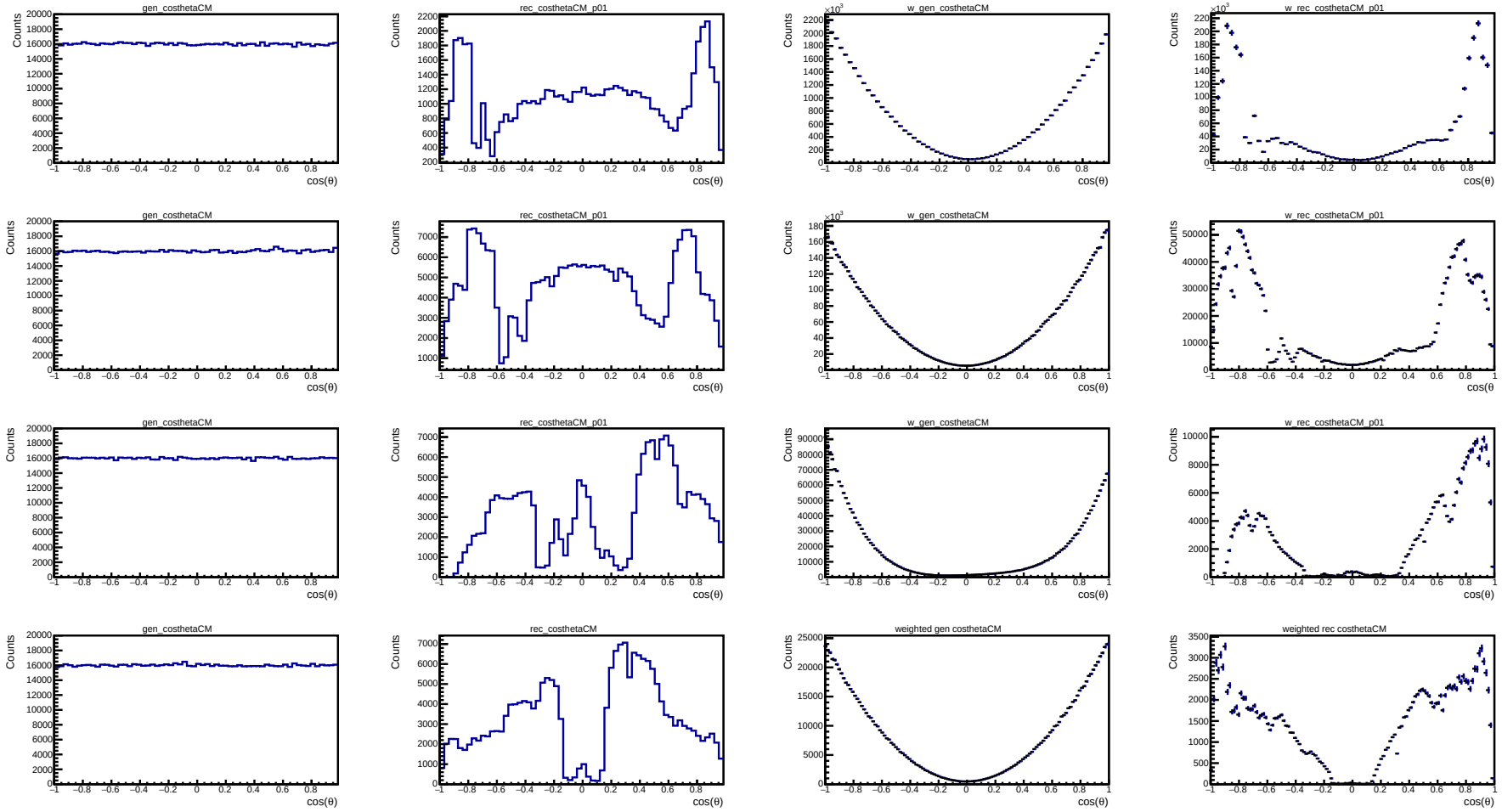

Figure 6.10: Plots of weighted and unweighted distributions of reconstructed and generated π^0. Each row corresponds to a different $\bar{p}$ incident momentum: $p_{\text{beam}} = 2.5\,\text{GeV}/c$ (top row), $p_{\text{beam}} = 5\,\text{GeV}/c$ (second row), $p_{\text{beam}} = 10\,\text{GeV}/c$ (third row), and $p_{\text{beam}} = 15\,\text{GeV}/c$ (bottom row).

Figure 6.11 shows the detector acceptance as a function of $\cos(\theta)$ for the reaction $\bar{p}p \to \pi^0\gamma$ at four different antiproton beam momenta: 2.5, 5, 10, and 15 GeV/c. The acceptance is defined as the ratio of reconstructed to generated events in each angular bin, and reflects the angular efficiency of the $\overline{\text{P}}$ANDA detector's electromagnetic calorimeter (EMC) for detecting the final-state photon. The EMC is composed of barrel and endcap sections, and its geometric coverage, segmentation, and material budget influence the acceptance across different angles.

At low beam momentum (2.5 GeV/c), the final-state photon tends to be emitted more centrally in the laboratory frame, resulting in relatively flat acceptance across the mid $\cos(\theta)$ region. However, the acceptance drops sharply in the forward and backward regions ($\cos(\theta) \approx \pm 1$) due to the limited coverage and geometric inefficiencies of the EMC in the forward and backward directions, where the endcaps transition into the beam pipe regions. Additionally, energy thresholds and clustering inefficiencies in the forward endcap may further suppress detection of low-energy photons.

At 5 GeV/c, the acceptance shows several sharp dips across the $\cos(\theta)$ range. These correspond to regions where photons fall into geometrical gaps between calorimeter modules or the transition zones between the barrel and endcap sections. The EMC's segmentation and the effects of photon energies near detection thresholds also contribute to this angular non-uniformity. As the beam momentum increases to 10 and 15 GeV/c, the overall acceptance shape becomes smoother and more structured. The central region around $\cos(\theta) \approx 0$ shows relatively higher and more uniform acceptance compared to the forward and backward angles, where moderate dips persist (particularly near $\cos(\theta) \approx \pm 0.9$). These features arise from reduced detection efficiency in the extreme forward and backward regions, where the photon may escape through less-instrumented areas or be absorbed in structural material. The smoother trends at higher energies are partly due to better photon containment and higher detection probabilities at those momenta. Overall, the observed acceptance patterns emphasize the need to apply acceptance corrections in the angular analysis to account for detector-induced distortions.

6.3.6 Acceptance Corrections

Once a satisfactory event sample is obtained, it must be corrected for the effects of finite detector acceptance and reconstruction efficiency. This is particularly important for angular distributions, as the geometrical coverage and response of the detector can vary significantly with the angle of the outgoing particles. Acceptance correction is applied to the unweighted distributions to recover the true physical angular dependence of the

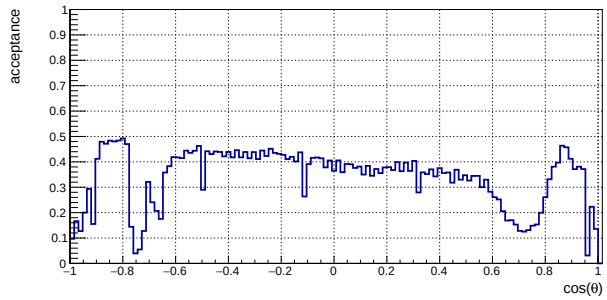

(a) $p_{\text{beam}} = 2.5$ GeV/c

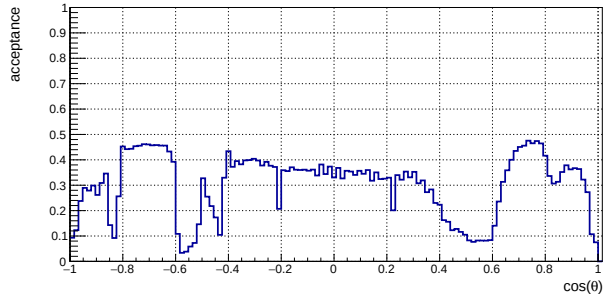

(b) $p_{\text{beam}} = 5$ GeV/c

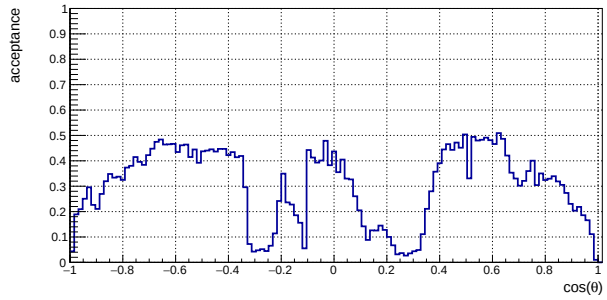

(c) $p_{\text{beam}} = 10$ GeV/c

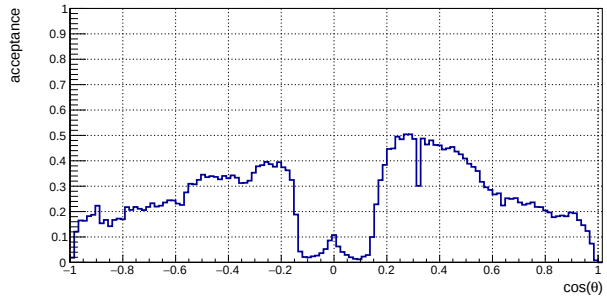

(d) $p_{\text{beam}} = 15$ GeV/c

Figure 6.11: Detector acceptance as a function of $\cos(\theta)$ for the reaction $\bar{p}p \to \pi^0\gamma$ at different beam momenta: (a) 2.5 GeV/c, (b) 5 GeV/c, (c) 10 GeV/c, and (d) 15 GeV/c. The acceptance is defined as the ratio of reconstructed to generated events in each angular bin, and reflects the angular efficiency of the $\overline{\text{P}}$ANDA detector's electromagnetic calorimeter for detecting the two-photon final state.

process.

Figure 6.12 shows the acceptance-corrected angular distributions of π^0 for three different antiproton beam momenta. The reconstructed $\cos\theta$ distributions, after applying the acceptance correction, are plotted in blue, whereas the original generated distributions are shown in red. The plots are presented for beam momenta of $p_{\text{beam}} = 2.5$ GeV/c (top row), 5 GeV/c (middle row), and 10 GeV/c (bottom row). It should be noted that the acceptance correction is applied to the same Monte Carlo (MC) data that was used to derive the acceptance in the first place. As a result, the corrected (reconstructed) distribution is expected to closely reproduce the original generated distribution. Therefore, in the context of this study, this serves primarily as a consistency check and helps to identify any acceptance holes or regions of reduced detector efficiency.

Notably, even at higher beam energies, where more forward-peaked distributions are expected, the acceptance-corrected reconstructed distributions closely follow the generated ones across the entire angular range. This consistency highlights the effectiveness of the correction procedure and confirms that the reconstruction and analysis chain preserves the underlying physics in the simulation. Since both the generated and reconstructed events originate from the same Monte Carlo simulation, the agreement also serves as an internal validation of the detector model and reconstruction algorithms used in this study.

6.3.7 Bin Migration

Bin migration can occur when there is a shift of events between bins when comparing their generated properties, i.e. momentum, energy, or angle, with their reconstructed properties. The reconstructed values may be assigned to a different bin than they need to. If the events in adjacent bins differ just slightly, as is the case for most of the bins, then this source of uncertainty is minimal. Bin migration and bin purity was analyzed using the simulated Monte Carlo (MC) data. Determining bin migration and bin purity help account for detector resolution and reconstruction effects in binned data. Bin migration is investigated by performing bin-by-bin method. For this 20 bins are used each with bin size of 0.5. Three cases were investigated and are classified as follows:

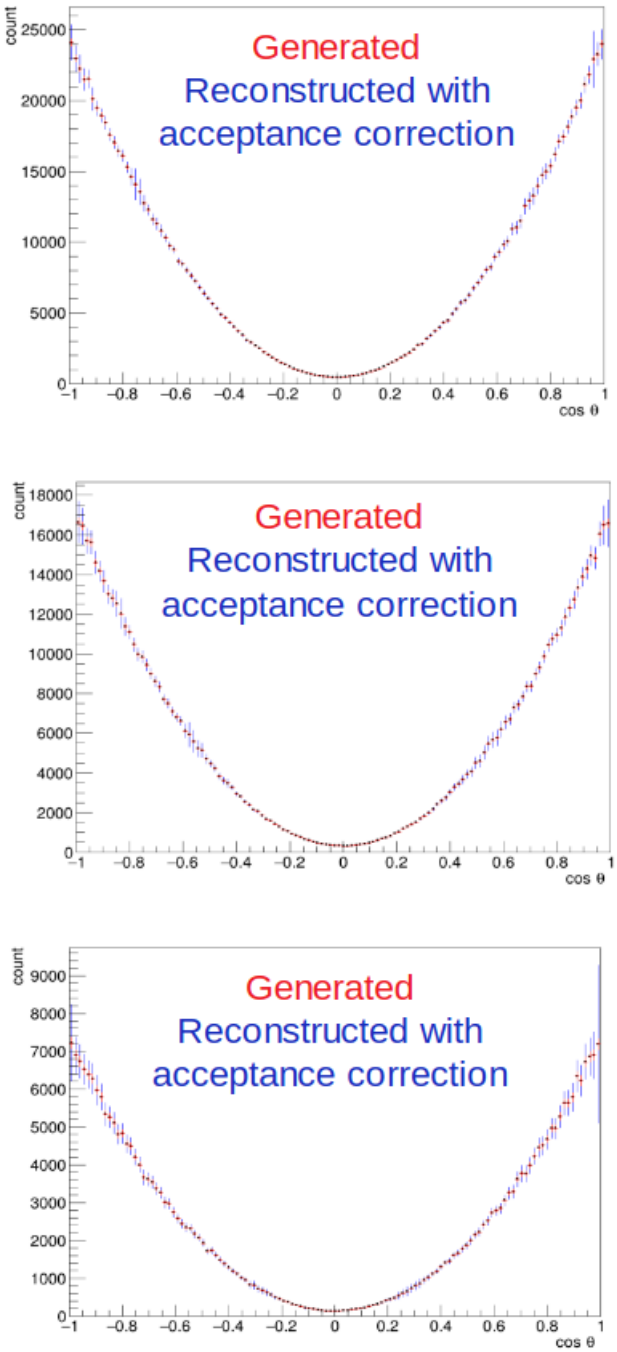

Figure 6.12: Acceptance corrections of the weighted distribution at different beam momenta. Reconstructed pions with acceptance correction are shown in blue and generated pions are shown in red. Each row correspond to a different incident beam momentum: $p_{beam} = 2.5$ GeV/c (top row), $p_{beam} = 5$ GeV/c (middle row) and $p_{beam} = 10$ GeV/c(bottom row).

Classifying the Events:

1. **No Migration:** Events where $i_{\text{gen}} = i_{\text{rec}}$; MC generated and reconstructed events are in bin i (no shift between bins).
2. **Migrated Events:**
   - Events where $i_{\text{gen}} = i_{\text{rec}} \pm 1$; events shifted in a neighbor bin $i-1$ or $i+1$
   - Events where $i_{\text{true}} \neq i_{\text{rec}}$; events shifted to neighboring or distant bins.

6.3.7.1 Migration Fraction

Figure 6.13 shows the migration fractions for the weighted distribution at various beam momenta. The migration fraction quantifies how many events, initially generated in a specific bin i, are reconstructed in a different bin. This migration is caused by detector smearing or imperfect reconstruction algorithms.

Red markers indicate the fraction of events that migrated away from their original bin i. Blue and green points show the fraction of events that migrated from neighboring bins $i-1$ and $i+1$, respectively. Ideally, these fractions should be small, indicating good resolution and reconstruction accuracy.

From the plots, it is observed that the migration fractions remain within a few percent across most bins, suggesting that bin migration is a minor effect in this study. However, the slight increase near the edges of the distribution can be attributed to reduced reconstruction accuracy or detector acceptance at very forward or backward angles. Each panel from top to bottom shows results for increasing beam momenta ($p_{\text{beam}} = 2.5$, 5, and 10 GeV/c), where a trend of decreasing migration with increasing momentum is also observed.

Quantifying Migration: The migration fraction is calculated as:

$$f_{\text{migration}} = \frac{\text{Number of migrated events from generated bin } i}{\text{Total events in generated bin } i}$$

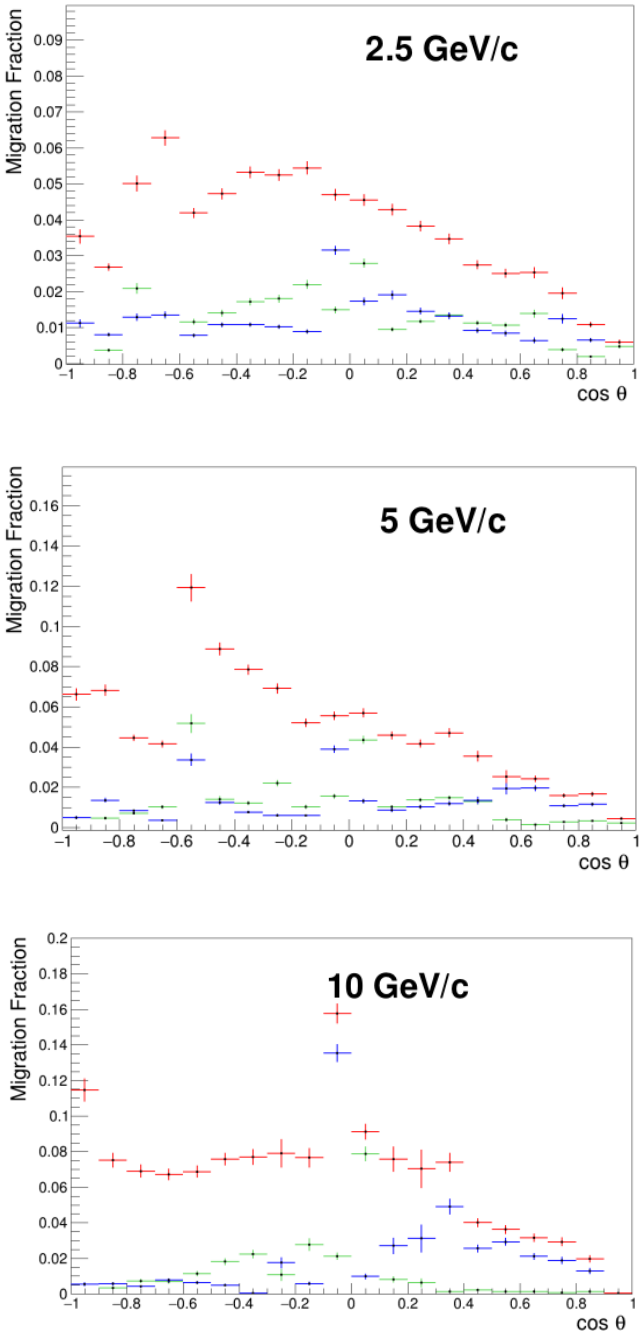

Figure 6.13: Migration fraction for the weighted distribution. Red shows the migrated bins, blue and green shows the case where MC events generated are in a neighbor bin $i-1$ and $i+1$ respectively. Each row represents a different beam momentum, with the top, middle, and bottom panels corresponding to $p_{beam} = 2.5$, 5 and 10 GeV/c respectively.

6.3.7.2 Bin Purity

Bin purity quantifies how many events reconstructed in a specific bin j were also generated in the same bin, providing a measure of how "clean" or uncontaminated the reconstructed bin is.

Bin purity is calculated as follow:

$$P_j = \frac{\text{Number of events that were both generated and reconstructed in the same bin } j}{\text{Total number of events reconstructed in bin } j}$$

or simply

$$Bin\ Purity = \frac{N_j^{rec\,\&gen}}{N_j^{rec}}$$

Figure 6.14 shows the bin purity for the weighted and flat distributions at different incident beam momenta, with the top, middle, and bottom panels corresponding to p_{beam} = 2.5, 5 and 10 GeV/c, respectively. The weighted distribution is shown in purple and the flat distribution is shown in black. As expected, the bin purity is highest in the central region and drops near the edges, which are more affected by smearing and detector acceptance limitations.

The comparison between the flat and weighted distributions indicates that the weighting procedure slightly improves purity in most bins, especially at higher momenta. This confirms that weighting helps mitigate the effect of non-uniform event distributions and enhances reconstruction reliability.

In the presented results, the migration fractions remain low across most bins and beam momenta, and the bin purity is consistently high, particularly in the central region of $\cos\theta$. This indicates that the reconstruction procedure performs reliably, with minimal contamination due to bin migration.

6.4 Event Rate and Cross-section Estimates

In this section, the method to calculate count rate and make an estimate of the differential cross-section and its statistical uncertainties is explained in detail.

To obtain the count rate estimate, differential cross section is obtained from the E760 data [1]. The scaled cross-section is multiplied with acceptance, bin size and integrated luminosity to give the count rate estimate.

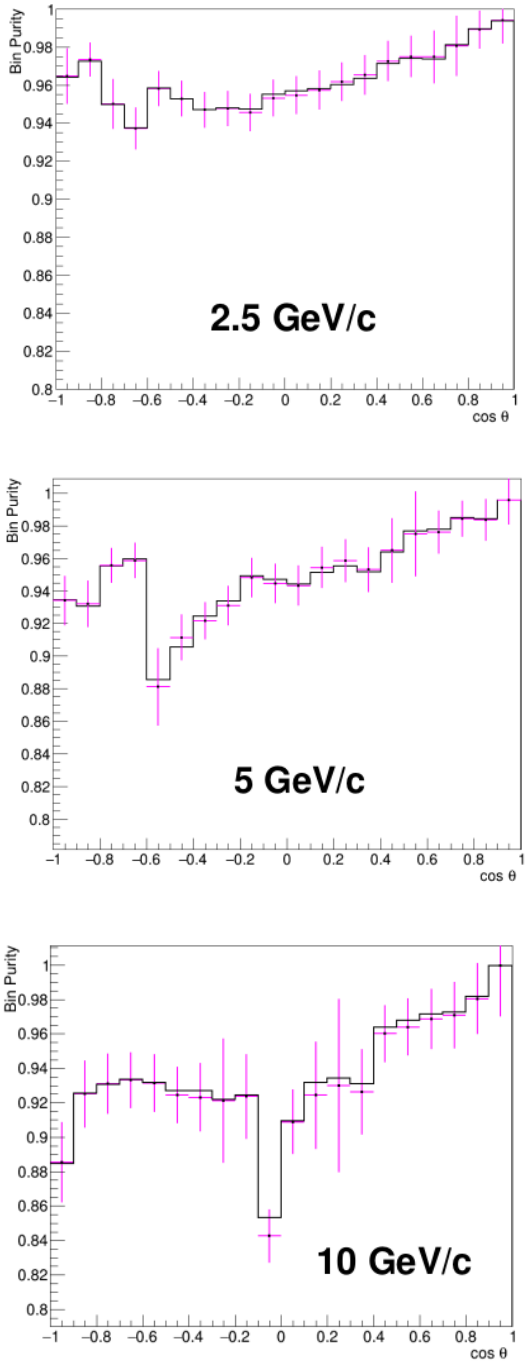

Figure 6.14: Bin purity for the weighted and flat distributions. Each row represents a different beam momentum, with the top, middle, and bottom panels corresponding to p_{beam} = 2.5, 5 and 10 GeV/c respectively.

Figure 6.15: Method to compute countrate.

Count rate = Cross section scaled × Acceptance × Bin Size × Integrated Luminosity

Figure. 6.16 shows integrated cross-section as a function of total centre of mass energy for the signal and background channels. The signal channel $\overline{p}p \to \pi^0\gamma$ is shown in red and background channel $\overline{p}p \to \gamma\gamma$ is shown in blue. The plots are extrapolated and the ratio of signal to background is obtained and correct background estimate.

After the data pre-selection steps outlined in Section 6.2.1, the following steps are performed to extract the relevant physical observables:

1. Both the signal sample (S) and the background sample (B) undergo the same pre-selection criteria to ensure consistency.
2. The signal sample S, which contains the expected number of signal events, is then used for the signal analysis.
3. As background factor is of the order 10^5 greater than the signal, a background subtraction is necessary to achieve minimal signal contamination.
4. A separate background analysis is performed on the background sample B. Once the signal analysis is complete, corresponding background distributions—scaled to match the expected number of background events—are prepared.
5. The complete data set (S+B) is constructed by combining the signal and background distributions bin by bin.
6. The final signal distribution is obtained by subtracting the background (B) from the total data set (S+B), resulting in the background-corrected signal (S+B-B).
7. Finally, the differential cross section and its associated systematic uncertainties are calculated.

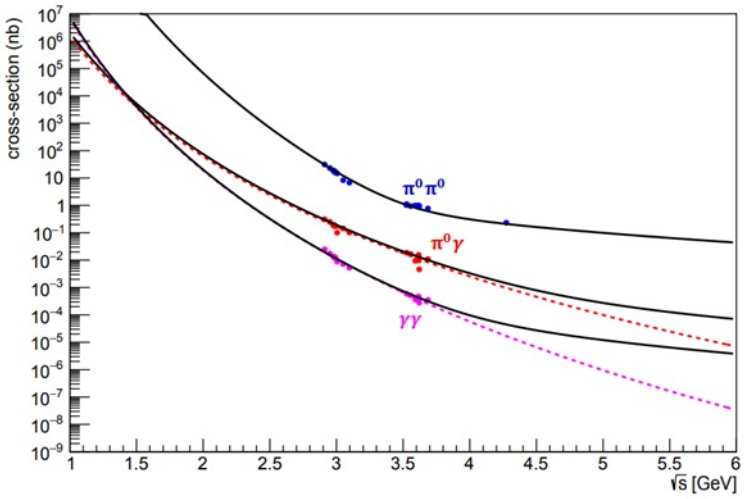

Figure 6.16: Cross-section as a function of total centre of mass energy and fits for final state particles; $\pi^0\pi^0$ (blue dots), $\pi^0\gamma$ (red dots) and $\gamma\gamma$ (magenta dots).

6.4.1 Count rate study at 2 fb^{-1} and 0.1 fb^{-1}

Figure 6.17 show count rate at an integrated luminosity of 2 fb^{-1} and 0.1 fb^{-1}. The different colors represent the three different beam momenta. The error bars are also plotted and are well within the points for the beam momenta of 2.5 and 5 GeV/c for the integrated luminosity of 2 fb^{-1} and 0.1 fb^{-1}. The error bars are much more pronounced for 10 GeV/c at integrated luminosity of 0.1 fb^{-1}.

Figure 6.18 shows the count rate for signal (left column) and background (right column) corresponding to a different beam momentum at an integrated luminosity of 2 fb^{-1}. The different colors correspond to different probabilities of the kinematic fit. The blue, magenta, red and black points correspond to kinematic fit probability of $p > 0.01$, $p > 0.1$, $p > 0.3$ and $p > 0.7$ respectively.

Collecting data at an integrated luminosity of 2 fb^{-1} corresponds to a six-month period with the $\overline{\text{P}}$ANDA setup, whereas merely a handful of days (10 days) are required to achieve an integrated luminosity of 0.1 fb^{-1}. A brief allocation of beam time would be ample to replicate the existing E760 data within overlapping kinematic conditions. $\overline{\text{P}}$ANDA offers the advantage of expanding the kinematic range and acquiring higher statistical data compared to the pre-existing E760 dataset.

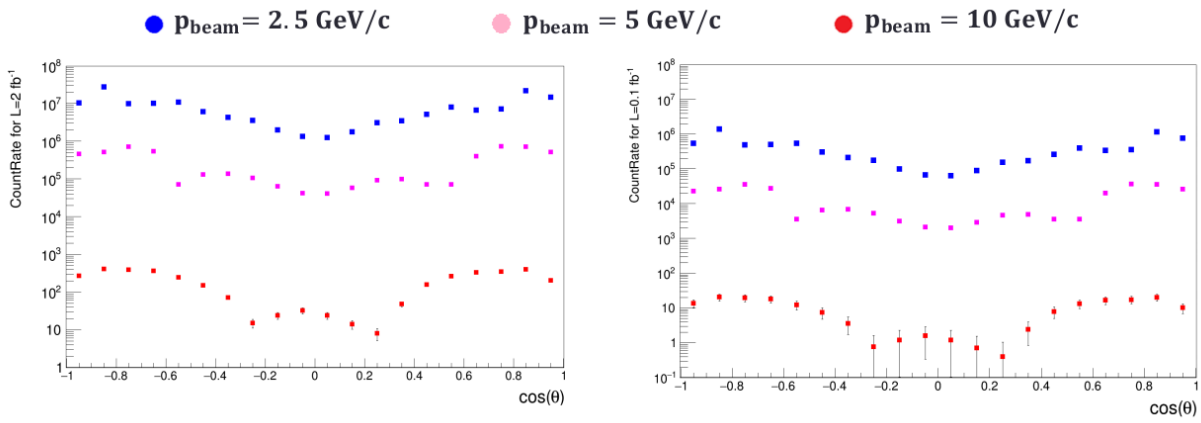

Figure 6.17: Count rate for integrated luminosity of 2 fb^{-1} (left column) and 0.1 fb^{-1} (right column) at $\overline{p}$ incident momentum: p_{beam} = 2.5, 5 and 10 GeV/c respectively.

6.4.2 Background subtraction and Reconstruction efficiency

The main contribution to the background for the measurement of the $\overline{p}p \to \pi^0\gamma$ cross-section comes from $\overline{p}p \to \pi^0\pi^0$. The same analysis strategies as for the signal are used to study the background events. The signal-to-background ratio is calculated as the ratio of true signal events and the sum of background events. The ratio is calculated in order to determine the purity of the final selection sample.

Based on the background estimate, we can look into the signal-to-background ratio. Figure 6.19 shows the plots for signal-to-background ratio at different beam momenta at different probabilities of the kinematic fit. It is observed that an increase of the kinematic fit threshold improves the signal to background ratio. Also, the signal-to-background ratio is better at low beam momenta.

6.4.3 Estimates of the expected statistical uncertainty

The expected statistical uncertainties were estimated, and the corresponding cross-section plots for integrated luminosities of 2 fb^{-1} and 0.1 fb^{-1}, including statistical error bars, are shown in Figure 6.20. The different colors correspond to different probabilities of the kinematic fit. The blue, magenta, red and black points correspond to kinematic fit probability of $p > 0.01$, $p > 0.1$, $p > 0.3$ and $p > 0.7$ respectively. The points in the plots have been shifted slightly within the bin so the cross-sections at different probabilities do not overlap. The plot shows that as the kinematic fit probability threshold increases, background is suppressed at the cost of reduced statistics, resulting in larger statistical uncertainties. It is seen that for a beam momentum of 10 GeV/c, the cross-section drops

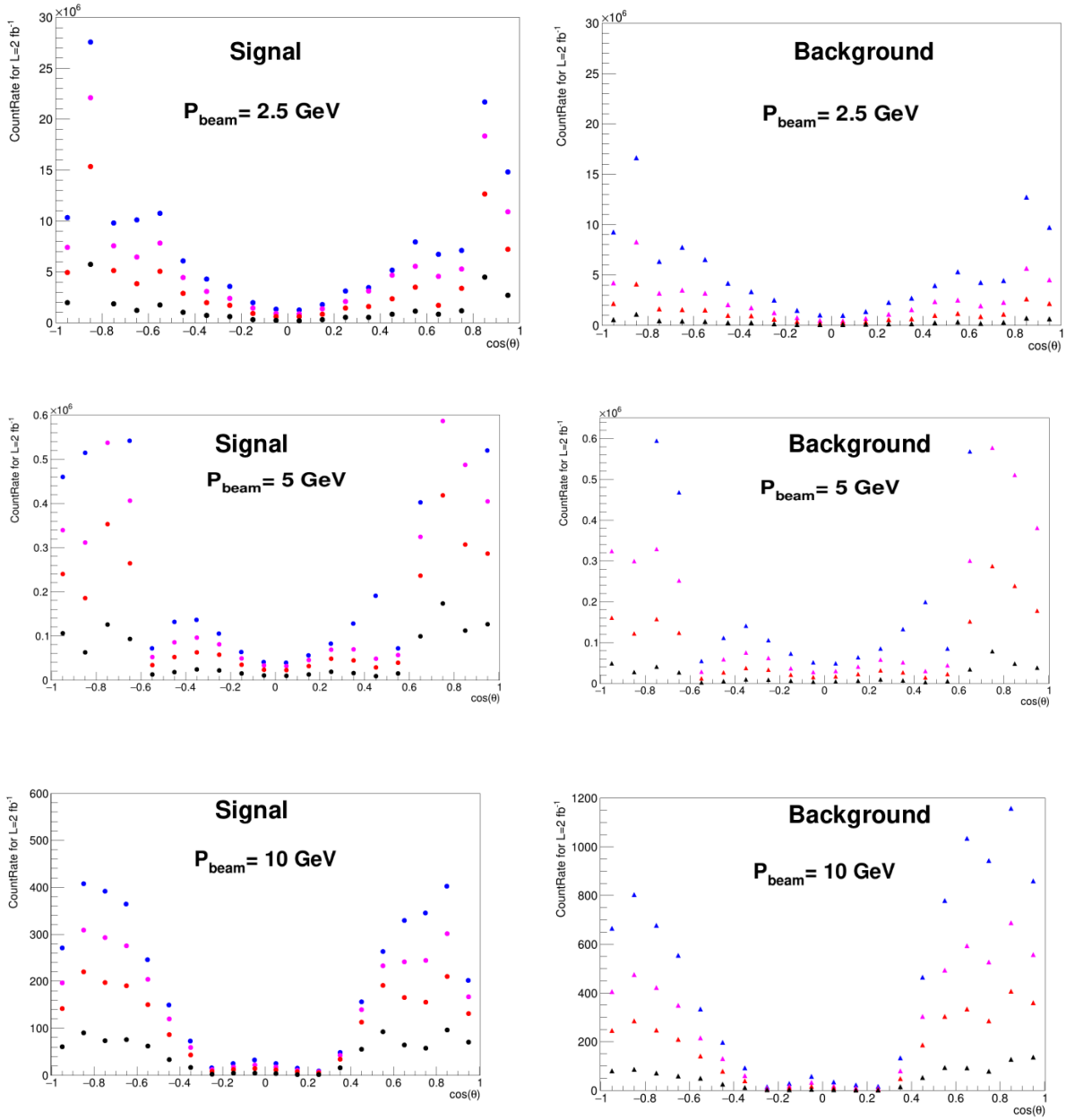

Figure 6.18: Count rates for the signal (left column) and background (right column) corresponding to different incident beam momentum: $p_{beam} = 2.5$ GeV/c (top row), $p_{beam} = 5$ GeV/c (middle row) and $p_{beam} = 10$ GeV/c (bottom row) respectively. The different colors correspond to different probabilities of the kinematic fit. The count rates are calculated for an integrated luminosity of 2 fb^{-1}.

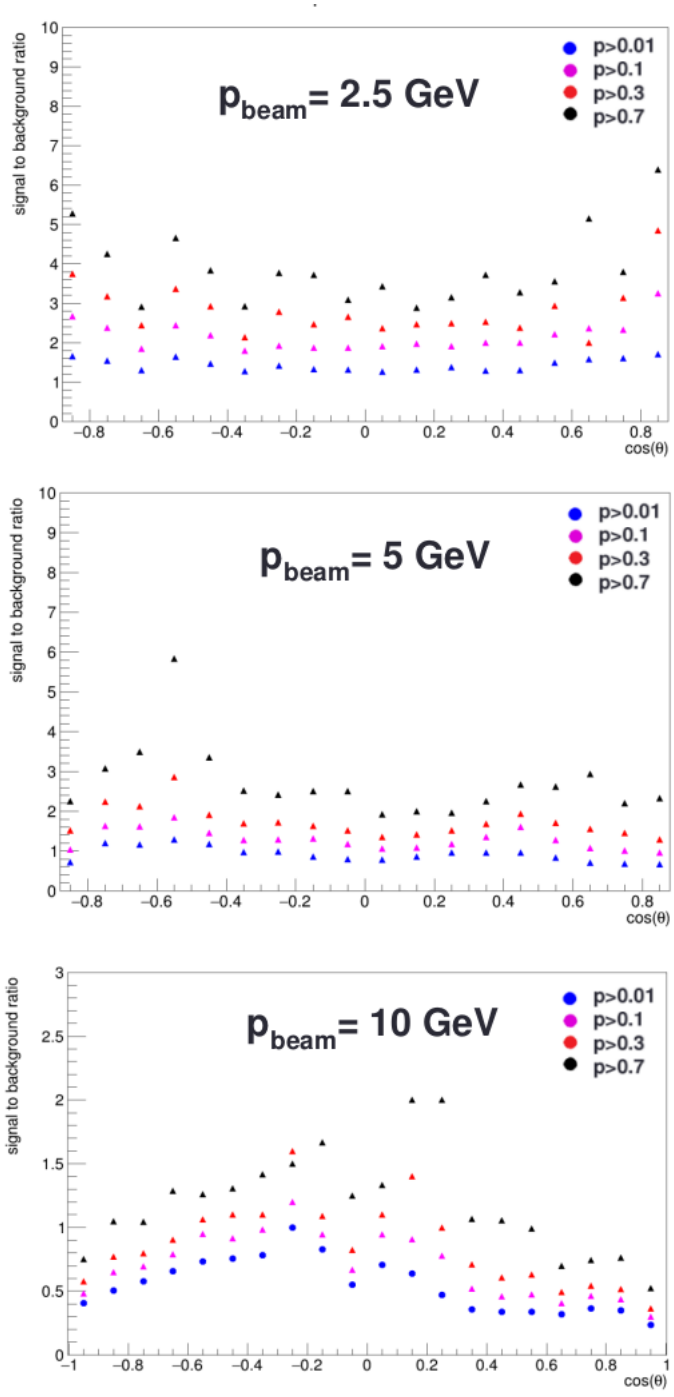

Figure 6.19: Signal to background ratio for different incident beam momentum: p_{beam} = 2.5 GeV/c (top row), p_{beam} = 5 GeV/c (middle row) and p_{beam} = 10 GeV/c (bottom row) respectively.

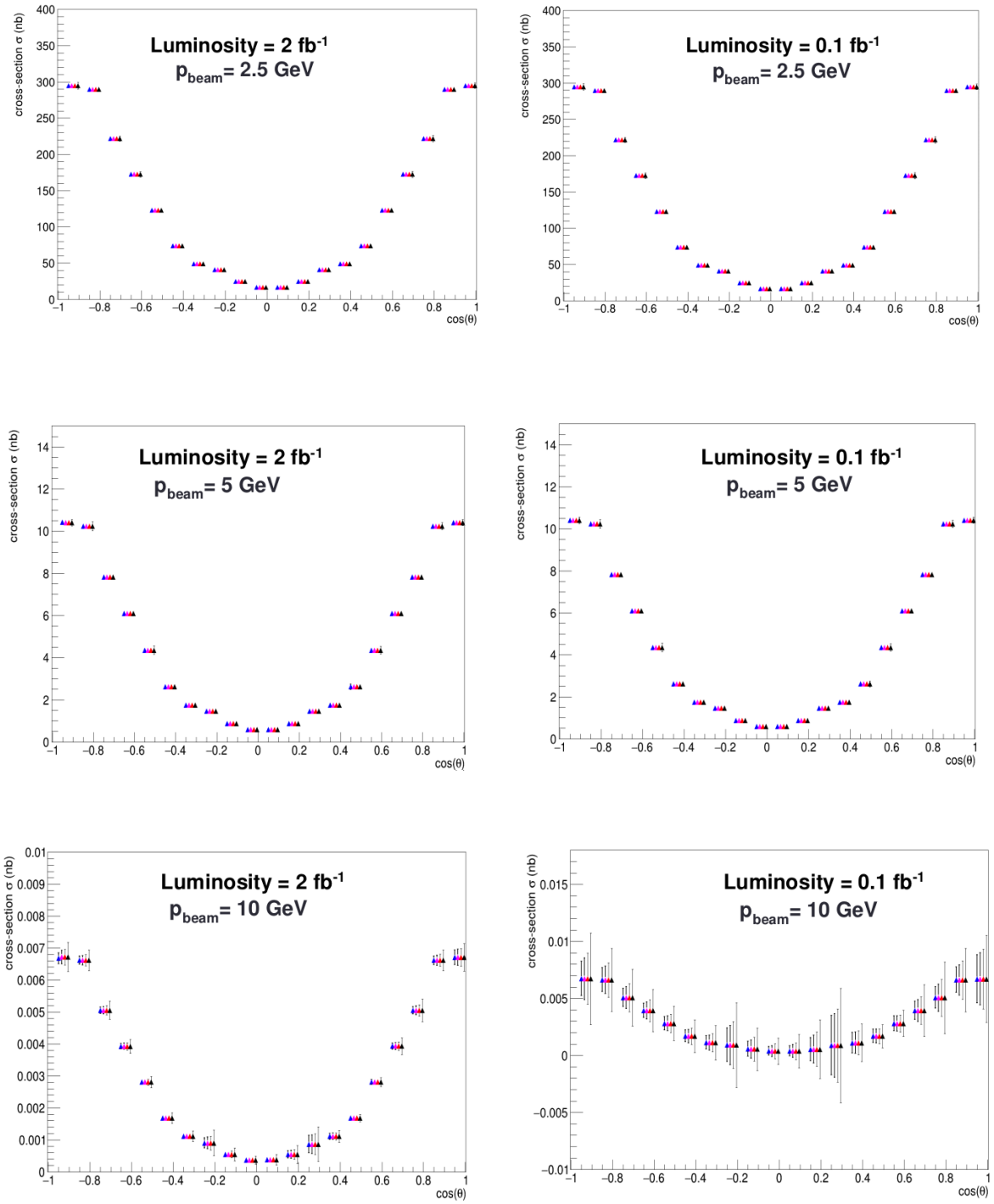

Figure 6.20: Expected statistical uncertainties for integrated luminosity of 2 fb^{-1} (left column) and 0.1 fb^{-1} (right column). The different rows correspond to different beam momenta.

below 0.01 nb for an integrated luminosity of 0.1 fb^{-1}, and the statistical uncertainties become critical. Hence, as the fluctuations are large, it becomes difficult to reliably constrain or compare with theoretical models. Therefore, the choice of the kinematic fit threshold determines the trade-off between higher statistical uncertainty and background suppression.

6.5 Optimization of signal efficiency using the correlation between reconstructed photon energy and opening angle

To improve the purity of reconstructed π^0 candidates, a selection method based on the correlation between the reconstructed photon energy and their opening angle was investigated. This technique aims to exploit the kinematic features of genuine $\pi^0 \to \gamma\gamma$ decays, which are typically not present in random photon combinations. The method is inspired by the approach detailed in Ref. [70], where further implementation details and performance studies can be found.

Neutral pions (π^0) are reconstructed through their two-photon ($\gamma\gamma$) decay channel by analyzing the invariant mass spectrum of all photon pairs within an event. The invariant mass distribution of π^0 includes contributions from both genuine decay photons and combinatorial background, which arises from randomly paired photons. This background can be significantly reduced by utilizing the kinematic correlation between decay photons from π^0, a feature that is not present in combinatorial $\gamma\gamma$ pairs.

To enhance signal purity and suppress combinatorial background, a selection criterion is applied based on the relationship between the opening angle and the average reconstructed photon energy. The applied constraints are defined as follows:

$$f_L(OA) < \frac{E_{\gamma_1} + E_{\gamma_2}}{2} < \begin{cases} \infty & \text{if } OA \leq a_2^U \\ f_U(OA) & \text{if } OA > a_2^U \end{cases} \tag{6.1}$$

where

$$f_L(x) = a_0^L + \frac{a_1^L}{x - a_2^L}, \quad \text{and} \quad f_U(x) = a_0^U + \frac{a_1^U}{x - a_2^U} \tag{6.2}$$

In this formulation, OA represents the opening angle between the two photons, while

E_{γ_1} and E_{γ_2} denote their respective energies. The parameters a_i^L and a_i^U $(i = 0, 1, 2)$ are coefficients of the parameterization, which are determined independently for each collision energy.

6.5.1 Invariant Mass Spectra

With these optimized selections, the combinatorial background is significantly reduced to a few percent while maintaining an efficiency more than 90% for pairs where both photons originate from π^0 decay. The impact of this cut is depicted in Figure 6.21, where the left plot shows the mass spectrum for all photon pairs, while the right plot displays the spectrum for photons originating from π^0 decays. Plots are shown for different incident beam momenta: the top, middle, and bottom rows correspond to beam momenta of 2.5 GeV/c, 5 GeV/c, and 10 GeV/c, respectively.

Additionally, an invariant mass selection criterion of 110 MeV/c^2 $< m_{\gamma\gamma} <$ 160 MeV/c^2 is applied to the two-photon system to further refine the signal selection. These kinematic constraints adapted from [70] offer an effective method for enhancing signal efficiency while minimizing background contamination.

The corresponding average reconstructed energy vs the opening angle for all the $\gamma\gamma$ pairs in the event is shown in the left panel of Figure 6.22. The right panel shows the $\gamma\gamma$ pairs originating from π^0 decays after the cut is applied. As depicted in earlier Figure, the plots are shown for various beam momenta: the top, middle, and bottom rows correspond to beam momenta of 2.5 GeV/c, 5 GeV/c, and 10 GeV/c, respectively.

Despite the significant reduction of the combinatorial background, additional cuts are needed to further improve the signal to background ratio.

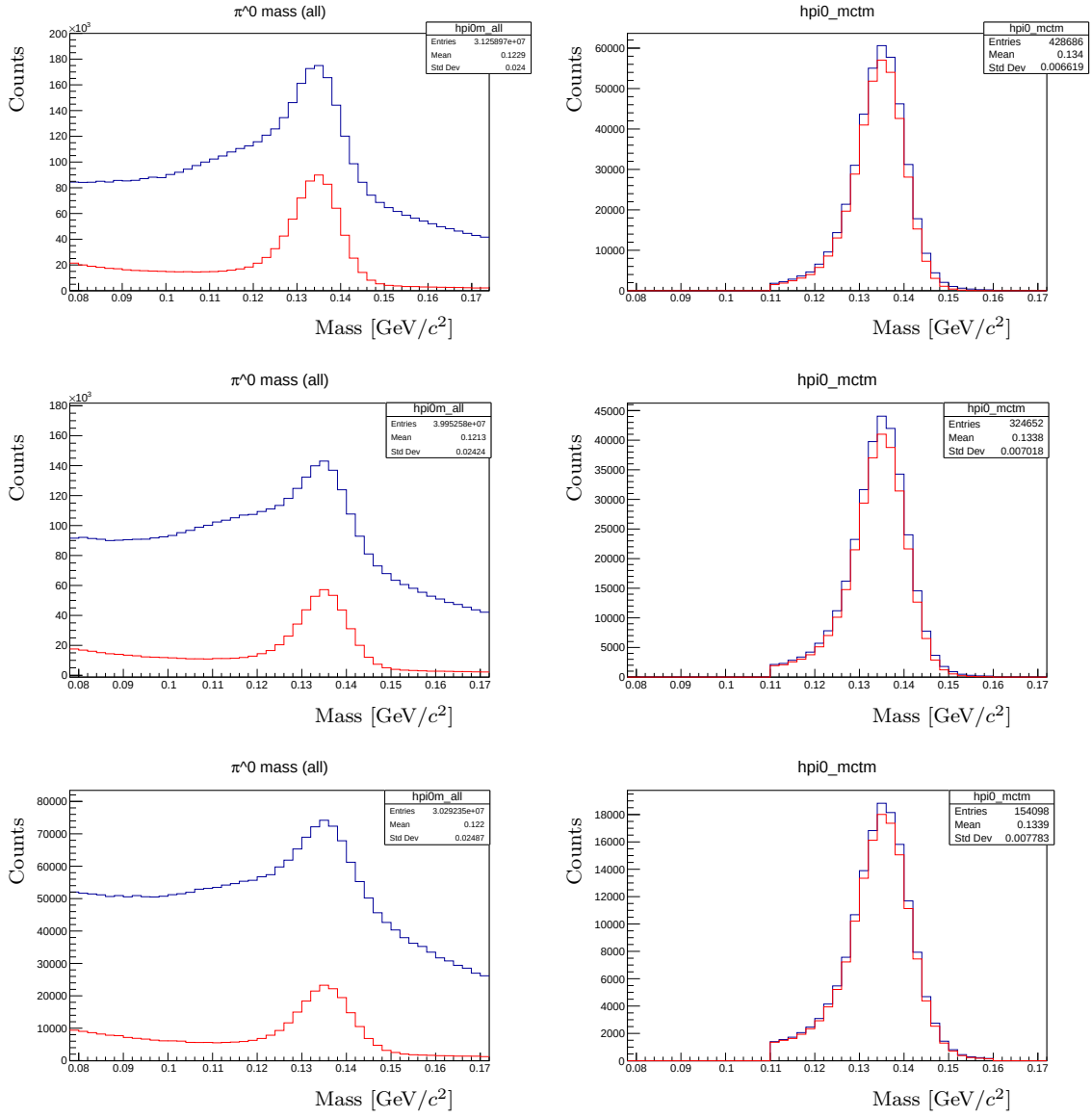

Figure 6.21: Invariant mass spectra of photon pairs for the signal channel $\bar{p}p \to \pi^0\gamma$. The left column shows the invariant mass spectra for all $\gamma\gamma$ pairs in the event, before the cut (blue line) and after the cut (red line). The right column shows the corresponding invariant mass distributions for reconstructed photon pairs from π^0 decay. Each row corresponds to a different incident beam momentum: 2.5 GeV/c (top row), 5 GeV/c (middle row), and 10 GeV/c (bottom row).

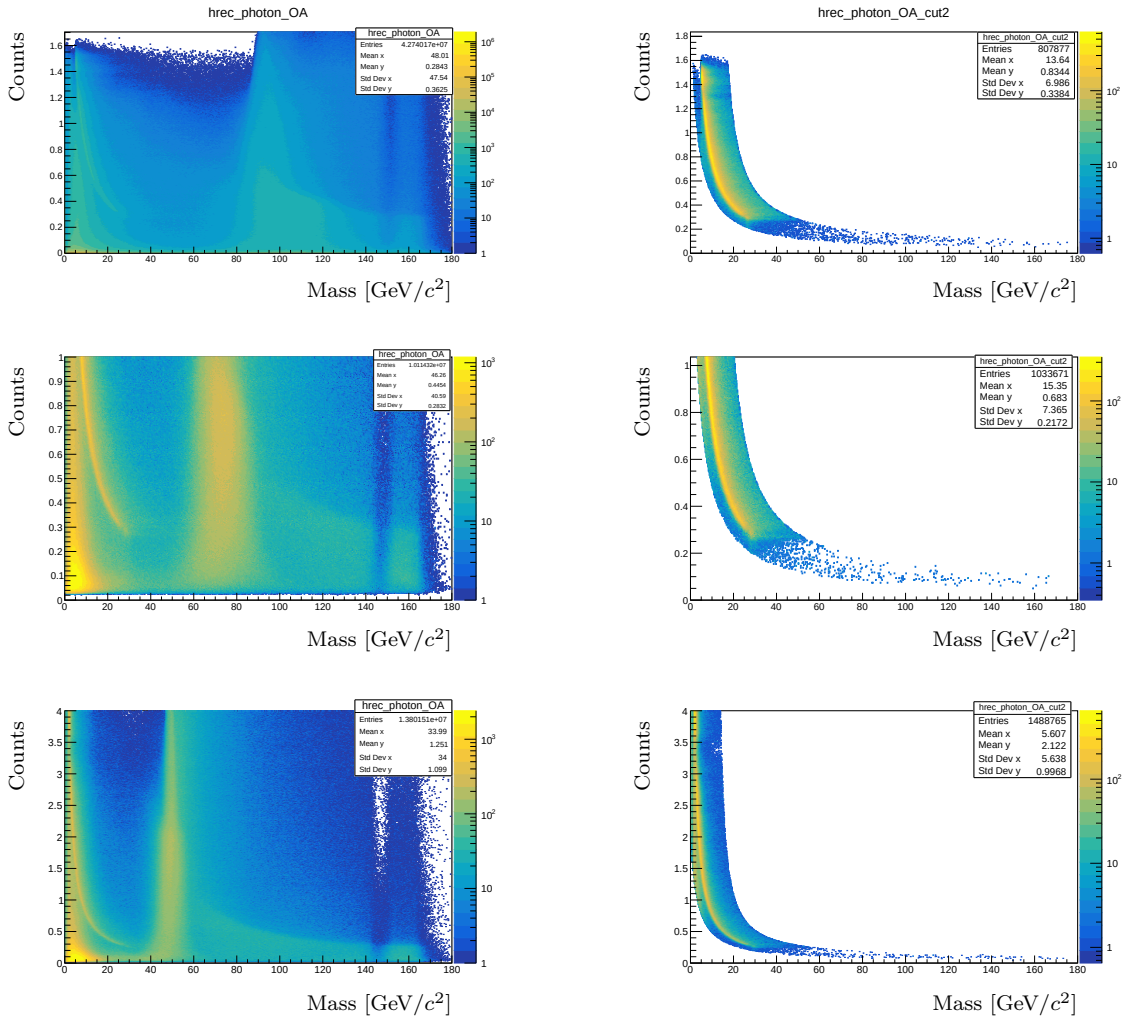

Figure 6.22: The average reconstructed energy vs the opening angle for all the $\gamma\gamma$ pairs in the event (left panel) and $\gamma\gamma$ pairs originating from π^0 decays after the cut is applied (right panel). Each row corresponds to a different $\bar{p}$ incident momentum: the top, middle, and bottom rows correspond to beam momenta of 2.5 GeV/c, 5 GeV/c, and 10 GeV/c, respectively.

6.5.2 Method I: Optimization of signal efficiency through improved pions obtained after applying opening and average energy cuts

Figure 6.23 and Figure 6.24 show the count rates for signal (left panel) and background (right panel) at two different beam momenta: 5 and 10 GeV/c. The blue and red markers represent raw counts, while the empty triangles indicate the results after implementing the cuts as discussed in Section 6.5.1.

These figures reveal several key differences. At 5 GeV/c, the signal count rate shows a strong peak near $\cos(\theta) \approx 0$, suggesting a central angular dominance, while the background remains relatively flat and lower in magnitude. With the improved π^0, the signal yield is enhanced and suppresses background, particularly in the forward region, as indicated by the empty triangle markers.

In contrast, at 10 GeV/c, both the signal and background rates increase significantly. The signal count shows a broader angular spread with enhanced rates, while the background also rises, particularly at forward and backward angles. However, the improved π^0 selection still manages to reduce the background component effectively.

Figure 6.25 illustrates the signal-to-background ratio for both momenta. At 5 GeV/c, the signal-to-background ratio is consistently higher, especially around central angles, whereas at 10 GeV/c, it decreases due to a more pronounced increase in background. The empty triangles, corresponding to the data after the improved π^0, show a marked improvement in the signal-to-background ratio at both energies, with a more significant improvement observed at the lower momentum. This indicates that the selection criteria are particularly effective at suppressing background at lower energy conditions.

Overall, increasing beam momentum results in an overall increase in both signal and background counts. However, while signal rates benefit from the energy increase, maintaining a high signal-to-background ratio becomes more challenging. The use of optimized π^0 events in this method proves crucial for enhancing signal quality across energies.

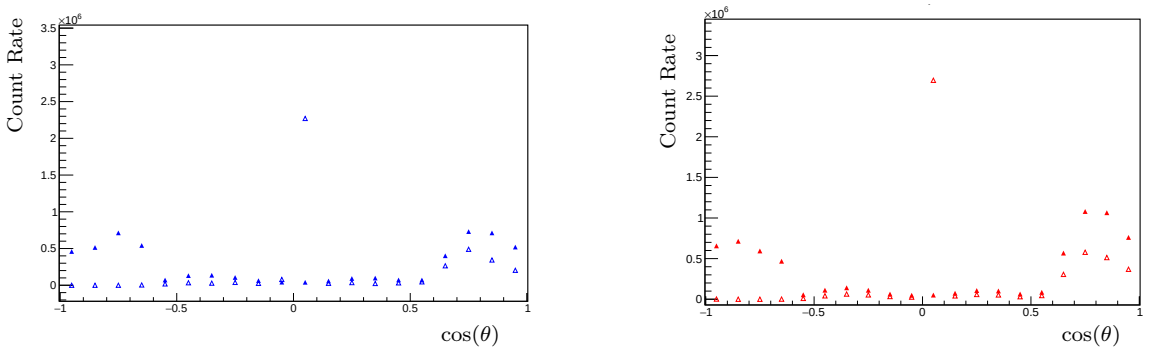

Figure 6.23: Count rate of signal (left) and background (right) for $p_{\overline{p}} = 5\ GeV/c$. Empty triangle show the count rate obtained after improved π^0.

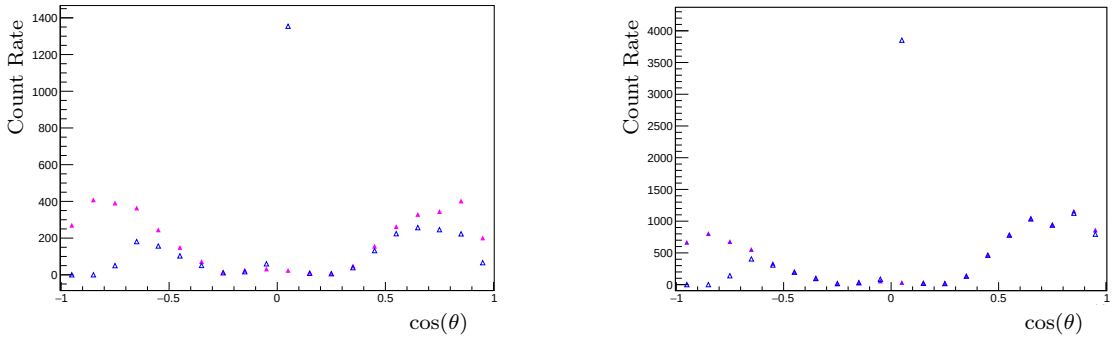

Figure 6.24: Count Rate of signal (left) and background (right) for $p_{\overline{p}} = 10\ GeV/c$. Empty triangle show the count rate obtained after improved π^0.

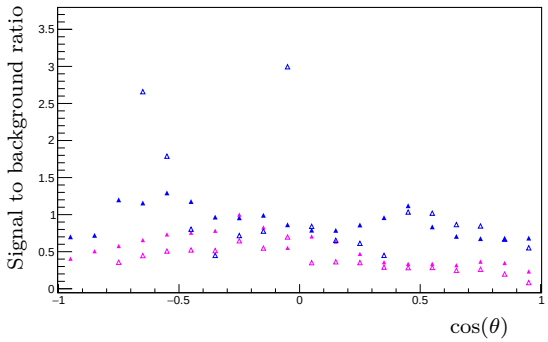

Figure 6.25: Signal to background for $p_{\overline{p}} = 5\ GeV/c$ (in blue) and $p_{\overline{p}} = 10\ GeV/c$ (in magenta). Empty triangles show the signal to background ratio obtained after improved π^0.

6.5.3 Method II: Optimization of signal efficiency through reconstructed gamma multiplicity

The following analysis investigates the impact of reconstructed gamma multiplicity and kinematic fit probability cuts on signal and background count rates, as well as the resulting signal-to-background ratio, for the process $p\bar{p} \to \pi^0\gamma$ at fixed transverse momentum $p_T = 5$ GeV/c. The figures compare two selection strategies:

- **Left Column:** Loose gamma selection with `countgamma` > 2
- **Right Column:** Strict selection requiring exactly three gammas, `countgamma` $= 3$

Each marker in the plots corresponds to a different kinematic fit probability threshold, with the black marker representing the strictest cut ($p > 0.7$) and the blue marker representing the loosest cut ($p > 0.01$).

Figure 6.26 shows how the signal count rate varies with different kinematic fit probabilities and photon multiplicity criteria.

- For `countgamma` > 2 (left column), the signal count rate is higher across all probability thresholds. This is expected, as this condition allows more events to pass, including those with extra photons due to detector noise or additional radiation.
- For `countgamma` $= 3$ (right column), the signal rate decreases, but it becomes more selective toward genuine signal events. The stricter condition filters out some true signal events that are misreconstructed but significantly improves purity.
- As the kinematic fit probability becomes stricter, the signal count rate decreases in both multiplicity conditions. This indicates that applying stricter event selection thresholds reduces the number of accepted signal events.

Figure 6.27 shows the background count rates which exhibit the following trends:

- For `countgamma` > 2 (left column), background rates remain relatively high across all kinematic fit probabilities due to the inclusion of events with additional or misidentified photons.
- For `countgamma` $= 3$ (right column), background counts are significantly reduced. This reflects effective suppression of combinatorial or misreconstructed background by enforcing the correct final-state configuration expected from the signal..
- Across both multiplicity conditions, tighter kinematic probability cuts (e.g., $p > 0.7$) lead to lower background counts, as these cuts select only well-reconstructed events.

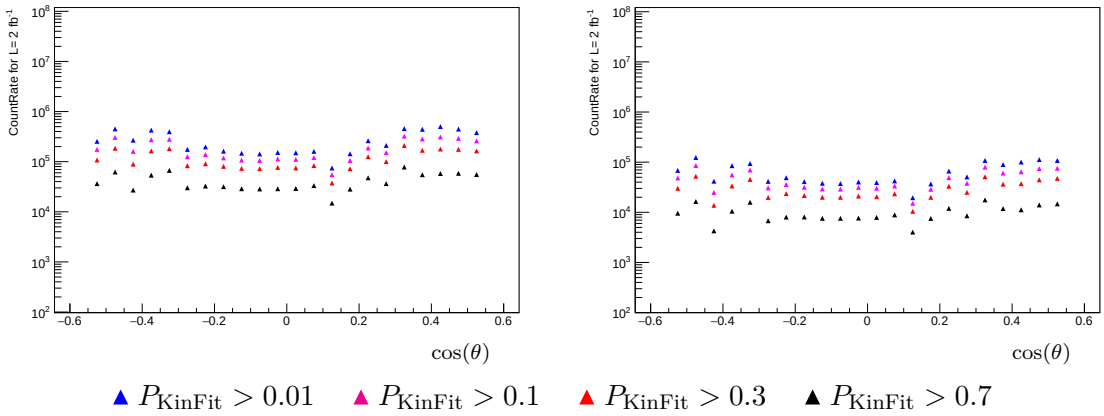

Figure 6.26: Signal count rate for beam momenta of 5 GeV/c at different kinematic probability conditions. The left column shows results for events with more than two detected photons, while the right column corresponds to events with exactly three detected photons.

Looser cuts (e.g., $p > 0.01$) result in higher background inclusion.

Signal-to-Background Ratio

The signal-to-background ratio is highly sensitive to both gamma multiplicity and the probability threshold: Figure 6.28 presents the signal-to-background ratio as a function of $\cos(\theta)$ for a beam momentum of 5 GeV/c, evaluated under various kinematic fit probability thresholds. The left column shows results for events with more than two detected photons, while the right column corresponds to events with exactly three detected photons. Different markers indicate different thresholds on the kinematic fit probability: $P_{\text{KinFit}} > 0.01$ (blue triangles), > 0.1 (magenta triangles), > 0.3 (red triangles), and > 0.7 (black triangles). As the kinematic fit probability requirement increases, a general improvement in the signal-to-background ratio is observed, particularly in the right panel. This improvement is more pronounced near central angles, suggesting that tighter kinematic constraints help suppress background more effectively. However, this comes at the cost of reduced statistics, especially at extreme angular regions.

The comparison between the panels shows that requiring events with at least three photons ($N_\gamma > 2$) retains a better signal-to-background ratio than selecting events with exactly three photons. While the latter matches the expected final state, it excludes genuine signal events with extra photons from split clusters. Overall, both photon multiplicity and kinematic fit probability cuts are important for optimizing signal selection.

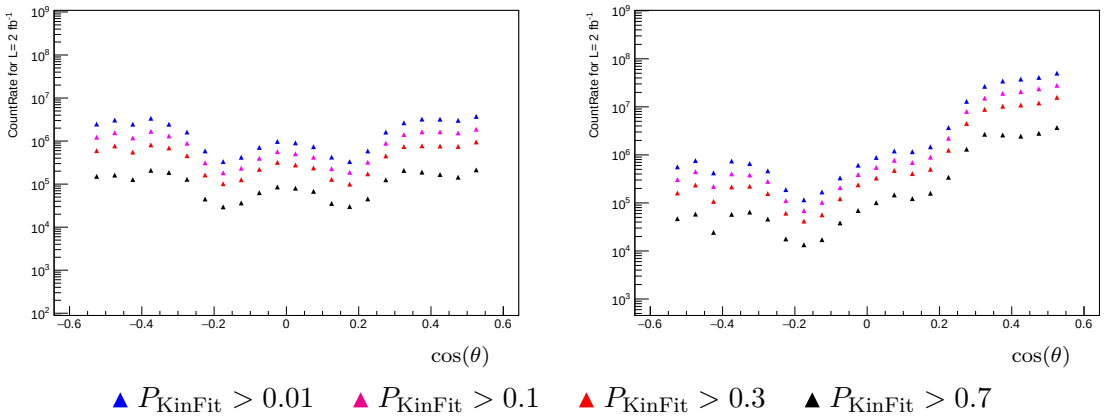

Figure 6.27: Background count rate for beam momenta of 5 GeV/c at different kinematic probability conditions. The left column shows results for events with more than two detected photons, while the right column corresponds to events with exactly three detected photons.

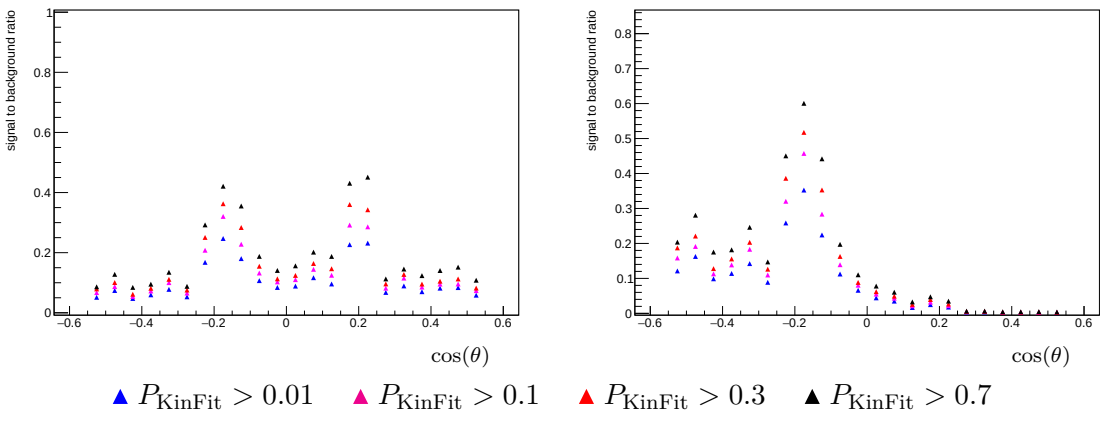

Figure 6.28: Signal to background ratio for beam momenta of 5 GeV/c at different kinematic probability conditions. The left column shows results for events with more than two detected photons, while the right column corresponds to events with exactly three detected photons.

6.5.4 Method III: Optimization of signal efficiency through kinematic cuts

To optimize signal efficiency while minimizing background contamination, various kinematic selection criteria are explored. The primary focus of this method is to investigate the impact of photon energy thresholds (E_γ) and the probability of kinematic fit (P_{KinFit}). A key part of this analysis involves studying the correlation between the reconstructed average photon energy and the opening angle, mainly for events simulated at a beam energy of 5 GeV.

In the following, various cases are considered and, by examining the correlation distributions, the effects of different selection cuts on the signal-to-background ratio can be quantified.

6.5.4.1 Photon Energy Threshold Cuts: $E_\gamma > 0.3$ GeV and $E_\gamma > 0.5$ GeV

A crucial aspect of enhancing signal selection is setting an appropriate threshold on photon energy. To evaluate its impact on background suppression and signal efficiency, two threshold values, $E_\gamma > 0.3$ GeV (top row) and $E_\gamma > 0.5$ GeV (bottom row), are investigated. These thresholds are chosen to suppress low-energy photons, which predominantly arise from bremsstrahlung, while retaining photons from genuine π^0 decays. The goal is to identify the optimal energy cut that maximizes signal retention while minimizing background contamination.

Figures 6.29 and 6.30 present the distribution of the reconstructed average energy of photon pairs as a function of their opening angle at a beam momentum of 5 GeV for signal and background, respectively. The left panel shows all $\gamma\gamma$ pairs, including background contributions. The middle panel focuses on photon pairs identified as originating from π^0 decays, where the π^0 particles were selected using Monte Carlo Truth Matching (MCTM), providing a clearer representation of the signal. Finally, the right panel displays the distribution after applying both the MCTM requirement and an additional cut on the opening angle (OA), which further refines the selection by reducing combinatorial background.

The application of photon energy and opening angle cuts enhances the separation between signal and background. As shown in Figures 6.29 and 6.30, increasing the energy threshold from 0.3 GeV to 0.5 GeV reduces the number of low-energy photon pairs in both cases, but the impact is more pronounced for the background, which contains a larger fraction of soft photons from bremsstrahlung. In contrast, signal events predominantly retain high-

energy pairs from $\pi^0 \to \gamma\gamma$ decays. The opening angle and average energy cut effectively suppress background contamination while retaining the essential features of the signal distribution.

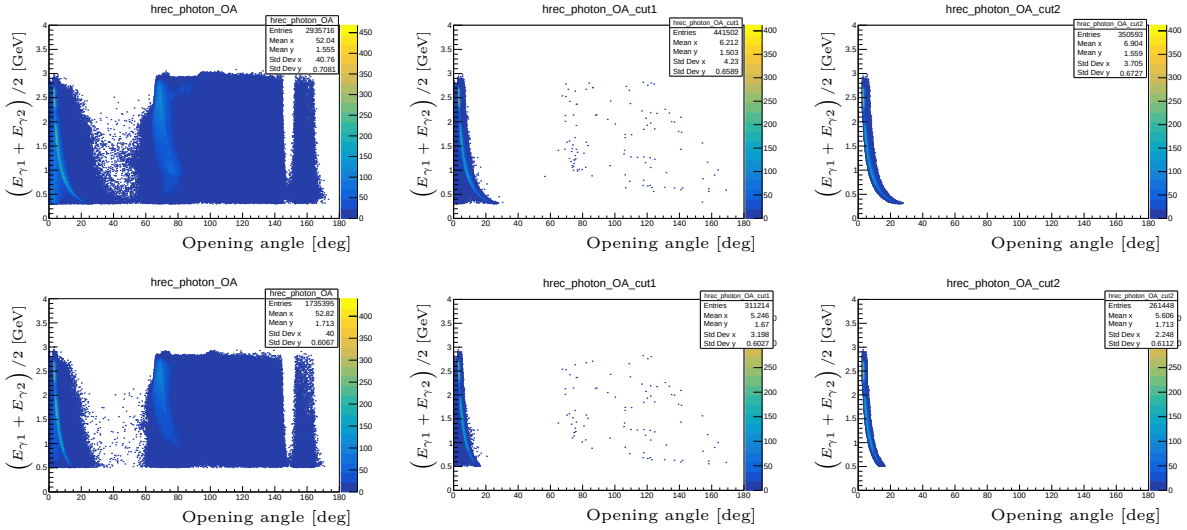

Figure 6.29: Distribution of reconstructed photon pairs for the signal sample. From left to right: all photon pairs, MCTM, and MCTM with the opening angle (OA) cut. The top and bottom rows correspond to energy thresholds of 0.3 GeV and 0.5 GeV, respectively.

6.5.4.2 Kinematic Fit Probability and Photon Energy Selection: $P_{\mathbf{KinFit}} > 0.01$, $E_\gamma > 0.1$, and $E_\gamma > 0.3$

The probability of the kinematic fit, P_{KinFit}, is used as an additional constraint to enhance event selection. Events with a kinematic fit probability greater than 0.01 are selected, in combination with photon energy thresholds of 0.1 GeV (top row) and 0.3 GeV (bottom row). This selection ensures that only well-reconstructed events with reliable kinematics are included in the analysis.

Figures 6.31 and 6.32 present the distribution of the reconstructed average energy of photon pairs as a function of their opening angle at a beam momentum of 5 GeV for signal and background, respectively. The left panel shows all $\gamma\gamma$ pairs, including background contributions. The middle panel focuses on photon pairs identified as originating from π^0 decays, where the π^0 particles were selected using Monte Carlo Truth Matching (MCTM), providing a clearer representation of the signal. Finally, the right panel displays the distribution after applying both the MCTM requirement and an additional cut on the opening angle (OA), which further refines the selection by reducing combinatorial background.

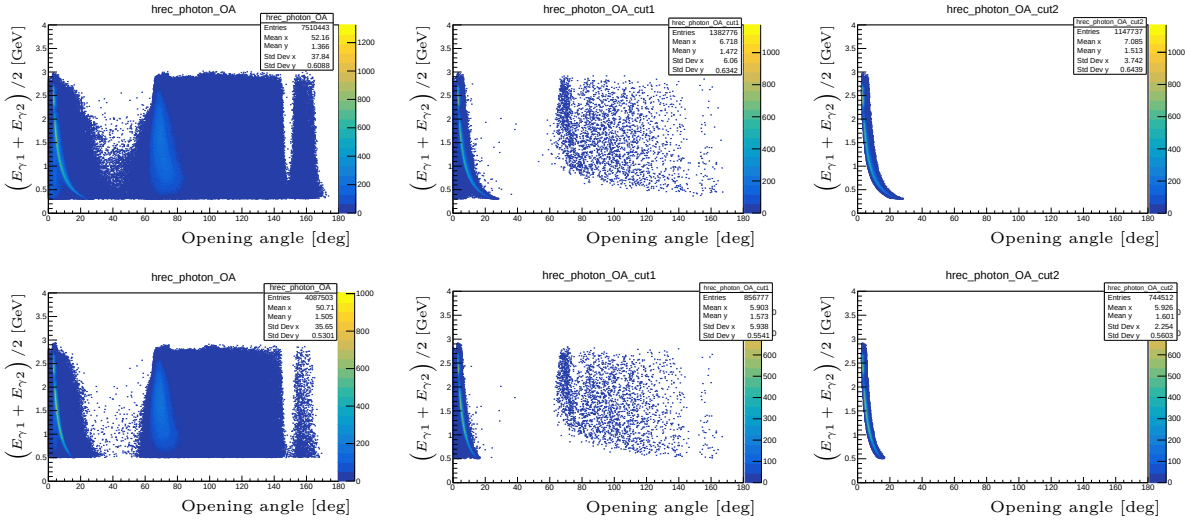

Figure 6.30: Distribution of reconstructed photon pairs for the background sample. From left to right: all photon pairs, MCTM, and MCTM with the opening angle (OA) cut. The top and bottom rows correspond to energy thresholds of 0.3 GeV and 0.5 GeV, respectively.

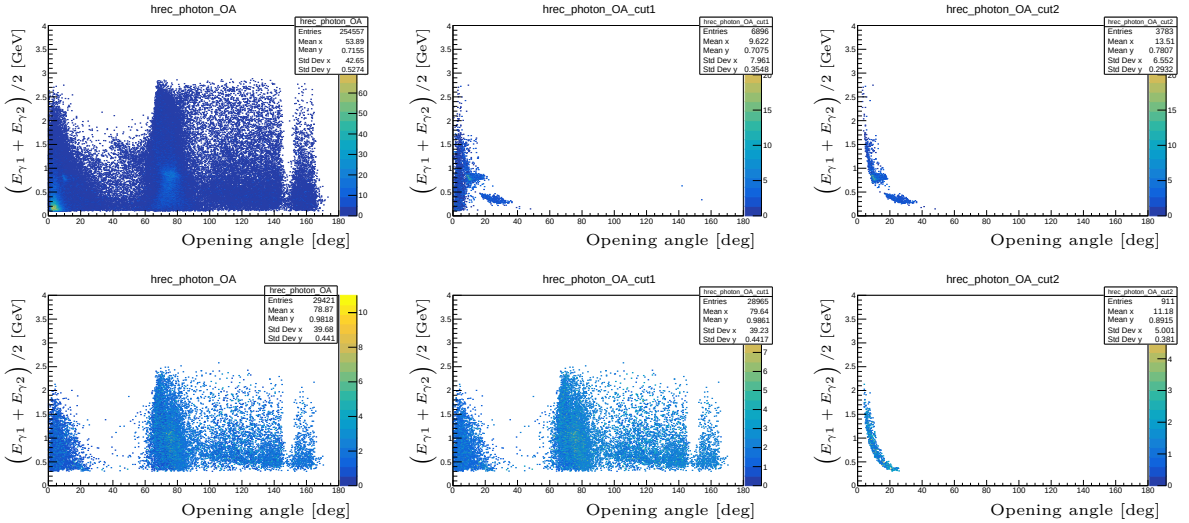

Figure 6.31: Distribution of reconstructed photon pairs for the signal sample. From left to right: all photon pairs, MCTM, and MCTM with the opening angle (OA) cut. The top and bottom rows correspond to energy thresholds of 0.1 GeV and 0.3 GeV, respectively.

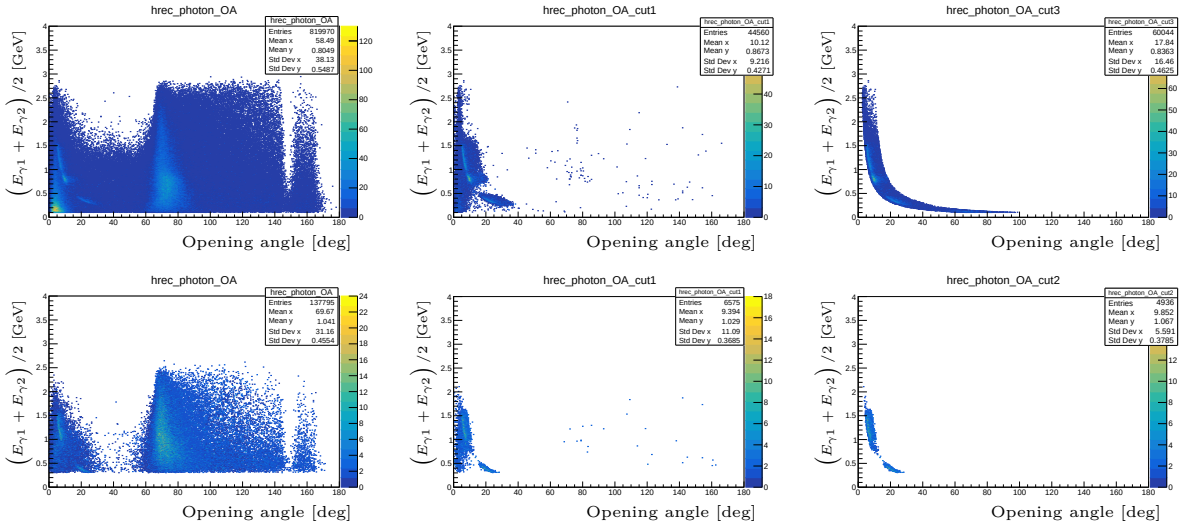

Figure 6.32: Distribution of reconstructed photon pairs for the background sample. From left to right: all photon pairs, MCTM, and MCTM with the opening angle (OA) cut. The top and bottom rows correspond to energy thresholds of 0.1 GeV and 0.3 GeV, respectively.

6.5.4.3 Neutral Pion Count Selection: $N_{\pi^0} = 1$ and $E_\gamma > 0.1$

In this selection, an event is required to contain exactly one reconstructed neutral pions (π^0) in addition to a photon energy threshold of $E_\gamma > 0.1$. Figure 6.33 presents the distribution of the reconstructed average energy of photon pairs as a function of their opening angle at a beam momentum of 5 GeV for signal (top row) and background (bottom row), respectively. The left panel shows all $\gamma\gamma$ pairs, including background contributions. The middle panel focuses on photon pairs identified as originating from π^0 decays, where the π^0 particles were selected using Monte Carlo Truth Matching (MCTM), providing a clearer representation of the signal. Finally, the right panel displays the distribution after applying both the MCTM requirement and an additional cut on the opening angle (OA), which further refines the selection by reducing combinatorial background. It is observed that these set of cuts cleanup the background quite well.

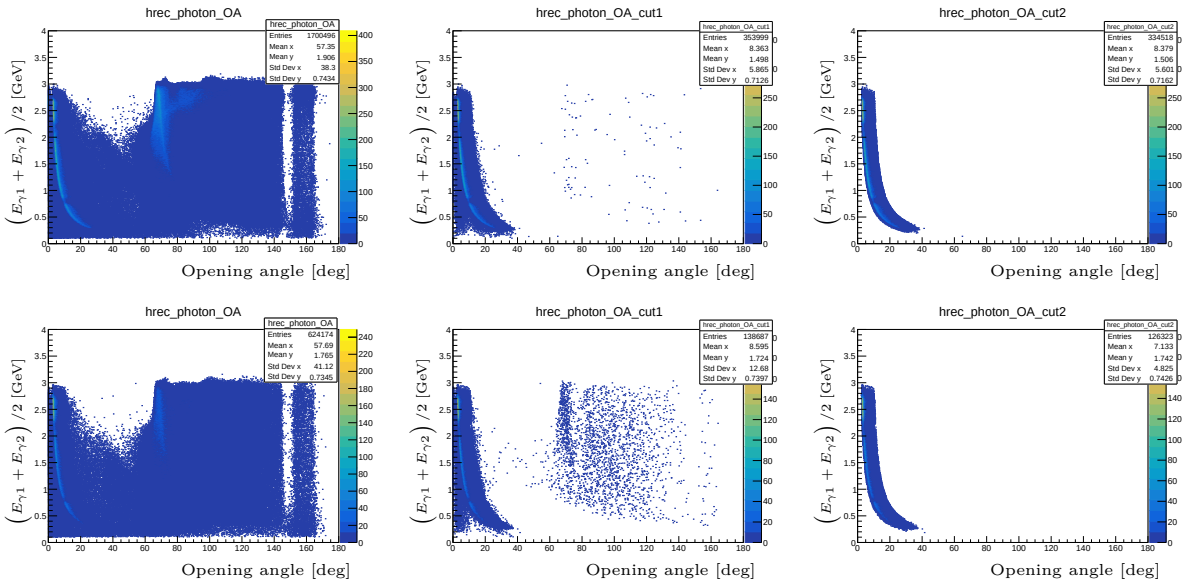

Figure 6.33: From left to right: all photon pairs, MCTM, and MCTM with the opening angle (OA) cut. The top and bottom rows correspond to signal and background distribution, respectively.

6.6 Signal-to-Background Ratio Under Different Optimization Strategies

This section examines how various cut configurations and selection criteria affect the signal-to-background ratio.

6.6.1 Signal-to-background ratio based on previous optimization approaches

Figure 6.34 illustrates the signal-to-background ratio as a function of $\cos(\theta)$ for a beam momentum of 5 GeV/c, comparing different event selection criteria as discussed in Section 6.5.4. The different markers correspond to different combinations of cuts aimed at improving the signal-to-background ratio. The blue markers represent the condition $E_\gamma > 0.3$ GeV, which serves as a basic energy threshold for photon candidates. The magenta markers include an additional constraint of kinematic fit probability $P_{\text{KinFit}} > 0.01$ alongside $E_\gamma > 0.1$ GeV, slightly tightening the selection. The red markers correspond to an even stricter photon energy condition of $E_\gamma > 0.3$ GeV combined with the same kinematic fit probability threshold. Finally, the black markers represent events where exactly one π^0 candidate was reconstructed ($N_{\pi^0} = 1$) and $E_\gamma > 0.1$ GeV. Among all selections,

the combination of $N_{\pi^0} = 1$ and $E_\gamma > 0.1$ shows the highest signal-to-background ratio across most angular bins, indicating effective background suppression. This demonstrates the advantage of incorporating π^0 multiplicity as a constraint to enhance signal purity, particularly around the central $\cos(\theta)$ region.

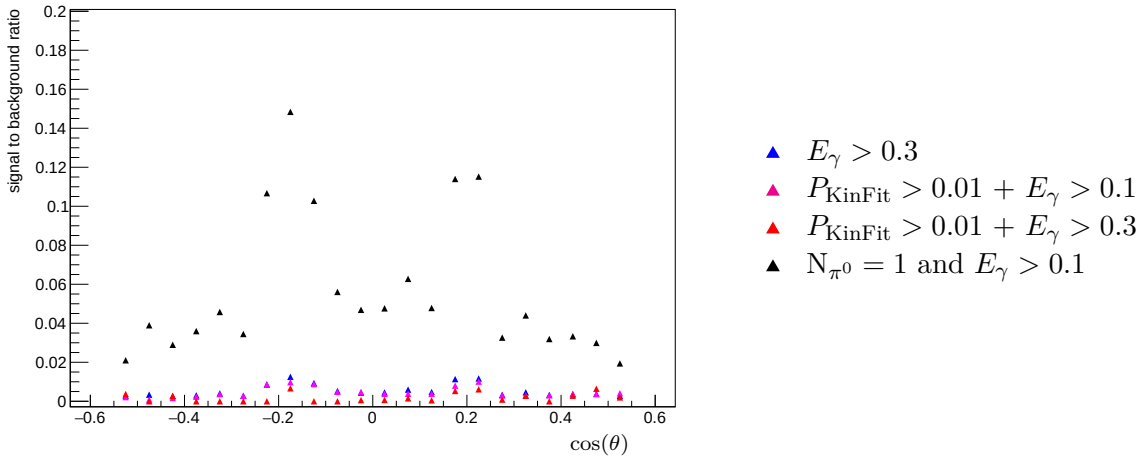

Figure 6.34: Signal to background ratio for $p_{\text{beam}} = 5$ GeV/c for the various cuts.

6.6.2 Signal to Background ratio for various energy thresholds

Figure 6.35 illustrates the signal-to-background ratio for different photon energy thresholds (E_γ) while incorporating additional selection criteria, including the average photon energy and opening angle cut, and the condition that exactly one neutral pion $N_{\pi^0} = 1$ is detected. Lower energy thresholds $E_\gamma > 0$ to $E_\gamma > 0.02$ include more background contributions, leading to a relatively lower signal-to-background ratio. As the photon energy threshold increases, the signal-to-background ratio initially improves due to better background suppression, particularly for thresholds around $E_\gamma > 0.03$ to $E_\gamma > 0.05$. However, for thresholds greater than $E_\gamma > 0.1$, the signal-to-background ratio starts to deteriorate. This decrease occurs because increasing the energy threshold too much begins to exclude genuine signal events along with background noise, which reduces the total number of events and makes the selection less effective. Therefore, optimizing the photon energy threshold is crucial to maintaining a balance between background suppression while retaining sufficient signal statistics.

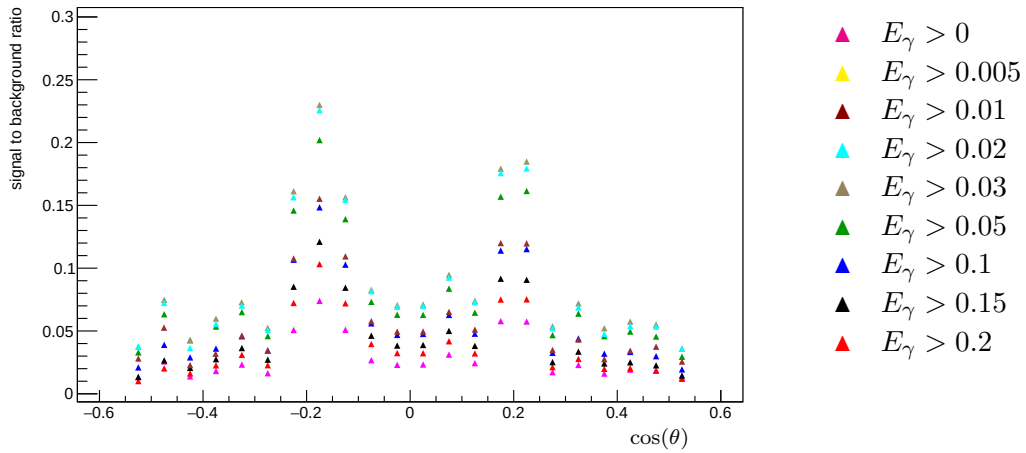

Figure 6.35: Signal-to-background ratio for $p_{\text{beam}} = 5$ GeV/c for various photon energy thresholds. All selections include the average photon energy and opening angle cut, and the condition that exactly one neutral pion ($N_{\pi^0} = 1$) is reconstructed.

6.6.3 Signal to Background ratio using `RhoGoodPhotonSelector`

In this section, the impact of different photon selection criteria and cut configurations on the signal to background ratio is analyzed. The subsequent plots illustrate the three cases considered.

6.6.3.1 `RhoGoodPhotonSelector`

This section presents the signal to background ratio for different photon selection criteria using `RhoGoodPhotonSelector`. Figure 6.36 compares the effects of PhotonVeryTight, PhotonTight, and PhotonLoose selections. The results indicate that there is no significant improvement in the signal to background ratio among these different selection criteria, as the values remain quite similar across all three cases. This suggests that the choice of photon selection criteria alone does not strongly influence the suppression of background or enhancement of the signal in this particular analysis.

6.6.3.2 `RhoGoodPhotonSelector` in comparison with the optimized cuts

Figure 6.37 compares the previously used photon selection criteria with the best-optimized cuts ($\text{N}_{\pi^0} = 1 + E_\gamma > 0.03 +$ OA) discussed in the previous section. We can observe that the optimized cuts result in a significantly improved signal-to-background ratio compared to the standard `RhoGoodPhotonSelector` criteria. This indicates that the refined

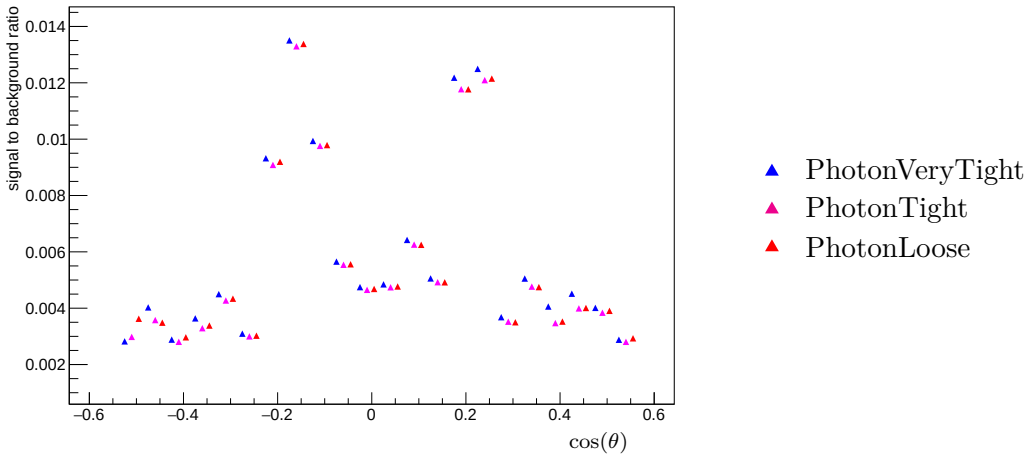

Figure 6.36: Signal to background ratio for different photon selection criteria using `RhoGoodPhotonSelector` at $p_{\text{beam}} = 5$ GeV/c.

selection cuts are more effective in enhancing the signal while suppressing background contributions.

6.6.3.3 `RhoGoodPhotonSelector` with different photon selection criteria and cut configurations.

The impact of different photon selection criteria combined with the opening angle (OA) cut and the requirement that exactly one neutral pion ($N_{\pi^0} = 1$) is detected is shown in Figure 6.38. The purple and black points, which correspond to the most optimized selection cuts ($N_{\pi^0} = 1 + E_\gamma > 0.03 +$ OA), exhibit the highest signal-to-background ratio, indicating that these cuts effectively suppress background while retaining the signal. Notably, the additional condition of applying the PhotonTight selection (purple points) does not lead to a noticeable improvement to the optimized cuts (black points). This suggests that once the opening angle and energy threshold cuts are applied, the photon selection criteria become less significant, as the dominant background have already been filtered out. Thus, the combination of $E_\gamma > 0.03$ and the opening angle cut plays a crucial role in optimizing the signal-to-background ratio, making further photon selection tightening redundant.

Figure 6.39 presents the energy (E_γ) and angular (θ) distributions of photons for different photon selection criteria, including All, Loose, Tight, and Very Tight selections. While there are slight variations in the distributions, it is evident that the photon selection criteria have minimal impact on the overall shape of the distributions. This aligns with the observation from the previous signal-to-background ratio plot, where the purple and

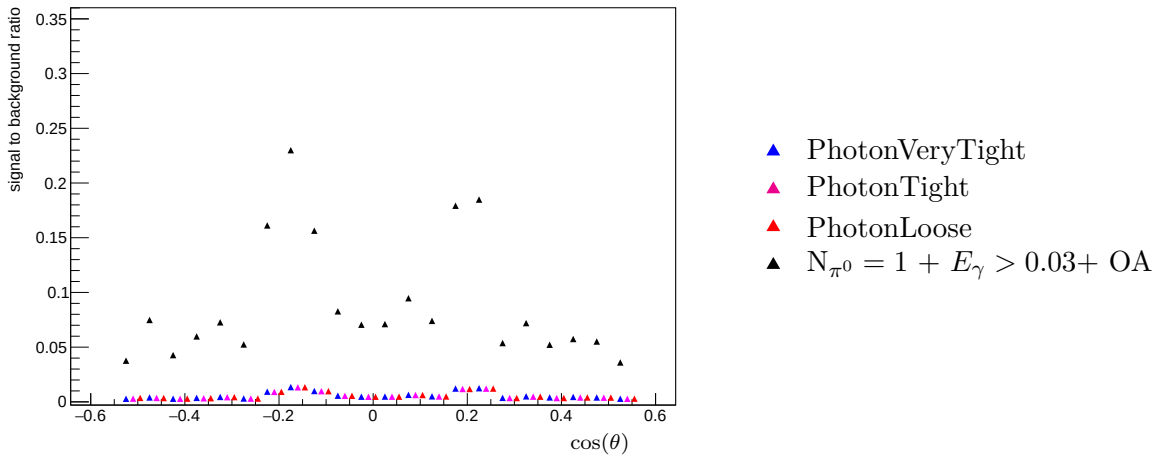

Figure 6.37: Signal to background ratio using `RhoGoodPhotonSelector` in comparison with the optimized cuts at $p_{\text{beam}} = 5$ GeV/c.

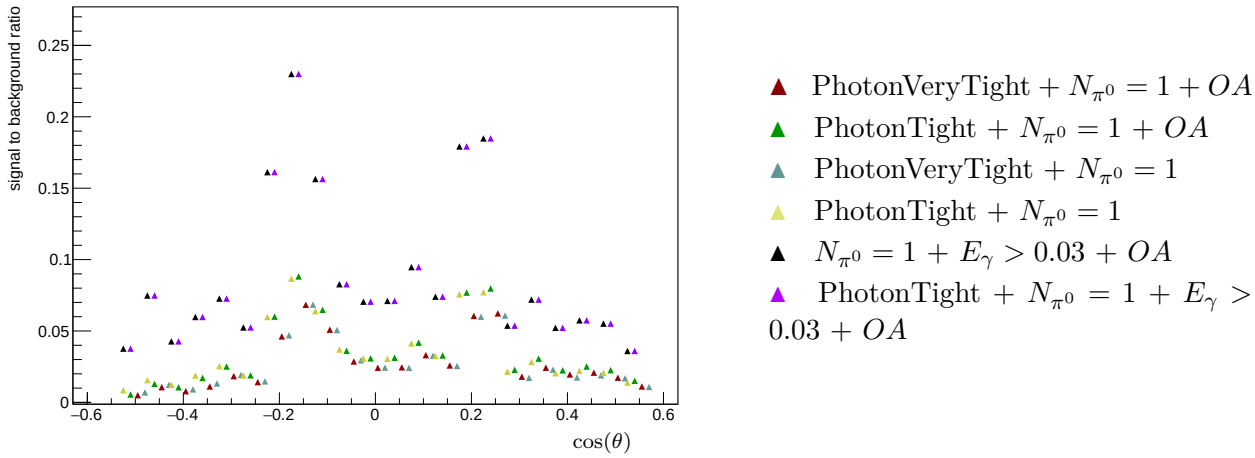

Figure 6.38: Signal to background ratio for $p_{\text{beam}} = 5$ GeV/c using `RhoGoodPhotonSelector` with different photon selection criteria and cut configurations.

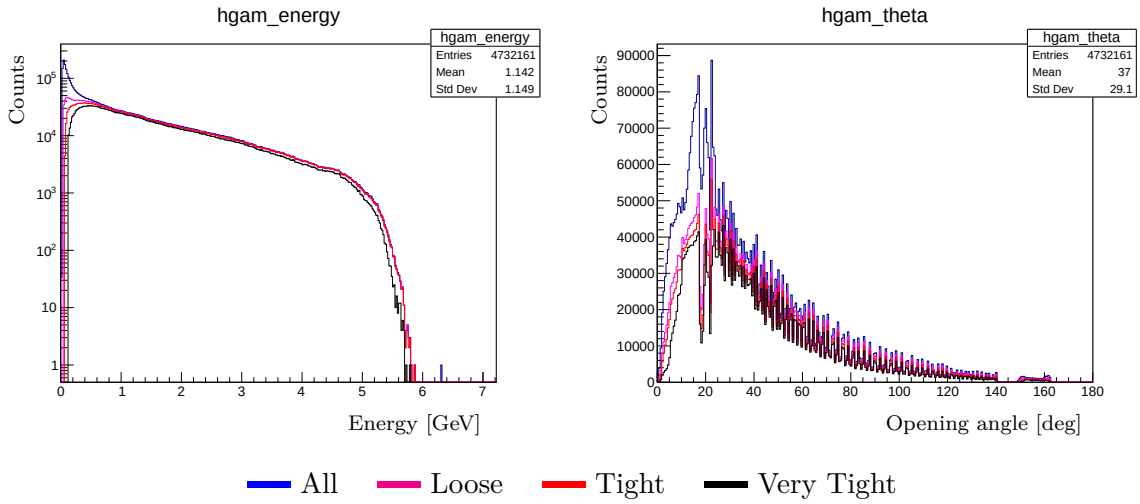

Figure 6.39: Energy and theta distribution of gammas at $p_{\text{beam}} = 5$ GeV/c for the different photon selection criteria.

black points were identical, indicating that the photon selection criteria had no effect after applying $E_\gamma > 0.03$. The reason for this is that the $E_\gamma > 0.03$ cut effectively removes most of the background, making additional photon selection requirements redundant. The tightening of photon selection criteria primarily aims at improving purity by rejecting lower-quality photons, but once the energy threshold is enforced, it becomes the dominant factor in suppressing background, leading to similar signal-to-background ratios regardless of the photon selection level.

6.6.4 Signal to Background ratio for various beam momenta using the optimized cuts

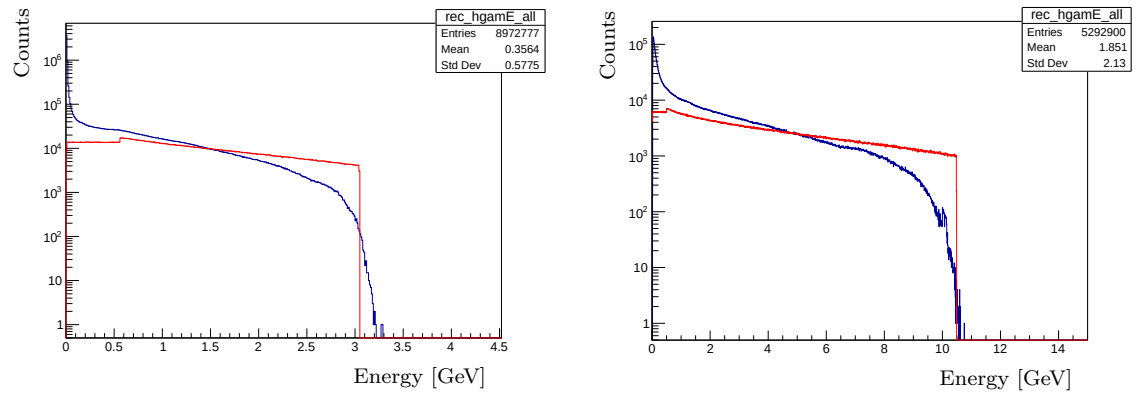

Figure 6.40: Energy distribution of gammas at $p_{\text{beam}} = 2.5$ GeV/c (left panel) and $p_{\text{beam}} = 10$ GeV/c (right panel).

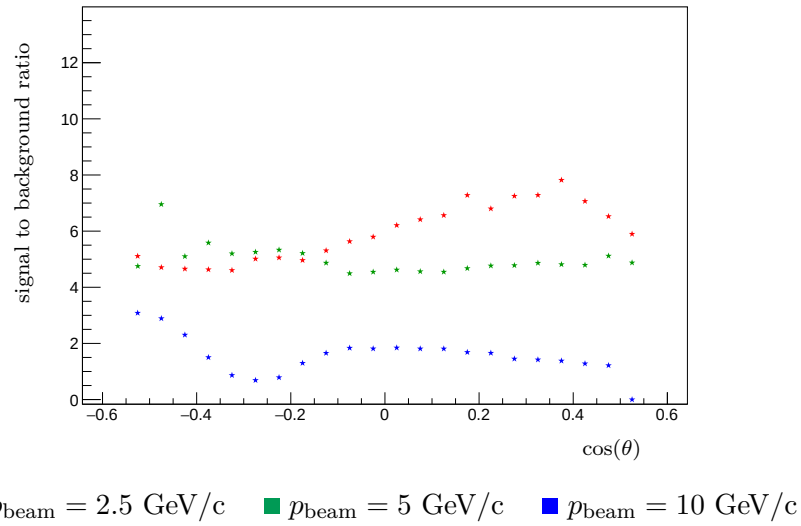

Figure 6.41: Signal to background ratio for different beam momenta assuming equal cross-section. The markers red, green and blue correspond to the p_{beam} = 2.5, 5 and 10 GeV/c respectively.

Figure 6.41 shows the signal-to-background ratio for three different beam momenta (2.5 GeV/c, 5 GeV/c, and 10 GeV/c) assuming that the cross-section are equal. The trend suggests that at lower beam momentum (2.5 GeV/c, red markers), the signal-to-background ratio is higher in some regions, while at higher beam momenta (10 GeV/c, blue markers), the ratio is consistently lower. This indicates that increasing the beam momentum leads to a greater relative contribution from background events, reducing the signal-to-background ratio when assuming an equal cross-section. The green markers (5 GeV/c) show an intermediate behavior, with a slightly better signal-to-background ratio than the highest momentum case. These plots take into account the different threshold energies at the different beam momenta as can be deduced from Figure 6.40.

Figure 6.42 presents the signal-to-background ratio without assuming an equal cross-section, meaning the actual cross-sections from the E760 data are taken into account. Here, the overall trend is similar, but the absolute values of the signal-to-background ratio are slightly different, particularly at lower momenta. Beam momenta of 2.5 and 5 GeV/c (red and green markers) still show a higher signal-to-background ratio than the 10 GeV/c (blue markers), indicating that at higher beam energies, background contribution becomes more significant.

Figure 6.43 shows the signal-to-background ratio as a function of $\cos(\theta)$ for different beam momenta: 2.5 GeV/c, 5 GeV/c, and 10 GeV/c. The black markers represent the ratio

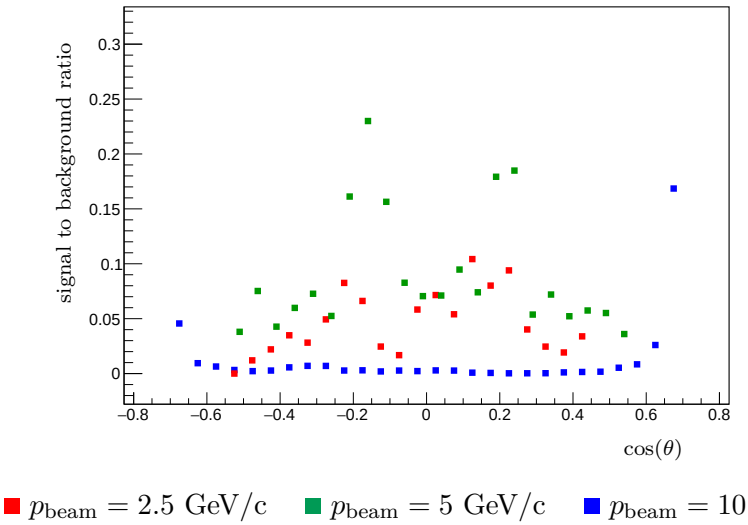

Figure 6.42: Signal to background ratio for different beam momenta. The markers red, green and blue correspond to the $p_{beam} = 2.5$, 5 and 10 GeV/c respectively.

of acceptances multiplied by the cross-section ratio from 5 GeV/c, serving as a reference. In contrast, the magenta markers show the same ratio calculated at the respective beam energies. The assumption of equal cross-sections provides a better estimate of the signal-to-background ratio. It is also observed that at lower beam momenta (2.5 GeV/c and 5 GeV/c), the signal-to-background ratio is relatively higher, especially in the central region, indicating a region where signal events are more distinguishable from the background. However, at higher beam momentum (10 GeV/c), the overall signal-to-background ratio is significantly reduced, as the signal acceptance decreases at higher energies. The results indicate that as the beam momentum increases, background suppression becomes more challenging, requiring more refined selection criteria to enhance the signal significance.

6.7 Other Investigative Methods for Background Suppression and Signal Optimization

Improving signal efficiency is crucial for optimizing the accuracy and reliability of the reconstructed events. Several investigative methods were employed to enhance signal selection while minimizing background contamination. These methods include:

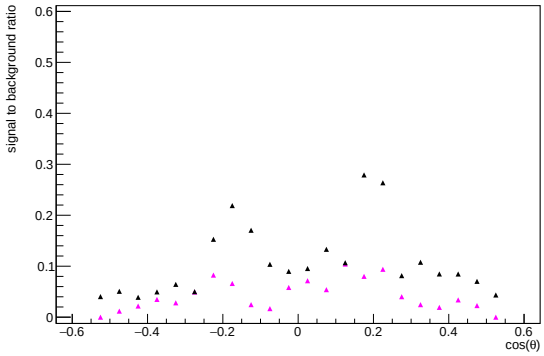

(a) $p_{\text{beam}} = 2.5$ GeV/c

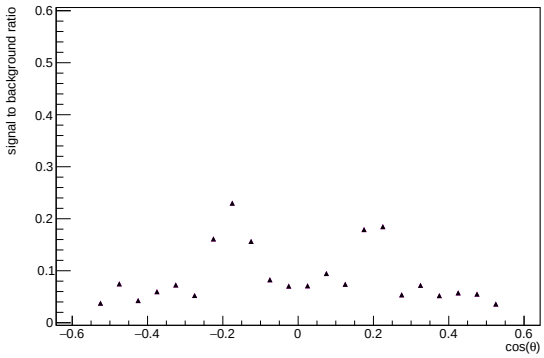

(b) $p_{\text{beam}} = 5$ GeV/c

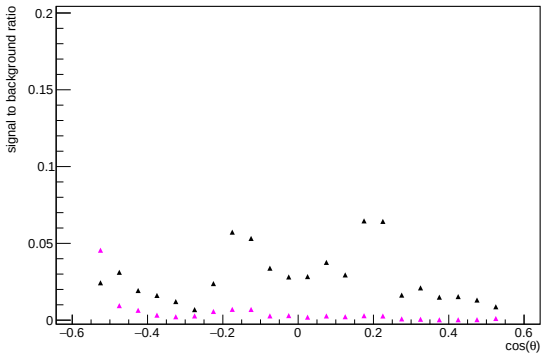

(c) $p_{\text{beam}} = 10$ GeV/c

▲ $\frac{Acceptance_{sig}}{Acceptance_{bkg}} \times$ cross-section ratio from 5 GeV/c data

▲ $\frac{Acceptance_{sig}}{Acceptance_{bkg}} \times$ cross-section ratio at respective energies

Figure 6.43: Signal to background ratio as a function of $\cos\theta$ for various beam momenta: $p_{beam} = 2.5$ GeV/c (top row), $p_{beam} = 5$ GeV/c (middle row) and $p_{beam} = 10$ GeV/c (bottom row). The black triangles indicate the estimated signal to background ratio using the acceptance ratio $\frac{\text{Acceptance}_{\text{sig}}}{\text{Acceptance}_{\text{bkg}}}$ scaled by the cross-section ratio derived from 5 GeV/c data. The magenta triangles show the corresponding estimate using cross-section ratios evaluated at the respective beam energies.

6.7.1 Optimizing Kinematic Cuts as inspired from [1]

Carefully chosen kinematic selection criteria, such as momentum, energy, and angular distributions, were applied to maximize signal retention while reducing background events. Different cut values were systematically tested to determine the optimal cut parameters.

6.7.1.1 χ^2_{4C} plot

The distribution of χ^2_{4C} values for signal (blue) and background (magenta) at a beam momenta of 5 GeV/c is shown in Figure 6.44. The left plot, displayed on a logarithmic scale, reveals that both signal and background are concentrated at low χ^2_{4C} values, with the signal being more dominant in this region. As χ^2_{4C} increases, the background remains significant, making it difficult to achieve a clean separation between the two. The right plot, shown on a linear scale, further emphasizes that most events cluster at low χ^2_{4C}, with both signal and background dropping off sharply as χ^2_{4C} increases.

Applying a cut of $\chi^2_{4C} < 40$ retains the majority of events while eliminating those with poorly constrained kinematic fits. However, since both signal and background primarily exist in the low χ^2_{4C} region, this cut does not significantly improve the signal-to-background ratio, as it reduces both components similarly. Therefore, while this selection criterion ensures better event quality, it does not enhance the overall purity of the signal.

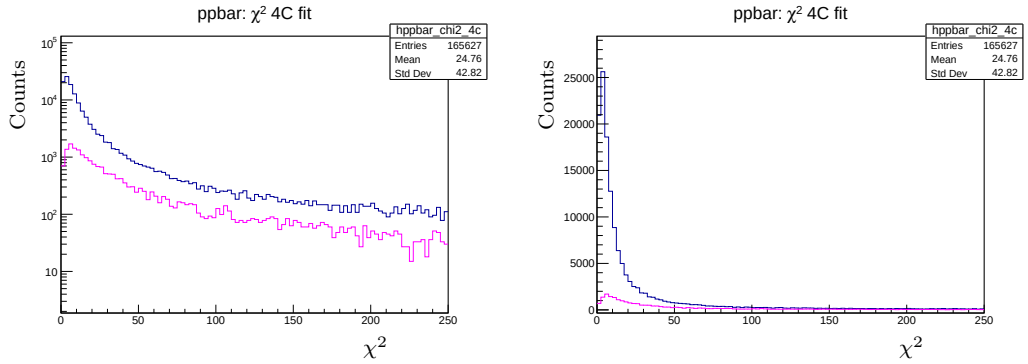

Figure 6.44: The distribution of χ^2_{4C} values for signal (blue) and background (magenta) at beam momenta of 5 GeV/c. The left panel displays the distribution on a logarithmic scale, while the right panel shows it on a linear scale.

6.8 Count Rate Estimate and Expected Cross-section with Statistical Uncertainties after Background Suppression

Figure 6.45 shows the estimated count rates with statistical uncertainties as a function of $\cos(\theta)$ at a luminosity of 2 fb^{-1} for three different beam momenta: 2.5, 5, and 10 GeV/c. Each subplot represents the distributions obtained after background suppression and event selection. To enhance readability, the points in the plots have been slightly shifted within the bins so that the different count rate distributions do not overlap. The left column presents the results with their original statistical uncertainties, while the right column displays the same distributions with magnified error bars (by factors of 500, 50, and 50, respectively) to make the propagated uncertainties more visible.

The different markers correspond to the count rates for the signal after background subtraction ($\mathrm{CR_{sig}}$, blue), the pure signal component ($\mathrm{CR_{sig,pure}}$, magenta), the combined signal and background ($\mathrm{CR_{S+B}}$, red), and the background contribution ($\mathrm{CR_{bkg}}$, black). At 2.5 GeV/c, the statistical uncertainties are relatively small due to the higher number of reconstructed events. As the beam momentum increases to 5 and 10 GeV/c, the overall event yield decreases, leading to larger relative statistical fluctuations. The uncertainty on the background-subtracted signal count rate ($CR_{\mathrm{sig,pure}}$) is noticeably higher than that of the raw signal (CR_{sig}), as it includes the propagated errors from both the signal and background distributions. This results in amplified statistical variations, especially in regions where the background contribution is comparable to the signal.

Figure 6.46 presents the differential cross sections ($d\sigma/d\Omega$) as a function of $\cos(\theta)$ for beam momenta of 2.5, 5, and 10 GeV/c, along with their associated statistical uncertainties. The left panel at 2.5 GeV/c shows the signal cross section obtained through propagation of statistical uncertainties after background subtraction. To help visualize the uncertainty at low statistics, the right-hand panel includes error bars magnified by a factor of 50. The cross section distribution is relatively flat in the forward and backward regions, with a slight dip near $\cos(\theta) \approx 0$, consistent with the count rate pattern observed earlier.

At $p_{\mathrm{beam}} = 5$ GeV/c, shown in the middle row, the propagated signal cross section is directly compared with existing data from the E760 experiment. The comparison with E760 data confirms the reliability of the background subtraction and reconstruction procedure, as reflected in the significantly smaller uncertainties observed in the present results.

For $p_{\mathrm{beam}} = 10$ GeV/c (bottom panel), although the error bars are relatively larger—reflecting

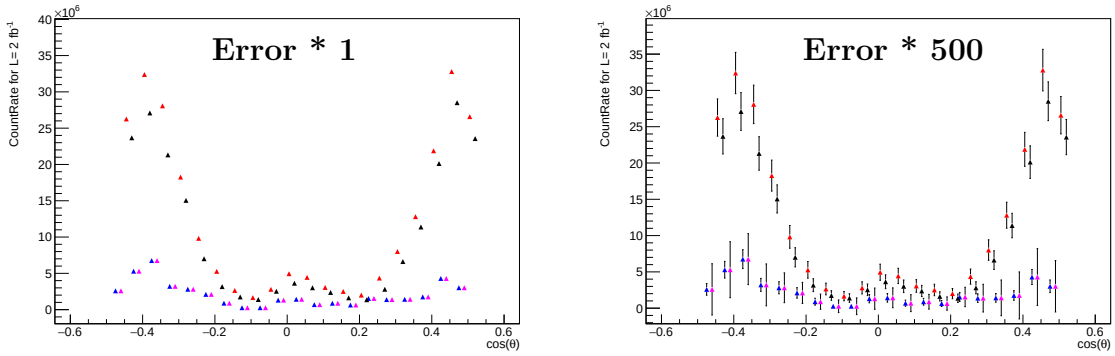

(a) $p_{\text{beam}} = 2.5$ GeV/c

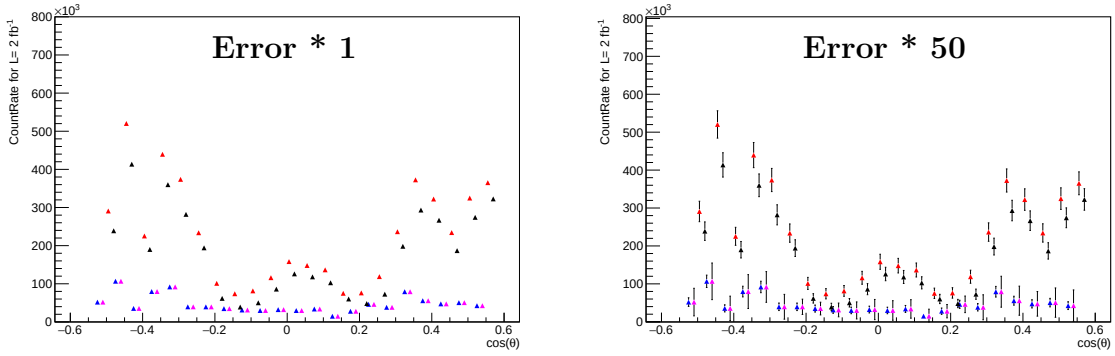

(b) $p_{\text{beam}} = 5$ GeV/c

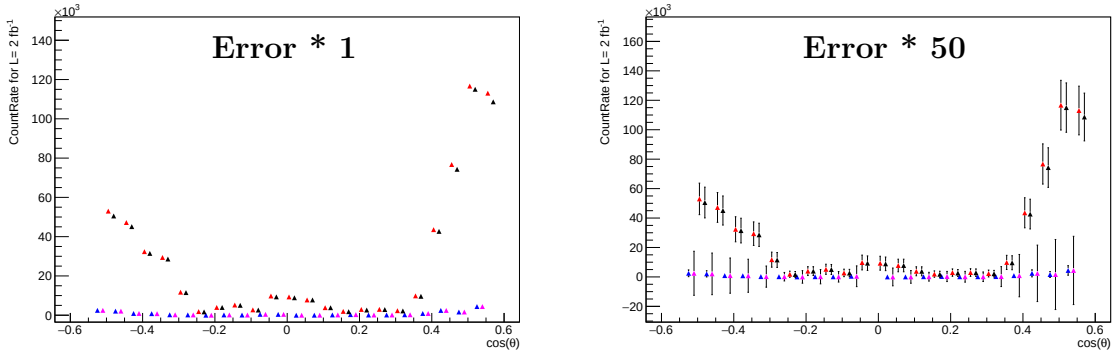

(c) $p_{\text{beam}} = 10$ GeV/c

▲ CR_{sig} ▲$CR_{sigpure}$ ▲ CR_{S+B} ▲ CR_{bkg}

Figure 6.45: Count Rate estimate at various beam momenta after background suppression. Each row corresponds to a different $\bar{p}$ incident momentum: 2.5 GeV/c (top row), 5 GeV/c (middle row), and 10 GeV/c (bottom row).

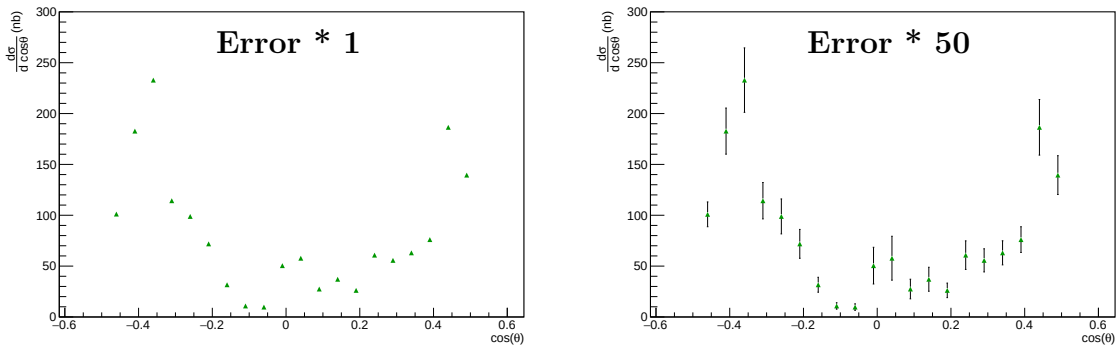

(a) $p_{\text{beam}} = 2.5$ GeV/c

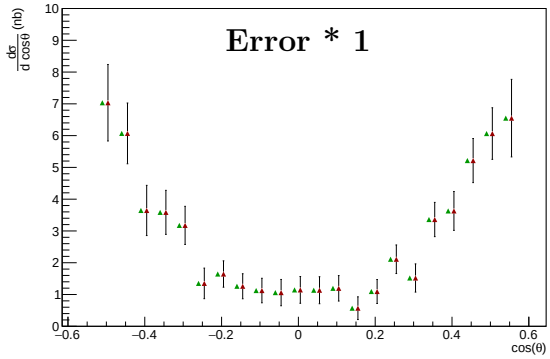

(b) $p_{\text{beam}} = 5$ GeV/c

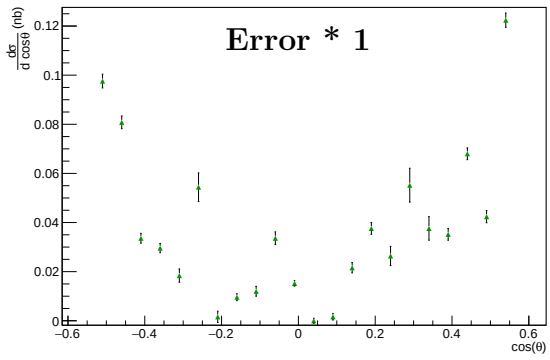

(c) $p_{\text{beam}} = 10$ GeV/c

▲ $\text{CS}_{\text{signal propagated}}$ ▲ CS_{E760}

Figure 6.46: Expected differential cross sections ($d\sigma/d\Omega$) with propagated statistical uncertainties for various beam momenta. For $p_{\text{beam}} = 5$ GeV/c, the extracted cross section is compared with E760 data. At 10 GeV/c, although statistical errors are larger, the cross section remains reliably measurable.

the statistical limitations at higher energies—the extracted differential cross section remains well measurable. The structure of the distribution remains visible, with distinguishable angular features, indicating cross section can be measured even at higher beam energies despite the larger uncertainties.

6.9 Conclusion and Discussion

This chapter focused on the feasibility of measuring the $\bar{p}p \to \pi^0\gamma$ channel at $\overline{\text{P}}$ANDA. The signal process, characterized by a final state with one neutral pion and one photon, was studied in the presence of significant background-namely the $\bar{p}p \to \pi^0\pi^0$ final state. This background process can mimic the signal topology and present a major challenge for clean signal extraction.

A complete Monte Carlo simulation chain was used, including event generation, detector simulation using the $\overline{\text{P}}$ANDA detector model within the Geant4 framework, and full reconstruction. Several strategies were developed to enhance the signal and suppress the background. These included kinematic constraints via a 4C-fit, cuts on the average energy and opening angle between photons, and reconstructed photon selection criteria. The signal optimization was developed for various beam momenta.

Signal-to-background ratios were evaluated for different optimization strategies, and the impact of selection cuts on signal efficiency was thoroughly investigated. Across the studied beam momenta, the signal extraction remained viable, with statistical uncertainties remaining within acceptable limits. Particularly at $p_{\text{beam}} = 5$ GeV/c, the extracted differential cross section $d\sigma/d\Omega$ was able to reproduce the generator input from the E760 experiment reasonably well, showing good consistency and validating both the simulation framework and analysis approach. At higher momenta, such as 10 GeV/c, although statistical uncertainties increased, the signal remained measurable with reasonable precision.

Overall, the results demonstrate that the $\bar{p}p \to \pi^0\gamma$ process is measurable at $\overline{\text{P}}$ANDA with reasonable accuracy, especially with an integrated luminosity of 2 fb^{-1}. The developed analysis techniques—such as background suppression using topological and kinematic variables—are robust and scalable to other rare electromagnetic processes.

7 | The $\overline{p}p \to \pi^0\pi^0$ Reaction

In this chapter, a feasibility study of the $\overline{\mathrm{p}}\mathrm{p} \to \pi^0\pi^0$ reaction at different beam momenta of $p_{\mathrm{beam}} = 2.5$, 5, 10 and 15 GeV/c is presented, with the objective of further understanding the $\overline{\mathrm{p}}\mathrm{p} \to \pi^0\pi^0$ reaction as a background channel to the reaction channel $\overline{\mathrm{p}}\mathrm{p} \to \pi^0\gamma$. The simulated data samples are presented in Section 7.1 and in Section 7.2, the event reconstruction and selection procedures are described. The effect of the kinematic fit and pion mass cuts on the missing energy distributions is presented in Section 7.3.1, and their impact on the signal-to-background ratio is discussed in Section 7.3.2.

7.1 Data Generation

The initial phase of the analysis involves simulating the signal channel and the relevant background channels, which are subsequently propagated through the complete PandaRoot simulation and analysis chain. This section provides a description of the simulated data samples.

All simulations for the present work were performed with the PandaRoot Software package with the recommended versions for analysis:

- FairSoft: apr22
- FairRoot: v18.6.8
- PANDARoot: sept22 (dev-version)
- Geant4 for particle propagation

The signal and background data samples in this study were generated using the EvtGen generator. Furthermore, as the experimental data and theoretical predictions are absent, a Phase Space(PHSP) model is chosen. The PHSP model ensures that the final-state particles are underlying the same detector acceptance by generating an isotropic angular distribution. Table 7.1 provides an overview of the number of simulated signal events and the various dedicated background channels.

7.1.1 Signal

The signal reaction is $\overline{\mathrm{p}}\mathrm{p} \to \pi^0\pi^0$, where π^0 subsequently decays into a pair $\gamma\gamma$. A total of 1 million (10^6) events were simulated for each of the four incident beam momenta: $p_{\mathrm{beam}} = 2.5, 5, 10$, and $15\,\mathrm{GeV/c}$. These beam momenta correspond to center-of-mass energy squared values of $s = 2.6, 3.36, 4.5$, and $5.5\,\mathrm{GeV}^2$, respectively. The signal channel $\overline{\mathrm{p}}\mathrm{p} \to \pi^0\pi^0$ is simulated using EvtGen with the decay file shown in Figure 7.1.

```
Decay pbarpSystem
1.0 pi0 pi0 PHSP;
Enddecay

Decay pi0
1.0 gamma gamma PHSP;
Enddecay

End
```

Figure 7.1: Decay file used in the simulation of $\overline{\mathrm{p}}\mathrm{p} \to \pi^0\pi^0$.

7.1.2 Background

The crucial background processes for this study are the reactions $\overline{\mathrm{p}}\mathrm{p} \to \pi^0\pi^0\pi^0$ and $\overline{\mathrm{p}}\mathrm{p} \to \pi^0\pi^0\gamma$. To simulate these processes, a total of 10^6 events were generated for each of the four incident antiproton beam momenta: $p_{\mathrm{beam}} = 2.5$, 5, 10 and $15\,\mathrm{GeV/c}$. These beam momenta correspond to center-of-mass energy squared values of $s = 2.6$, 3.36, 4.5 and $5.5\,\mathrm{GeV}^2$, respectively. The event generation was performed with a flat phase-space distribution to ensure uniform sampling of the kinematic variables. Furthermore, the events were constrained within the angular range $|\cos\theta| \leq 1.0$, ensuring coverage of the full physical region. These simulations provide an essential reference for understanding the background contributions in the analysis. The background processes are simulated using the decay files shown in Figure 7.2 and 7.3.

```
Decay pbarpSystem
1.0 pi0 pi0 pi0 PHSP;
Enddecay

Decay pi0
1.0 gamma gamma PHSP;
Enddecay

End
```

Figure 7.2: Decay file used in the simulation of $\overline{\mathrm{p}}\mathrm{p} \to \pi^0\pi^0\pi^0$.

```
Decay pbarpSystem
1.0 pi0 pi0 gamma PHSP;
Enddecay

Decay pi0
1.0 gamma gamma PHSP;
Enddecay

End
```

Figure 7.3: Decay file used in the simulation of $\overline{\mathrm{p}}\mathrm{p} \to \pi^0\pi^0\gamma$.

	Signal	**Background I**	**Background II**
Channel	$\bar{p}p \to \pi^0\pi^0$	$\bar{p}p \to \pi^0\pi^0\pi^0$	$\bar{p}p \to \pi^0\pi^0\gamma$
No. of events	1,000,000	1,000,000	1,000,000

Table 7.1: Generated events for the signal and background channels.

7.2 Event Reconstruction and Event Selection

The simulation employed the default geometry, which models all detectors and simulates their responses according to the current capabilities of the software. During event reconstruction, all reconstructed neutral particles are considered under the pion mass hypothesis. No particle identification (PID) cuts are applied during this reconstruction stage.

7.2.1 Data Pre-Selection

All the data sample undergoes the pre-selection process with the goal of selecting candidate for exclusive $\overline{p}p \to \pi^0\pi^0$ events. Each event has to satisfy the following pre-selection criteria:

Reconstructing the $\overline{p}p$ System:

- Calorimeter clusters each with threshold > 30 MeV are accepted and stored for further analysis.
- For each event, all possible $\gamma\gamma$ combinations are combined to form π^0 candidates.
- Three π^0 are combined to form the initial $\overline{p}p$ system.

Subsequent section provide a detailed explanation of the pre-selection criteria.

7.2.1.1 Reconstruction of the $\overline{\mathrm{p}}\mathrm{p}$ system and Combinatorics

The reconstruction procedure begins by selecting all photons with energy greater than 30 MeV. Photons that do not satisfy this condition are removed. This energy cut helps reduce combinatorics and suppresses low-energy clusters arising from electronic noise and radiative photons. Three π^0 are subsequently combined to form the initial $\overline{p}p$ system.

7.2.2 Final Data Selection

After subjecting exclusive candidate events to the initial pre-selection, additional criteria are applied to enhance background suppression. The array of selection criteria is as follows:

- Each $\gamma\gamma$ pair must have an invariant mass in the range $100 < M(\pi^0) < 170$ MeV/c^2 to be identified as a π^0 candidate.

- 4C kinematic fit is applied and events with confidence level less than 10 % are rejected.

7.3 Analysis

In this section, the analysis of the simulated data is presented. The goal is to achieve optimal suppression of the background while maximizing the signal efficiency and optimizing the signal-to-background ratio. Due to practical computational limitations, conducting a full-scale simulation of a large enough background dataset within a reasonable time frame is unfeasible. Therefore, a quantity of 1×10^6 events is chosen for each of the background data samples. This quantity suffices for determining the background suppression factor and facilitating background subtraction. The selection strategy—previously outlined in the Section 7.2—was applied consistently across all beam momenta. The analysis at beam momenta of 2.5, 5, and 10 GeV/c is described in detail in the following subsections.

7.3.1 Effect of Kinematic Fit and Pion Mass Cuts on Missing Energy Distributions

Figure 7.4 presents the missing energy distribution at a beam momentum of $p_{\text{beam}} = 5\,\text{GeV}/c$, shown on a logarithmic scale to illustrate the full range of signal and background contributions. The signal channel $\bar{p}p \to \pi^0\pi^0$ is shown in dark blue and the primary background channels, $\pi^0\pi^0\pi^0$ and $\pi^0\pi^0\gamma$ are shown in light green and red, respectively. The application of a kinematic fit (blue, dark green, and magenta curves for the respective processes) effectively suppresses the background, particularly in the low missing energy region where signal events dominate. A further cut on the reconstructed pion mass leads to an even more pronounced reduction in the background, with the background curves (dark green and magenta) dropping by more than an order of magnitude. This sequential application of selection criteria—kinematic fit followed by pion mass constraint—demonstrates a clear strategy to produce a cleaner $\pi^0\pi^0$ signal and eliminate unwanted contributions from background processes.

The effectiveness of this background rejection strategy is further illustrated in Figure 7.5, which shows the missing energy distributions for the same signal and background channels at three different beam momenta. Without any selection, there is significant overlap among these channels, complicating signal extraction. Applying the kinematic fit introduces partial background suppression, although remnants of the $\pi^0\pi^0\pi^0$ and $\pi^0\pi^0\gamma$ backgrounds persist. The inclusion of the pion mass cut leads to a marked reduction in

background across all beam energies, confirming the robustness of the method. Thus, the applied selection criteria significantly enhance the purity of the $\pi^0\pi^0$ signal.

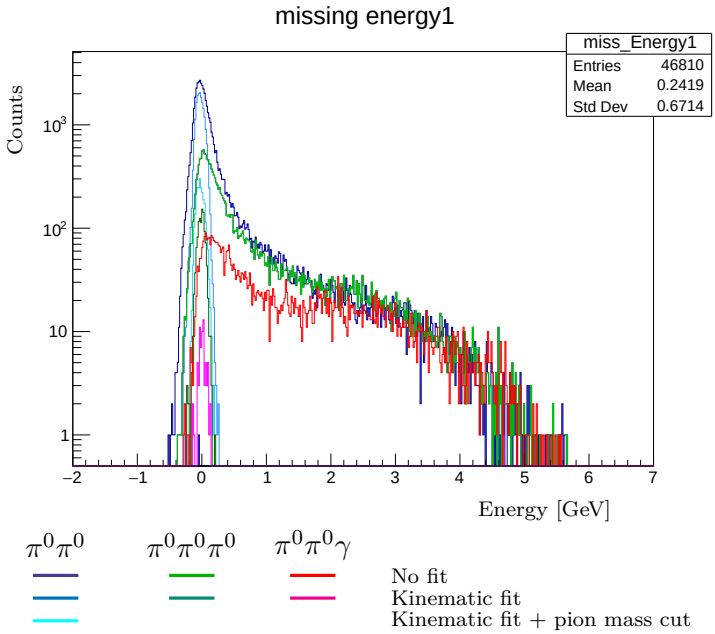

Figure 7.4: Missing energy distributions at $p_{\text{beam}} = 5$ GeV/c for the signal channel and background channels. Distributions are shown after sequential application of selection criteria: no fit, kinematic fit, and kinematic fit with an additional π^0 mass window cut.

7.3.2 Impact of the Kinematic and Mass Cuts on Signal-to-Background Ratio

The signal-to-background ratios for the two dominant background channels, $\pi^0\pi^0\pi^0$ and $\pi^0\pi^0\gamma$, are shown in Figures 7.6 and 7.7, respectively. These plots represent the ratio of reconstructed events after applying the full set of selection criteria, evaluated at three beam momenta: $p_{\text{beam}} = 2.5$, 5, and 10 GeV/c. For the $\pi^0\pi^0\pi^0$ background, the signal to background ratio is highest at 2.5 GeV/c, as indicated by the blue markers in Figs. 7.6 and 7.7, and progressively decreases with increasing beam energy. This pattern indicates that the combinatorial background from the three neutral pions becomes more prominent at higher energies, thereby reducing the overall effectiveness of the selection cuts. A similar trend is observed for the $\pi^0\pi^0\gamma$ background, although the absolute signal to background values are generally higher than those for the $\pi^0\pi^0\pi^0$ background, indicating better suppression. The log-scale panels clearly emphasize that even though the background is effectively suppressed across all energies, the purity of the signal deteriorates somewhat with increasing beam momentum.

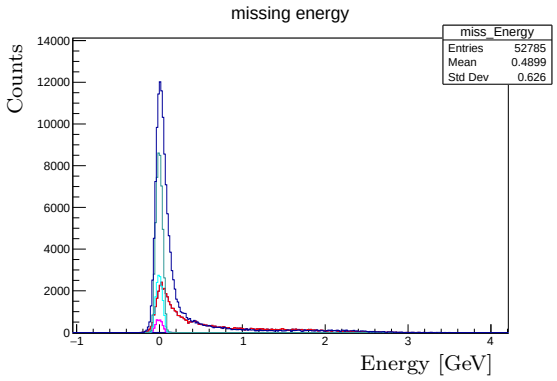

(a) $p_{\text{beam}} = 2.5$ GeV/c

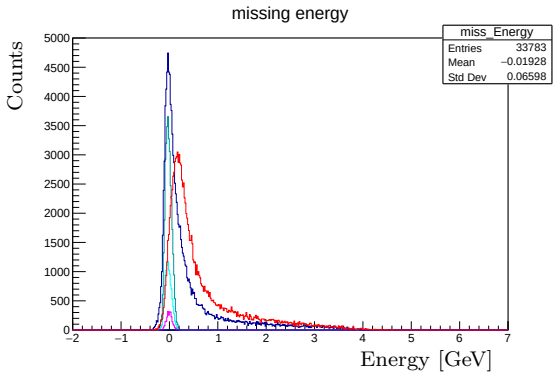

(b) $p_{\text{beam}} = 5$ GeV/c

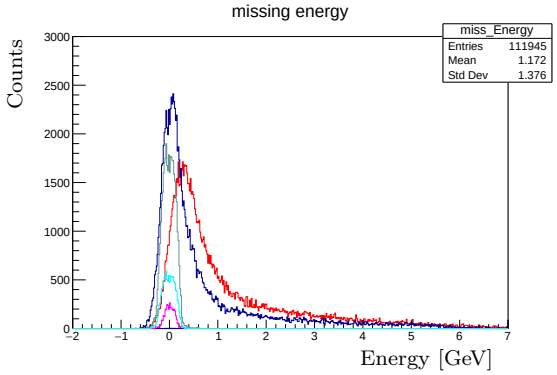

(c) $p_{\text{beam}} = 10$ GeV/c

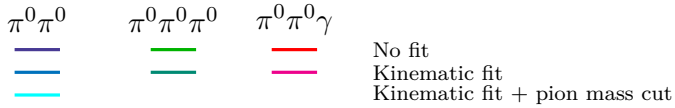

Figure 7.5: Missing energy distribution for the signal and backgrounds shown with different selection steps: at various beam momenta: 2.5 GeV/c (top row), 5 GeV/c (middle row), and 10 GeV/c (bottom row). The application of kinematic fit and pion mass cut significantly suppresses the background.

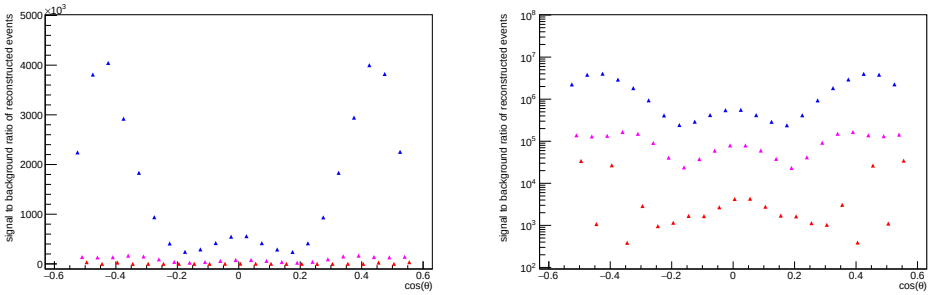

▲ $p_{\text{beam}} = 2.5$ GeV/c ▲ $p_{\text{beam}} = 5$ GeV/c ▲ $p_{\text{beam}} = 10$ GeV/c

Figure 7.6: Signal to backgrond ratio of reconstructed events for the background $\pi^0\pi^0\pi^0$ at different beam momenta. Right panel shows the ratio on log scale.

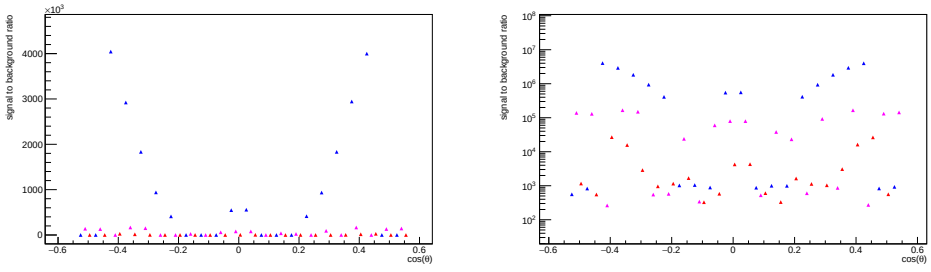

▲ $p_{\text{beam}} = 2.5$ GeV/c ▲ $p_{\text{beam}} = 5$ GeV/c ▲ $p_{\text{beam}} = 10$ GeV/c

Figure 7.7: Signal to background ratio of reconstructed events for the background $\pi^0\pi^0\gamma$ at different beam momenta. Right panel shows the ratio on log scale.

7.4 Conclusion and Discussion

In conclusion, the sequential application of a kinematic fit and a reconstructed pion mass cut has proven highly effective in enhancing the signal purity for the channel $\bar{p}p \to \pi^0\pi^0$. The missing energy distributions demonstrate a clear suppression of the dominant backgrounds $\pi^0\pi^0\pi^0$ and $\pi^0\pi^0\gamma$, particularly after the pion mass constraint is applied. This observation is further supported by the signal-to-background ratio plots, which confirm that the $\pi^0\pi^0$ final state can be reliably reconstructed and distinguished from background contributions across a wide energy range. Importantly, since the $\bar{p}p \to \pi^0\pi^0$ channel itself can be efficiently measured and suppressed when needed, this enhances our ability to reduce its contribution as a background in other analyses — most notably, in the measurement of the $\bar{p}p \to \pi^0\gamma$ signal channel. A detailed understanding of the $\pi^0\pi^0$ channel's behavior under different selection criteria thus plays a critical role in improving the overall background rejection and purity in channels where it appears as a contaminant.

8 | The $\overline{p}p \rightarrow \gamma\gamma$ Reaction

In this chapter, a feasibility study of the $\overline{\mathrm{p}}\mathrm{p} \rightarrow \gamma\gamma$ reaction is presented for various beam momenta: p_{beam} = 2.5, 5, 10, and 15 GeV/c. The simulated data samples used for this study are described in Section 8.1. Event reconstruction and selection procedures are discussed in Section 8.2, followed by a detailed explanation of the analysis procedure in Section 8.3. Various background suppression techniques are discussed in Section 8.4. Finally, the expected cross-sections with statistical uncertainties, after background suppression, are presented in Section 8.5 for integrated luminosities of 2 fb^{-1} and 0.1 fb^{-1}.

8.1 Data Generation

The initial phase of the analysis involves simulating the signal channel and the relevant background channels, which are subsequently propagated through the complete PandaRoot simulation and analysis chain. This section provides a description of the simulated data samples.

All simulations for the present work were performed with the PandaRoot Software package with the recommended versions for analysis:

- FairSoft: apr22
- FairRoot: v18.6.8
- PANDARoot: sept22 (dev-version)
- Geant4 for particle propagation

The signal and background data samples in this study were generated using the EvtGen generator. Furthermore, as the experimental data and theoretical predictions are absent, a Phase Space(PHSP) model is chosen. The PHSP model ensures that the final-state particles are underlying the same detector acceptance by generating an isotropic angular distribution. Table 8.1 provides an overview of the number of simulated signal events and the various dedicated background channels.

8.1.1 Signal

The signal reaction is $\overline{\mathrm{p}}\mathrm{p} \to \gamma\gamma$. A total of 1 million ($10^6$) events were simulated for each of the four incident beam momenta: $p_{\mathrm{beam}} = 2.5, 5, 10$, and $15\,\mathrm{GeV/c}$. These correspond to center-of-mass squared energies of $s = 2.6, 3.36, 4.5$, and $5.5\,\mathrm{GeV}^2$, respectively. The $\gamma\gamma$ pair is simulated using EvtGen with the decay file shown in Figure 8.1.

```
Decay pbarpSystem
1.0 gamma gamma PHSP;
Enddecay

End
```

Figure 8.1: Decay file used in the simulation of $\overline{\mathrm{p}}\mathrm{p} \to \gamma\gamma$.

8.1.2 Background

The background processes for this study are the reactions $\overline{\mathrm{p}}\mathrm{p} \to \pi^0\gamma$ and $\overline{\mathrm{p}}\mathrm{p} \to \pi^0\pi^0$. To simulate this process, a total of 10^6 events were generated for each of the four incident antiproton beam momenta: $p_{\mathrm{beam}} = 2.5$, 5, 10 and $15\,\mathrm{GeV/c}$. These beam momenta correspond to center-of-mass energy squared values of $s = 2.6$, 3.36, 4.5 and $5.5\,\mathrm{GeV}^2$, respectively. The event generation was performed with a flat phase-space distribution to ensure uniform sampling of the kinematic variables. Furthermore, the events were constrained within the angular range $|\cos\theta| \leq 1.0$, ensuring coverage of the full physical region. This simulation provides an essential reference for understanding the background contributions in the analysis. The $\pi^0\gamma$ and $\pi^0\pi^0$ pairs are simulated with the decay files shown in Figure 8.2 and Figure 8.3 respectively.

```
Decay pbarpSystem
1.0 pi0 gamma PHSP;
Enddecay

Decay pi0
1.0 gamma gamma PHSP;
Enddecay

End
```

Figure 8.2: Decay file used in the simulation of the background $\overline{\mathrm{p}}\mathrm{p} \to \pi^0\gamma$.

```
Decay pbarpSystem
1.0 pi0 pi0 PHSP;
Enddecay

Decay pi0
1.0 gamma gamma PHSP;
Enddecay

End
```

Figure 8.3: Decay file used in the simulation of the background $\overline{\mathrm{p}}\mathrm{p} \to \pi^0\pi^0$.

	Signal	**Background I**	**Background II**
Channel	$\bar{p}p \to \gamma\gamma$	$\bar{p}p \to \pi^0\gamma$	$\bar{p}p \to \pi^0\pi^0$
No. of events	1,000,000	1,000,000	1,000,000

Table 8.1: Generated events for the signal and background channels.

8.2 Event Reconstruction and Event Selection

The simulation employed the default geometry, which models all detectors and simulates their responses according to the current capabilities of the software. During event reconstruction, all reconstructed neutral particles are considered under the pion mass hypothesis. No particle identification (PID) cuts are applied during this reconstruction stage.

8.2.1 Data Pre-Selection

All the data sample undergo the pre-selection process with the goal of selecting candidates for exclusive $\overline{p}p \to \gamma\gamma$ events. Certain cuts were fixed across all the s values, whereas others were adjusted to more appropriately align with the detector response at various energies.

Reconstructing the $\overline{p}p$ System:

- Calorimeter clusters each with energy threshold > 20 MeV are accepted and stored for further analysis.
- All possible $\gamma\gamma$ pairs are combined to form the initial $\overline{p}p$ system.
- 4C kinematic fit is applied and the effect of different probability cuts (rejection

power) is investigated.

8.2.1.1 Reconstructing the $\overline{\mathrm{p}}\mathrm{p}$ system

The analyses starts with selecting all photons having energy > 20 MeV. Photons that do not satisfy this condition are removed. This energy cut on the calorimeter clusters helps to reduce the combinatorics as well as reject wrong clusters due to electronic noise and radiative photons. Subsequently, all $\gamma\gamma$ pairs are then combined to construct the $\overline{p}p$ system. A kinematic fit is performed, wherein energy and momentum are constrained to adhere to the characteristics of the initial system.

8.2.2 Final Data Selection

After subjecting exclusive candidate events to the initial pre-selection, additional criteria are applied to enhance background suppression. The array of selection criteria is as follows:

- Exactly two clusters required to have energies greater than 100MeV
- For cluster pairs, no invariant mass should fall between 80 and 200 GeV/c^2, to avoid selecting events with unwanted π^0.

8.3 Analysis

In this section, the analysis of the simulated data is presented. The goal is to achieve optimal suppression of the background while maximizing the signal efficiency and optimizing the signal-to-background ratio. Due to practical computational limitations, conducting a full-scale simulation of a large enough background dataset within a reasonable time frame is unfeasible. Therefore, a quantity of 1×10^6 events is chosen for each of the background data samples. This quantity suffices for determining the background suppression factor and facilitating background subtraction. The selection strategy—previously outlined in the Section 8.2—was applied consistently across all beam momenta. The analysis at p_{beam} = 2.5, 5, 10 and 15 GeV/c is described in detail in the following subsections.

8.3.1 Particle distributions

Figure 8.4 illustrates the comparison between the generated (red) and reconstructed (blue) distributions of photons for various incident antiproton beam momenta. Each row corresponds to a specific beam momentum: 2.5 GeV/c (top row), 5 GeV/c (second row),

10 GeV/c (third row), and 15 GeV/c (bottom row). The three columns, respectively, show the distributions of momentum, polar angle (θ), and azimuthal angle (ϕ). The generated distributions reflect the phase space (PHSP) kinematics of the $\bar{p}p \to \gamma\gamma$ process, while the reconstructed distributions are obtained after applying full detector simulation and event reconstruction. Notably, the reconstructed momentum and angular distributions deviate from the generated ones due to the influence of detector acceptance and resolution effects. The dips and discontinuities observed in the reconstructed θ distributions arise from the geometric segmentation and coverage gaps of the electromagnetic calorimeter (EMC), especially in the forward and backward regions. The flatness of the generated ϕ distribution, as expected from isotropic emission in azimuth, is not preserved in the reconstructed data, indicating non-uniform reconstruction efficiency across ϕ. These plots highlight the importance of accounting for detector effects when interpreting measured angular distributions.

8.3.2 Signal Efficiency

After obtaining a suitable event sample, it is necessary to apply acceptance corrections to account for both the detector's acceptance and the analysis process.

In Figure 8.5, the first column shows the generated distribution as a function of $\cos\theta$ which is a flat distribution. The reconstructed distribution of $\gamma\gamma$ as a function of $\cos\theta$ is shown in the second column. The reconstructed is shown in PHSP distribution and it exhibits discontinuities attributed to the transitional zones between distinct segments of the EMC. The generated (MC) and reconstructed distributions are scaled according to the weights obtained from fits to the E760 data (see Figure 6.7), to give more realistic plots. The weighted distributions are shown in the third and fourth column respectively. Each row in Figure 8.5 corresponds to a different antiproton beam momentum: $p_{\text{beam}} = 2.5$ GeV/c (top row), 5 GeV/c (second row), 10 GeV/c (third row), and 15 GeV/c (bottom row).

In order to perform the acceptance corrections, we first extract signal efficiency of the channel $\bar{p}p \to \gamma\gamma$. The signal efficiency is derived from events generated based on PHSP for individual $\cos\theta$ bins. The efficiency, depicted as a function of the angular distribution, $\cos\theta$, is computed as the ratio of number of reconstructed events divided by Monte Carlo generated events, denoted by N_{rec} and N_{MC} respectively.

$$Acceptance = \frac{N_{rec}}{N_{MC}}$$

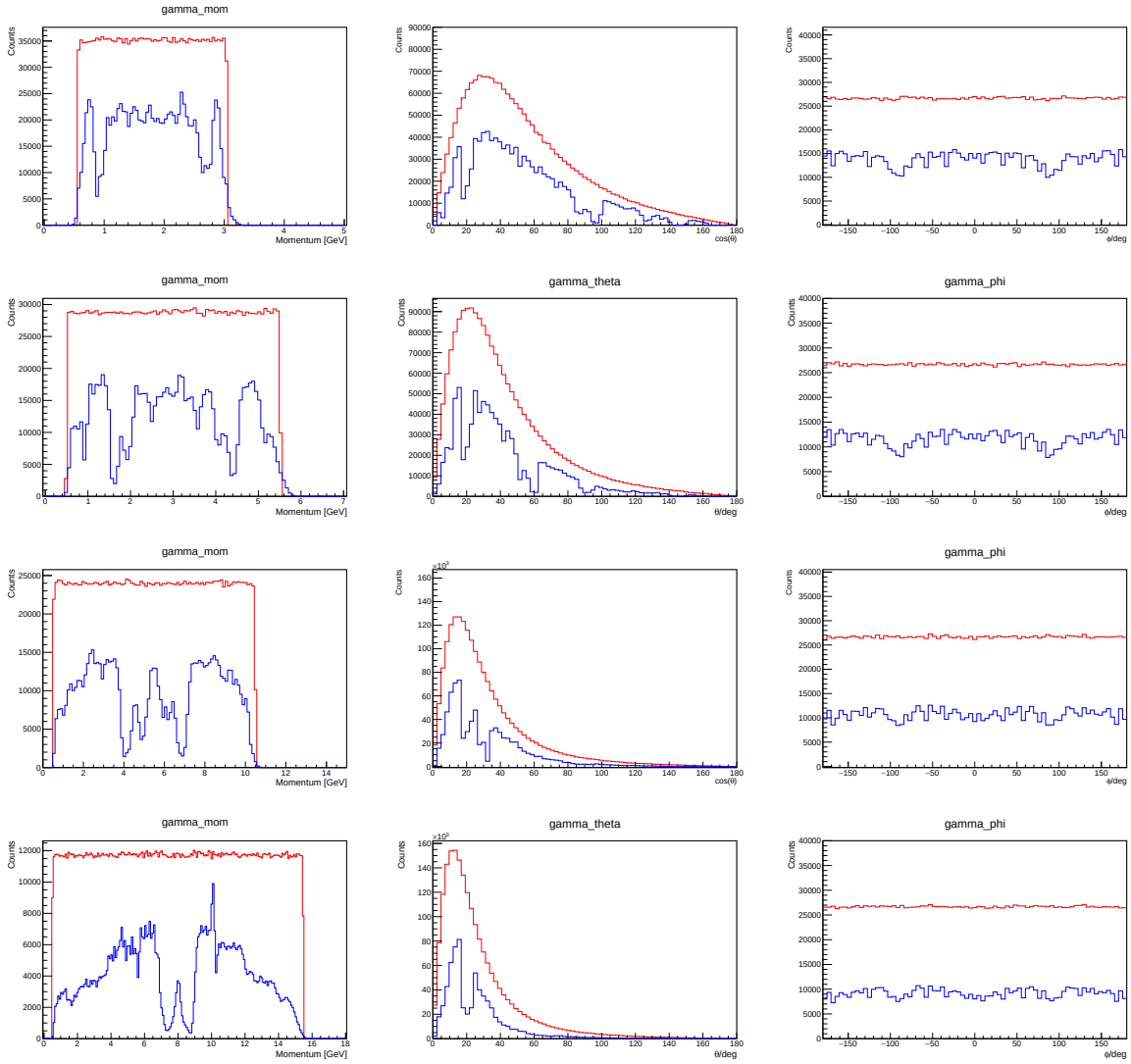

Figure 8.4: Plots of momentum, theta and phi distributions of generated (red) and reconstructed (blue) γ candidates. The comparison illustrates how reconstruction effects impact the observed kinematic properties at different beam momenta. Each row corresponds to a different $\bar{p}$ incident momentum: $p_{\text{beam}} = 2.5\,\text{GeV}/c$ (top row), $p_{\text{beam}} = 5\,\text{GeV}/c$ (second row), $p_{\text{beam}} = 10\,\text{GeV}/c$ (third row), and $p_{\text{beam}} = 15\,\text{GeV}/c$ (bottom row).

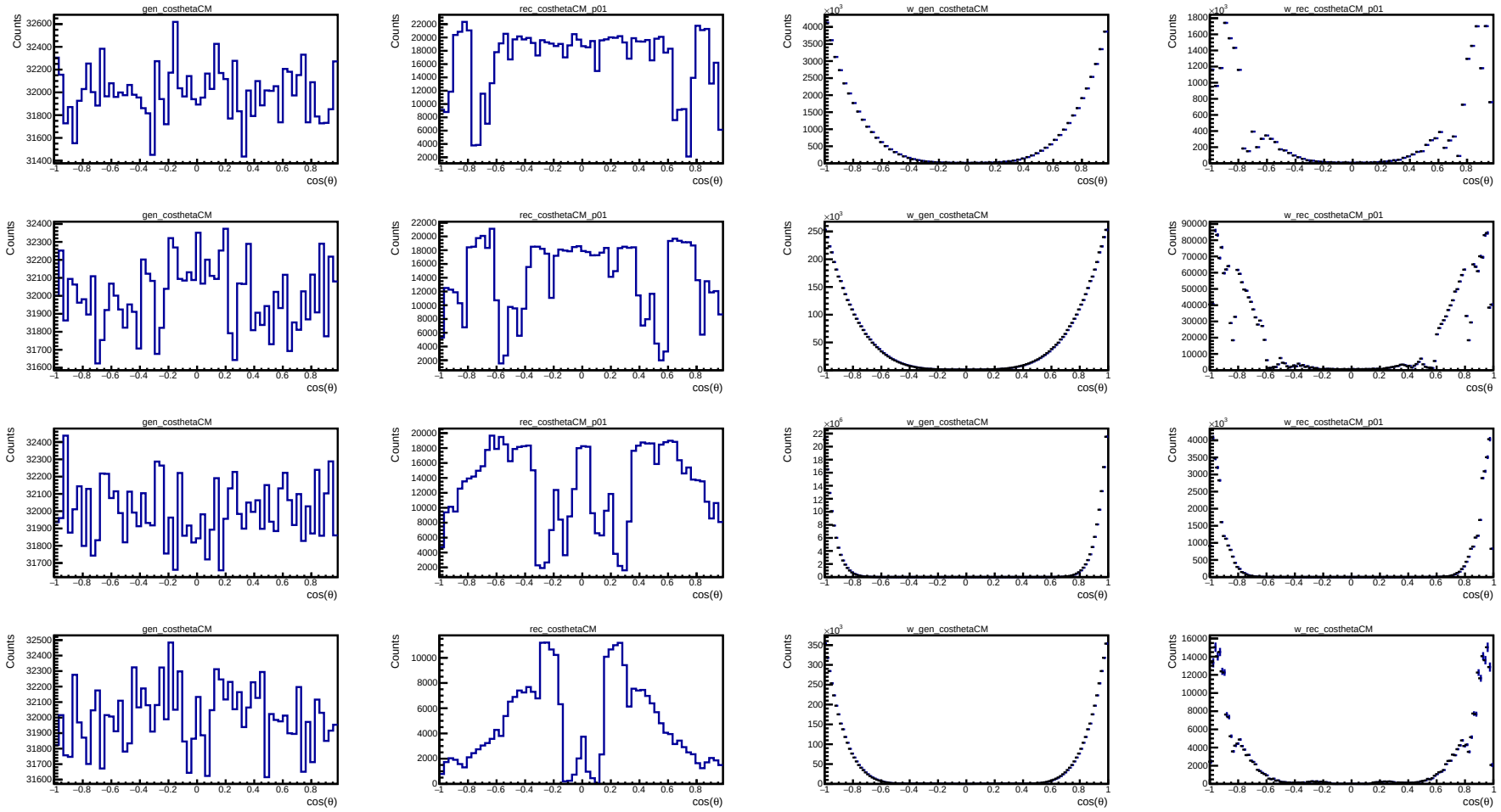

Figure 8.5: Plots of weighted and unweighted distributions of reconstructed and generated $\gamma\gamma$. Each row corresponds to a different $\bar{p}$ incident momentum: $p_{\text{beam}} = 2.5\,\text{GeV}/c$ (top row), $p_{\text{beam}} = 5\,\text{GeV}/c$ (second row), $p_{\text{beam}} = 10\,\text{GeV}/c$ (third row), and $p_{\text{beam}} = 15\,\text{GeV}/c$ (bottom row).

Figure 8.6 shows acceptance as a function of $\cos(\theta)$ for four different antiproton beam momenta: $p_{\text{beam}} = 2.5$, 5, 10, and 15 GeV/c, for the exclusive reaction channel $\bar{p}p \to \gamma\gamma$. The acceptance is calculated as the ratio of the number of reconstructed events to the number of generated events in each $\cos(\theta)$ bin and represents the detector's efficiency in detecting both photons from the final state. The acceptance is inherently influenced by the geometric coverage, granularity, and material composition of the $\overline{\text{P}}$ANDA electromagnetic calorimeter (EMC), which is primarily responsible for photon detection.

At lower beam momentum (2.5 GeV/c), the acceptance is relatively high and stable over a broad central angular range, with a decline near the forward and backward regions ($\cos(\theta) \approx \pm 1$) due to reduced coverage and increased photon losses. As the beam momentum increases (5–15 GeV/c), the acceptance patterns become increasingly complex, showing pronounced dips and fluctuations throughout the angular range. These dips arise from multiple factors, including regions of reduced calorimeter efficiency, photon conversion in the detector material before reaching the EMC, and reconstruction challenges due to overlapping showers at high energies. Notably, the dips near $\cos(\theta) = 0$ are associated with the transition region between the barrel and forward endcap of the EMC, where acceptance is reduced due to structural gaps or limited detector resolution. The evolving shape of the acceptance with increasing beam momentum reflects the broader photon angular distribution and more forward-peaked kinematics at higher energies. Understanding and correcting for these acceptance effects is essential for reliable extraction of physical observables, such as angular distributions, in this two-photon channel.

8.3.3 Acceptance Corrections

Once a satisfactory event sample is obtained, it must be corrected for the effects of finite detector acceptance and reconstruction efficiency. This is particularly important for angular distributions, as the geometrical coverage and response of the detector can vary significantly with the angle of the outgoing particles. Acceptance correction is applied to the unweighted distributions to recover the true physical angular dependence of the process.

Figure 8.7 shows the acceptance-corrected angular distributions of π^0 for three different beam momenta. The reconstructed $\cos\theta$ distributions, after applying the acceptance correction, are plotted in blue, whereas the original generated distributions are shown in red. The plots are presented for beam momenta of $p_{\text{beam}} = 2.5$ GeV/c (top row), 5 GeV/c (middle row), and 10 GeV/c (bottom row). It should be noted that the acceptance correction is applied to the same Monte Carlo (MC) data that was used to derive the acceptance

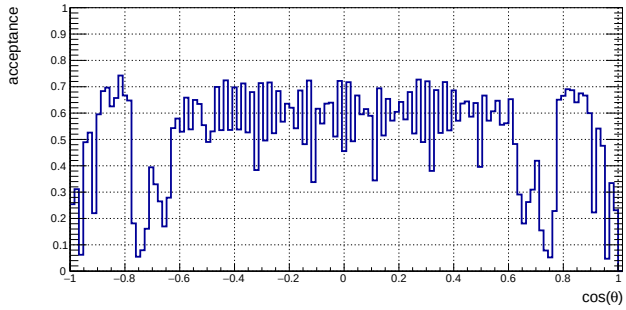

(a) $p_{\text{beam}} = 2.5$ GeV/c

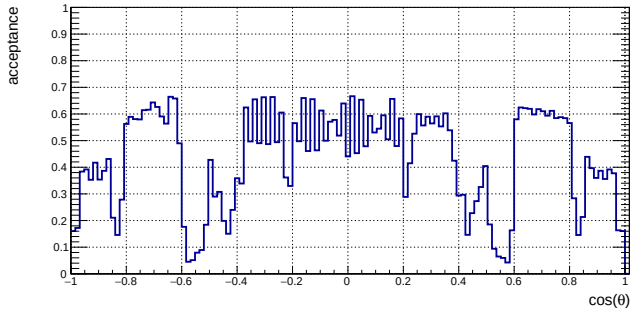

(b) $p_{\text{beam}} = 5$ GeV/c

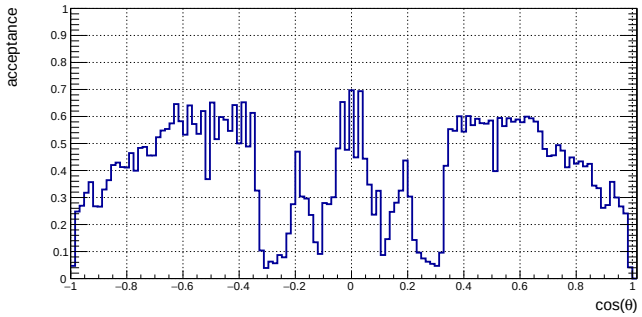

(c) $p_{\text{beam}} = 10$ GeV/c

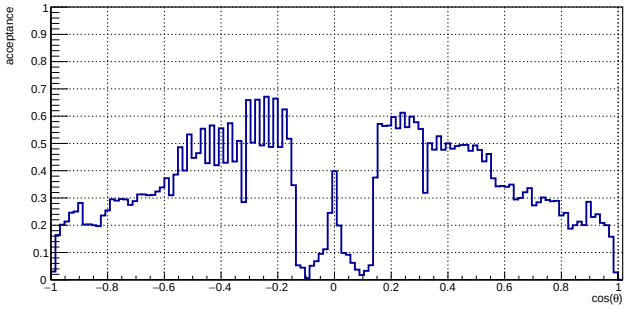

(d) $p_{\text{beam}} = 15$ GeV/c

Figure 8.6: Acceptance as a function of $\cos(\theta)$ for the reaction $\bar{p}p \to \gamma\gamma$ at different beam momenta: (a) 2.5 GeV/c, (b) 5 GeV/c, (c) 10 GeV/c, and (d) 15 GeV/c. The acceptance is defined as the ratio of reconstructed to generated events in each angular bin, and reflects the angular efficiency of the $\overline{\text{P}}$ANDA detector's electromagnetic calorimeter for detecting the two-photon final state.

in the first place. As a result, the corrected (reconstructed) distribution is expected to closely reproduce the original generated distribution. Therefore, in the context of this study, this serves primarily as a consistency check and helps to identify any acceptance holes or regions of reduced detector efficiency.

Notably, even at higher beam energies, where more forward-peaked distributions are expected, the acceptance-corrected reconstructed distributions closely follow the generated ones across the entire angular range. This consistency highlights the effectiveness of the correction procedure and confirms that the reconstruction and analysis chain preserves the underlying physics in the simulation. Since both the generated and reconstructed events originate from the same Monte Carlo simulation, the agreement also serves as an internal validation of the detector model and reconstruction algorithms used in this study.

8.4 Background Suppression and Signal Optimization Methods

This section outlines the strategies employed to suppress background contributions and enhance the purity of the signal in the analysis of the $\bar{p}p \to \gamma\gamma$ channel. Various selection criteria and kinematic cuts were investigated to reduce contamination from competing or misidentified processes, such as photon pairs originating from π^0 decays. To evaluate the effectiveness of such selection techniques, signal-to-background ratios are computed before and after applying each cut. Comparative plots are presented in subsequent sections to illustrate the impact of individual and combined cuts on background rejection and signal efficiency. These optimization steps are essential to ensure a clean signal sample and the reliable extraction of physical observables from the reconstructed data.

8.4.1 Angular and Invariant Mass Cuts on $\bar{p}p$ System

To optimize the signal selection and suppress background events, angular and invariant mass cuts are applied to the reconstructed $\bar{p}p$ system. The following distributions illustrate the motivation and effectiveness of these selection criteria. Figure 8.8 shows two key distributions used in the event selection. Figure 8.8a presents the opening angle distribution (in the center-of-mass frame) for signal (blue) and background (magenta) events. A distinct peak near $\theta \approx 180°$ is observed for the signal, reflecting the expected back-to-back configuration of the $\bar{p}p$ system. Applying a cut of $\theta > 178°$ effectively retains a large portion of the signal while significantly suppressing background contamination. Figure 8.8b displays the four-constraint (4C) kinematic fit probability distribution for the $\bar{p}p$ system.

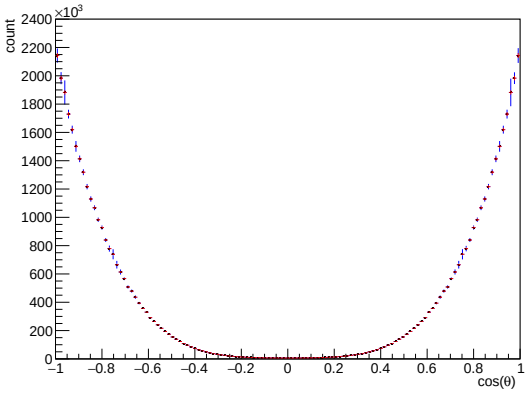

(a) $p_{\text{beam}} = 2.5$ GeV/c

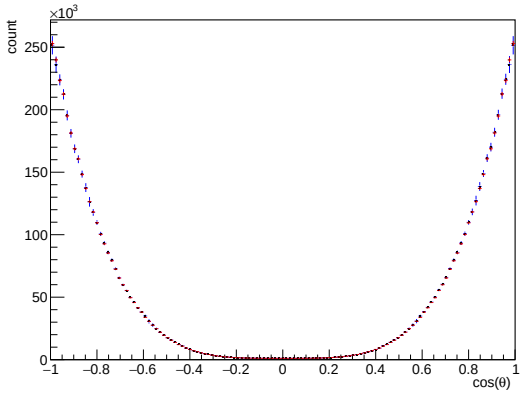

(b) $p_{\text{beam}} = 5$ GeV/c

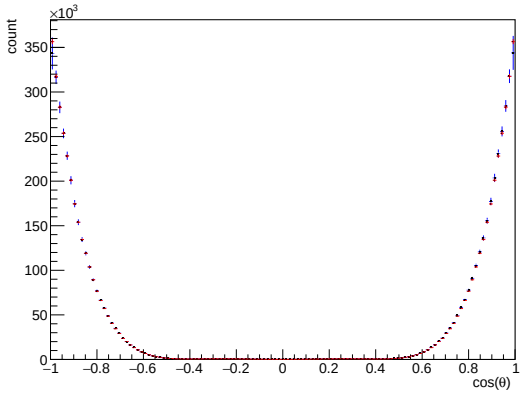

(c) $p_{\text{beam}} = 10$ GeV/c

Figure 8.7: Acceptance corrections of the weighted distribution at different beam momenta. Reconstructed pions with acceptance correction are shown in blue and generated pions are shown in red. Each row correspond to a different incident beam momentum: $p_{beam} = 2.5$ GeV/c (top row), $p_{beam} = 5$ GeV/c (middle row) and $p_{beam} = 10$ GeV/c (bottom row).

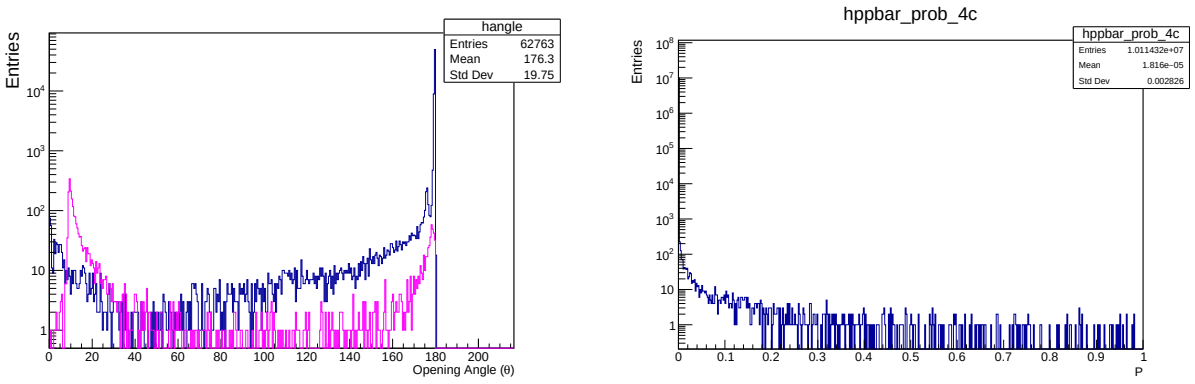

(a) **(b)**

Figure 8.8: (a) Opening angle distribution for signal (blue) and background (magenta) in the center-of-mass frame. (b) Four-constraint fit probability distribution for the $\bar{p}p$ system.

Events with a fit probability $p > 0.01$ are considered well-reconstructed and are selected to further reduce the background.

To evaluate whether the angular and invariant mass cuts, along with the 4C kinematic fit, improve signal efficiency and background suppression, the background-to-signal ratio was determined. Figure 8.9 shows the background-to-signal ratio as a function of $\cos(\theta)$ for the dominant background channels $\bar{p}p \to \pi^0\gamma$ (top panel) and $\bar{p}p \to \pi^0\pi^0$ (bottom panel) at a beam momentum of $p_{\text{beam}} = 2.5$ GeV/c. Two sets of distributions are shown: one before (blue markers) and one after (magenta markers) applying angular and invariant mass cuts. The applied cuts include a restriction on the opening angle in the center of mass frame, $\theta > 178°$, and a $\bar{p}p$ invariant mass window of $\pm 3\sigma$, in addition to a cut on the 4C kinematic fit probability ($P_{\text{KinFit}} > 0.01$). As evident from the plots, the application of these cuts results in negligible improvement in the background-to-signal ratio for both background channels. This observation is consistent with the fact that the 4C kinematic fit enforces energy and momentum conservation, which indirectly constrains angular and invariant mass distributions. As a result, applying additional cuts on these variables has minimal impact beyond what is already achieved by the kinematic fit selection.

8.4.2 Optimization of Kinematic Cuts Inspired by Ref. [1]

The background suppression strategy was further refined by implementing a set of kinematic selection criteria motivated by the work of Armstrong [1], which focused on two-body neutral final states in $\bar{p}p$ annihilations within the energy range $2.911 \leq \sqrt{s} \leq 3.686$ GeV. The applied cuts are designed to enhance the selection purity of signal-like

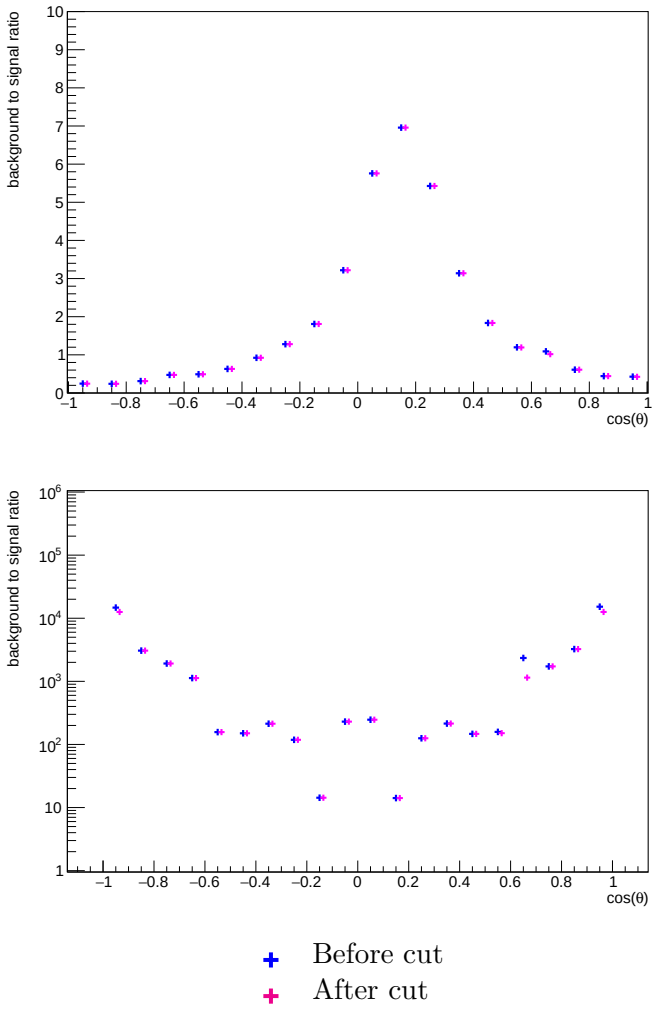

Figure 8.9: Background-to-signal ratio before and after applying background suppression cuts at a beam momentum of $p_{\text{beam}} = 2.5$ GeV/c. The top panel corresponds to the background channel $\bar{p}p \to \pi^0\gamma$, while the bottom panel shows results for $\bar{p}p \to \pi^0\pi^0$.

events and reduce contamination from backgrounds such as those involving low-energy photon clusters or unwanted intermediate states. Specifically, all calorimeter clusters were required to have energies greater than 50 MeV, ensuring that noise and spurious hits were suppressed. In addition, exactly two clusters were required to exceed an energy threshold of 100 MeV, ensuring a clean selection of photon candidates. To eliminate contamination from π^0 decays, any cluster pair with an invariant mass between 80 and 200 MeV/c^2 was rejected. Finally, a 4C kinematic fit was applied, and only events with a confidence level (CL) greater than 10% were retained.

The impact of the above-mentioned background suppression cuts on the background-to-signal ratio is illustrated in Figure 8.10 across different beam momenta: 2.5 GeV/c, 5 GeV/c, and 10 GeV/c. Each row corresponds to a specific beam momentum, with the left panel representing the background-to-signal ratio for the background channel $\bar{p}p \to \pi^0\gamma$ and the right panel showing the same for $\bar{p}p \to \pi^0\pi^0$. For each case, the ratios are plotted before (blue) and after (magenta) applying background suppression cuts. Across all beam momenta and angular ranges, a notable reduction in the background-to-signal ratio is observed after applying the cuts, particularly in regions where the background initially dominates. This demonstrates the effectiveness and robustness of the selection criteria in enhancing the signal purity of the reconstructed $\gamma\gamma$ final state across different beam momenta.

8.4.3 Optimization Using Photon Opening Angle and Energy

Figures 8.11 and 8.12 illustrate the distribution of the opening angle versus energy and opening angle versus momentum for the signal and background processes at a beam momentum of 5 GeV/c.

In Figure 8.11, the panels show the raw distributions before any additional cuts are applied beyond basic event reconstruction. Panels (a) and (b) represent the signal process $\bar{p}p \to \gamma\,\gamma$, showing plot of opening angle versus energy and opening angle versus momentum, respectively. Panels (c) and (d) depict the corresponding distributions for the main background process $\bar{p}p \to \pi^0\pi^0$. As seen in the background panels, events are predominantly clustered in the region of low opening angles and low energies, where signal contamination is minimal.

To suppress this background effectively, a set of cuts was applied, resulting in the distributions shown in Figure 8.12. The applied selection includes: (1) exactly two reconstructed photons ($N_\gamma = 2$), (2) reconstructed $\bar{p}p$ energy greater than 5.6 GeV, and (3) an opening angle cut defined as $\theta_{\text{open}} > 0.219 + \frac{0.424}{E_{\bar{p}p} - 0.740}$. These cuts were designed to eliminate

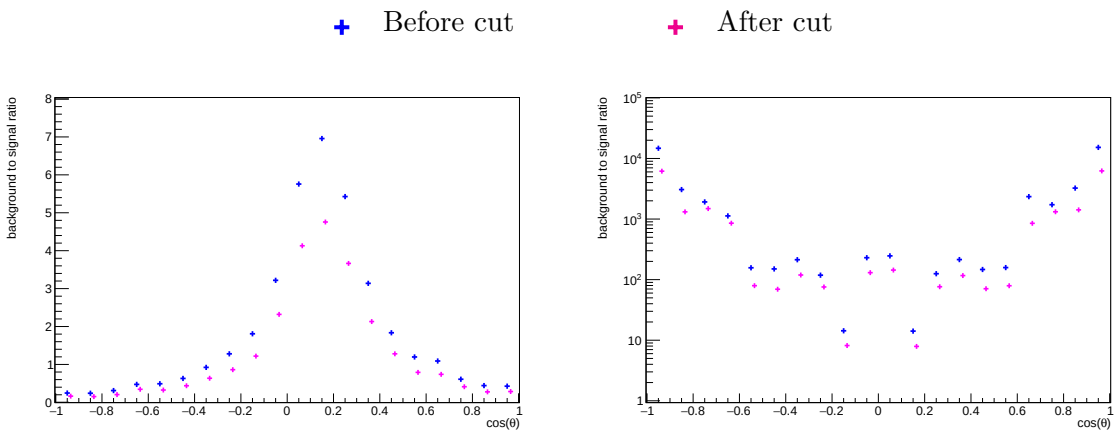

(a) $p_{\text{beam}} = 2.5$ GeV/c

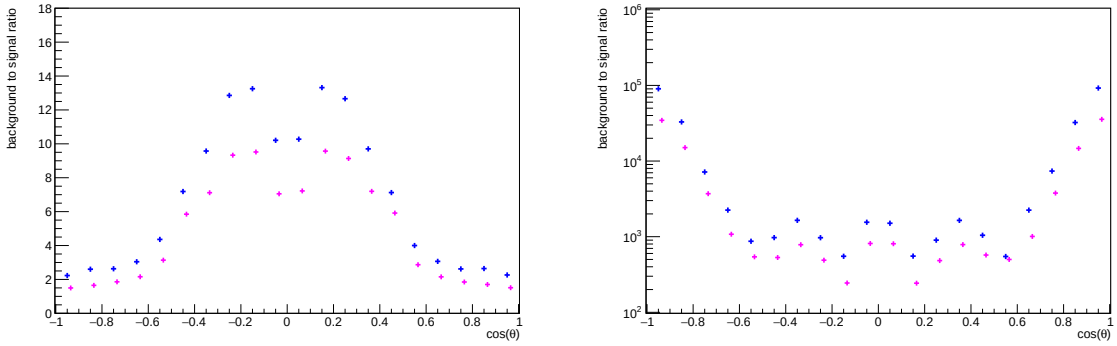

(b) $p_{\text{beam}} = 5$ GeV/c

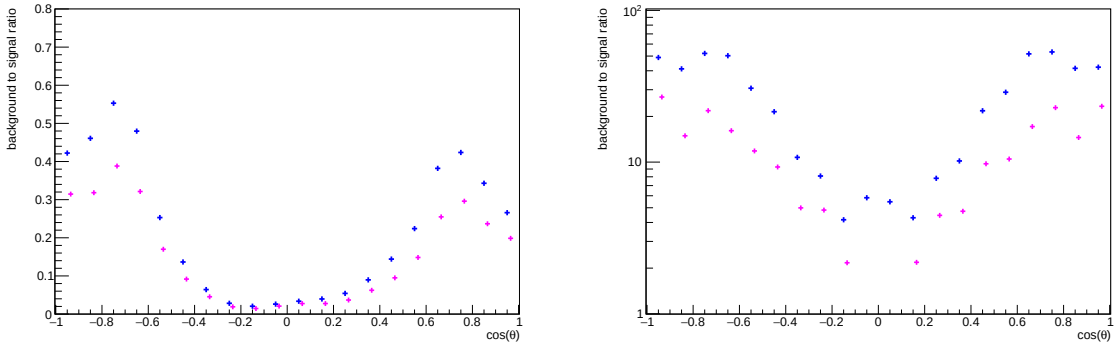

(c) $p_{\text{beam}} = 10$ GeV/c

Figure 8.10: Background-to-signal ratio before (blue) and after (magenta) applying background suppression cuts at various beam momenta. Each row corresponds to a different incident beam momentum: 2.5 GeV/c (top row), 5 GeV/c (middle row), and 10 GeV/c (bottom row). The left panel corresponds to the background-to-signal ratio for the background channel $\bar{p}p \to \pi^0\gamma$, while the right panel shows results for $\bar{p}p \to \pi^0\pi^0$. A reduction in the background relative to the signal is observed after applying the cuts.

background-dense regions, especially those at low energies and narrow opening angles, which are evident in the pre-cut background plots.

Post-selection, the background distribution (right panel of Figure 8.12) shows significant suppression, particularly in the regions of low opening angles and low energies, while the signal distribution (left panel) retains a high concentration of events. The observed reduction in background-dense regions suggests that the applied cuts have the potential to enhance the signal-to-background ratio and improve the purity of the selected signal sample. Given the trends seen in Figures 8.11 and 8.12, the selection strategy appears to be effective in improving event quality for the $\bar{p}p \to \gamma\,\gamma$ channel at $5\,\mathrm{GeV}/c$ beam momentum.

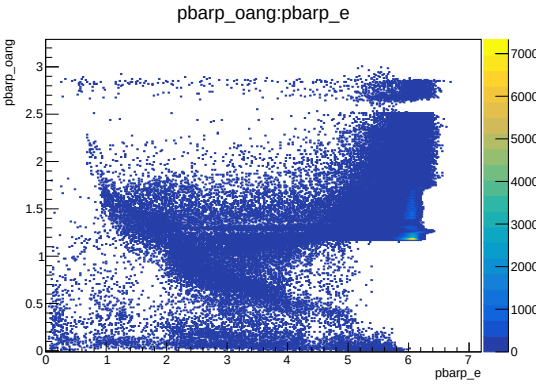

(a) Signal: opening angle vs. energy

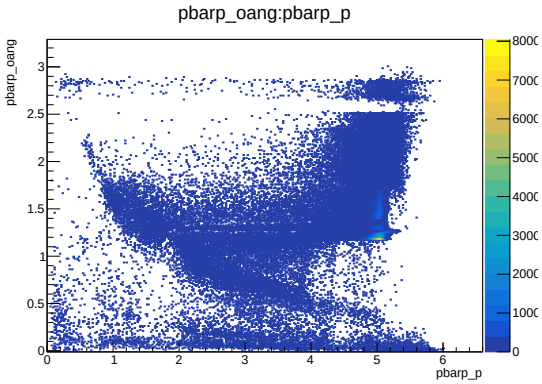

(b) Signal: opening angle vs. momentum

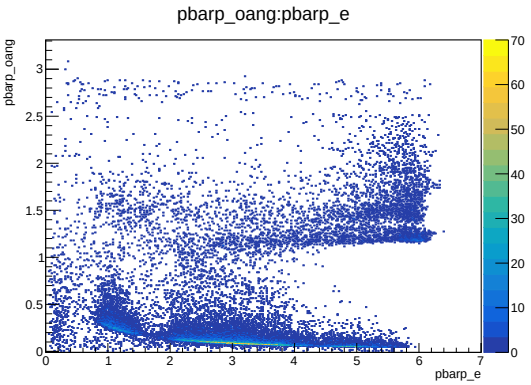

(c) Bkg: opening angle vs. energy

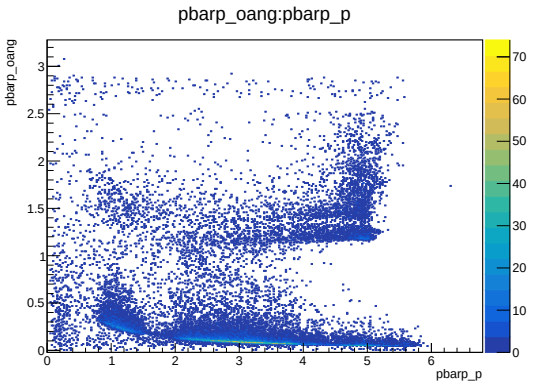

(d) Bkg: opening angle vs. momentum

Figure 8.11: Two-dimensional distributions of opening angle versus energy and momentum at a beam momentum of $5\,\mathrm{GeV}/c$, shown before applying any additional selection cuts. Panels (a) and (b) correspond to the signal process $\bar{p}p \to \gamma\,\gamma$, while panels (c) and (d) correspond to the main background $\bar{p}p \to \pi^0\pi^0$. These plots illustrate the kinematic characteristics of both channels prior to optimization.

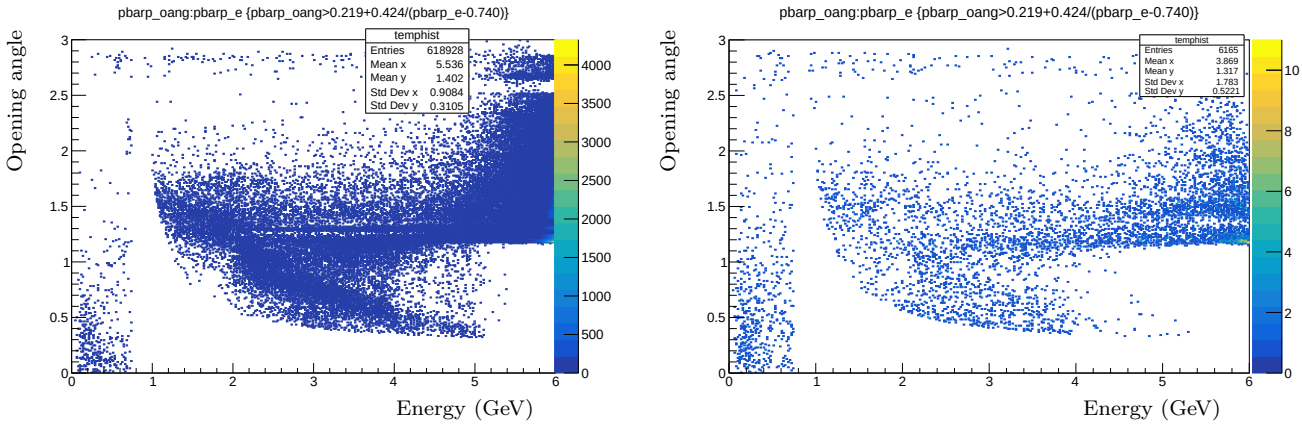

Figure 8.12: Distributions of the opening angle versus energy at a beam momentum of 5 GeV/c, after applying the optimized selection cuts. The left panel shows the signal channel $\gamma\gamma$, while the right panel shows the background channel $\pi^0\pi^0$. The applied selection includes: (1) exactly two reconstructed photons, (2) $\bar{p}p$ system energy greater than 5.6 GeV, and (3) an opening angle cut defined as $\theta_{\text{open}} > 0.219 + \frac{0.424}{E_{\bar{p}p}-0.740}$. These cuts enhance signal purity by excluding background-dense regions.

Comparison of Count Rate Estimates

Figure 8.13 presents the count rate distributions of the signal and background channels as a function of $\cos\theta$ at a beam momentum of 5 GeV/c, comparing different criteria of event selection. The top row (a) corresponds to the signal process $\bar{p}p \to \gamma\gamma$, while rows (b) and (c) show the dominant background channels $\pi^0\gamma$ and $\pi^0\pi^0$, respectively. For each channel, the left and right plots illustrate the effect of the kinematic fit probability cuts $P_{\text{KinFit}} > 0.3$ and $P_{\text{KinFit}} > 0.7$.

Across all channels, the red points represent events with no selection, showing the highest count rates, including substantial background contributions. The magenta points correspond to cuts taken from Ref. [1], which reduce background but still retain a sizable number of background events. The blue points show the effect of the optimized cuts proposed in this section, which include requiring exactly two reconstructed photons, a $\bar{p}p$ energy above 5.6 GeV, and an opening angle cut that depends on energy.

For the signal channel (row a), the optimized cuts (blue) retain a significant portion of the distribution across $\cos\theta$, indicating good signal preservation. In contrast, for the background channels (rows b and c), the optimized cuts suppress the count rate by several orders of magnitude. This contrast between signal retention and background suppression leads to an improved signal-to-background ratio.

Additionally, increasing the kinematic fit probability threshold from 0.3 to 0.7 further

reduces the background, particularly for the $\pi^0\pi^0$ channel. This suggests that P_{KinFit} can be an effective handle to enhance signal purity. Overall, these plots support the effectiveness of the optimized selection strategy in isolating the signal while minimizing contamination from dominant backgrounds.

Signal to Background Ratio

Figure 8.14 illustrates the signal-to-background ratio for the two main background channels, $\pi^0\gamma$ and $\pi^0\pi^0$, at a beam momentum of 5 GeV/c. The distributions are shown as a function of $\cos\theta$, with different panels comparing results obtained with two thresholds on the kinematic fit probability: $P_{\text{KinFit}} > 0.3$ (left) and $P_{\text{KinFit}} > 0.7$ (right). Each plot compares three sets of cuts: no selection (red), reference cuts from Ref. [1] (magenta), and the optimized selection developed in this study (blue).

The results clearly demonstrate that the optimized selection provides the highest signal-to-background ratio across most $\cos\theta$ bins, particularly for the $\pi^0\pi^0$ background, where an improvement of over two orders of magnitude is observed compared to the no-cut scenario. The $\pi^0\gamma$ background also shows a significant reduction under the optimized selection, though its signal-to-background ratio remains higher than $\pi^0\pi^0$, indicating it's the more dominant background after cuts.

Increasing the P_{KinFit} threshold from 0.3 to 0.7 further enhances the signal-to-background ratio, especially in the forward and backward regions, where background contributions are more significant. This shows the effectiveness of using kinematic constraints in combination with optimized energy and angle selections. These findings support the use of this optimized cut strategy for significantly improving analysis sensitivity by efficiently suppressing background while preserving the signal.

8.4.4 Optimization Based on Photon Multiplicity

This section presents the optimization strategy for improving the signal-to-background ratio based on the photon multiplicity observed in the final state. Two main selection criteria were studied: a loose selection requiring more than one reconstructed photon ($N_\gamma > 1$), and a stricter selection requiring exactly two reconstructed photons ($N_\gamma = 2$). Additionally, further cuts on the kinematic fit probability and photon energy were investigated to enhance the purity of the signal. The following subsections provide a comparative analysis of these criteria and their effect on the signal and background channels.

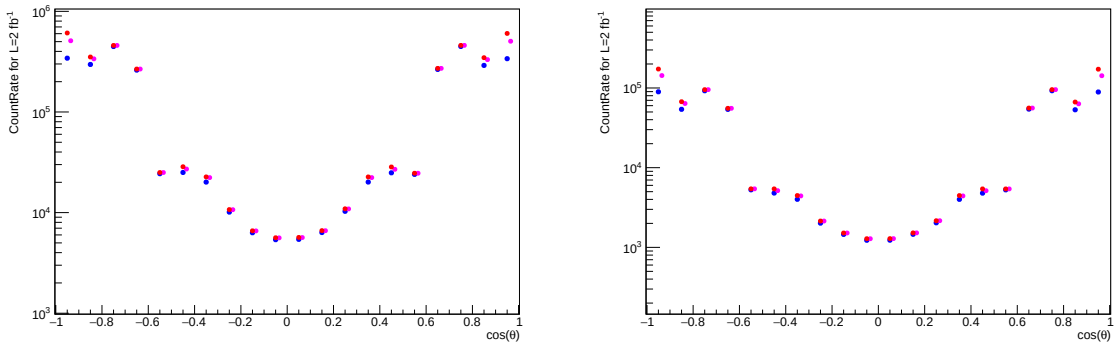

(a) Count rate of signal channel $\gamma\,\gamma$

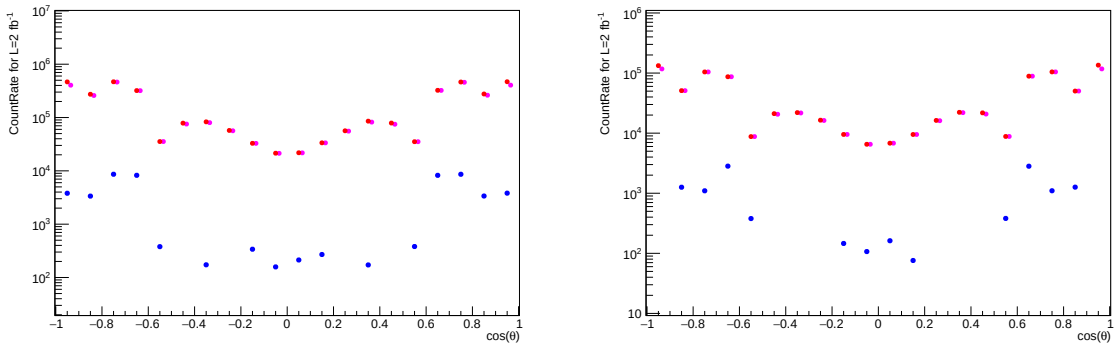

(b) Count rate of background channel $\pi^0\,\gamma$

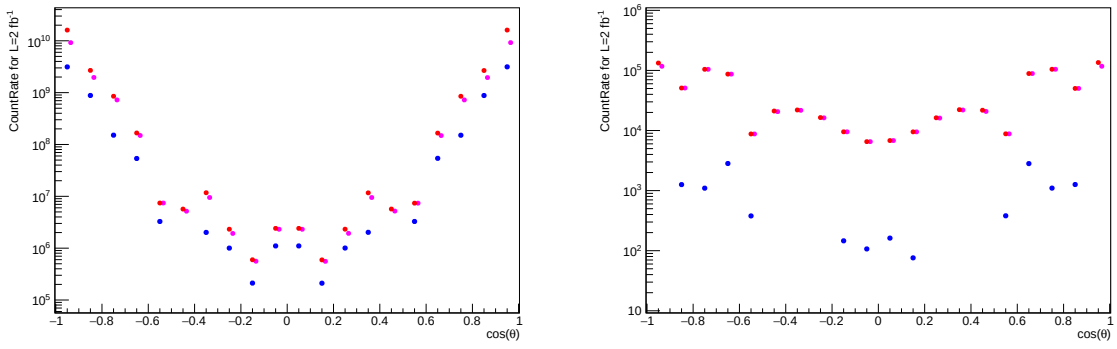

(c) Count rate of background channel $\pi^0\,\pi^0$

- Opening angle cut + $N_\gamma = 2$ + $E_{\bar{p}p} > 5.6$
- Cuts from Ref. [1]
- No Cuts

Figure 8.13: Count rate distributions as a function of $\cos\theta$ for the signal and background channels at a beam momentum of 5 GeV/c. Each row corresponds to a different channel: (a) signal $\gamma\gamma$, (b) background $\pi^0\gamma$, and (c) background $\pi^0\pi^0$. The left column shows the distributions after applying a kinematic fit probability cut of $P_{\text{KinFit}} > 0.3$, while the right column corresponds to a stricter selection with $P_{\text{KinFit}} > 0.7$. Three different sets of selection criteria are compared.

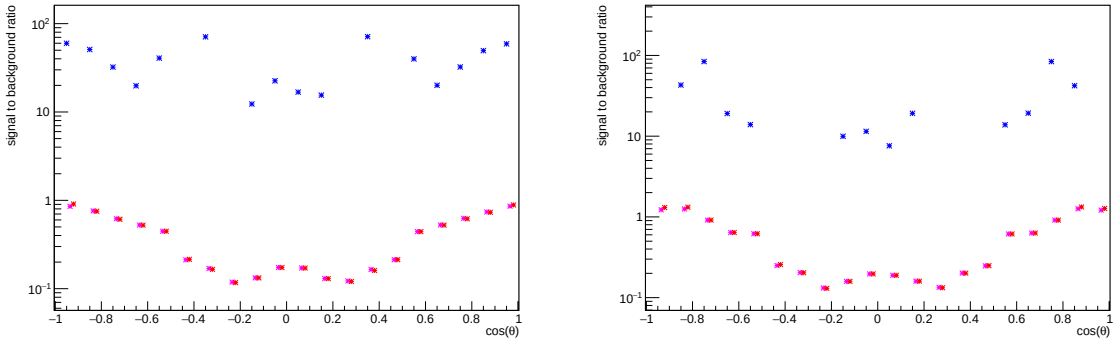

(a) Signal-to-background ratio for the background channel $\pi^0\,\gamma$

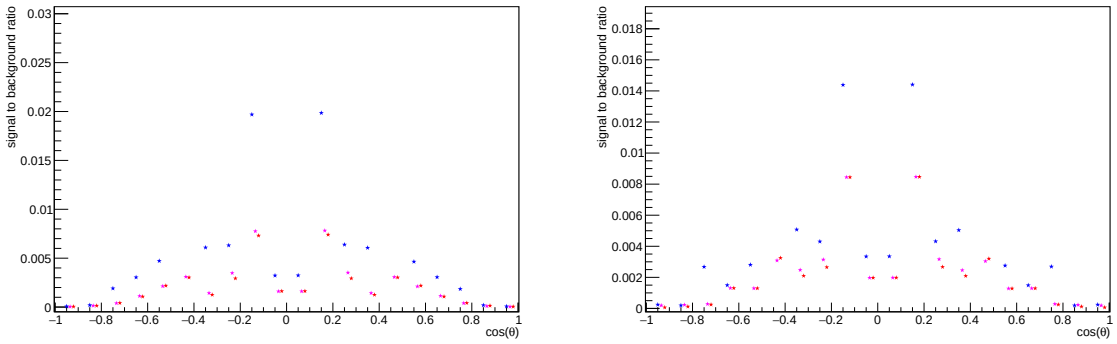

(b) Signal-to-background ratio for the background channel $\pi^0\,\pi^0$

- Opening angle cut + $N_\gamma = 2$ + $E_{\bar{p}p} > 5.6$
- Cuts from Ref. [1]
- No Cuts

Figure 8.14: Signal-to-background ratio distributions for the dominant background channels at a beam momentum of 5 GeV/c, plotted as a function of $\cos\theta^*$. Row (a) corresponds to the background channel $\pi^0\gamma$, while row (b) shows results for the background channel $\pi^0\pi^0$. The left column presents the results for a kinematic fit probability requirement of $P_{\text{KinFit}} > 0.3$, and the right column for $P_{\text{KinFit}} > 0.7$. Three sets of selection criteria are compared: no cuts (red), cuts from Ref. [1] (magenta), and the optimized selection used in this work (blue), which includes an opening angle cut, a requirement of exactly two photons, and $E_{\bar{p}p} > 5.6$ GeV.

8.4.4.1 Comparison Between $N_\gamma > 1$ and $N_\gamma = 2$ Conditions

Figure 8.15 shows the energy distribution of the reconstructed $\bar{p}p$ system for the signal process $\gamma\gamma$ and the background process $\pi^0\pi^0$, at a beam momentum of 5 GeV/c. The distribution is plotted on a logarithmic y-axis to capture the wide range of event counts. For each process, two different photon selection criteria are considered: a loose selection requiring more than one reconstructed photon ($N_\gamma > 1$), and a stricter selection requiring exactly two reconstructed photons ($N_\gamma = 2$).

For the signal channel, the stricter selection enhances the peak structure near the nominal beam energy, indicating that requiring two clean photon candidates helps isolate signal events more effectively. In contrast, the $\pi^0\pi^0$ background shows a broader and more diffuse energy distribution, especially for the looser selection. The stricter requirement of $N_\gamma = 2$ significantly suppresses the background, emphasizing the importance of photon multiplicity cuts in enhancing signal-to-background separation.

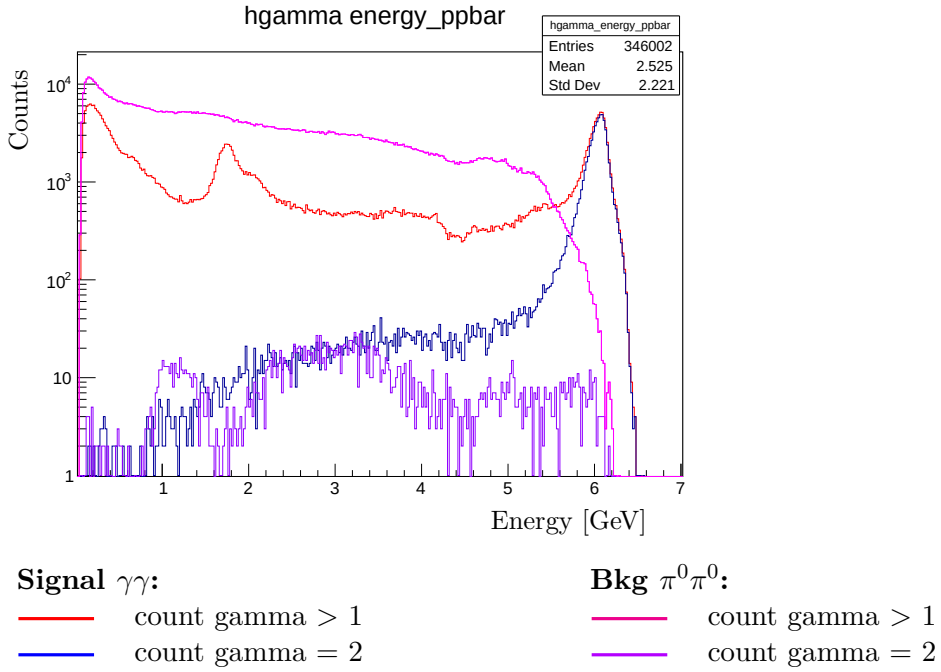

Figure 8.15: Energy distribution of the reconstructed $\bar{p}p$ system for the signal channel ($\gamma\gamma$) and background channel ($\pi^0\pi^0$) at a beam momentum of 5 GeV/c. The y-axis represents event counts on a logarithmic scale. For both signal and background, two selection criteria are shown: events with more than one reconstructed photon ($N_\gamma > 1$) and those with exactly two reconstructed photons ($N_\gamma = 2$).

8.4.4.2 Comparison of $N_\gamma = 2$ with Additional Kinematic Fit and Energy Cuts

The energy distribution of the reconstructed $\bar{p}p$ system is shown in Figure 8.16 for a beam momentum of 5 GeV/c. The plot compares signal events from the $\bar{p}p \to \gamma\gamma$ channel to background processes $\pi^0\pi^0$ and $\pi^0\gamma$. For each channel, two sets of selection criteria are applied: one requiring only two reconstructed photons ($N_\gamma = 2$), and another with stricter conditions involving a 4C kinematic fit ($P_{\text{KinFit}} > 0.01$) and a minimum photon energy of $E_\gamma > 5.7$ GeV. The signal without cuts (red line) shows a pronounced peak around 5.9 GeV, corresponding to the well-reconstructed $\gamma\gamma$ final state. Applying the tighter selection (blue line) reduces low-energy background and sharpens the signal. Backgrounds from $\pi^0\pi^0$ and $\pi^0\gamma$ are more prominent in the low-energy region when only loose cuts are applied (purple and green), but are significantly suppressed with the tighter selection (magenta and brown), illustrating the effectiveness of the additional constraints in enhancing the signal-to-background ratio.

Signal to Background Ratio

Figure 8.17 presents the signal-to-background ratios obtained after applying optimized selection criteria, including the photon multiplicity requirement ($N_\gamma = 2$), an energy threshold cut, and various probabilities for the 4C kinematic fit ($P_{\text{KinFit}} > 0.01$, 0.1, 0.3, and 0.7). The plots are shown for beam momenta of 2.5 GeV/c, 5 GeV/c, and 10 GeV/c, with the left column corresponding to the background channel $\bar{p}p \to \pi^0\gamma$ and the right column to $\bar{p}p \to \pi^0\pi^0$.

At 2.5 GeV/c, a reasonable signal-to-background ratio is observed only for the $\pi^0\gamma$ background, while for the $\pi^0\pi^0$ channel, no events survive the selection cuts, preventing signal-to-background computation. This is due to insufficient background statistics in this channel after applying tight cuts, particularly at low beam energies. At 5 GeV/c and 10 GeV/c, the signal-to-background ratio is observed across both background channels. As expected, the signal-to-background ratio improves significantly with tighter kinematic fit probabilities, with $P_{\text{KinFit}} > 0.7$ yielding the cleanest signal for most regions in $\cos\theta$. The improvement is more pronounced for the $\pi^0\gamma$ channel, whereas the $\pi^0\pi^0$ background tends to dominate at forward and backward angles even with stricter selection.

Overall, increasing the beam momentum and tightening the kinematic fit constraint both contribute to enhanced background suppression, though the effectiveness varies depending on the background channel and angular region.

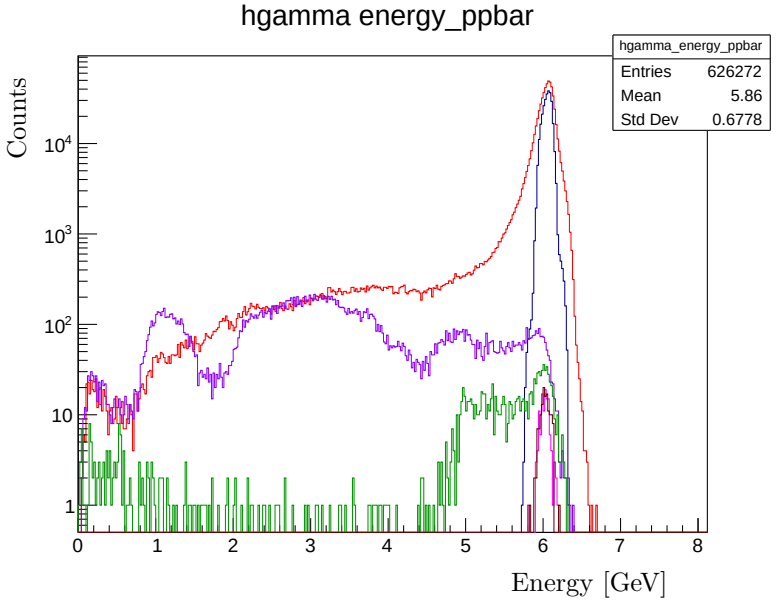

Signal:

count gamma = 2

count gamma = 2 + $P_{\text{KinFit}} > 0.01$ + $E_\gamma > 5.7\,\text{GeV}$

Bkg $\pi^0\pi^0$:

count gamma = 2

count gamma = 2 + $P_{\text{KinFit}} > 0.01$ + $E_\gamma > 5.7\,\text{GeV}$

Bkg $\pi^0\gamma$:

count gamma = 2

count gamma = 2 + $P_{\text{KinFit}} > 0.01$ + $E_\gamma > 5.7\,\text{GeV}$

Figure 8.16: Energy distribution of the reconstructed $\bar{p}p$ system for signal ($\gamma\gamma$) and background channels ($\pi^0\pi^0$, $\pi^0\gamma$) at a beam momentum of $5\,\text{GeV}/c$. The y-axis shows event counts on a logarithmic scale. Each channel is plotted for two selection criteria: a loose selection ($\text{N}_\gamma = 2$) and a tighter selection including a kinematic fit ($P_{\text{KinFit}} > 0.01$) and energy threshold ($E_\gamma > 5.7\,\text{GeV}$).

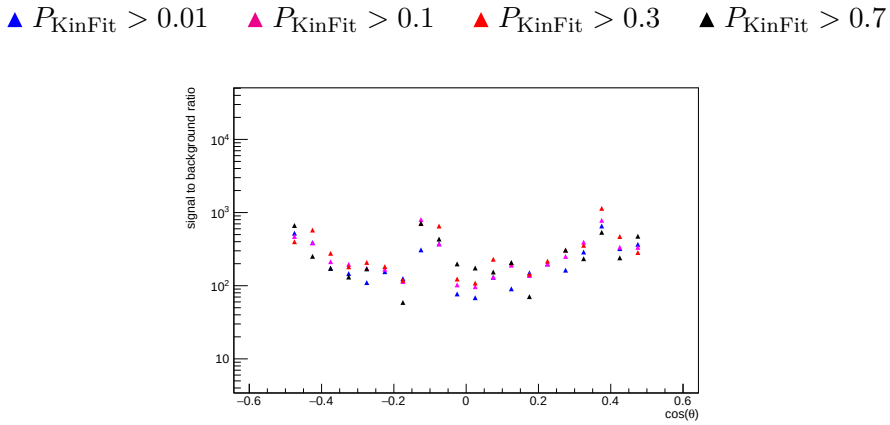

(a) $p_{\text{beam}} = 2.5$ GeV/c

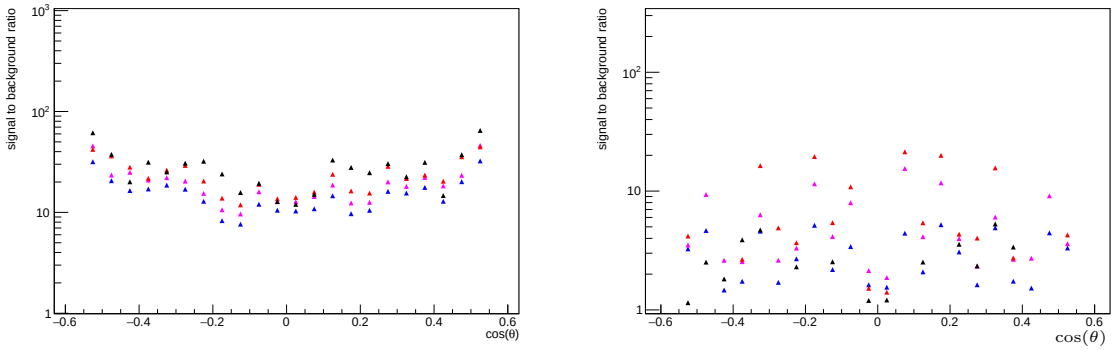

(b) $p_{\text{beam}} = 5$ GeV/c

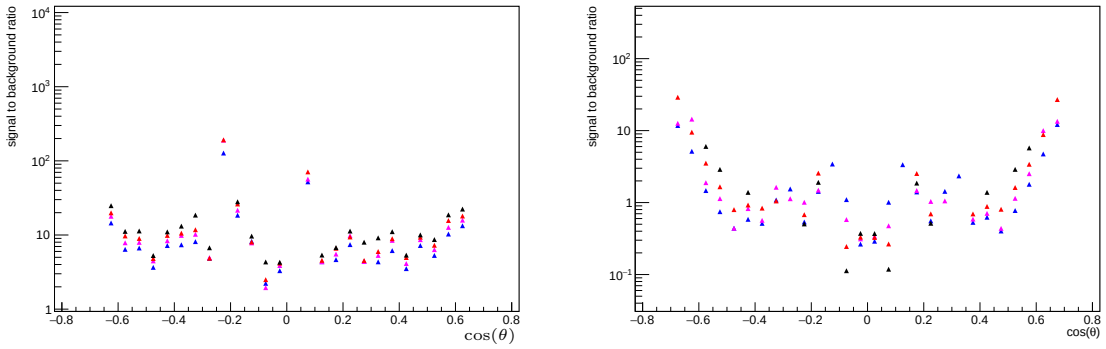

(c) $p_{\text{beam}} = 10$ GeV/c

Figure 8.17: Signal-to-background ratio as a function of $\cos\theta$ at different beam momenta and for various kinematic fit probabilities P_{KinFit}. The left column shows results for the $\bar{p}p \to \pi^0\gamma$ background, while the right column corresponds to $\bar{p}p \to \pi^0\pi^0$. At 2.5 GeV/c, the signal-to-background ratio is shown only for the $\pi^0\gamma$ channel, as no $\pi^0\pi^0$ background events survive the selection cuts, due to limited statistics. Tighter fit probabilities improve the signal-to-background ratio across all momenta, with the cleanest separation achieved at $P_{\text{KinFit}} > 0.7$.

8.4.5 Effect of Conditional Kinematic Fitting Based on Energy for $p_{\bar{p}} = 5$ GeV/c

In order to optimize the signal-to-background ratio, the effect of conditionally applying the kinematic fit based on the energy $E_{\bar{p}p}$ was investigated. Specifically, the fit was applied only for events with $E_{\bar{p}p} < 6.1$ GeV, while events above this threshold were left unfit. The energy cut-off value of 6.1 GeV is motivated by the energy distribution of the signal and background channels, as shown in the energy spectrum in Figure 8.16 (see previous section), where the signal exhibits a pronounced peak near this value.

Figure 8.18 presents the resulting signal-to-background ratios for four different minimum kinematic fit probability thresholds: $P_{\text{KinFit}} > 0.01$, 0.1, 0.3 and 0.7. In each case, empty triangle markers denote the signal-to-background ratio before applying the conditional kinematic fit and energy selection, while filled triangles represent the signal-to-background ratio after the cuts. Contrary to expectations, the application of these selection criteria leads to a reduction in the signal-to-background ratio across all probability thresholds, particularly in the central region of $\cos\theta$, where signal contributions typically dominate. This indicates that while background is being suppressed, the cuts also significantly reduce the signal events. The gradual tightening of the kinematic fit probability threshold contributes to further background suppression, but at the cost of diminishing the overall signal-to-background ratio ratio.

Signal to Background Ratio

To provide a consolidated view of the signal-to-background ratio behavior across different kinematic fit probability thresholds, Figure 8.19 presents a compact summary of the results previously shown in separate plots. The upper panel illustrates the signal-to-background ratio distributions after applying four distinct thresholds on the kinematic fit probability: $P_{\text{KinFit}} > 0.01$, 0.1, 0.3 and 0.7.

The lower panel complements this by comparing the pre-cut (empty triangles) and post-cut (filled triangles) results. Across all selected kinematic fit probability thresholds, the signal-to-background ratio is generally lower after the cuts, particularly in the central angular region. This indicates that while the cuts reduce background, they also suppress the signal more severely, resulting in an overall reduction in the signal-to-background ratio.

Although the cuts succeed in eliminating a fraction of the background, the modest or even negative impact on the signal-to-background ratio suggests limited effectiveness. Among

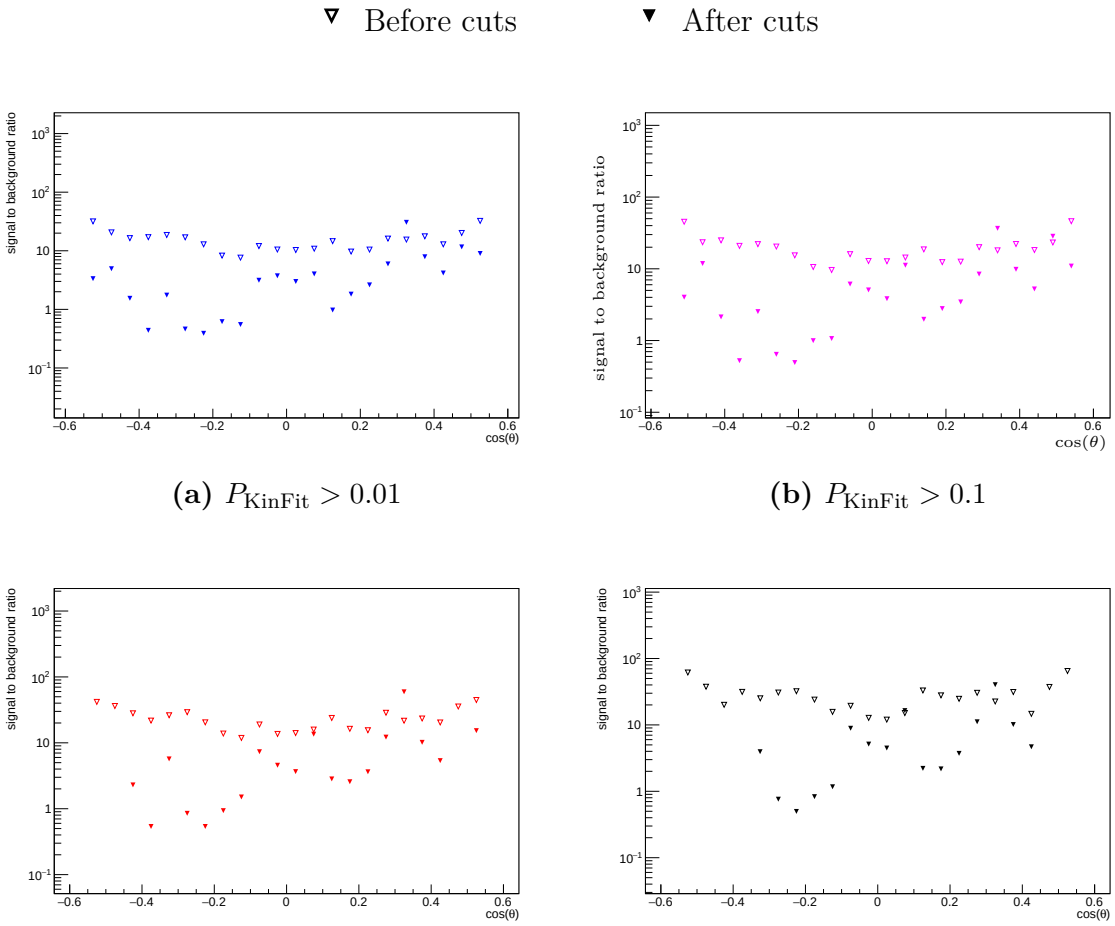

(a) $P_{\text{KinFit}} > 0.01$ **(b)** $P_{\text{KinFit}} > 0.1$

(c) $P_{\text{KinFit}} > 0.3$ **(d)** $P_{\text{KinFit}} > 0.7$

Figure 8.18: Signal-to-background ratio distributions for the $\bar{p}p \to \gamma\gamma$ signal channel at $p_{\bar{p}} = 5$ GeV/c, under the application of conditional kinematic fit constraints. In all plots, a kinematic fit is applied only if $E_{\bar{p}p} < 6.1$ GeV and skipped otherwise. Each panel corresponds to a different threshold on the kinematic fit probability: (a) $P_{\text{KinFit}} > 0.01$, (b) $P_{\text{KinFit}} > 0.1$, (c) $P_{\text{KinFit}} > 0.3$, and (d) $P_{\text{KinFit}} > 0.7$. Empty triangles indicate the signal-to-background ratio before applying the conditional kinematic fit and energy cuts, while filled triangles show the signal-to-background ratio after the cuts.

the thresholds tested, $P_{\text{KinFit}} > 0.3$ and > 0.7 perform slightly better, but not to a degree that justifies their use as a default suppression strategy. Consequently, this method will not be adopted in subsequent stages of the analysis.

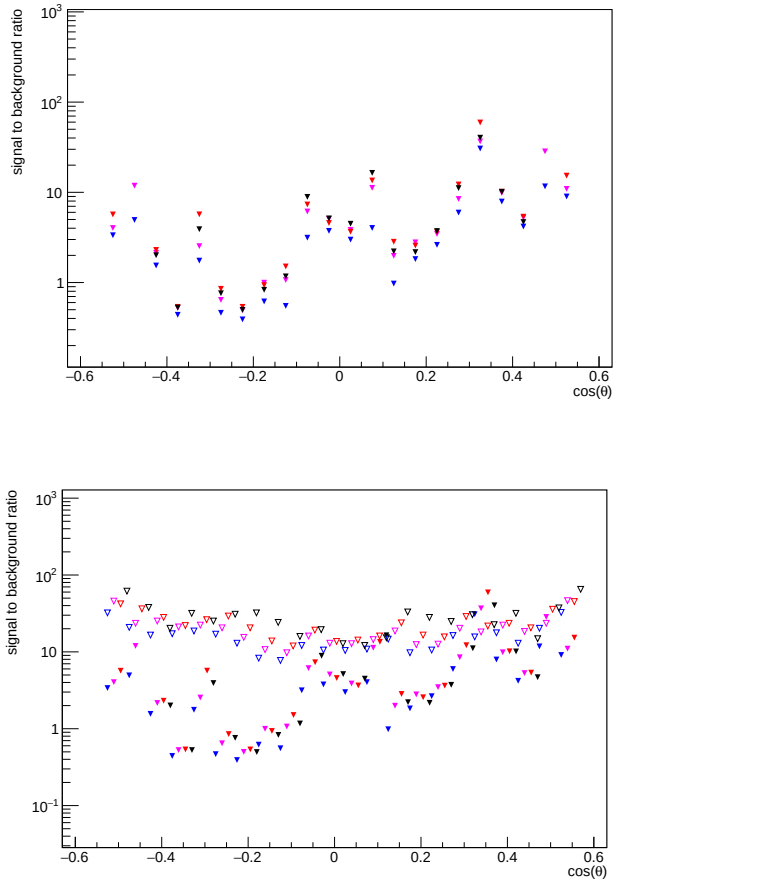

Figure 8.19: Compact representation of the signal-to-background ratio at different P_{KinFit} thresholds for beam momentum $p_{\bar{p}} = 5\,\text{GeV}/c$. The upper panel shows the signal-to-background ratio after applying kinematic fit probability cuts of $P_{\text{KinFit}} > 0.01$, 0.1, 0.3, and 0.7. The lower panel includes both the post-cut (filled triangles) and pre-cut (empty triangles) signal-to-background ratios for each case, enabling a direct visual comparison of the improvement achieved by the fit probability selection.

8.4.6 Figure of Merit (FoM)

To evaluate how effectively the kinematic fit improves the signal purity across different angular regions, we define and calculate a Figure of Merit (FoM) as follows:

1. Select a probability threshold for the kinematic fit, P_{KinFit}, e.g., 0.3.
2. Choose an angular bin in $\cos(\theta)$, such as $-0.5 < \cos(\theta) < -0.2$.
3. For that angular bin, calculate the average signal-to-background ratio:

$$\left\langle \frac{S}{B} \right\rangle = \frac{1}{N} \sum_{i=1}^{N} \left(\frac{S}{B} \right)_i$$

   where N is the number of data points in the selected bin.

4. Compute the average signal count rate (efficiency) in the same bin:

$$\langle S \rangle = \frac{1}{N} \sum_{i=1}^{N} S_i$$

5. Calculate the Figure of Merit:

$$\text{FoM} = \frac{\left\langle \frac{S}{B} \right\rangle}{\langle S \rangle}$$

6. Repeat the calculation for different values of P_{KinFit} to observe how FoM varies with the fit quality.
7. Repeat steps 2–6 for other angular ranges, such as:
   - $-0.1 < \cos(\theta) < 0.1$
   - $0.1 < \cos(\theta) < 0.2$
   - $0.2 < \cos(\theta) < 0.5$
8. Plot the Figure of Merit as a function of P_{KinFit} for each angular range to visualize the results.

This procedure provides a quantitative way to assess the balance between signal purity and efficiency achieved through the kinematic fit in different angular regions.

The Figure of Merit (FoM), shown in Figure 8.20, quantifies the effectiveness of the optimized selection criteria in enhancing signal purity. It is calculated as the ratio of the average signal-to-background ratio to the average signal count rate within a given angular bin, as described in the procedure above.

This analysis uses the best-performing selection cuts, as determined in Section 8.4.4, which focused on optimizing the signal-to-background ratio based on photon multiplicity. The selection included requiring exactly two reconstructed photons ($N_\gamma = 2$), along with additional constraints on kinematic fit probability and photon energy.

The plot presents the FoM as a function of the kinematic fit probability threshold for different $\cos\theta$ ranges. It is observed that for the central region ($0.1 < \cos\theta < 0.2$), the FoM reaches a peak at a moderate probability cut (around 0.3), indicating an optimal balance between background suppression and signal retention. A similar, though less pronounced, trend is observed for the $-0.1 < \cos\theta < 0.1$ range. In contrast, the backward region ($-0.5 < \cos\theta < -0.2$) shows a lower overall FoM and weaker dependence on the probability threshold.

These results suggest that the effectiveness of kinematic fit cuts varies with angular region, and that a probability threshold of approximately 0.3 may offer an optimal choice for signal enhancement in the central $\cos\theta$ range.

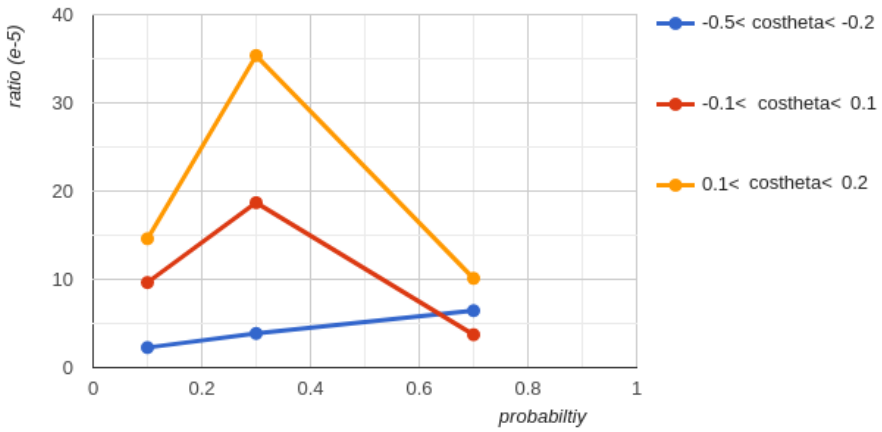

Figure 8.20: Figure of Merit (FoM) as a function of the kinematic fit probability for three different angular regions in $\cos\theta$. The FoM is computed using the optimized selection cuts discussed in Section 8.4.4, combining the effects of photon multiplicity, photon energy, and kinematic fit criteria. A peak is observed in the central region ($0.1 < \cos\theta < 0.2$) around $P_{\text{KinFit}} > 0.3$, indicating the most effective background suppression relative to signal retention.

8.5 Expected Cross-Sections with Statistical Uncertainties after Background Suppression at Integrated Luminosities of 2 fb^{-1} and 0.1 fb^{-1}

Figure 8.21 presents the differential cross sections as a function of $\cos\theta$ for three beam momenta: 2.5 GeV/c, 5 GeV/c, and 10 GeV/c. The left column shows the extracted signal cross section for the process $\bar{p}p \to \gamma\gamma$ after subtraction of the $\pi^0\gamma$ background, assuming an integrated luminosity of $2\,\mathrm{fb}^{-1}$, while the right column presents results at a lower luminosity of $0.1\,\mathrm{fb}^{-1}$. The plotted differential cross sections include the propagation of statistical uncertainties following background subtraction.

The differential cross section is computed using the relation:

$$\frac{d\sigma}{d\cos\theta} = \frac{N}{\mathcal{A} \cdot \Delta\cos\theta \cdot \mathcal{L}}$$

where N is the event count, $\mathcal{A}$ is the acceptance, $\Delta\cos\theta$ is the bin size, and $\mathcal{L}$ is the integrated luminosity.

Each distribution in the figure is shown for various cuts on the probability of the 4C kinematic fit: $P_{\mathrm{KinFit}} > 0.01$, 0.1, 0.3 and 0.7. To improve readability, the data points for the different probability thresholds have been slightly shifted to the right within each bin to avoid overlap in the plots.

The angular distributions exhibit a pronounced dip in the central region ($\cos\theta \approx 0$) with enhancements in the forward and backward directions, which is characteristic of the production kinematics in two-photon annihilation processes. The differential shape remains largely unchanged across different kinematic fit probability thresholds, confirming the stability of the result under increasingly stringent selection criteria.

A clear difference in the size of statistical uncertainties is visible between the left and right panels. The error bars are significantly smaller in the left column due to the higher integrated luminosity ($2\,\mathrm{fb}^{-1}$), which provides greater event statistics. In contrast, the larger uncertainties in the right column (especially for the 10 GeV/c case) are primarily a result of the much lower luminosity ($0.1\,\mathrm{fb}^{-1}$), further affected by reduced event yields due to tighter kinematic fit requirements, which selectively suppress background but also reduce signal yield.

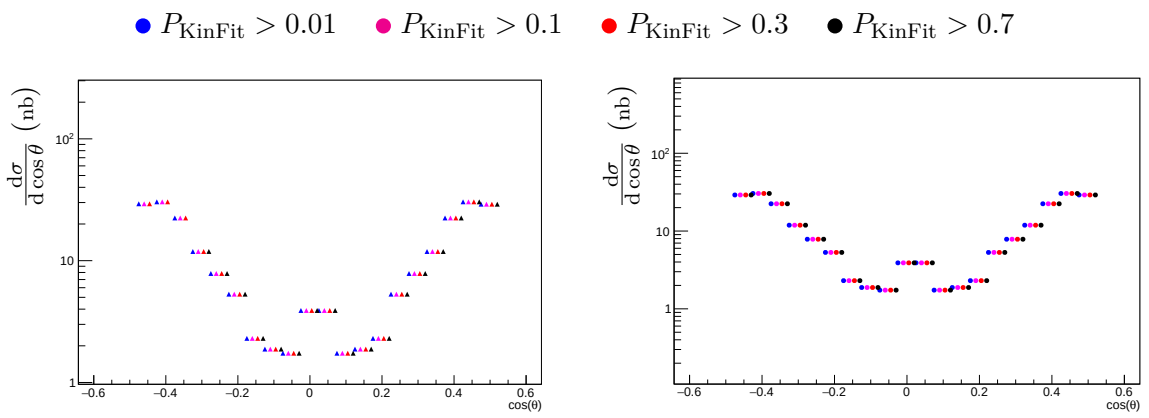

(a) $p_{\text{beam}} = 2.5$ GeV/c

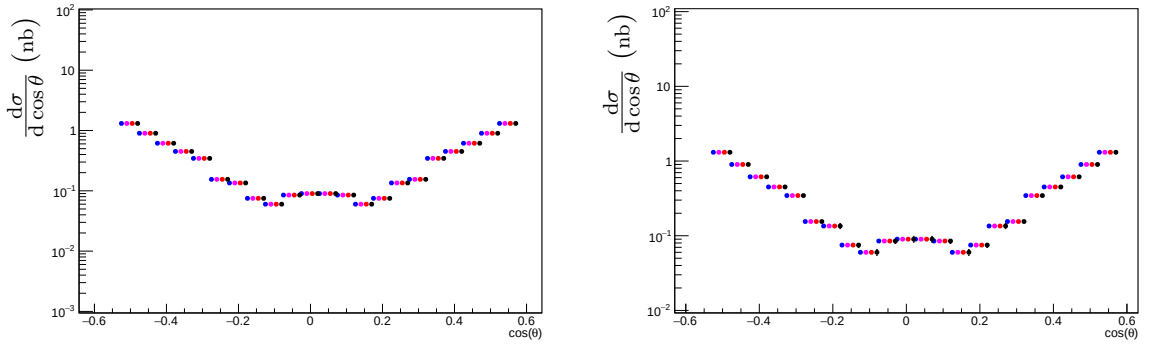

(b) $p_{\text{beam}} = 5$ GeV/c

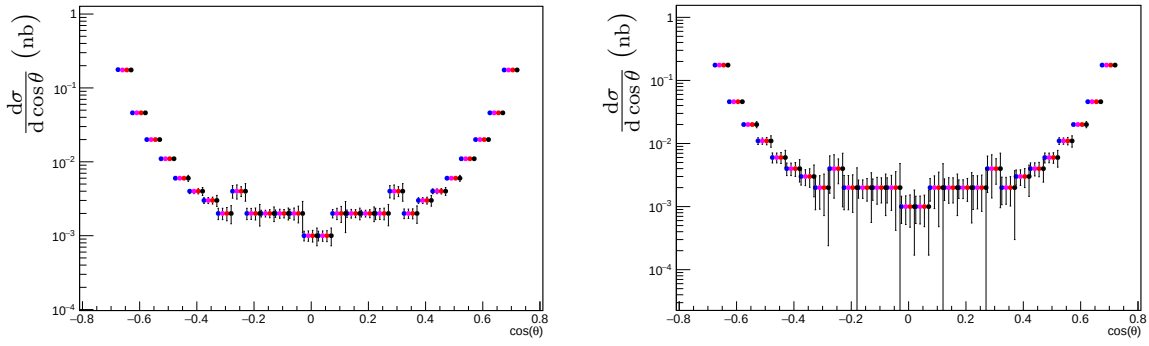

(c) $p_{\text{beam}} = 10$ GeV/c

Figure 8.21: Differential cross section as a function of $\cos\theta$ for the signal channel $\bar{p}p \to \gamma\gamma$ at three different beam momenta: (a) $p_{\text{beam}} = 2.5\,\text{GeV}/c$, (b) $p_{\text{beam}} = 5\,\text{GeV}/c$, and (c) $p_{\text{beam}} = 10\,\text{GeV}/c$. The left column corresponds to an integrated luminosity of $2\,\text{fb}^{-1}$, while the right column shows results for $0.1\,\text{fb}^{-1}$. Each plot displays the differential cross section for various selection thresholds on the 4C kinematic fit probability P_{KinFit}. The points corresponding to different P_{KinFit} thresholds are slightly shifted along the x-axis for better visibility, although they represent the same $\cos\theta$ bin centers.

8.6 Impact of GEM Geometry Improvements on Photon Reconstruction Efficiency

In this study, the reconstruction efficiency under the updated GEM configuration was also investigated. The analysis, focusing on the impact of improved GEM geometry on photon reconstruction, is discussed below.

Figure 8.22 illustrates the reconstruction efficiency of photons as a function of $\cos\theta$, comparing two different GEM geometries. The red points represent the performance with the improved GEM geometry, while the blue points correspond to the original configuration. Despite the fact that the same random seed was not used in both simulations—which can introduce some statistical variation—the overall trend is clearly visible: the red points consistently lie above the blue in most regions of $\cos\theta$. This indicates a general improvement in the reconstruction efficiency of photons after implementing the enhanced GEM geometry. The effect is particularly notable in the central region, suggesting that the modifications to the detector layout have led to better photon tracking and acceptance. These results support the conclusion that the updated GEM configuration offers superior reconstruction performance and should be preferred for future analyses.

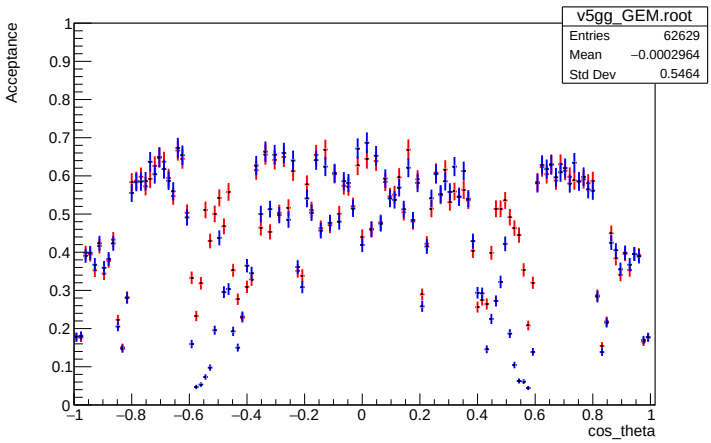

Figure 8.22: Red points show the reconstruction efficiency of photons using the improved GEM geometry, compared to the previous geometry shown in blue. Although the same random seed was not used in both simulations, the overall trend clearly indicates an increase in reconstruction efficiency across most $\cos\theta$ bins. This suggests that the updated GEM geometry enhances photon detection performance, particularly in the central region, thereby validating the effectiveness of the geometry improvements.

8.7 Conclusion and Discussion

This chapter presented a detailed study of the feasibility of measuring the $\bar{p}p \to \gamma\gamma$ reaction within the $\overline{\text{P}}$ANDA experiment. The analysis focused on the identification and suppression of the dominant background channels, namely $\bar{p}p \to \pi^0\gamma$ and $\bar{p}p \to \pi^0\pi^0$, which mimic the signal through the production of neutral mesons that decay into photons. By exploiting kinematic properties such as photon opening angles, total energy, and photon multiplicity, along with conditional kinematic fitting, a set of optimized selection criteria was developed to enhance the signal-to-background ratio.

The results demonstrate that the reaction can indeed be measured with sufficient statistical significance, particularly at beam momenta around 5 GeV/c. The background suppression techniques applied—most notably the opening angle cuts, energy thresholds, and selection based on kinematic fit probability—were shown to significantly reduce contamination from π^0-associated channels, improving the purity of the selected sample.

The figure-of-merit (FoM) analysis and signal efficiency calculations further validate the reliability of the proposed strategy. Based on the expected cross-section and the performance of the applied cuts, it was estimated that a statistically significant measurement of the $\bar{p}p \to \gamma\gamma$ process can be achieved with an integrated luminosity of approximately 2 fb^{-1}. Assuming a typical $\overline{\text{P}}$ANDA running luminosity of $\mathcal{L} = 2 \times 10^{31}$ cm^{-2}s^{-1}, an integrated luminosity of 2 fb^{-1} would correspond to roughly 100 days of data taking, accounting for realistic detector uptime and data acquisition efficiency.

Despite the presence of significant background contributions, this reaction remains a promising probe of hadronic structure in the timelike region. Furthermore, the analysis techniques developed here are applicable to other exclusive channels of interest within the broader $\overline{\text{P}}$ANDA physics program.

In conclusion, the optimization strategy developed in this chapter lays the foundation for a clean and efficient selection of the $\gamma\gamma$ final state in antiproton-proton annihilation, paving the way for future studies of the reaction dynamics and its implications in the context of hadronic structure and two-photon physics.

9 | Summary and Outlook

This work has explored the potential of studying exclusive two-photon and photon-meson final states in antiproton-proton annihilation using the $\overline{\text{P}}$ANDA detector at FAIR, with a particular focus on the reactions $\bar{p}p \to \pi^0\gamma$, $\bar{p}p \to \pi^0\pi^0$, and $\bar{p}p \to \gamma\gamma$. The $\pi^0\gamma$ and $\gamma\gamma$ channels are of particular interest due to their sensitivity to the internal dynamics of hadrons and their potential to access Generalized Distribution Amplitudes (GDAs). In contrast, the $\pi^0\pi^0$ channel does not provide direct access to GDAs but was studied in detail as a dominant background process that must be reliably identified and subtracted in the analysis of the other two channels.

The analysis was based on detailed Monte Carlo simulations using the PandaRoot framework. For each channel, a complete analysis chain was implemented, including event generation, detector simulation, photon reconstruction, invariant mass analysis, background suppression techniques, and signal extraction. Differential cross sections were successfully extracted for the $\pi^0\gamma$ and $\gamma\gamma$ channels across multiple beam momenta, while the $\pi^0\pi^0$ channel was studied with a focus on signal reconstruction and background control.

Although these studies were conducted with full detector simulations, the results also provide insight into the feasibility of performing such measurements during the early operation of $\overline{\text{P}}$ANDA, referred to as *Phase-1*. During this stage, $\overline{\text{P}}$ANDA will operate with a partial detector configuration and reduced luminosity. Nevertheless, the photon-based final states investigated here are particularly well-suited for early data-taking, owing to the wide angular acceptance and excellent resolution of the electromagnetic calorimeter, even in its initial configuration.

This work demonstrates that the studied channels are not only theoretically significant for exploring nucleon structure via GDAs, but also experimentally measurable during $\overline{\text{P}}$ANDA Phase-1. The expected event rates and detector coverage are sufficient to validate reconstruction methods and refine analysis strategies ahead of full operation.

Looking ahead, future work can incorporate Phase-1-specific detector geometry and beam conditions into simulations for more accurate projections. Improved background modeling and increased Monte Carlo statistics will further enhance the precision of signal extraction

and uncertainty estimation. Once real data becomes available, comparison with simulations will be essential for validating reconstruction performance and extracting differential observables with high confidence.

The approaches developed in this thesis—ranging from photon reconstruction to cross-section extraction—can be extended to more complex final states and higher-mass meson production channels. These will further deepen our understanding of GDAs and the partonic structure of hadrons. $\overline{\text{P}}$ANDA's capabilities in accessing time-like regimes through exclusive processes will play a key role in shaping future studies of QCD and hadron dynamics.

Bibliography

[1] T. A. Armstrong and et al. Two-Body Neutral Final States Produced in Antiproton-Proton Annihilations at $2.911 < \sqrt{s} < 3.686$ GeV. *Phys. Rev. D*, 56(5):2509–2531, Sep 1997.

[2] M. Lutz and et al. PANDA Physics Performance Report. *arXiv:0903.3905v1 [hep-ex]*, 2009.

[3] Paola Gianotti. Results and Perspectives in Hadron Spectroscopy. *Physica Scripta*, 2012(T150):014014, 2012.

[4] Stephen Godfrey and Stephen L. Olsen. The Exotic XYZ Charmonium-Like Mesons. *Ann. Rev. Nucl. Part. Sci.*, 58:51–73, 2008.

[5] Chang-Zheng Yuan and Stephen Lars Olsen. The BESIII Physics Programme. *Nature Reviews Physics*, 1(8):480–494, 2019.

[6] S. Dubynskiy and M. B. Voloshin. Hadro-Charmonium. *Phys. Lett. B*, 666(4):344–346, September 2008.

[7] C. J. Morningstar and M. Peardon. Glueball Spectrum from an Anisotropic Lattice Study. *Phys. Rev. D*, 60:034509, 1999.

[8] Y. Chen et al. Glueball Spectrum and Matrix Elements on Anisotropic Lattices. *Phys. Rev. D*, 73(1), January 2006.

[9] Eberhard Klempt and Alexander Zaitsev. Glueballs, Hybrids, Multiquarks. *Phys. Rep.*, 454(1–4):1–202, December 2007.

[10] Murray Gell-Mann. A Schematic Model of Baryons and Mesons. *Phys. Lett.*, 8:214–215, 1964.

[11] L. Maiani, F. Piccinini, A. D. Polosa, and V. Riquer. Diquark-Antidiquark States with Hidden or Open Charm and the Nature of X(3872). *Phys. Rev. D*, 71(1), January 2005.

[12] Nora Brambilla et al. Substructure of Multiquark Hadrons (Snowmass 2021 White Paper), 2022.

[13] Sören Lange, Martin Galuska, Simon Reiter, Elisabetta Prencipe, and Stefano Spataro. New Studies of XYZ States at PANDA, 2013.

[14] M. Diehl, T. Gousset, and B. Pire. Exclusive Production of Pion Pairs in $\gamma^*\gamma$ Collisions at Large Q^2. *Phys. Rev. D*, 62(7):073014, Sep 2000.

[15] B. Singh et al. Feasibility Studies of Time-Like Proton Electromagnetic Form Factors at PANDA at FAIR. *Eur. Phys. J. A*, 52:325, 2016.

[16] I. Zimmermann. *Feasibility Studies for the Measurement of the Time-Like Electromagnetic Proton Form Factors at the PANDA Experiment.* PhD thesis, Johannes Gutenberg University, 2018.

[17] A. Z. Dubnickova, S. Dubnicka, and M. P. Rekalo. Investigation of Nucleon Electromagnetic Form-Factors in the Unphysical Region by Means of the $\overline{\mathrm{N}}\mathrm{N} \to \pi^0 \mathrm{l}^+\mathrm{l}^-$ Reactions. *Z. Phys. C*, 70:473, 1996.

[18] J. P. Lansberg, B. Pire, and L. Szymanowski. On the Physical Relevance of the Study of $\gamma^\star\gamma \to \pi^0\pi^0$ at Small t and Large Q^2. *Phys. Rev. D*, 76(111502), 2007.

[19] B. Pire and L. Szymanowski et al. Production of a Pion in Association with a High-Q^2 Dilepton Pair in $\overline{p}p \to$ Annihilation at GSI-FAIR. *Phys. Lett. B*, 622:83, 2005.

[20] D. Müller. Wave Functions, Evolution Equations and Evolution Kernels from Light-Ray Operators of QCD. *Fortschr. Phys.*, 42(2):101–141, 1994.

[21] A. V. Radyushkin. Scaling Limit of Deeply Virtual Compton Scattering. *Phys. Lett. B*, 380(3):417–425, 1996.

[22] A. V. Radyushkin. Nonforward Parton Distributions. *Phys. Rev. D*, 56(9):5524–5557, November 1997.

[23] Xiangdong Ji. Gauge-Invariant Decomposition of Nucleon Spin. *Phys. Rev. Lett.*, 78(4):610–613, Jan 1997.

[24] Xiangdong Ji. Deeply Virtual Compton Scattering. *Phys. Rev. D*, 55(11):7114–7125, Jun 1997.

[25] M. Diehl. Generalized Parton Distributions. *Phys. Rep.*, 388(2–4):41–277, December 2003.

[26] Cédric Mezrag. An Introductory Lecture on Generalised Parton Distributions. *Few-Body Systems*, 63(3), August 2022.

[27] Benali, Meriem and Mazouz, Malek and Fonvieille, Helene. Deeply Virtual Compton Scattering on the Neutron: JLab Experiment E08-025. *EPJ Web of Conferences*, 112:01004, 2016.

[28] J. Marroncle. Feasibility Studies for GPD's Measurement at COMPASS. In *10th International Workshop on High-Energy Spin Physics (SPIN 03)*, pages 331–336, Dubna, 2004. JINR.

[29] Jacques Soffer. Summary of the Workshop DUBNA-SPIN 07, 2008.

[30] Ventura, Brian. *Study of Deeply Virtual Compton Scattering at COMPASS at CERN.* PhD thesis, HAL CCSD, U. Paris-Saclay, 2021.

[31] Krešimir Kumerički, Simonetta Liuti, and Hervé Moutarde. GPD Phenomenology and DVCS Fitting: Entering the High-Precision Era. *Eur. Phys. J. A*, 52(6), June 2016.

[32] Stefan Diehl. Experimental Exploration of the 3D Nucleon Structure. *Prog. Part. Nucl. Phys.*, 133:104069, 2023.

[33] A. V. Belitsky, D. Müller, and A. Kirchner. Theory of Deeply Virtual Compton Scattering on the Nucleon. *Nucl. Phys. B*, 629(1–3):323–392, May 2002.

[34] Chatagnon, Pierre. *Nucleon Structure Studies with CLAS12 at Jefferson Lab: Time-like Compton Scattering and the Central Neutron Detector.* PhD thesis, IJCLab, Orsay, 2020.

[35] P. Chatagnon and et al. First Measurement of Timelike Compton Scattering. *Phys. Rev. Lett.*, 127(26):262501, December 2021.

[36] L. Favart, M. Guidal, T. Horn, and P. Kroll. Deeply Virtual Meson Production on the Nucleon. *Eur. Phys. J. A*, 52(6), June 2016.

[37] Nabil Chouika. *Generalized Parton Distributions and Their Covariant Extension: Towards Nucleon Tomography.* PhD thesis, Université Paris-Saclay, September 2018.

[38] M. Diehl, T. Gousset, B. Pire, and O. Teryaev. Probing Partonic Structure in $\gamma^*\gamma \to \pi\pi$ near Threshold. *Phys. Rev. Lett.*, 81(9):1782–1785, August 1998.

[39] P. Kroll and A. Schaefer. Probing Moments of Baryon-Antibaryon Generalized Parton Distributions at BELLE and FAIR, 2013.

[40] M. Diehl, P. Kroll, and C. Vogt. Two-Photon Annihilation into Baryon-Antibaryon Pairs. *The European Physical Journal C*, 26(4):567–577, February 2003.

[41] M. Artuso et al. Measurement of the Cross Section for $\gamma\gamma \to p\bar{p}$. *Phys. Rev. D*, 50(9):5484–5490, Nov 1994.

[42] H. Hamasaki et al. Measurement of the Proton-Antiproton Pair Production from Two-Photon Collisions at TRISTAN. *Phys. Lett. B*, 407(2):185–192, 1997.

[43] G. Abbiendi et al. Measurement of the Cross Section for the Process $\gamma\gamma \to p\overline{p}$ at $\sqrt{s_{ee}} = 183$–189 GeV at LEP. *Eur. Phys. J. C*, 28(1):45–54, May 2003.

[44] C. C. Kuo et al. Measurement of $\gamma\gamma \to p\overline{p}$ Production at Belle. *Phys. Lett. B*, 621(1):41–55, 2005.

[45] C. C. Kuo. Studies of $\gamma\gamma \to \Lambda\overline{\Lambda}$, $\Sigma^0\overline{\Sigma^0}$ Production at Belle, 2006.

[46] P. Achard et al. Λ and Σ^0 Pair Production in Two-Photon Collisions at LEP. *Phys. Lett. B*, 536(1):24–33, 2002.

[47] S. Anderson et al. $\Lambda\bar{\Lambda}$ Production in Two-Photon Interactions. *Phys. Rev. D*, 56(5):R2485–R2490, Sep 1997.

[48] Igor Vorobiev. Exclusive $\rho\rho$ Production in $\gamma\gamma$ Interaction at LEP. *AIP Conf. Proc.*, 892:301–304, 2007.

[49] Qin-Tao Song. Generalized Distribution Amplitudes and Gravitational Form Factors for Pion, 2018.

[50] P. Kroll and A. Schäfer. The Process $\bar{p} \to \gamma\pi$ Within the Handbag Approach. *Eur. Phys. J. A*, 26(1), Oct 2005.

[51] M. Durante, P. Indelicato, B. Jonson, V. Koch, K. Langanke, U.-G. Meißner, E. Nappi, T. Nilsson, Th. Stöhlker, E. Widmann, and M. Wiescher. All the Fun of the FAIR: Fundamental Physics at the Facility for Antiproton and Ion Research. *Phys. Scr.*, 94(3):033001, Jan 2019.

[52] H. Gutbrod. *FAIR Baseline Technical Report – Volume 1 Executive Summary.* GSI, Darmstadt, 2006.

[53] The PANDA Collaboration. Precision Resonance Energy Scans with the PANDA Experiment at FAIR – Sensitivity Study for Width and Line-Shape Measurements of the X(3872), 2019.

[54] FAIR Center. Research at FAIR – Facility for Antiproton and Ion Research. https://fair-center.eu/overview/research, 2025. Accessed: 2024-10-16.

[55] PANDA Collaboration. PANDA Experiment Homepage. https://panda.gsi.de/, 2023. Accessed: 2024-01-30.

[56] PANDA Collaboration. Technical Design Report for the PANDA Solenoid and Dipole Spectrometer Magnets, 2009.

[57] PANDA Collaboration. Technical Design Report for the: PANDA Micro Vertex Detector, 2012.

[58] PANDA Collaboration. Technical Design Report for the $\overline{P}$ANDA (AntiProton Annihilations at Darmstadt) Straw Tube Tracker: Strong Interaction Studies with Antiprotons. *The European Physical Journal A*, 49(2), February 2013.

[59] PANDA Collaboration. GEM Tracker. https://panda.gsi.de/article/gem-tracker, n.d. Accessed: 2024-01-03.

[60] PANDA Collaboration. Technical Design Report for the PANDA Forward Time-of-Flight Detector. https://panda.gsi.de/publication/re-tdr-2016-004, 2018. RE-TDR-2016-004.

[61] PANDA Collaboration. Technical Design Report for PANDA Electromagnetic Calorimeter (EMC), 2008.

[62] PANDA Collaboration. Technical Design Report for the PANDA Barrel DIRC Detector, 2017.

[63] PANDA Collaboration. Technical Design Report for the PANDA Muon System. https://panda.gsi.de/publication/re-tdr-2012-003, 2013. RE-TDR-2012-003.

[64] J. Smyrski et al. Design of the forward straw tube tracker for the PANDA experiment. *JINST*, 12(06):C06032, 2017.

[65] PANDA Collaboration. Technical Design Report for the Panda Forward Spectrometer Calorimeter, 2017.

[66] PANDA Collaboration. Technical Design Report for the PANDA Forward Time of Flight Detector. https://panda.gsi.de/publication/re-tdr-2016-004, 2018. RE-TDR-2016-004.

[67] PANDA Collaboration. Technical Design Report for the PANDA Luminosity De-

tector. https://panda.gsi.de/publication/re-tdr-2015-001, 2018. RE-TDR-2015-001.

[68] Stefano Spataro and (for the PANDA Collaboration). The PandaRoot framework for simulation, reconstruction and analysis. *Journal of Physics: Conference Series*, 331(3):032031, dec 2011.

[69] PANDA Collaboration. PandaRoot Rho Tutorial - General Documentation of Rho Classes, 2023. [Accessed: 2024-09-12].

[70] Baljeet Saharan. Feasibility Study for the Measurement of πN Transition Distribution Amplitudes at PANDA in $p \to J/\psi\pi^0$. *Physical Review D*, 95, Feb 2017.

List of Figures

List of Tables

Acknowledgements

First and foremost, I would like to express my sincere gratitude to Prof. Kai-Thomas Brinkmann for giving me the opportunity to pursue my PhD in Germany. His continuous support, both academically and personally, has been invaluable, and I am deeply grateful for the trust he placed in me throughout this journey. I am also truly thankful to Dr. Stefan Diehl for being my principal investigator, mentor, and guide. His patience with my learning curve and his willingness to give me the space to grow both as a researcher and as a person have been invaluable. I would like to extend special thanks to Dr. Hans-Georg Zaunick, who was always available when I needed guidance or a listening ear. His practical advice and thoughtful support, both within the institute and beyond, helped me more times than I can count. I would like to thank my external supervisor, Prof. Karin Schönning from Uppsala University, for her helpful insights and suggestions as a member of my PhD committee. Her support was greatly appreciated throughout my research. I would also like to thank Aron for his hands-on support, especially when I ran into ROOT-related issues. I am particularly grateful for the help he offered during my early days. Not only did his guidance help me find my feet from scratch, but our conversations about navigating life in Germany as expats were always enlightening and encouraging. I would also like to thank Dr. Marc Strickert from the fifth floor for his timely technical assistance and for providing essential licenses, including Overleaf Premium and Microsoft Office, which greatly facilitated my work.

On a personal note, I wish to thank my husband, whom I met during my time in Germany. His love and support have been my anchor during the most challenging moments of this PhD. Finally, my deepest gratitude goes to my family—my father and sisters—who supported me unconditionally from afar. My father, in particular, has been a constant source of encouragement throughout this journey. His thoughtful messages and ongoing interest in my progress kept me focused and motivated.

Erklärung der Urheberschaft

Ich erkläre: Ich habe die vorgelegte Dissertation selbstständig und ohne unerlaubte fremde Hilfe und nur mit den Hilfen angefertigt, die ich in der Dissertation angegeben habe. Alle Textstellen, die wörtlich oder sinngemäß aus veröffentlichen Schriften entnommen sind, und alle Angaben, die auf mündlichen Auskünften beruhen, sind als solche kentlich gemacht. Bei den von mir durchgeführten und in der Dissertation erwähnten Untersuchungen habe ich die Grundsätze guter wissenschaftlicher Praxis, wie sie in der "Satzung der Justus-Liebig- Universität Gießen zur Sicherung guter wissenschaftlicher Praxis" niedergelegt sind, eingehalten.

Faiza Khalid

Giessen, Juli 2025